Experimental Investigation into the Enhanced Diamagnetic Perturbations and Electric Currents Downstream of the High Power Helicon Plasma Thruster

B. Race Roberson

A dissertation

submitted in partial fulfillment of the

requirements for the degree of

Doctor of Philosophy

University of Washington

2013

Reading Committee:

Robert Winglee, Chair

Robert Holzworth

Michael McCarthy

Program Authorized to Offer Degree:

Earth and Space Sciences

University of Washington

Abstract

Experimental Investigation into the Enhanced Diamagnetic Perturbations and Electric Currents Downstream of the High Power Helicon Plasma Thruster

B. Race Roberson

Chair of the Supervisory Committee:

Professor Robert Winglee

Earth and Space Sciences

The high power helicon (HPH) is a compact plasma source that can generate downstream densities of 10^{17}-10^{18} m^{-3} and directed ion energies of 50-70 eV, without the need for grids that can corrode with use or requiring a larger engine diameter. Generating a quasi-neutral plasma beam that can stay collimated and impart significant power and momentum to a distant target in space has a variety of potential applications including beamed propulsion and the remediation of space debris. In order to understand and improve the coupling mechanism between the helicon source antenna and the downstream plasma, measurements were made in the plasma plume downstream of the propagating wave magnetic field and the diamagnetic perturbation of the background magnetic field with the presence of the plasma. This magnetic

field perturbation (ΔB) peaks at more than 15 gauss in magnitude downstream of the plasma source and propagates tens of centimeters downstream, cancelling the base magnetic field provided by the experiment as it propagates. Taking the curl of this measured magnetic perturbation suggests a peak current density of 20 kA m^{-2}. These diamagnetic perturbations and electric currents were correlated with an increase in wave-plasma coupling and increased acceleration of the plasma particles downstream. In order to increase the energy coupled into the plasma and drive a larger diamagnetic perturbation a further distance downstream a second, larger radius antenna was added roughly one wavelength downstream co-axially with the first antenna and driven in phase with the first. This resulted in improved collimation of the plasma beam over a meter downstream, increased diamagnetic perturbation, and an increase in the ion energies downstream of more than 20 eV. This work includes the development of a high power plasma source that is capable of generating a dense, collimated plasma beam with exhaust velocities comparable to devices of similar power levels but in a compact size without the need of electric grids; as well as measuring diamagnetic plasma perturbations that are larger than in any similar plasma experiment previously published, suggesting new capabilities for studying high beta (but cold and directed) plasmas in a laboratory setting.

Table of Contents:

Figure List with Abbreviated Captions:

Table List

Acknowledgments:

First I would like to thank Professor Robert Winglee for his expert guidance and support over the years, and for providing me with the role model of the energetic, creative scientist that the 21st century needs more than anything else.

Thank you as well to Professors Robert Holzworth and Michael McCarthy, for serving on my advisory committee as well as the years of advice and assistance whenever asked. I would also thank Professor Peter Rhines for serving on my committee and giving me his support when I needed it, despite the long years between milestones.

Thank you to my lab mates former, Dr. Tim Ziemba, Dr. Louis Giersch, and Dr. James Prager for all your help and company along the long road here.

Thank you to the other students in the lab who joined with me in our endeavors and I wish you all the future success in the world, David Peters, Ilia Slobodov, Ian Johnson, Nao Murakami, and everyone else who has taken up Robert's banner in the pursuit of more powerful plasma devices.

Thank you to the other students and faculty of the space group, friends past and present, whose advice and company helped me reach this point. Thanks as well to Robert Frost, for volunteering his expertise and enthusiasm to the research group.

Thank you to all my friends, who came along for the ride.

Lastly, thank you to my family for bearing with me all these years, and for everything else as well, far too much to list here, in a document that's already on the long side.

Chapter 1: Introduction to Electric Propulsion and the High Power Helicon

Section 1.1: Motivation for the Research:

Beyond the atmosphere of Earth, there is a rich wealth of scientific discoveries to be gained by those with the technology to reach it. Mars has had a geological history, perhaps even a biological history, as long and as fascinating as Earth's and of which we have only begun to scratch the surface with shallow digging robotic probes. The same investigative methods we've used for decades to study our own world's atmosphere, surface, and interior could be easily applied to Mars and would answer many of our questions if the right instruments could be put in place. Each of the other planets and moons of the solar system could benefit from the same attention, but their accessibility from Earth has so far prevented us from doing more than observing them from afar with infrequent orbiters or flybys. At the edge of the solar system is a host of objects that remain mostly frozen from the early formation of the solar system and contain within them physics evidence of the processes that were taking place billions of years ago and have been otherwise lost. Even as close to Earth as our own magnetosphere, the region being studied is so large that not nearly enough spacecraft are available to simultaneous measure the relevant regions to be able to answer a host of questions about its dynamics and processes.

The current technology for exploring space is prohibitively expensive and limited in scope. These problems tie into the propulsion systems used in space for exploration being inefficient and unsuited to the task of moving large amounts of equipment around the solar system cheaply. Advanced electric propulsion can be used to fill this gap.

Section 1.2: Chemical Propulsion and its Limitations:

The only technology currently available that is capable of lifting spacecraft payloads off of Earth's surface and entering orbit is chemical rocket power. These rockets operate by combining one or more chemicals (possibly with a catalyst) to release stored chemical energy so that the by-products of the reaction are at a much higher temperature than the components. As the temperature rises, the fluid by-products begin to build up to a high pressure inside the reaction chamber. When the reaction chamber pressure is higher than the pressure outside the rocket, the difference in pressure begins to force fuel by-products out of the exhaust port. With increasing pressure, the pressure gradient will force more material out of the exhaust port in the same unit of time, so that the exhaust velocity V_{ex} will increase as well as the thrust of the rocket:

$$T = \frac{\partial m}{\partial t} v_{ex} \tag{1.1}$$

Here T is the thrust in newtons, V_{ex} is the exhaust velocity of the fuel, and m is the mass of the fuel being expelled within a length of time t in seconds.

In addition to increasing the energy released and the temperature of the fluid, most chemical rockets also constrict the flow of the exhaust out of the rocket with a nozzle to increase V_{ex}. As the exhaust port narrows down, the fluid must travel faster in order to conserve mass flux through a narrower area in the same unit of time without compressing it. This will increase V_{ex} up until the fluid begins to travel as fast as the sound speed, or goes super-sonic. The energy for this increase in flow speed comes from the thermal energy of the fluid, so that it cools in temperature as the V_{ex} increases while passing through the nozzle. Chemical rocket engines therefore seek to increase the temperature of the reaction by-products as high as possible, limited by the energy of the reaction and the ability of the chamber and nozzle to withstand the heat and pressure of the exhaust [1].

This emphasis on increasing exhaust velocity comes from the fact that once the spacecraft is in space and is no longer subjected to large external forces from gravity or aerodynamic drag, the efficiency of the thruster is mostly determined by the exhaust velocity. For an ideal rocket in space not subject to external forces, the thrust of the rocket will be equal and opposite to the rate of change of its momentum:

$$\frac{\Delta P}{\Delta t} = -T \tag{1.2}$$

$$m\frac{\partial v}{\partial t} = -\frac{\partial m}{\partial t} v_{ex} \tag{1.3}$$

for a rocket propelling itself in a vacuum. If the thruster maintains a constant V_{ex} and mass flow rate, then the total change in velocity is given by the classic Tsiolkovsky rocket equation, given here in the form:

$$\frac{M_i}{M_f} = e^{\Delta V / V_{ex}} \tag{1.4}$$

where ΔV is the total change in velocity, M_i is the weight of the spacecraft with all of its fuel, and M_f is the mass after it has all been expended. By increasing the exhaust velocity, this allows the rocket to achieve large changes in velocity without requiring exponentially more fuel mass. This requires making improvements to the exhaust velocity that are significant compared to the total velocity required for the trip, and these values are typically quite high.

	Mars	Jupiter	Saturn
ΔV	14 km/s	64 km/s	110 km/s

Table 1-1: Approximate ΔV required for a one way Hohmann transfer orbit

Some approximate values for the required ΔV are shown in table 1-1 (Prager [2]). These are close to minimum values for the transfer orbits necessary to reach these planets without using other non-rocket sources of ΔV.

Chemical rockets tend to have an exhaust velocity of 3-5 km/s. This is primarily due to the limitations in how the rocket can accelerate the chemical by-products. The exhaust is normally composed of neutral molecules and atoms, that can really only be made more energetic by heating them. This is done by increasing the flow of the reactants into the chamber to release more energy and build to a higher pressure, with the neutral collisions leading to a higher temperature. However, there are structural limits to how high of a temperature the fuel can be raised to, and not all of this thermal energy can be converted to directed kinetic energy by the nozzle. Improvements can be made through careful engineering, but do not go significantly above 5 km/s. Though they provide the large amount of thrust necessary to lift payloads off of Earth, chemical rockets require an enormous amount of fuel to achieve the large ΔV to reach the rest of the solar system because of this limitation in their exhaust velocity [1].

In order to make efficient thrusters for in-space use that can achieve a high V_{ex} and reach distant parts of the solar system with a reasonable amount of fuel, the exhaust needs to be accelerated by other methods besides those used in chemical rockets. Instead of the heated neutral atoms and molecules used for exhaust in chemical rockets, an ionized gas of positive ions and free electrons, a plasma, is used. This plasma can be accelerated and guided by electric and magnetic fields, allowing for many mechanisms that can couple energy into the plasma to give a high exhaust velocity.

Section 1.3A: Description of Laboratory and Thruster Plasmas

Plasma is generally referred to as the fourth state of matter, because of the presence of free charges. The motions of the charged particles in the plasma are affected by both externally applied electric and magnetic fields, and by internal electric and magnetic fields generated by the interaction of the charged particles with each other. This allows plasmas to be capable of organized behaviors over a large volume; as opposed to a neutral fluid where each finite element can only interact through collisions with its immediate neighbors. The composition of the plasma will vary based on the method of ionization, the neutral source material that is ionized, and the collisions between the charged particles of the plasma and the remaining neutrals (if any). Laboratory plasmas like those used in this experiment are typically formed from energetic electrons colliding with neutral gas atoms, with the collision imparting enough energy to one of the electrons in the neutral gas atom to break it free of the nucleus. These collisions result in plasma consisting of singly-charged positive ions of the source gas, free electrons, and neutral atoms of the source gas [3].

The ionization fraction will depend on how much energy is being put into maintaining the plasma against the loss mechanisms. The primary loss mechanism is recombination, with the positive ion capturing an electron and becoming a neutral gas atom again. This occurs through either interaction with the chamber wall with the ion pulling an electron from the wall or through the ion capturing a free electron of low enough energy in the plasma far away from the wall. Other mechanisms that lead to loss of energy from the plasma particles can make them more likely to re-combine. One mechanism is charge exchange, where an energetic ion will collide with a colder neutral atom and capture an electron, resulting in an energetic neutral and a cold ion that is more likely to re-combine with a free electron. Another energy loss mechanism is the discrete emission of photons from the bound electrons of the positive ion [4].

In laboratory plasmas enough energy is added to keep the ionization fraction high so that plasma effects dominate over neutral collisions while the experiment is running. This is followed by an "afterglow" period where the energy is lost due to the mechanisms mentioned and the plasma returns to a neutral gas. In this experiment the ionization fraction was well over 90%, which will be discussed more in Ch. 2.

Section 1.3B: Acceleration of Plasma by Electric Field and the Electrostatic Ion Thruster

The acceleration of charged particles by an electric field forms the basis for one of the standard electric propulsion devices: the electrostatic ion thruster. Charged particles in the presence of electric and magnetic fields will be accelerated by the Lorenz force:

$$\vec{F} = q\left(\vec{E} + \vec{v} \times \vec{B}\right), \tag{1.5}$$

which in the absence of a magnetic field will result in positive ions accelerated along the electric field and free electrons accelerated anti-parallel to the field. Laboratory plasmas that are generated from a neutral gas as described above will have roughly the same number of positive ions and free electrons. In the presence of an external electric field the ions and electrons will move in opposite directions, creating an imbalance of charge that will yield an internally produced electric field in the opposite direction:

$$\nabla \cdot \vec{E} = \frac{e}{\varepsilon_0}\left(n_i - n_e\right), \tag{1.6}$$

to cancel out the imposed electric field, if there are sufficient numbers of electrons and positive ions in the volume [3].

While there is an acceleration of the particles due to the electric field, the ions and electrons are not motionless to begin with. The thermal energy of the ions and the electrons, expressed in their temperatures T_i and T_e, give them a thermal speed so that they are constantly in motion throughout the plasma cloud. The thermal speed of the free electrons is typically orders of magnitude higher than the thermal speed of the comparatively heavy ions so therefore much of the thermal motion of the plasma is taken up by the electrons, with the ions relatively stationary compared to them. This rapid thermal motion of the electrons will work against setting up imbalances in charge between ions and electrons that would lead to internal electric fields as in equation (1.7).

The balance between large numbers of ions and electrons available to move in the presence of an external electric field with the thermal motion of the electrons acting to smooth out any imbalance is represented in the plasma parameter known as the Debye length:

$$\lambda_D = \left(\frac{\varepsilon_0 T_e}{e^2 n_0} \right)^{1/2}, \qquad (1.7)$$

with n_0 being the average plasma density without the external electric field being present. The Debye length roughly represents the diameter of a volume within the plasma where $n_i \neq n_e$ and strong electric fields can develop due to the imbalance of charge. For volumes of plasma significantly larger than this length the plasma is "quasi-neutral", with $n_i \approx n_e \approx n_0$, and there are no large electric fields across the volume of the plasma. If an external voltage is applied across a sufficiently dense plasma, then the ions and electrons within a distance of the plasma edge on order of the Debye length will move to build up an electric field to cancel out the applied field, leaving the rest of the plasma volume unperturbed by it [3].

In order for a thruster to exert an external electric field across the whole volume of plasma to accelerate it, the Debye length must be on the order of the size of the thruster. This is fundamental to the operation of the electrostatic ion thruster, represented in figure: (1.1).

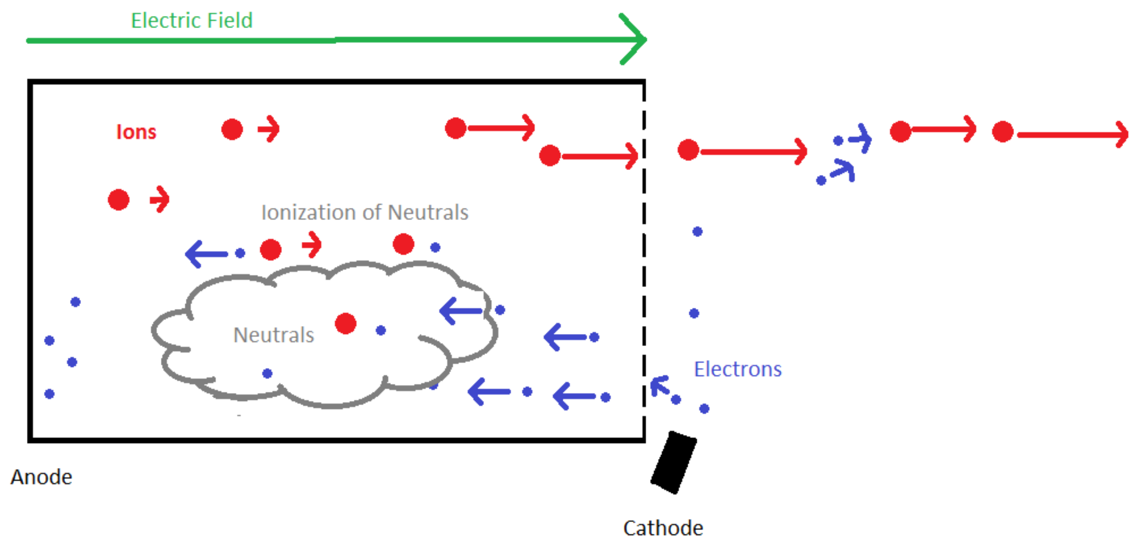

Figure 1.1: Basic Electrostatic Ion Thruster Operation

A cathode at the negative end of the electric potential emits a small number of free electrons outside the exit grid of the thruster. These electrons are accelerated upstream through the thruster by the large electric field generated by the high voltage potential. These energetic electrons collide with neutral gas atoms and ionize them, generating positive ions and additional electrons. These additional electrons accelerate towards the anode at the rear end of the thruster and continue the ionization process, while the positive ions are accelerated by the large electric field towards the cathode. This large drop in electric potential accelerates the positive ions to a high directed velocity, and as they leave the thruster these ions will generate an electric field between the ions downstream and the cloud of electrons emitted from the cathode that have not entered the thruster. This electric field will accelerate electrons from the cathode up to the velocity of the ions, so that the plasma outflow will be quasi-neutral and the thruster won't develop a net charge. The V_{ex} of an electrostatic ion thruster is typically on the order of tens of km/s, with NASA's NSTAR-1 engine having an exhaust velocity between 10-30 km/s depending on the input power [5].

One difficulty with the ion thruster is that the plasma density cannot be increased to improve the ion outflow and the mass flow rate. If the plasma density were increased, the Debye length would decrease and more of the interior of the thruster would be shielded from the accelerating potential drop, decreasing the exhaust velocity. The primary method for increasing the ion outflow rate for an ion thruster is to make the thruster wider and increase the power so as to provide the same potential drop over a larger volume. These both lead to an increase in engine mass, so scaling to higher power (more than tens of kilowatts) is difficult.

Section 1.3C: Guiding Plasma Particles with Magnetic Fields and the Hall Effect Thruster

For electrostatic ion thrusters, the plasma density could not be increased because the electrons in the plasma would adjust themselves to screen out the external electric field as the Debye length decreased. One method of getting around this problem is to use magnetic fields to guide and limit the motion of the electrons to prevent them from building up an internal electric field to cancel out the external field. This is the key process for another standard electric propulsion system, the Hall effect thruster. The force on a charged particle due to the magnetic field in the Lorenz force equation (1.6) depends on the direction of motion of the particle relative to the magnetic field. Motion of the charged particle parallel with the magnetic field does not exert a force on the particle, while any motion perpendicular to the field direction exerts a force on the particle perpendicular to both velocity and magnetic field direction. This perpendicular force on a perpendicular velocity will drive the particle into circular motion around the magnetic field axis, effectively gyrating around the magnetic field. The motion of the charged particle gyrating around the field line will be approximately a circle, with the radius determined by the strength of the magnetic field compared to the momentum of the particle perpendicular to the field, given by the Larmor radius:

$$r_L = \frac{mv_\perp}{|q|B} \tag{1.8}$$

this applies to both the free electrons and the positive ions, and is also referred to as the gyro-radius. If the Larmor radius of the particle is large compared to the length scale over which the magnetic field is established, then the particle will not be significantly deflected by the magnetic field and pass through it in a mostly straight path. If the Larmor radius of the particle is small compared to the length scale of the magnetic field, then the particle will be gyrating in a tight orbit around the magnetic field and not move significantly across the field lines. Movement of the particle parallel to the field will still be uninhibited, but movement across the field will be stopped, and the particle is said to be "well magnetized" and bound to the magnetic field [3].

If the equation for the Larmor radius is re-written to express the perpendicular momentum in terms of perpendicular temperature for the ions compared to the electrons:

$$r_{Li} = \frac{\sqrt{2m_i T_{i\perp}}}{eB} \qquad (1.9) \qquad\qquad r_{Le} = \frac{\sqrt{2m_e T_{e\perp}}}{eB} \qquad (1.10)$$

it becomes apparent that the ion Larmor radius will be dramatically larger than the electron radius. The difference in temperature between the two species will typically be negligible compared to the enormous mass difference between the electrons and the ions. With the appropriate magnetic field strength the electrons can be well magnetized and bound to the field lines while the ions are not, which is the requirement for the operation of the Hall effect thruster, as seen in Figure (1.2).

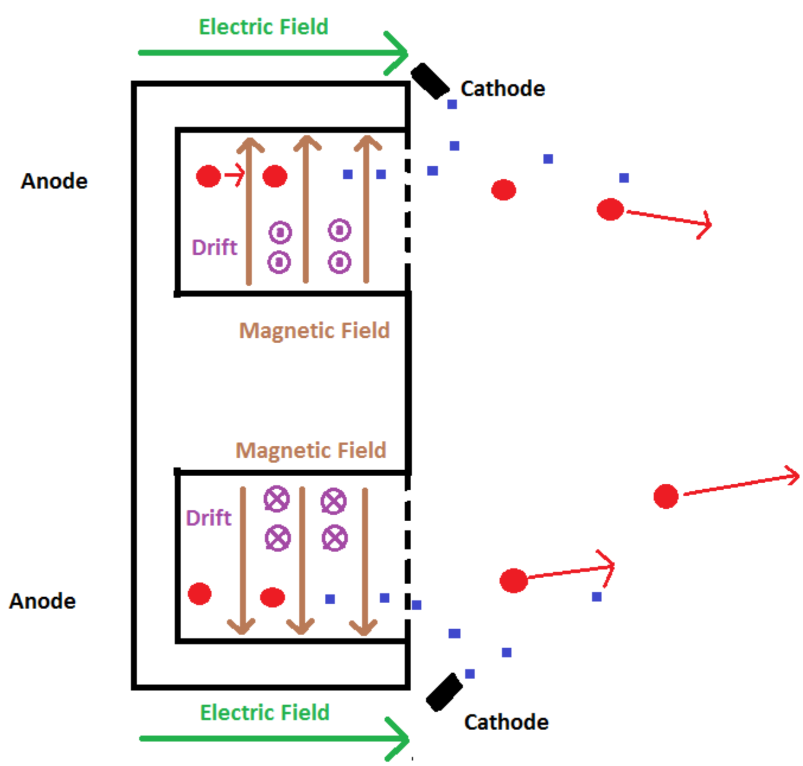

Figure 1.2: Cross section showing basic operation of a Hall effect thruster

The Hall effect thruster has an external cathode that emits electrons and a large voltage difference between the cathode and the anode to accelerate particles similar to what was present in the electrostatic ion thruster. The new component to the Hall thruster is a magnetic field that is perpendicular to the electric field. This magnetic field is intense enough to make the electron Larmor radius small compared to the size of the thruster while the ion Larmor is large compared to the thruster. After the electric field accelerates the electrons into the thruster, they begin to gyrate around the magnetic field and are no longer being accelerated along the electric field. Instead, they move perpendicular to both fields, in the direction given by:

$$\vec{v}_{drift} = \frac{\vec{E} \times \vec{B}}{B^2} \tag{1.11}$$

as a result of the electron moving both parallel and anti-parallel to the electric field during its gyration around the magnetic field, resulting in an asymmetric velocity perpendicular to B. With a sufficiently high electric field, this drift velocity for the electrons can be made sufficiently high such that a collision between the electron and a neutral atom can produce ionization. This will generate a positive ion and another free electron, both of which will now feel the effect of the electric and magnetic fields. The electron will begin to gyrate around the magnetic field and drift with the other electrons azimuthally around the thruster, which is built with azimuthal symmetry for this reason. The positive ions will be accelerated by the electric field towards the cathode and gain a large directed energy, similar to the ion thruster, and their path won't be significantly deflected by the magnetic field [3].

Each time the electrons collide with a neutral atom, whether it ionizes the atom or not, this collision will interfere with its gyration around the magnetic field. This disruption will temporarily keep it from circling around the field or drifting perpendicular to it, and instead the electron will be accelerated by the electric field towards the anode. If more neutrals are added to the system it will result in more collisions and thus more positive ions to be accelerated, but it will also increase the collision rate with the electrons and therefore the rate at which electrons will be able to move across the magnetic field and reach the anode of the thruster. These electrons near the anode will weaken the electric field across the thruster, and lower the directed velocity of the ions leaving the thruster. Hence a balance is reached: between increased neutral mass flow into the thruster to dramatically increase the ion outflow rate over the electrostatic ion thruster, and the collisions with neutrals allowing the electrons to move across the field lines and shield the electrodes from the plasma. The advantage of the Hall effect thruster is the ability to increase the ion outflow rate by increasing the input power (both of the magnetic field and the ionizing electron current) without needing to increase the diameter of the thruster. For example, the Hall effect thruster that powered the SMART-1 space probe launched by the ESA was smaller in size than the NSTAR ion thruster but achieved similar thrust and exhaust speeds for similar input power [6].

A problem shared by both electrostatic ion thrusters and Hall effect thrusters is the erosion of the cathode due to electron loss by emission and through ion impacts. This can act to limit the lifetime of the thruster, though both thruster types have been operated in space for thousands of hours and some have been operated continuously for hundreds of hours without the cathode failing. The larger issue is that of DC electric fields being applied across the plasma with electrodes, which can then be shielded from the plasma by electrons and their effect limited. If the formula for the Larmor radius (1.9) is re-written in terms of the angular frequency of the particles as they gyrate around the field line, called the cyclotron frequency:

$$\omega_c = \frac{|q|B}{m} \qquad (1.12)$$

it is clear that the lighter electrons will gyrate around the field lines thousands of times faster than the comparatively heavy ions. If other particles or external fields act on the charged particle fast enough to interfere with its motion during this gyration, its overall motion will be affected. This was seen in the case of the Hall effect thruster, where collisions with neutrals interfered with the gyro-orbit and resulted in limiting the electron's ability to drift perpendicular to the field.

Section 1.4A: Oscillating Wave Fields and Electrode-less Helicon Sources

If an externally applied electric or magnetic field oscillates with time at a rate that is slow compared to the cyclotron frequency of a charged particle, then the particle will go through the whole gyration with an effectively constant field being applied, and so it will move and drift in a similar fashion to if the field was constant. If the field oscillates at a rate that is fast compared to the cyclotron frequency, the particle will not have time to move a significant distance in response to the field before it has changed direction. The particle will be too slow to respond, and the field will have no net effect on the motion of the particle. The large difference in mass between the electrons and positive ions puts their cyclotron frequencies far enough to allow a frequency range such that:

$$\omega_i << \omega_{field} << \omega_e \qquad (1.13)$$

where ω_{field} is the angular frequency of the oscillating electric or magnetic field. This oscillating field will be too fast to significantly affect the ion motion, but too slow to change direction or strength during the course of an electron's gyro-motion around a magnetic field. The ability to inductively drive electric and magnetic fields that can accelerate the electrons without affecting the ions, and without the use of electrodes, is a key element to the operation of the plasma sources generally known as "helicons".

Helicon plasma sources use a helical shaped antenna to inductively drive electric and magnetic fields to ionize and accelerate plasma without the use of electrodes or grids. The helicon antennas operate over a range of frequencies, but are in the gap between the ion and electron cyclotron frequencies as in equation (1.13). The antennas are designed to oscillate at the resonant frequency of an electromagnetic plasma wave known as a "helicon wave", which is a wave of the same form as the "whistler wave" seen naturally in space plasma environments. The mechanism by which the antenna drives the helicon wave and the details of the wave properties will be described in Chapter 2.

In general terms, the helicon wave is an electromagnetic perturbation of base magnetic field B_0, with wave components B_w and E_w perpendicular to B_0. These wave components twist around B_0 in a helix, and also rotate in time around B_0 at the driven frequency in the range given by (1.13). The wave component is oscillating too fast for the ions to respond, but the electrons are gyrating around the magnetic field (B_0 + B_w) and so when the wave magnetic field vector rotates in time, the electrons are driven around B_0 as well. This rotational velocity for the electrons is perpendicular to the wave magnetic field B_w, and so the Lorenz force (1.6) acts to accelerate the electrons along the base magnetic field B_0. The rotational velocity is also perpendicular to B_0, so there is an additional component of the accelerating the electrons towards the centerline anti-parallel to B_w. Since the helicon wave is accelerating the electrons and not the ions, the electrons moving away from the ions build up a strong electric field that acts to accelerate the ions towards them while decelerating the electrons, the opposite effect to the ions leaving the electrostatic ion thruster or the Hall effect thruster. This electric field is referred to as an "ambipolar electric field" and is illustrated below in Figure 1.3.

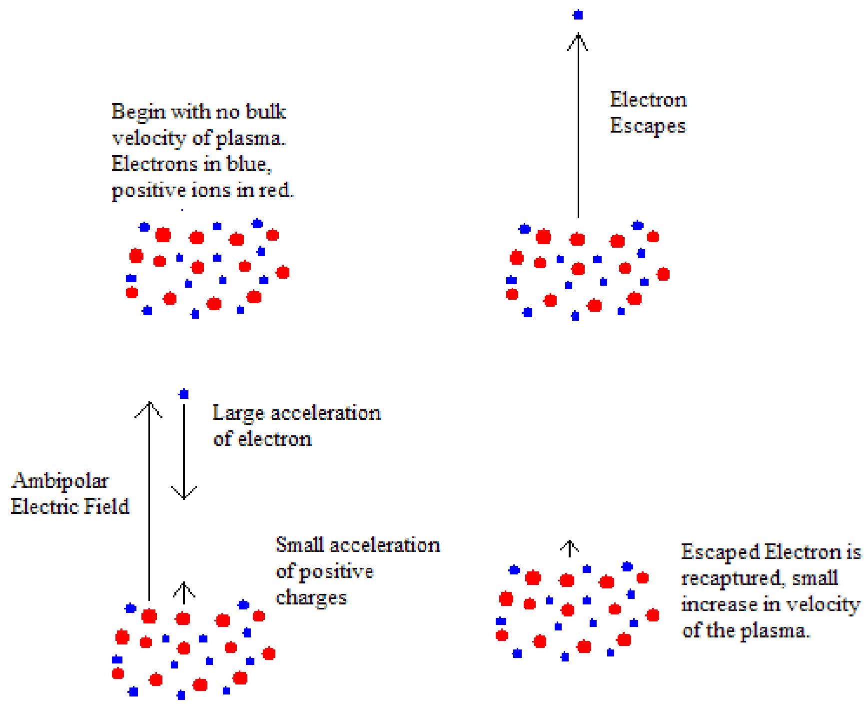

Figure 1.3: Ambipolar acceleration of the ions by the electrons.

This mechanism allows helicons to drive electrons around a base magnetic field to ionize neutrals and generate additional electrons and ions, as well as providing a mechanism to accelerate the plasma downstream out of the thruster without the need for electrodes in the plasma. Similar to the previous thrusters, a balance will be reached between: strength of the base magnetic field (B_0), input wave energy (B_w), collision rate with the neutrals, plasma density, and the exhaust velocity of the plasma. This balance will depend greatly on the balance between the resultant energy of the plasma particles after being ionized and the energy in the magnetic fields.

Section 1.4B: Plasma Beta and the Dynamic Plasma Pressure

So far the discussion of the interaction between the plasma and the magnetic field has involved the interaction of individual charged particles in the plasma with the field, rather than a collective behavior. A more general way to describe the relationship between the particles of the plasma and the background field is to consider the relationship between the thermal pressure of the particles and the magnetic pressure of the background field, called the "plasma beta":

$$\beta = \frac{nkT_e}{\left(B^2 / 2\mu_0 \right)} \tag{1.14}$$

where n is the plasma density and the contribution of the ions to the thermal pressure is insignificant. In regions where the magnetic field is high and the magnetic pressure dominates, $\beta < 1$, the electrons (and possibly the ions) will be well magnetized and the plasma will be guided to flow along the magnetic field lines. When the thermal pressure of the plasma particles dominates over the magnetic pressure, $\beta > 1$, the plasma will expand outward and drag the magnetic field with it instead of being guided by the field. This is accomplished by currents flowing in the plasma (driven by the thermal energy) that induce a magnetic field which modifies the existing field, expanding it out and altering it as the plasma expands. Inside of electric propulsion devices, magnetic fields used to guide the flow of plasma and help confine the plasma from interacting with the walls will be strong enough so that $\beta < 1$ and the magnetic pressure can confine the plasma. Once the plasma leaves the thruster however, the plasma needs to move off of the magnetic field lines attached to the spacecraft so that the plasma does not simply flow back around and impact the spacecraft. This means the plasma needs to transition to a state where $\beta > 1$ and is no longer dominated by the magnetic pressure [3].

If the thruster relied on just increasing the electron temperature and density to push the plasma off of the field lines, it would result in a wide thermal expansion of the plasma rather than a directed flow, with most of the energy not being useful in terms of generating thrust. Another important relationship for the plasma is the ratio of the directed kinetic energy or "dynamic plasma pressure" to the magnetic field pressure. This can be written in terms of the plasma exhaust speed parallel to field in proportion to the Alfven speed, in the form of the Alfven mach number squared:

$$M_a^{\ 2} = \left(\frac{V_{\parallel}}{V_a}\right)^2 = \frac{n_i m_i V_{\parallel}^{\ 2}}{\left(B^2 \big/ \mu_0\right)} \qquad (1.15)$$

which in this case is dominated by the ion terms since their mass is higher. Similarly to the ratio of plasma beta, if the directed kinetic energy of the plasma dominates over the magnetic pressure of the plasma, then the plasma will not be guided by the field lines. Instead, the magnetic field will be dragged along by the plasma as it flows downstream. This will limit the plume divergence due to following the magnetic field lines, and high parallel velocity along the axis results in a high exhaust velocity for the plasma plume. Having a high exhaust velocity is beneficial for a thruster, as shown in the rocket equation (1.5), and so much of the development work for my experiment focused on increasing the directed ion energies of the plasma plume [7].

Section 1.5A: Overview of Previous Research on the Experiment

The high power helicon (HPH) plasma thruster developed at the University of Washington was designed to produce a dense plasma that is accelerated downstream at a high exhaust velocity without the need for electrodes. The HPH accomplished this by coupling significantly more power into the plasma than other helicons of the time, driving a B_w that was a significant fraction of B_0. This led to non-linear wave interactions with the plasma and resulted in interesting physics occurring downstream of the plasma thruster. Early investigation by Ziemba et al. [8] measuring the time of flight of the plasma between points downstream indicated that the plasma was accelerating downstream of the antenna. It was unclear whether this acceleration was due to continued interaction with the helicon wave or some other mechanism, but the measurements showed that the plasma was high beta ($\beta > 1$) and super-Alfvenic ($M_a > 1$) downstream of the thruster. In addition to the acceleration, the plasma had a "diamagnetic" effect on the base magnetic field downstream of the thruster, meaning that the strength of the field was decreased in the presence of the plasma. The diamagnetic perturbation was small, but not insignificant compared to the weak magnetic field far downstream of the thruster [9].

Further work by Winglee et al. [7] combining multi-fluid plasma modeling with experimental tests indicated that a magnetic nozzle system, positioned downstream of the plasma source so that the plasma transitioned to super-Alfvenic in the throat of the nozzle, would result in a significant increase in exhaust speed combined with a further collimation of the plasma plume downstream of the nozzle. This suggested that a combination of increased plasma source power with the right magnetic nozzle geometry could produce a plasma beam that remains collimated for a significant distance downstream of the thruster [7].

Additional investigation of the ion energies downstream by Prager et al [10] confirmed that the plasma was accelerating downstream of the plasma source, as well as measuring the magnetic component of the plasma wave propagating downstream of the antenna. This plasma wave matched well with a whistler-like wave being launched from the helicon antenna and propagating along the axis. The diamagnetic signal was again measured, and evidence suggested it was correlated with the plasma wave and with the increasing ion energies downstream. At the same time, several other explanations for the ion acceleration were ruled out by the observations [2].

As a consequence of each of these observations: modifications and improvements were made to the HPH system to improve thruster parameters such as exhaust speed, plasma density, and beam width. These modifications included increasing the input wave power, altering the magnetic field geometry in the plasma source and downstream, adjusting the flow of neutral gas into the system, and the geometry of the helicon antenna. These changes revealed more interesting plasma dynamics occurring in the plume downstream of the thruster, and suggested more elements of the experiment to adjust to improve performance and better understand the plasma physics governing the behavior of the plasma plume.

Section 1.5B: Overview of this Research on the Experiment:

The high power helicon (HPH) system was intended to satisfy the need for a plasma source that could be scaled up to high output power levels without significantly increasing the physical size of the system or requiring grids that can erode and limit the lifetime of the device. This would be accomplished by designing a system that could use the intense electric and magnetic fields of a non-linear helicon wave to ionize and accelerate a dense plasma to a large exit velocity without the need for a cathode neutralizing gun or static electric fields. Some possible applications include: propelling a spacecraft as a thruster, a larger station pushing a spacecraft with a plasma beam, or a large station de-orbiting space debris by decelerating the pieces with a plasma beam. Previous work with the HPH [2] [9] had already established that the helicon source was generating a dense plasma and accelerating it downstream at energy levels comparable to other plasma thrusters, but had identified problems with the system including inefficient losses of energy in the source region and weaker coupling of the helicon wave to the plasma particles downstream of the source.

The first goal of this research was to improve the coupling between the helicon wave and the plasma particles downstream of the plasma source to increase the output performance of the device. The methodology for accomplishing the first goal included: characterizing the properties of the helicon wave downstream of the source with the adjustment of magnetic field and the orientation of the propagating wave field in a continuation of the work performed by Prager [2], modifying the source antenna to substantially improve the coupling between the helicon wave and the plasma particles, and finally measuring the magnetic perturbations of the plasma particles and their associated currents as a result of interaction with the helicon antenna.

The second goal was to introduce new methods of increasing the power input from the device into the plasma to further improve the output performance (density, exit velocity) without significantly increasing the size of the device. The methodology for accomplishing the second goal included: adjusting the position and intensity of the downstream magnetic field with magnetic nozzles to improve collimation and acceleration of the plasma beam, and the implementation of a second antenna downstream to increase the helicon wave power coupling into the plasma where the loss of energy due to collisions was decreased compared to the source region.

The most significant new result that arose from accomplishing the first goal was generation of a much larger diamagnetic perturbation of the background field than had been previously observed in laboratory plasma experiments with similar plasma properties (density, temperature). This allows both for laboratory studies of high beta plasmas that were previously difficult to achieve, and allows a possible mechanism for detaching plasma particles from spacecraft magnetic fields in space propulsion applications. The most significant result from accomplishing the second goal was the success in using a second antenna to drive additional helicon wave magnetic field energy downstream and directly accelerate the plasma particles up to a higher exhaust velocity. This provides a mechanism to further increase the amount of power the system can input into the plasma without significantly increasing the size of the apparatus, allowing the HPH system (with further improvements in the future) to fill the niche of a high power plasma source with exhaust velocities comparable or better to other electric propulsion devices with similar power levels but in a compact form. The results with the second antenna also indicate a further collimation of the plasma beam, which would allow the HPH system to be able to generate a plasma beam in space that can provide thrust over a longer distance to an object (payload or space debris) than other plasma sources at comparable power levels.

The details of these results, including the large diamagnetic effect achieved by the plasma source which had not been previously observed in laboratory plasmas, will be presented in the subsequent chapters.

Section 1.6: Organization of the Dissertation:

The remainder of this dissertation is organized as follows: Chapter 2 will discuss the experimental apparatus including: the vacuum system, the gas feed system, the magnetic coils and nozzles, the antenna power supply, and the helicon antenna. The generation of a helicon wave by the antenna will be discussed, as well as the collisional processes at work between plasma and neutral particles in the thruster and downstream.

Chapter 3 will introduce the plasma diagnostics used in the experiment to measure the plasma parameters of the thruster’s outflow. The Langmuir probes used to measure plasma density and temperature will be described, and deviations from the standard model of the behavior of a Langmuir probe in our plasma will be discussed. The magnetic coils used to measure perturbations to the magnetic field will be detailed, as well a more complex electrostatic probe used to estimate the ion energy distribution in the plasma plume.

Chapter 4 will discuss diamagnetic perturbations of the magnetic field measured in the experiment. These will be compared to observations in other experiments, and the source of the perturbations will be discussed in terms of the helicon wave versus other possible mechanisms.

Chapter 5 presents estimates of the currents flowing downstream of the source, as measured by an array of magnetic coils. The shape and dynamics of the current region are discussed, as well as possible effects on the energies of the ion population downstream of the current carrying region.

Chapter 6 describes the introduction of magnetic nozzles downstream of HPH and their effect on ion energy, plasma density, and the perturbation of the magnetic field. Results indicating improved collimation of the beam and acceleration of the ions will be discussed, along with some possible options for improvement.

Chapter 7 will present initial results from the introduction of a second helicon antenna downstream to increase the input wave power into the plasma. Operations at different frequencies will be compared, and the limitations of the prototype second antenna will be discussed. Possible improvements for a more effective second antenna will be presented.

Chapter 2: Experimental Apparatus

The operation of the high power helicon plasma source (HPH) which is shown below in Figure 2.1 in a simulated, space-like environment involves several different systems to: establish a vacuum background similar to space, inject neutral propellant into the system, establish a magnetic field to confine and direct the plasma, and generate the plasma wave that ionizes and accelerates the propellant. Each of these sub-systems will be outlined and compared to those used in other helicon or laboratory plasma experiments. Emphasis will be put on the characteristics that distinguish the HPH experiment from other plasma sources or thrusters.

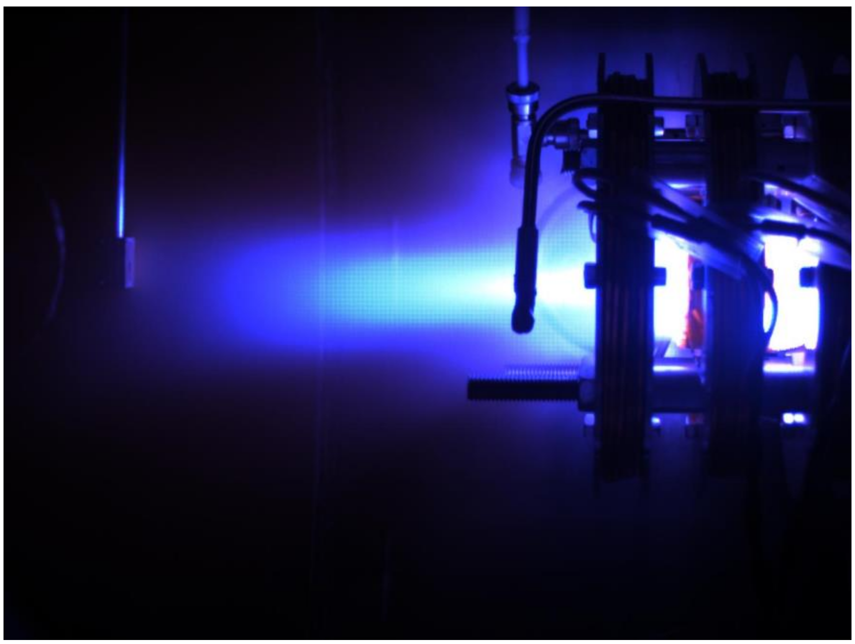

Figure 2.1: Picture of HPH Source Firing for 200 μs.

Section 2.1 Helicon Wave:

The helicon wave is a low frequency electromagnetic wave that travels through plasma along a base magnetic field B_0. The wave has electric and magnetic components oscillating along the guiding magnetic field, with the magnetic field component of the wave (the component measured experimentally in subsequent sections) given by [11]:

$$\tilde{B}_{wave} = B_{wave0} \exp\left[i\left(k_{\parallel} z + m\theta - \omega t\right)\right], \qquad 2.1$$

where $k_{\parallel}$ is the parallel wavenumber for the wave propagating along the z axis, m represents the mode of the wave (m=1 for all the results in this dissertation), and ω is angular frequency of the wave. The angular frequency of the wave is chosen that it's well above the ion cyclotron frequency and well below the electron cyclotron frequency [9]:

$$\omega_{ci} << \omega << \omega_{ce} \qquad 2.2$$

so that the ions are relatively motionless over one period of the wave oscillation while the electrons undergo many gyro-orbits in the same period. The parallel wavenumber $k_{\parallel}$ is determined by the plasma parameters and the boundary conditions imposed on the wave.

When there are relatively few boundary conditions, the parallel wavenumber is identical to the freely propagating whistler wave observed in nature, given by [11]:

$$k_{\parallel} = \frac{\omega_{pe}}{c}\sqrt{\frac{\omega}{\omega_{ce}}}, \qquad 2.3$$

where ω_{pe} is the electron plasmafrequency. As additional radial boundary conditions are imposed such as a varying magnetic field, varying plasma density, or a physical boundary, the behavior of the wave deviates from the unbounded whistler wave. Typical helicon plasma sources have a uniform magnetic field and an insulating boundary at the walls of the chamber, leading to a different condition for the parallel wavenumber given by [2]:

$$k_{\parallel} = \frac{{\omega_{pe}}^2}{c^2}\frac{\omega}{\omega_{ce} k_{\perp}}, \qquad 2.4$$

where $k_{\perp}$ is the perpendicular wavenumber established by the radial boundary conditions. Previous work by Prager et al [11] determined that downstream of the HPH source, the parallel wavenumber closely matched that of the unbounded whistler wave given in eq. 2.3 [11]. With propagation of the wave parallel to the base magnetic field B_0 along the z axis, eq. 2.1 suggests the wave component of the field B_{wave} should decrease in θ as z increases, leading to a counterclockwise (left-handed) rotation around the z axis with position. Equation 2.1 also indicates that as time increases, θ should also increase leading to a clockwise (right-handed) rotation about the z axis with time. Both of these characteristics were experimentally observed by measuring B_{wave} with the results shown below for four separate times in Figure 2.2:

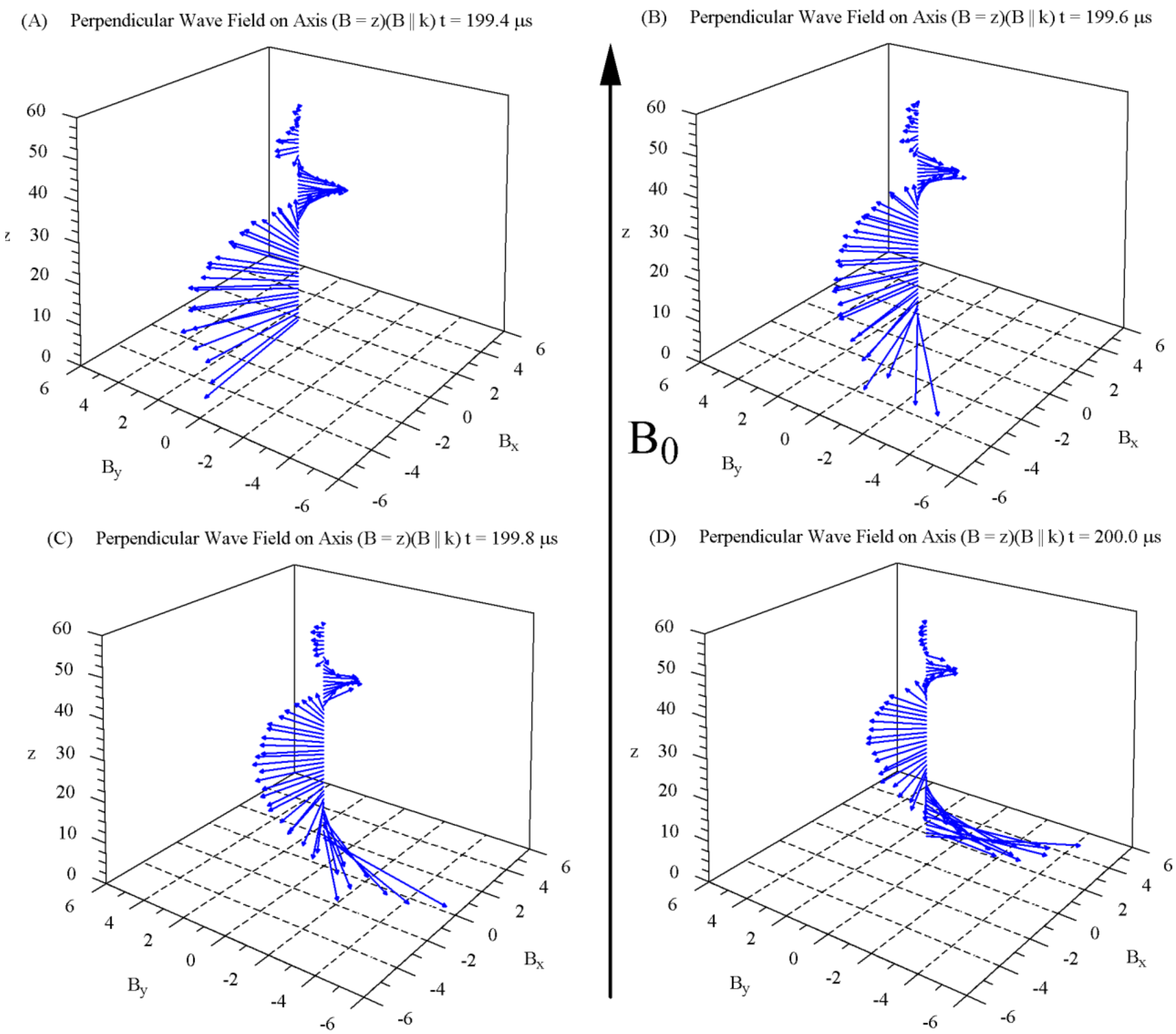

Figure 2.2: Measured B_{wave} downstream near 200 μs. The direction of B_{wave} rotates left-handed about the z axis moving along the z axis, while each frame shows the wave vectors all rotating right-handed about the axis as time advances.

The magnetic component of the helicon wave along the z axis shown in Figure 2.2 propagates downstream of the source where there is a base magnetic field and plasma to sustain it, with more detailed observations described later in Chapter 4. The magnetic and electric field components of this helicon wave have been described analytically by Chen et al [12] for the case of a uniform magnetic field, uniform plasma density, and an insulated chamber wall boundary. While this model can match well with experimental results in other helicon experiments with similar conditions such as in Chen [12], Boswell [13], and others, it does not match well with the HPH results outside of the source region where the wave is generated. Downstream of the source the wave behavior more closely matches that of an unbounded whistler wave [11]. The antenna used to drive this wave is described in the following section.

Section 2.2 High Power Helicon Antenna:

The high power helicon antenna is designed to generate electric and magnetic fields that couple into the helicon wave which propagates through the plasma. These antenna fields only line up with the plasma wave fields for part of the time and in a limited location, but with enough power can overcome the damping mechanisms and generate a helicon wave that can propagate through the source region and downstream for one or more wavelengths before damping out.

In the simplest case, the antenna can be considered to be a single loop of wire that runs along the top of the quartz tube, splits in two to run down on opposite sides of the quartz tube, goes back along the bottom of the tube, and then splits in two again to run up the sides and meet back at the beginning. As current flows through the loop it induces a magnetic field $B_{induced}$ through the loop that is perpendicular to the base magnetic field B_0. As the $B_{induced}$ field rises and falls with the oscillating current in the antenna, this induces an $E_{induced}$ that is inside the quartz tube and anti-parallel to the direction of $J_{antenna}$. This initial system of $J_{antenna}$, $E_{induced}$, and B_0 is illustrated in Figure 2.3A [12].

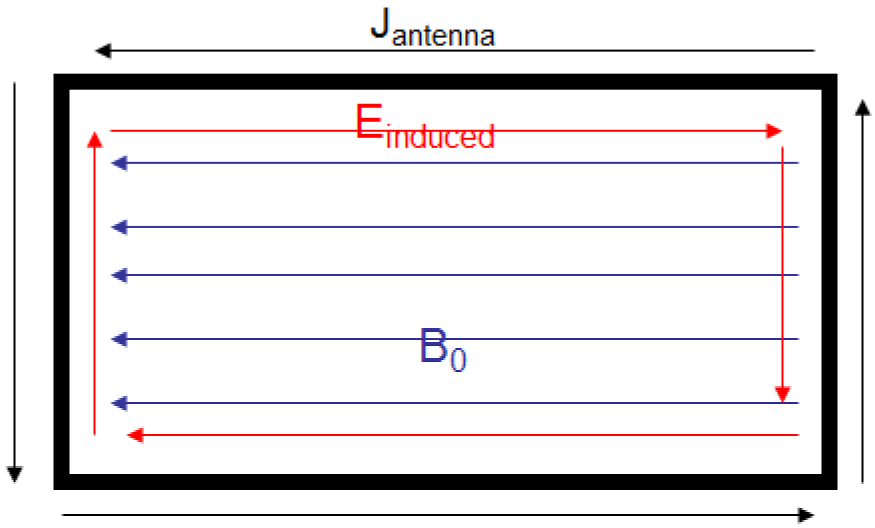

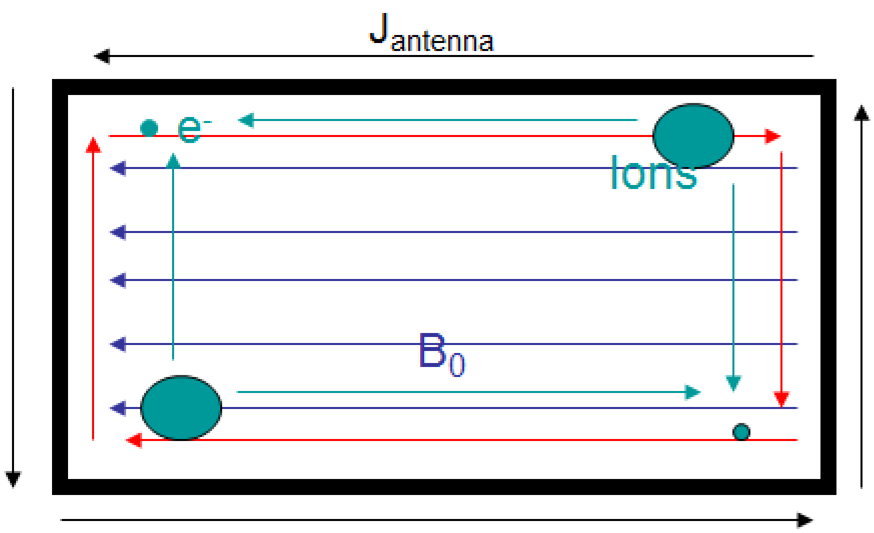

Figure 2.3: Relationship between the antenna curents (black), induced electric field (red), and electric field from the movement of charge (blue).

With the ions remaining relatively motionless, the electrons in the plasma are accelerated by the $E_{induced}$ along the top and bottom legs of the antenna parallel to B_0, until the electric field between the charges is large enough to cancel out the $E_{induced}$ along the axis of the quartz tube. The magnetic field B_0 prevents electrons from moving up or down across the tube perpendicular to the magnetic field, leading to an electric field between the plasma particles that reinforces the $E_{induced}$ across the quartz tube. This arrangement of charges relative to the $E_{induced}$ field is illustrated in Figure 2.3B [12].

The result is a radial electric field that is perpendicular to the base magnetic field B_0, strongest near the ends of the antenna and switching sign in the middle. Additionally there is the radial magnetic field ($B_{induced}$) across the antenna that doesn't switch sign in the middle, and both fields are illustrated in Figure 2.4. A simple loop antenna in this configuration will drive waves both parallel and anti-parallel to B_0.

In order to better match a wave propagating parallel to B_0 a left-handed, half-turn twist is made in the antenna as seen in Figure 2.5. This re-aligns the $E_{induced}$ to coincide in space with the E_w of the left-handed helicon wave. This electric field rotates in space with the same handedness of the helicon wave, but does not rotate in time the same way that the helicon wave does. The wave fields of the antenna are able to couple into the helicon wave mode for only a limited time, but are still able to effectively drive the helicon wave.

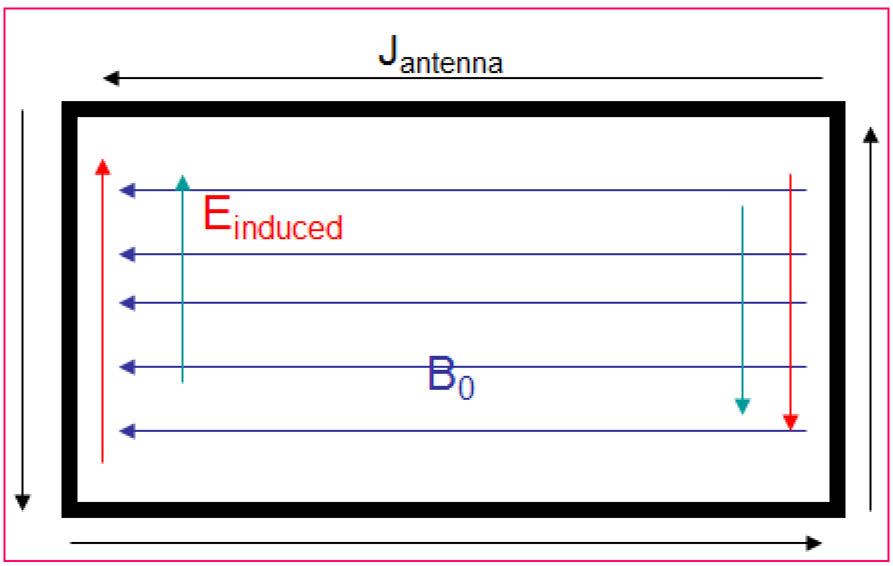

Figure 2.4: Superposition of induced electric fields across the antenna from the antenna and the charge add together constructively.

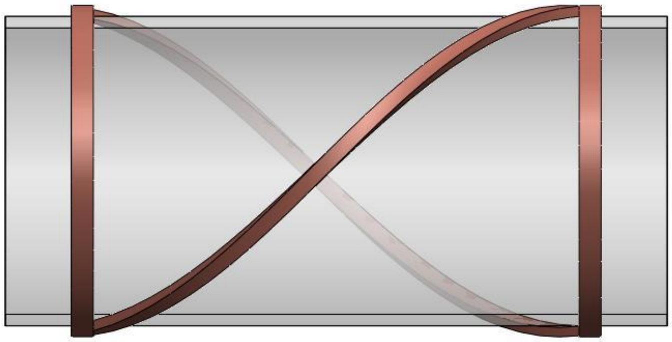

Figure 2.5: Schematic of left-handed copper antenna wrapped around quartz tube [2].

The antennas used in HPH are constructed by wrapping braided copper wire around the outside of a quartz tube, with the current splitting to run in parallel down the sides of the quartz. Each coil is wrapped with two turns around the tube, with Kapton tape insulating the layers from each other. The plasma produced is inside the quartz tube and very little will be present on the outside where the antenna is, limiting the issue of arcing between the layers. An example antenna is shown in Figure 2.5b.

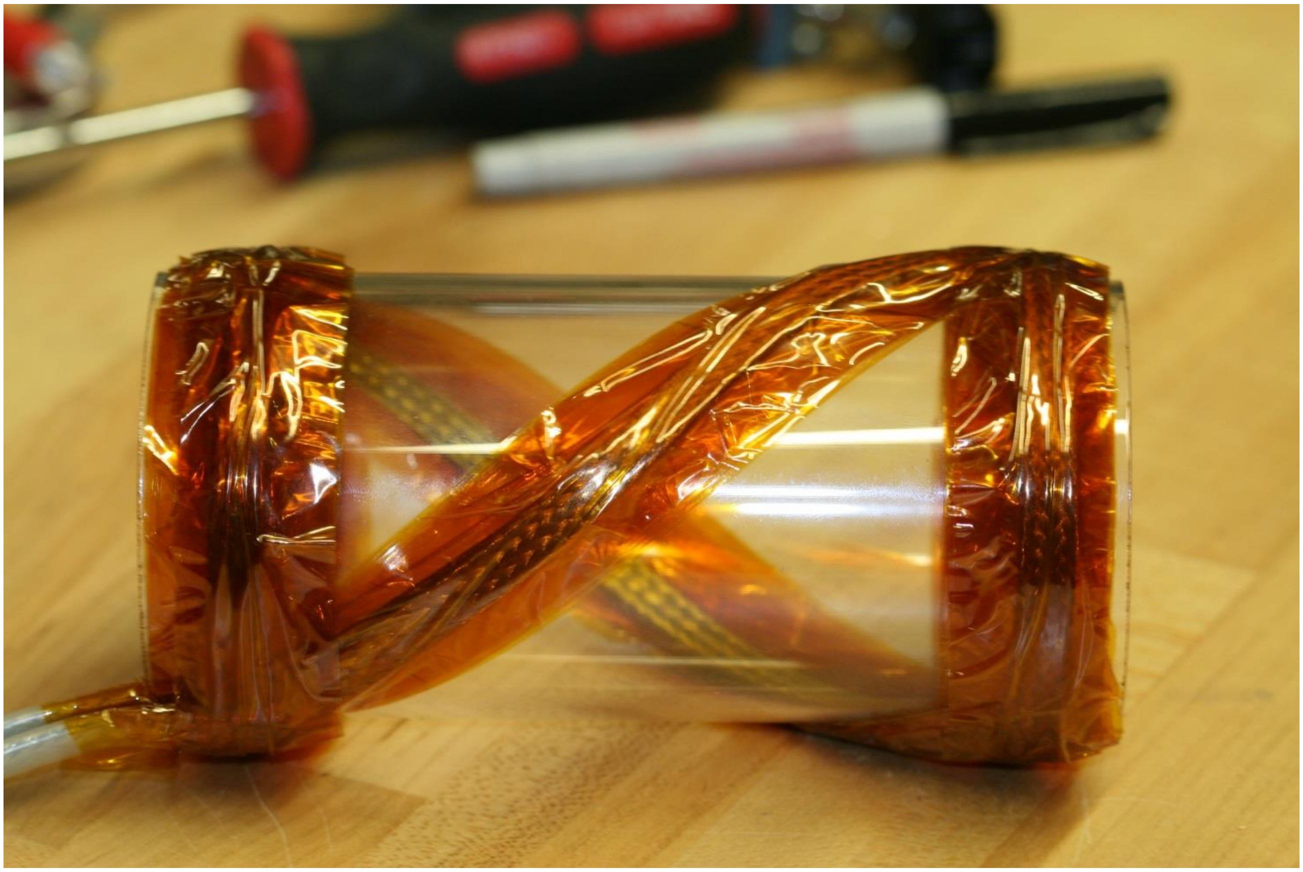

Figure 2.5b: Photo of a left-handed antenna used in the experiment similar to that described above.

Section 2.3 RF Antenna Power Supply:

The power supply for the HPH antenna is built around a tuned resonant LRC network, with the schematic shown in Figure 2.6. The power supply takes advantage of high power solid state devices called insulated gate bi-polar transistors (IGBTs) that can switch high currents on and off within hundreds of nano-seconds, allowing the antenna to be driven at a frequency of up to 1.2 MHz.

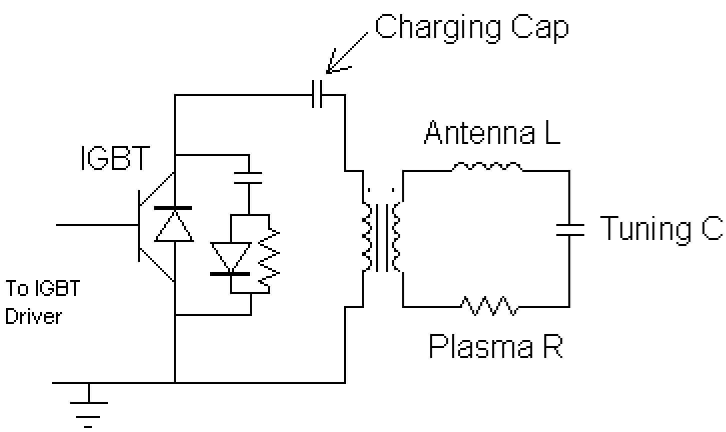

Figure 2.6: Circuit schematic of tuned LRC network with the antenna operating as the inductor [2].

On the primary side of the circuit, optical pulses from the control computer trigger the IGBT driver circuit to close or open the bank of IGBTs. When the IGBTs switch closed: current flows out of the storage/charging capacitor bank through the transformer and the IGBT bank. When the IGBTs open again there is a voltage spike across the IGBTs associated with the rapid decrease in current, which is kept low by a snubbing circuit to keep the voltage spikes from destroying the circuit. With the IGBTs open, current then flows in the opposite direction through the diode bank that is in parallel with the IGBT bank, running the opposite direction through the transformer and re-charging the storage/charging capacitor bank.

On the secondary side of the transformer, the helicon antenna is put in series with a capacitor bank, forming a resonant LC network with the resistance initially just being the resistance of the individual components, and later will add in the resistance of the plasma under the antenna. This capacitor bank is referred to as the tuning capacitor because its capacitance can be shifted up or down to adjust the resonant frequency of the circuit, given by:

$$f_0 = \frac{1}{2\pi\sqrt{LC}} \qquad 2.5$$

where f_0 is the resonant frequency in Hz, L is the inductance of the antenna, and C is the capacitance of the tuning capacitor bank. The storage/charging capacitor is switched on and off and pulses of current are driven through the primary side of the transformer at the resonant frequency of the circuit, leading to a large oscillating current at the resonant frequency in the secondary side of the circuit. With no plasma present the resistance in the circuit is low and the oscillating current through the antenna builds to large value, ~1500 Amps peak to peak, as seen in Figure 2.7A. The current oscillates sinusoidally at the antenna frequency until the circuit stops being driven on the primary side by the computer. Not shown is the voltage across the antenna, which also oscillates sinusoidally and is typically ~8-10 kilovolts peak to peak.

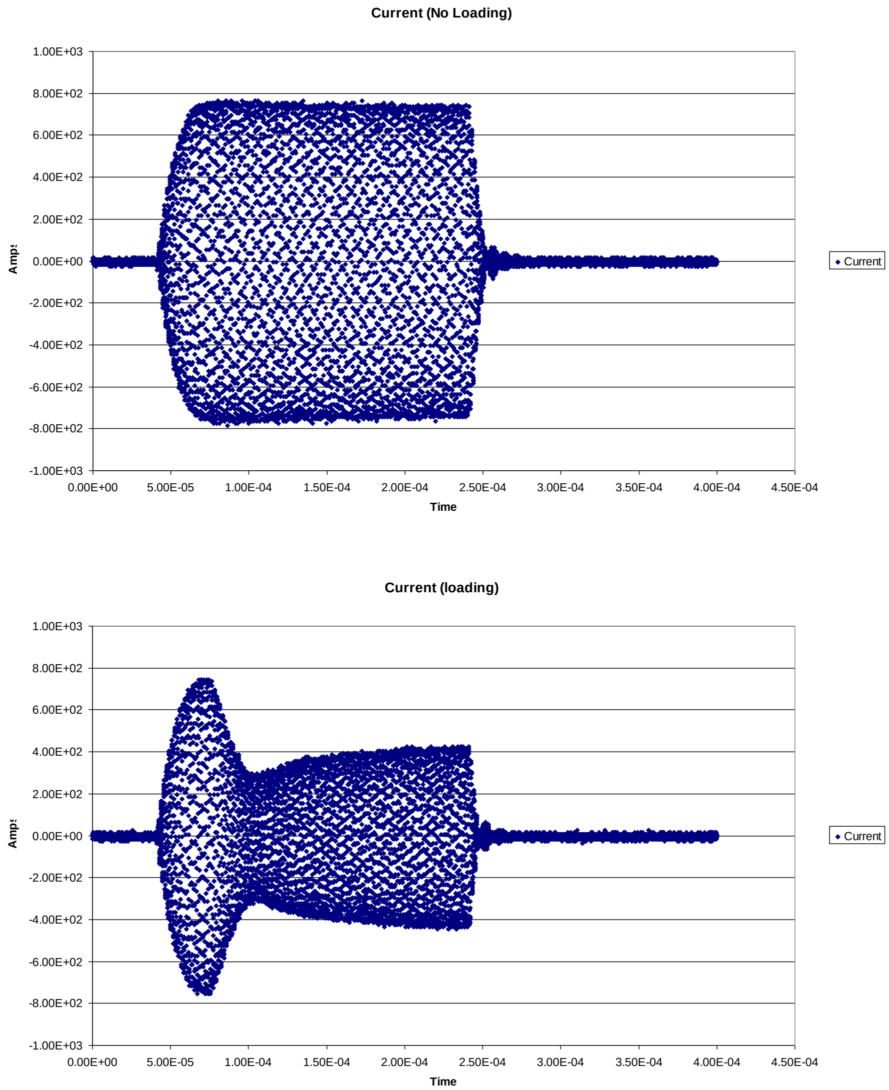

Figure 2.7: Current oscillating in the HPH antenna as a function of time without the presence of neutral gas (first panel) and with the neutral gas (second panel).

When the antenna is fired with neutral fuel gas present, the antenna will ionize the gas into plasma and accelerate it out, which draws energy out of the secondary side of the circuit with the antenna. The plasma acts as an additional resistance in the LRC circuit and puts a load on the antenna, as seen in Figure 2.7. The oscillating current drops as there is more plasma present, and then begins to increase again as plasma is ejected from the source until the antenna is shut off.

Two examples of RF power supplies are shown in Figure 2.8. The black chips are the banks of IGBTs and diodes that behave as the high power switch, with the copper stripline to carry the current. The green boards are the IGBT drivers, which receive the logic pulses from the control computer and provide the voltage to the IGBTs to make them open or close. The large black loop is the 1:1 transformer that connects the primary side of the power supply with the IGBT banks with the secondary side of the supply, which includes the tuning capacitor and the antenna (which is inside the vacuum chamber).

Figure 2.8: Photos of two power supplies used to drive an HPH antenna.

Each of these power supplies had their best performance operated at a frequency of ~600 kHz. At this frequency, the oscillating current reached 1500 amps peak to peak, with an oscillating voltage of ~8-10 kV peak to peak in both of the power supplies. The power being input into the plasma by the antenna with these supplies was measured to be in the tens of kilowatts [2]. In Chapter 7 the results from operating the power supplies at other frequencies will be discussed, but there were performance decreases as follows: when operating these supplies at a higher frequency (~1.2 MHz) the oscillating current decreased to ~500 amps pk to pk while the voltage increased to ~13 kV pk to pk, and when operating the supplies at a lower frequency (~350 kHz) the current decreased to ~1000 amps pk to pk while the voltage decreased to 4-5 kV pk to pk. Operation at the nominal frequency of ~600 kHz yields the results discussed in Chapters 4-6.

Section 2.4 Base Magnetic Field B_0:

The magnetic field in the source region serves multiple purposes for the production and acceleration of the plasma. First, it restricts the flow of electrons perpendicular to the field and into the walls of the source antenna. When there is sufficient energy in the magnetic field compared to the thermal energy of the electrons, i.e. that $\beta < 1$ as given in eq. 1.14, then the Larmor radius of the electrons given in eq. 1.9 is small compared to the width of the antenna. This will limit the motion of the electrons to along the magnetic field lines except for collisions with neutral particles or ions, which will be discussed later in this chapter.

Second, it allows the source antenna to drive a helicon wave along the magnetic field to ionize the plasma. The restriction of the electrons from moving perpendicular to the base field B_0 allowed the helicon antenna to generate the radial electric field necessary to couple into the helicon wave field. The frequency of the helicon wave is required to be between the electron cyclotron frequency and the ion cyclotron frequency as given in eq. 1.13, so that the wave fields act on the electrons but leave the ions un-perturbed. For a relatively low frequency helicon wave of 600 kHz, this required the magnetic field in the source to be on the order of a few hundred gauss to keep the cyclotron frequencies in the appropriate range, as shown in Figure 2.9:

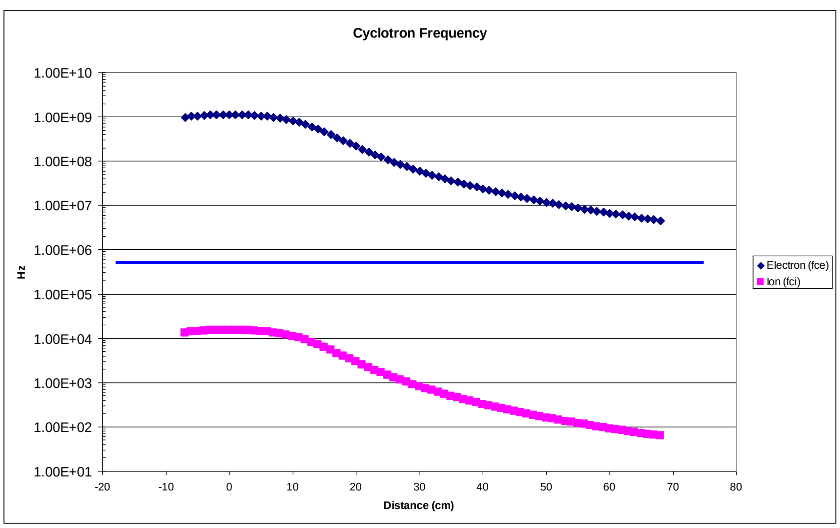

Figure 2.9: Comparison of the antenna frequency to the cyclotron frequencies of the ions and electrons in the HPH source region and downstream.

And lastly, the extended magnetic field allows the helicon wave to propagate along the magnetic field through the plasma downstream of the antenna. This allows the electron currents in the plasma to exert a Lorentz force on the plasma particles perpendicular to the current and the magnetic field at that position. This acts to accelerate the ions and electrons along the axis as the magnetic field diverges as shown visually in Figure 2.10.

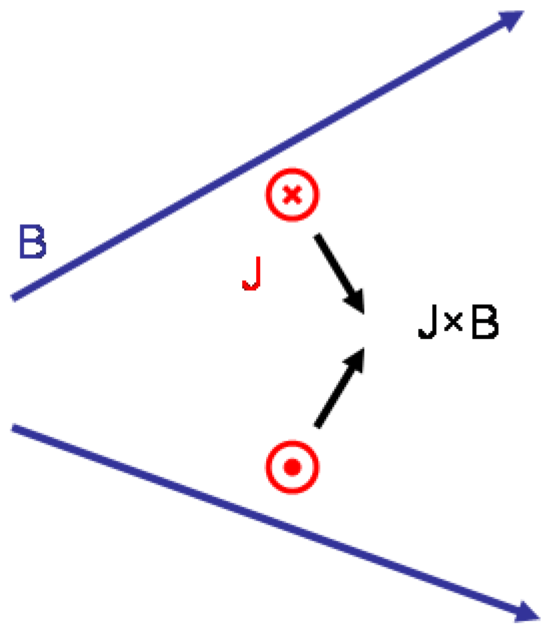

Figure 2.10: The force on the charged ions and electrons for a current flowing around the axis of the diverging magnetic field results in an acceleration towards the axis and away from the source region.

The base magnetic field B_0 in the source region is generated by six magnetic coils in series, each 15 cm in diameter and spaced with 3 cm gaps in between, and lined up along the thruster axis (Figure 2.11). This was done to provide a relatively uniform field near the center of the magnet, while having the field fall off like a dipole outside the source region. The axial component of this magnetic field is illustrated in Figure 2.12. The vertical black lines represent the front and back of the quartz tube. The strength of the magnetic field peaks roughly 1/3rd of the way from the back end of the quartz tube and varies by less than 20% over the length of the antenna.

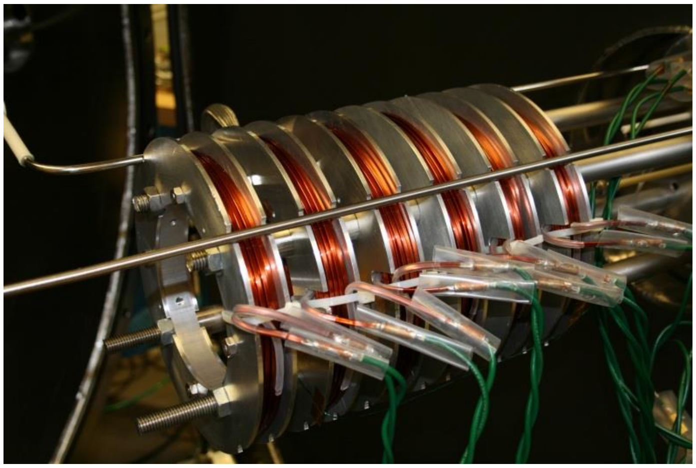

Figure 2.11: Photo of the six magnetic coils used to establish the base magnetic field in the source region.

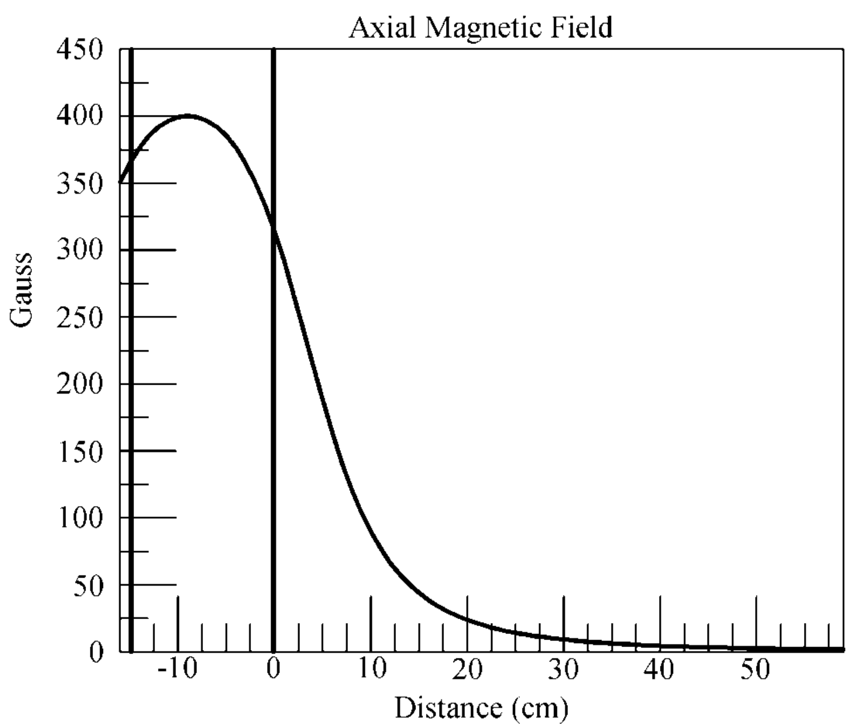

Figure 2.12: Profile of the axial component of the magnetic field in the source region and downstream. The vertical black bars represent the position of the HPH antenna.

While most helicon experiments in the past have provided a uniform field for their experiment both under the antenna and downstream, ours required space-like conditions for the plasma downstream and that includes a decreasing and diverging magnetic field as the plasma moves away from the spacecraft.

The magnitude of the base field peaks on axis and is ~400 gauss. This is approximately what was predicted to be optimal based on the frequency of the antenna, wavelength of the antenna, and the expected plasma density. The final value we used was determined experimentally to be the optimal value based on a sweep of the magnetic field. The magnetic field is established two seconds before the experiment begins and is maintained at a constant current until after the experimental shot concludes.

Section 2.5 Vacuum Chamber:

In order to simulate space-like conditions my experiments were conducted in a large, cylindrical vacuum system that is roughly 9' long and 5' in diameter, shown in Figure 2.13. The plasma source is hung from the back end of the chamber within the vacuum environment, to simulate firing the system in a space environment. Each of the magnetic nozzles, when implemented, were also under vacuum. A turbo-molecular pump is used to keep the background neutral pressure of leaked air and outgassed water below $2x10^{-6}$ Torr between shots. The low neutral pressure limits the collisions between the plasma from the source region and the neutral particles that aren't part of the fuel gas in the source. The mean free path for collisions between the plasma and the neutral background is given by [3]:

$$\lambda_m = \frac{1}{n_n \sigma} \qquad 2.6$$

where n_n is the background neutral density and σ is the approximate cross section of the neutral atoms. With the background pressure below $2x10^{-6}$ Torr, the mean free path is >100 m, or well above the dimensions of the chamber. This makes it unlikely that the plasma will collide with the air not pumped out of the chamber before it hits the chamber walls, and the neutral background is sufficiently space-like for this experiment.

Figure 2.13: Photo of B. Race Roberson cleaning the inner surface of the vacuum system.

Maintaining an environment where the plasma from the experiment can flow downstream without strong modifications by the background neutrals is critical for simulating the performance of the experiment in space, where the neutral background will be significantly lower. Other helicon experiments [12][13] will often have a neutral background of fuel gas downstream of the source that is in the range of 3-10 mTorr, or more than a thousand times higher. This yields a mean free path of ~10 cm or less. Depending on the size of the chamber this will mean a significant interaction with the background neutral population that wouldn't occur under space-like conditions.

The plasma is not initially in contact with the walls of the chamber and the electrical ground, but with the high exhaust velocity of the plasma it can reach the chamber wall and begin to build a sheath within ~130 μs of being emitted. Therefore the pulse length of the experiment is kept short, partially to prevent plasma interactions with the wall from dominating the behavior and maintain the space-like conditions. Other helicon experiments are typically operated in the range of miliseconds [13], tens of miliseconds [12], or for seconds and higher [14], and so these experiments come into equilibrium with the vacuum chamber wall for most of their operating time.

In the source region when the ionization of the neutrals is taking place, the relationship between the electron gyrofrequency, electron-neutral collision frequency, and antenna frequency is given by:

$$f_0 << \nu_{ne} << \omega_{ce}/2\pi \qquad 2.7$$

600 kHz << 22.8 MHz << 1.2 GHz

so that each electron is expected to make many gyro-orbits without colliding with a neutral, but is expected to collide with many neutrals in one antenna period. The electron gyrofrequency is determined by eq 1.12 and the electron-neutral collision frequency is determind by [3]:

$$\nu_{ne} = n_n \upsilon_e \sigma \qquad 2.8$$

where n_n is the neutral density, v_e is the electron velocity (which is dominated by the thermal velocity), and the approximate cross section of the neutral atom. This collision rate increases with the electron temperature as the velocity of the electrons increase. As the neutrals in the source are ionized and it switches from low ionization fraction plasma to a high ionization fraction, the electron-ion collision rate becomes dominant, given by [3]:

$$\nu_{ei} = \frac{n_e e^2}{m_e}\eta \qquad 2.9$$

where η is the specific resistivity of the plasma, which can be approximated by:

$$\eta \approx \frac{\pi e^2}{(4\pi\varepsilon_0)^2}\sqrt{\frac{m_e}{(kT_e)^3}}\ln\Lambda \qquad 2.10$$

with the last term approximated by:

$$\ln\Lambda = \ln\left(12\pi n_e \lambda_D{}^3\right) \approx 10 \qquad 2.11$$

for laboratory plasmas like those produced by helicons. In the source region once the plasma is mostly ionized, the electron-ion collision frequency is ~92 MHz. The electron-ion collision is governed by the electric force between the negative electron and the positive ion when they are within close proximity. As a consequence, the electron-ion collision rate decreases as the electron temperature increases because the electron spends less time near the positive ion and is not as significantly deflected [3].

Once the plasma leaves the source region the neutral density drops dramatically and the electron-neutral collision rate becomes negligible, but the electron-ion collision rate decreases at a slower rate given the high plasma density on axis immediately downstream of the antenna. As the plasma density drops the collision rate decreases, until within about one wavelength of the source exit the collision frequency has dropped to be on the same order as the antenna frequency.

Section 2.6 Neutral Propellant Injection:

Feeding the neutral propellant gas into the source region at an appropriate rate to sustain the outflow is difficult. Many of the previous helicon experiments [12][13] fueled the source region by backfilling the chamber with neutral gas. With neutral gas at a high density filling the source antenna region and downstream of the antenna, there would be sufficient neutral particles to flow into the source region from downstream as ions left the source region to sustain the plasma flow. Work by Chen et. Al. [15] studied how high of a plasma density could be reached with this method by pointing two helicon antennas at each other in an attempt to build a higher density plasma between them, and resulted in a lower plasma density because the outflow of plasma limited the number of neutrals that could flow into the gap between the two helicon sources. The plasma density was ~8×10^{19} m^{-3} near the exit of each antenna but dropped to half of that in the region between them.

Other experiments such as VASIMR [14] use a physical choke point between the source region and the rest of the vacuum system to allow for a high density neutral gas under the helicon antenna while not having as large of neutral background in the rest of the vacuum chamber. Converging magnetic field lines in the choke make the plasma density high enough that the flow of neutrals through the choke is limited. Rather than having the source region neutrals replenished by gas flowing from downstream as above, additional gas flows into the source region radially from the sides [14].

For HPH to maintain a low neutral background downstream of the source region, while simultaneously having a high neutral pressure in the source region, we used a fast opening puff gate to inject neutral gas into the source region with a tube from outside the vacuum chamber. After 10 ms enough of the neutral gas (typically argon) has flowed into the source to feed the plasma production, but the pressure downstream of the source has not risen significantly. The experiment is fired for typically 200-400 μs and the data is collected over a maximum duration of 1 ms, so the downstream neutral pressure will not change significantly over the course of the shot. The gas feed is shown in Figure 2.14 by itself in the left panel, and inserted into the back of the antenna in the right panel of Figure 2.14.

Figure 2.14: The neutral gas feed system shown by itself (left panel) and inserted into the rear of the source region (right panel).

After the neutral gas puff has expanded to fill the interior of the quartz tube but before it has had time to expand downstream, an ignitor circuit is triggered to generate a small amount of seed electrons in the neutral puff for the antenna to immediately act on. The ignitor is a 1500 V potential drop between two steel grids at the end of the gas feed which draws a current of ~15 A for 25 μs. The antenna is turned on at the same time and the neutrals begin to be ionized into plasma. The ionization fraction of the plasma is typically >90% for helicon discharges and the best way to confirm this for HPH is to look at the line emission spectra from the source region while it is in operation. When energetic electrons collide with neutral gas atoms, the electrons in the outer shell of the atom can be excited and release the energy as photons. The same is true for when energetic electrons collide with the singly ionized atom. The spectrum of lines observed from the source region while in operation is shown in Figure 2.15.

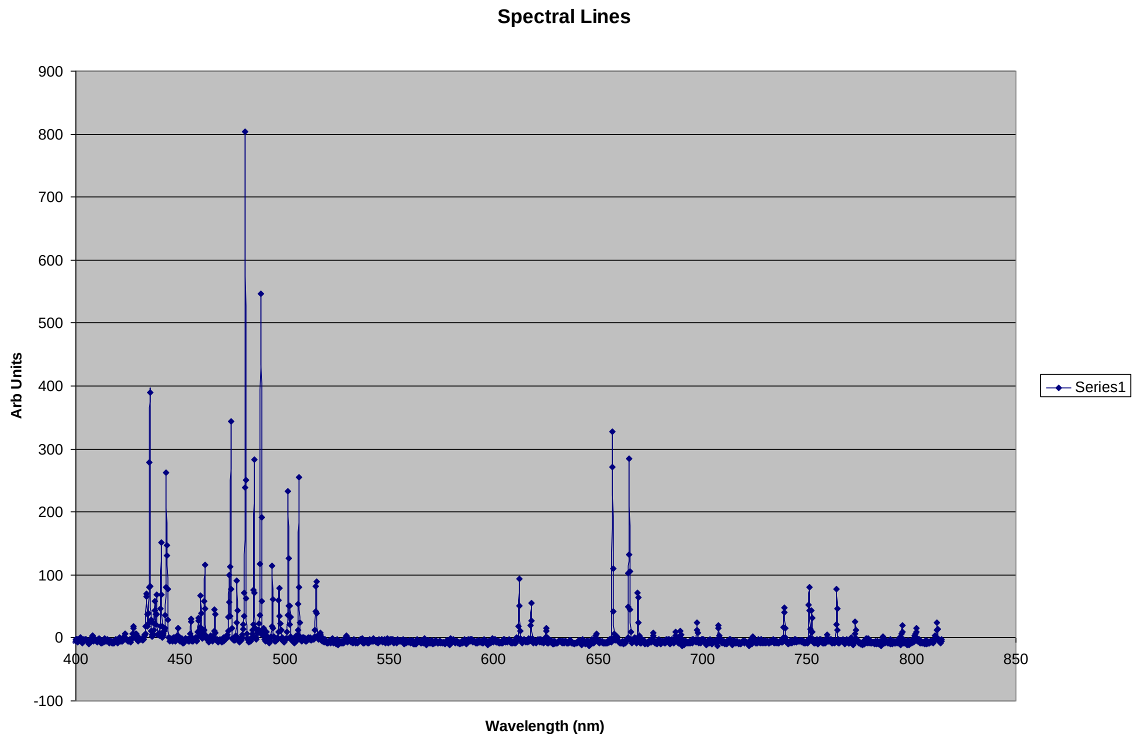

Figure 2.15: Emission spectra measured from HPH.

The emission spectra from singly ionized argon atoms, Ar II, dominate the spectra from 400-670 nm [16]. The bulk of the light production is near the blue end of the color spectrum, leading to the bluish-white color of the discharge. The only detected neutral argon emission lines, Ar I, are found around 750 nm and are a factor of ten smaller in light measured than the peak Ar II emission lines. Additionally, measurements of the plasma density in the source region give a peak plasma density of ~1-2x10^{20} m^{-3} while an estimate of the neutral density in the source region based on expanding gas at room temperature gives a neutral density of ~1.2x10^{20} m^{-3} prior to antenna turn-on. This also suggests that the ionization fraction is high [16].

Section 2.7 Downstream Magnetic Nozzles:

Two magnetic nozzles were used in the course of my experiments to modify the magnetic field downstream of the source region. Changing the shape or strength of the magnetic field outside the source region allowed me to study the effect of the magnetic field of the plasma after it was created, without significantly altering the production of the plasma in the source region, as would happen through adjusting the base magnetic field around the source. These two nozzles are pictured together in Figure 2.16.

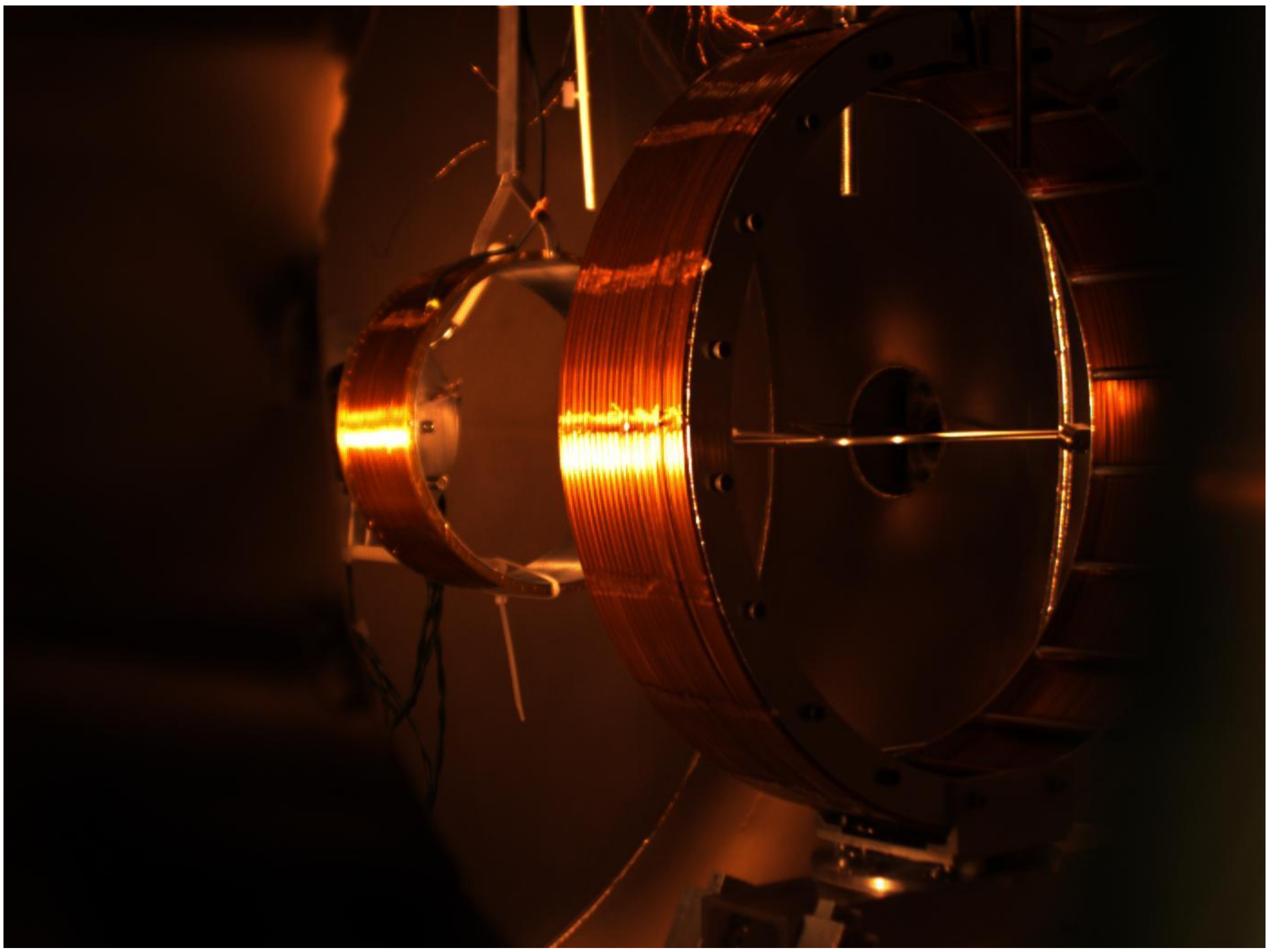

Figure 2.16: Photo of the magnetic coils used as magnetic nozzles hanging in the chamber, centered on the HPH source axis.

The first nozzle was designed to be roughly twice the diameter of the base magnets, ~26 cm, and was positioned downstream so that the peak of the nozzle field would overlap the point where the base magnetic field began to strongly diverge, 20-30 cm downstream. This resulted in a magnetic field geometry where the magnetic flux diverged after leaving the source, re-converged through the nozzle, then diverged again slower than before. This had the effect of lengthening the region where the electrons were magnetized. The axial component of the magnetic field is plotted in Figure 2.17.

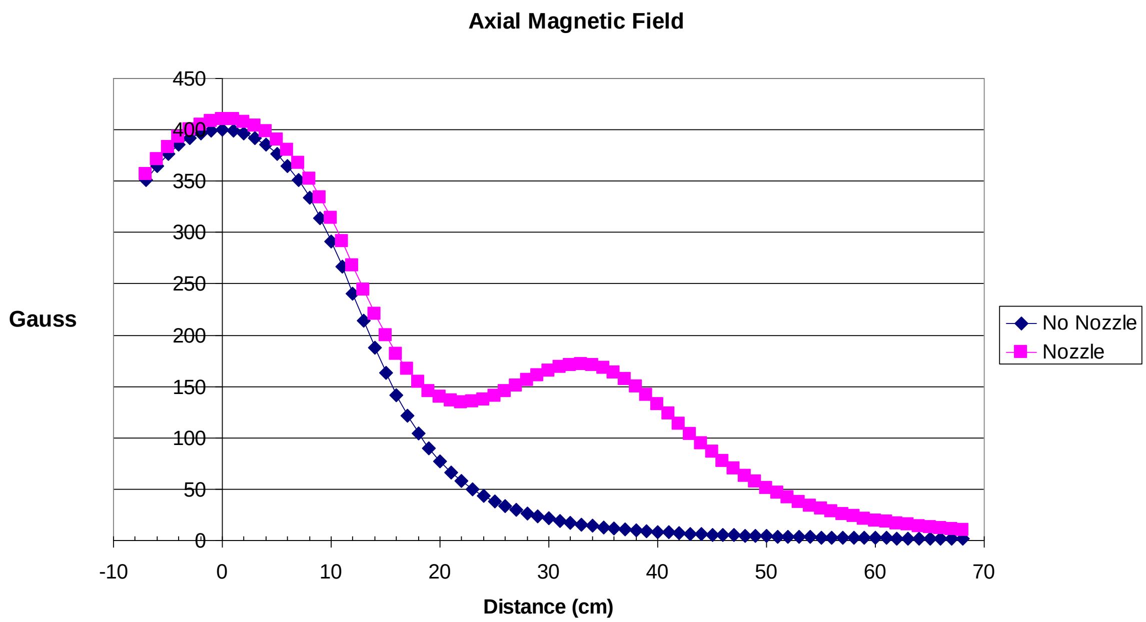

Figure 2.17: Axial component of the magnetic field with a single nozzle added downstream.

A second nozzle was added, with a diameter twice as large as the first nozzle, ~50 cm, and the two nozzles were moved in close to the source magnets to limit the amount of the field re-converging. This new configuration had flux lines that expanded through each nozzle, before diverging at the exit of the second nozzle. This had the effect of keeping the electrons magnetized even further downstream, but also limited the amount of flux lines re-converging. The flux lines were almost everywhere diverging in this configuration. The effect of the nozzles on the HPH experiment will be discussed in more detail in Chapter 6.

Chapter 3: Experimental Diagnostics, Theory and Operation

Section 3.1: Summary of the Diagnostics used in the HPH Experiment:

This chapter describes the diagnostic tools used to study the plasma in the High Power Helicon experiment and some of the basic advantages and limitations of those tools. These focus on measuring changes to the magnetic field induced by the plasma particles, the plasma density and electron temperature, and the directed velocity of the ions downstream of the source. These will be detailed in the following sections.

Section 3.2: Shot to Shot Repeatability of the Experiment

The pulsed nature of the experiment required diagnostics that could measure the evolution of the plasma as it flowed downstream on a time scale short compared to the experiment length of a few hundred microseconds. Fortunately the shot to shot repeatability of the experiment was excellent, and so for electrostatic diagnostics that required a range of voltages it was straightforward to take a succession of pulses with varying settings. This was also true when it came to moving probes in position relative to the plasma source to study the changes with distance from the source as it evolved and flowed downstream. For each data run a set of control diagnostics was used to determine that the plasma pulses were repeatable, measuring things like the plasma density in the source region and the input current of the antenna, while a separate diagnostic was varied in either position or configuration to measure changes to the plume downstream.

Section 3.3A: Measuring Magnetic Field

The experiment uses a series of magnetic coils to supply a background magnetic field in the source region and for a short distance downstream. This background field will be perturbed during the experiment by the actions of the plasma particles and the magnetic field of the plasma waves generated by the antenna. The short pulse length of the experiment made it more practical to measure changes to the background magnetic field over a few hundred microseconds rather than measure the total field. Changes to the magnetic field are measured with B-dot coils, which are coils of fine copper wire that generate a voltage across the output leads proportional to the change in the magnetic field through the coil based on those described in Hutchinson [4]:

$$V = NA\frac{\partial B}{\partial t} \qquad 3.1$$

where N is the number of turns of wire, A is the surface area of the coil, and B is the magnetic field. Integrating this voltage over time gives the changes in the magnetic field from when the measurement began. The number of turns and surface area were varied with the coils depending on the magnitude and length scale of the perturbation being measured. The voltage trace was also filtered through a combination of hardware and software filters before being integrated depending on the source of the magnetic perturbation. Depending on its filter, the system could be used to measure the wave magnetic field that varied at the frequency of the antenna or the changes to the background magnetic field that varied at a much slower rate.

Section 3.3B: Description of Magnetic Diagnostics

The first magnetic coil of interest was used to measure the change in the axial component of the background magnetic field along the axis of the thruster. It was ~2 cm in diameter with 25 turns of wire, aligned so the normal of the coil was along the axis of the thruster. The copper wire and connections were coated in Torr Seal to prevent interaction with the plasma, and the ring was left open so that plasma could flow through it. The voltage trace was filtered through a 1.5 µs low-pass RC filter to cut down on the antenna noise picked up by the coil, as well as a second software filter. This diagnostic was used to study the diamagnetic change in the axial component of the background field due to the plasma and the currents flowing in it, with a time resolution of ~2 µs. It was mounted on the end of a rod so the coil could be slid along the axis from 60 cm downstream to within a few centimeters of the source region.

The second magnetic coil used was a set of three perpendicular coils designed to measure the magnetic field components of the plasma wave driven by the antenna. The probe was made to be .25 inches in diameter so that all three components of the wave magnetic field could be measured at approximately the same position. Each coil was made of 50 turns of fine copper wire, and the set of coils was coated in Torr Seal to prevent interaction with the plasma. This diagnostic did not use a hardware filter to remove antenna noise, and instead a band-pass filter was applied in software to filter out the data outside the desired frequency range.

A third set of magnetic coils was made to study the radial profile of the perturbations to the magnetic field background in finer detail near the axis. This probe contained seven sets of three perpendicular coils. Each set of coils was ~2 cm in diameter and made with 25 turns of wire for each set of perpendicular rings. These rings were embedded in nylon rod and covered in Torr Seal. This line of seven probes in array was hung from a movable track along the top of the chamber and lowered down into the plasma so that the center of the array was on axis. The track allowed the array to be moved from 10 cm downstream of the source region out to 60 cm downstream. The voltage trace from each coil was filtered a 1.5 μs low-pass RC filter, and this bulk B-dot array was used to study all three components of the perturbation to the background magnetic field near the axis in detail so that an estimate of the current density could be made.

Each coil of each probe was calibrated using a commercial Bell gauss-meter before being put under vacuum. This was done by using the gauss-meter to measure the strength of the base magnetic field accurately, while the probes measured the change in field related to the switching on and off of the base magnetic field. This allowed the voltage trace over time to be calibrated with a known magnetic field. Cartesian coordinates are used to relate the direction of the measured magnetic perturbations and the chamber reference frame: with the z axis along the thruster axis, the y axis pointed vertically upward, and the x axis perpendicular to the others.

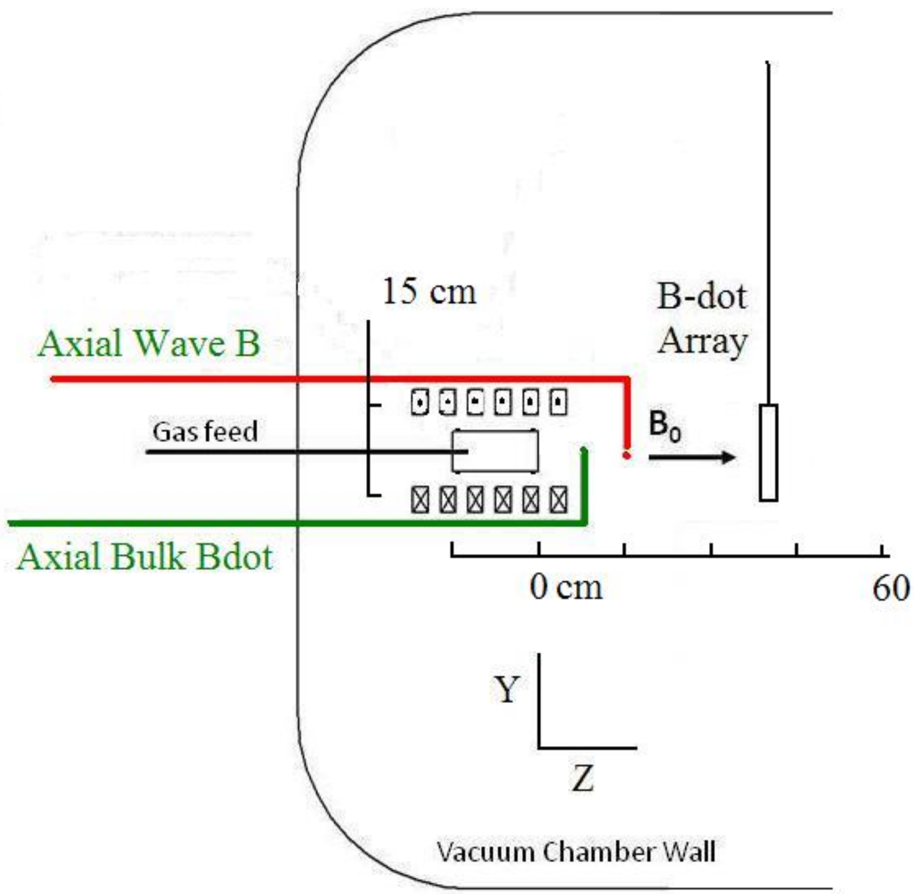

Figure 3.1: Orientation of Magnetic Diagnostics relative to source region

Section 3.4A: Measuring Plasma Density and Electron Temperature with Langmuir Probes

Electron density and temperature were measured with a set of Langmuir probes similar to those described in Hutchinson [4]. These probes operate on the principle of using a bias voltage on the probe tips to affect the electron and ion currents from the plasma to that surface. One or more small tungsten electrodes are inserted into the plasma, and are biased with a fixed voltage. In the case of a single Langmuir probe, the probe tip is biased relative to the chamber wall (which is attached to earth ground). For a double Langmuir probe, the probe tips can be biased relative to each other without grounding either. When used in the single probe configuration, a series of shots are taken in which the bias voltage is varied from strongly negative relative to the chamber ground to strongly positive relative to the chamber ground. In the double probe configuration the two tips are given a large bias relative to each other, but are left floating relative to the chamber ground. The current between the probe tips, or between the probe tip and ground, is measured during the experiment as the plasma interacts with the probe. These measured currents, taken along with some assumptions about the behavior of the plasma near the probe tips, give estimates of the electron density and temperature near the probe tips. A brief summary of the underlying assumptions being made and the basic operation of the Langmuir probe will be given here, followed by a description of each of the probes used in the experiment.

Section 3.4B: Typical Langmuir Assumptions and Theory of Operation

The initial assumptions for the plasma are that it is quasi-neutral and well thermalized, with roughly equal numbers of electrons and ions at the same temperature. The positive ions are all singly ionized of the same species and are assumed to be much more massive than the free electrons. This plasma is then assumed to be exhausted at speeds much less than the electron thermal speed into a large vacuum chamber with conductive walls, which are tied to ground. The free electrons travel to the plasma edge much faster than the ions and so the chamber wall is hit with significantly more electrons than ions, giving the chamber wall a negative charge relative to the center of the plasma. This potential difference between the center of the plasma and the chamber wall is referred to as the plasma potential (V_p), and is usually a few times the electron temperature in units of eV. Even if the plasma has not yet made contact with the walls, there will still be a significant potential difference between the center of the plasma and the plasma edge, as a result of a small deviation from quasi-neutrality with the electrons more likely to be found at the plasma edge than the center due to their high thermal speed.

This potential difference will act to accelerate the ions in the plasma towards the plasma edge and the chamber wall, at a rate determined by the electron temperature. Specifically, the electron interaction with the chamber wall will build up a potential sheath between the wall (at ground) and the plasma (at V_p), and the ions will be accelerated into the wall through this sheath. The sheath region is usually not wider than a few Debye lengths, where the Debye length is defined as:

$$\lambda_D = \left(\frac{\varepsilon_0 T_e}{e^2 n_0} \right)^{1/2} \qquad 3.2$$

with T_e being the electron temperature and n_0 being the electron density in the unperturbed plasma. The Debye length is an approximation of the distance over which electric fields between the plasma particles effect the motion of the particles, and beyond which there are sufficient charged particles of opposite charge that the total electric field over the plasma volume is small. In this case, the electrons have moved to the edge due to their electron temperature and an electric field is built up, but only over a region on the scale of the Debye length [4].

There is also an extended "pre-sheath" region extending a significant distance into the plasma from the sheath edge. It is this pre-sheath region's potential drop that will slowly accelerate ions towards the plasma edge and the beginning of the sheath. The flux of ions to the chamber wall will be limited by the rate at which ions drift through the pre-sheath region to the sheath edge as well as the final speed obtained by the ions falling through the sheath. This final speed of the ions toward the wall is called the "Bohm speed" and is determined by the electron temperature, which establishes the size of the potential difference across the sheath.

$$V_{Bohm} = \left(\frac{T_e}{m_i} \right)^{1/2} \qquad 3.3$$

$$V_{sheath} = \frac{-T_e}{2e} \qquad 3.4$$

When a metal probe is inserted into the plasma, a similar sheath develops around the probe surface area. If the probe is not connected to ground or biased relative to the chamber wall, then electrons hitting the probe surface will begin to charge the probe until it is negative relative to the plasma potential. This will continue until the probe is sufficiently negative to attract an equal (and small) number of ions and additional electrons, so that the total current to the probe is negligible. This potential is called the "floating potential" because it is the potential that probes not connected to ground will float to. In order for measurable currents to flow through the probe and obtain data, the probe will need to be connected either to ground or another probe tip. The basic case of a single Langmuir probe requires the probe tip to be connected to ground and will be discussed first [4].

When the probe tip is connected to ground, current can flow from the probe to ground freely. If the probe tip is biased positive relative to ground so that the tip is at the plasma potential Vp, then there will effectively be no sheath around the probe tip. This will allow all the electrons impacting the probe to be conducted to ground and with no sheath accelerating ions into the probe surface the ion current to the probe will be minimal. This will yield a large negative current to ground, and is generally referred to as being in "electron saturation" since the probe is collecting all the electrons that interact with it. The next step is to bias the probe tip negative relative to the plasma potential, by lowering its bias voltage relative to ground. As the potential on the probe tip gets more negative relative to the plasma potential, more of the electron population is prevented from impacting the probe surface and the electron current will decrease. At the same time, the potential difference between the probe tip and the plasma potential grows and a sheath will form around the probe. The potential difference across the sheath increases and the ion current to the probe will increase, though it will be limited by the surface area of the sheath around the probe. Eventually the probe tip will be so negative relative to the plasma potential that most of the electrons will be repelled from the probe tip and the current of ions through the sheath to the probe surface will reach a rough maximum determined by the surface area of the sheath around the probe. This will yield a small positive current to ground and is generally referred to as being in "ion saturation", where the probe is collecting all the ions it can through the probe sheath and very few electrons. This current is given by [4]:

$$I_{sat} = .61 A_{sheath} n_i \left(\frac{T_e}{m_i} \right)^{1/2} \qquad 3.5$$

By measuring the current to the probe tip as a function of bias voltage between the ion saturation point and the electron saturation point, as the electron current to the probe varies from its minimum to its maximum, an estimate of the electron temperature can be obtained. By measuring the maximum positive current to the probe at the ion saturation point an estimate can be made of the ion density, which due to the quasi-neutral assumption of the plasma should roughly equal the electron density. Since the shot length of this experiment is short compared to the length of time necessary to gather data over a large range of voltages, a series of shots are taken each with the probe tip biased at a different potential.

For the case of the double Langmuir probe, neither tip is required to be connected to ground. If both tips are left floating relative to ground, then both tips will be driven by the electron current to the probes to the floating potential and the current between them will be minimal. If a bias voltage is applied between the two probes, each probe tip will be biased either positive or negative of the floating potential. This will allow the negative probe tip to collect fewer electrons and more ions, while the positive probe will collect more electrons and fewer ions. This leads to a current from the negative probe tip towards the positive probe tip, in order to keep the net current to the two probe tips at zero since the probe is floating. As the voltage difference between the probe tips increase one will be driven towards ion saturation and the other towards electron saturation. Since the total current to the probe must be zero and the ion saturation current is small, once the negative probe tip reaches ion saturation a rough maximum in current is reached and increasing the voltage difference between the tips does not significantly increase the current measured [4].

As in the case of the single Langmuir probe, measuring the current as a function of bias voltage can yield an estimate of the electron temperature and the ion saturation current gives an estimate of the plasma density. In this experiment it was typical to measure the electron temperature initially to give a rough estimate, and then typically just keep the double Langmuir probes in ion saturation to estimate plasma density as a function of time and position. While the electron temperature did vary downstream over the course of the plasma shot, this variability was small (less than a few eV) compared to the changes in plasma density over the same time.

Section 3.4C: Deviations of the Experiment from the typical Langmuir Assumptions

The initial assumptions that went into the operation of the Langmuir probes do not entirely apply to this experiment. It is assumed initially that the positive ions and electrons are at equal temperatures, so that the ion motion is small compared to that of the lighter electrons. In this experiment the ion temperatures can be significantly colder than the electron temperatures, but this does not interfere with the “cold ion” assumption being made in the probe description.

Another assumption is that there is no impediment of the flow the electrons due to the magnetic field. In this experiment there are magnetic coils around the source region that establishes a strong enough magnetic field to magnetize the electrons in the source region and for a short distance downstream of the antenna, while not effectively magnetizing the ions anywhere (this will be discussed further in Chapter 4). In this configuration the magnetic field is still not an impediment to sufficient number of ions and electrons impacting the probe tips. The Langmuir probes used were typically positioned along the axis of the thruster, so that there was plenty of plasma available to move along the magnetic field towards the probe without the need of crossing magnetic field lines. When plasma density was measured off the axis downstream of the source, it was typically far enough away from the magnet coils that the electron gyro-orbit was large compared to the size of the Langmuir probe. This means that the effect of the magnetic field on the estimates of electron temperature and density should be minimal.

The ambipolar electric field generated by the electrons moving away from the ions accelerates the ions downstream without significantly changing their temperature, so that the ions instead have high directed energy compared to their thermal energy, flowing downstream like a cold plasma beam. This has several effects on the behavior of the Langmuir probes. The first is that it is more difficult to keep ions from impacting the probe surface, so that the floating potential of the probe is more positive (closer to the plasma potential) than is normal. Effectively the ion current to the probe is large enough to draw an increased electron current to the probe to cancel it out.

The second effect is that the Langmuir probes do not easily go into saturation. In the case of the stationary plasma, a probe tip at the plasma potential or higher can effectively draw in all electrons nearby and can saturate. The same effect occurs when the tip is at a potential strongly negative compared to the plasma potential and it effectively draws in all the ions nearby capable of falling through the sheath. With a steady flow of plasma across the probe there is an increased supply of ions and electrons to interact with the probe tip. As the potential of the tip increases further away from the plasma potential, positive or negative, more of the incoming ions or electrons can enter the sheath and the probe does not saturate as quickly. For the case of ion saturation, the slope of the current vs. voltage plot decreases when the saturation point nears rather than approaching zero. For the case of electron saturation, the probe does not reach saturation even for reasonably high voltages of more than a hundred volts. Both of these cases can be seen in Figure 3.2.

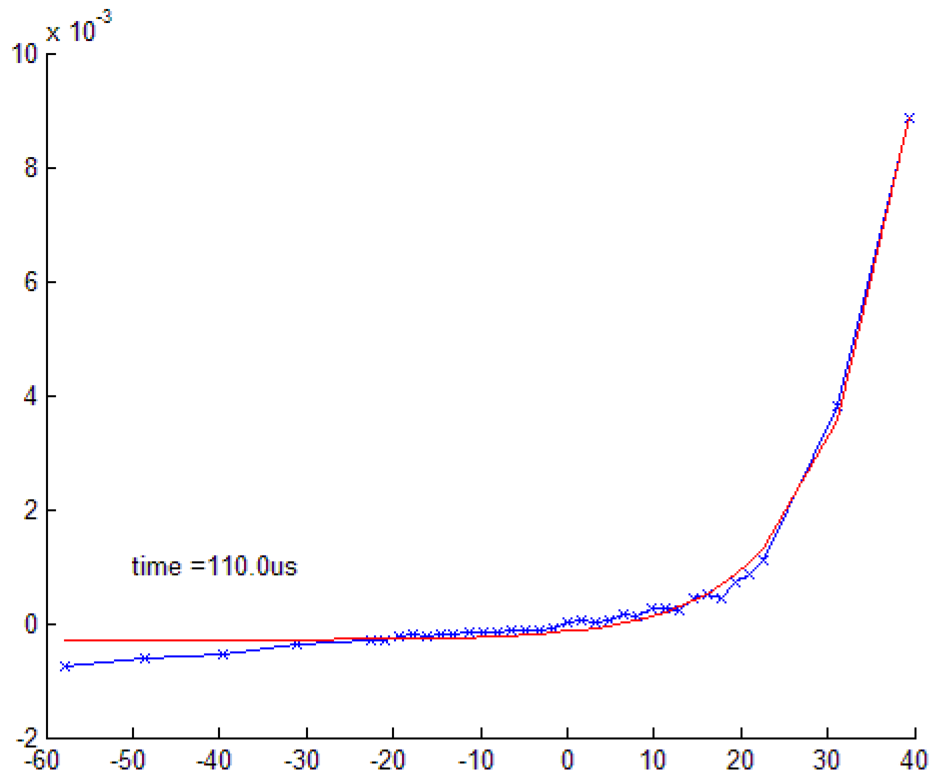

Figure 3.2: Langmuir current as a function of bias potential. At higher positive potentials the probe does not enter electron saturation, and at negative potentials it does not enter ion saturation either. Probe current continues to increase with a different slope to the distribution.

The third effect that the flowing plasma has on the Langmuir probes is that in the case of the double probe that is left floating it is difficult for the probe to establish separate sheathes around each probe tip that are isolated from each other. In order for the double probe to work it needs to have two tips close enough to each other that they are still sampling the same volume of plasma, but far enough apart that a separate sheath forms around each tip to isolate it from the bulk of the plasma between the tips. This allows for one probe tip to go into ion saturation and the other tip to draw a sufficient electron current to compensate. With the plasma flowing past both probe tips, neither tip goes into saturation. As the voltage difference between the probe tips increase, the width of the sheaths between the probe tips and the plasma extends until they overlap with each other and neither tip now has an effective sheath between it and the plasma. In this condition current can flow directly from one probe tip to the other tip through the plasma, leading to a spike in the measured current that is no longer representative of the plasma density. This will be referred to as "arcing" the Langmuir probe, and unfortunately became more common as the downstream plasma density and directed velocity increased with improvements to the experiment.

These difficulties in bringing the Langmuir probes into saturation due to the flowing plasma required some adjustments to the calibration of our density measurements and introduced some uncertainties into the estimates of density and temperature. The difficulty in bringing the double floating Langmuir probes into ion saturation would result in the measurement underestimating the plasma density, sometimes by as much as a factor of two. In the case of the single Langmuir probe, the difficulty in getting to electron saturation of the probe meant that the measurements used to estimate the electron temperature tended to be closer in potential to the floating potential rather than the plasma potential, which was difficult to estimate. The ease of getting electrons and ions to impact the probe tended to push the estimates of the temperature to be hotter than the actual temperature.

Section 3.4D: Description of the Langmuir Probes Used

Several Langmuir probes were used to estimate electron temperature and plasma density downstream of the source region and in the source region itself. The first Langmuir probe of interest was designed for use in the source region. It was constructed with two tungsten tips .5 mm in diameter and 3 mm long with a spacing of 3 mm, and was inserted into the center of the source region along the axis of the thruster. This probe was normally operated as a double floating Langmuir probe, with voltages typically of 20-60 V across the probe tips. It could also be operated as a single Langmuir probe when the circuit was biased relative to ground, and the current from the tip to ground was measured instead, with voltages ranging from -60 V to over 100 V.

The second probe of interest was used to measure plasma density downstream of the source along the thruster axis. It was constructed with two tungsten tips, 1 mm in diameter and

5mm long, and was positioned on along the thruster axis with the tips not shadowing each other from the flowing plasma. It could be moved as close as 8 cm from the source region and as far as 60 cm downstream.

Another Langmuir probe used to measure the density of the flowing plasma along the axis was an asymmetric double Langmuir probe called a planar probe. It was constructed with a flat disk 7 mm in diameter oriented normal to the flow to collect plasma ions, and a stinger that was 8 mm long and 1 mm in diameter for collecting electrons. This probe was designed to have a larger ion collecting surface area to increase the ion current to the probe and increase the measured current for lower density regions far downstream.

The current for each probe was run through a Stangenes transformer to electrically isolate the probe tips from the measurement circuitry, and the output signal from each probe was again filtered with a 1.5 μs low-pass RC filter to cut down on the antenna noise picked up by the wire leads to the tips.

Section 3.5A: Retarding Field Energy Analyzers:

In addition to the Langmuir probes used to measure plasma density and electron temperature, additional electrostatic diagnostics were used to look at the energy distribution of the plasma particles flowing downstream. These diagnostics used retarding electric potentials to shield a variable amount of lower energy plasma particles from interacting with the probe, and are referred to as "retarding field energy analyzers (RFA)". As the retarding potential is raised, more of the particle population is prevented from reaching the collector until the current reaches zero. This measures the energy per charge of the particle population reaching the probe. The RFA diagnostics used in this experiment measured the energy per charge of the ion population downstream of the source region. Since the plasma population flowing downstream was almost entirely singly ionized argon, the energy / charge measurement of the RFA could be used to estimate the velocity of the plasma ions. The exhaust velocity of the plasma as it leaves the thruster system is critical to the efficiency of the thruster, and is one of the parameters that was sought to be improved in this experimental work. A brief description of the construction of the RFA devices and their operation will be given, as well well some discussion of the interpretation of the results.

The outer chassis of the RFA is a steel box that is grounded to the chamber, with a small hole to allow plasma particles to flow into the diagnostic. The interior of the box consists of several partially transparent (50%) nickel grids, which can be biased to a potential while still allowing plasma to pass through. Each of the grids is electrically isolated from the others with ceramic discs. At the far end of the interior is metal disk that collects the ion current of the particles that made it through the retarding potential. The first grid is positioned right at the orifice of the RFA box and is tied to ground like the chassis, and is normally referred to as the "emitter grid". This prevents the RFA box from drifting in potential relative to the plasma over the course of the shot. Both ions and electrons will pass through this grid and into the RFA box.

The second grid in the box is the first retarding potential grid, normally called the "repeller grid". This grid is designed to repel the plasma electrons from passing further into the box while allowing the ions through, and is biased -90 V relative to ground. This will turn away most if not all of the electrons and accelerate the plasma ions through the grid and further into the RFA. The third grid is biased at a variable voltage and is used to screen out portions of the plasma ions from passing further into the RFA, normally called the "discriminator grid". Initially the grid is tied to ground, and so all the plasma ions that passed through the first two grids can pass through the third, letting the whole population through. Then a positive bias voltage relative to ground is added with successive shots, turning back more and more of the ion population. Eventually the grid is at a high enough potential so that most if not all of the plasma ions are turned back and cannot pass further into the RFA.

The fourth grid and the collector plate that follows it are both connected to the Stangenes transformer that measures the ion current to the end of the RFA. The collector plate is biased -115 V relative to ground, and the fourth grid is biased -18 V relative to the collector plate. This means that ions impacting the fourth grid or the plate will both add to the signal. This extra grid is added after the variable retarding potential grid in order to prevent secondary electrons emitted from the collector plate from escaping. As ions impact the collector plate, some can pull off more than one electron, and this results in relatively cold electrons being emitted from the collector plate. If these secondary electrons were allowed to flow from the collector plate to another part of the RFA, this would result in a current that would appear the same way as ion current to the probe and make the signal higher than reality. The fourth grid, biased negative compared to the collector plate, turns these electrons back so they impact with the collector again and so do not generate a current from the plate. But at the same time, any ions that get past the third grid are the ions the probe is trying to measure, so any ions impacting the fourth grid are counted as part of the signal. Because of its role in suppressing the secondary electron current, this fourth grid is normally called the "suppressor grid". The potential of each grid is plotted in figure 3.3, with both the maximum and minimum value of the discriminator grid.

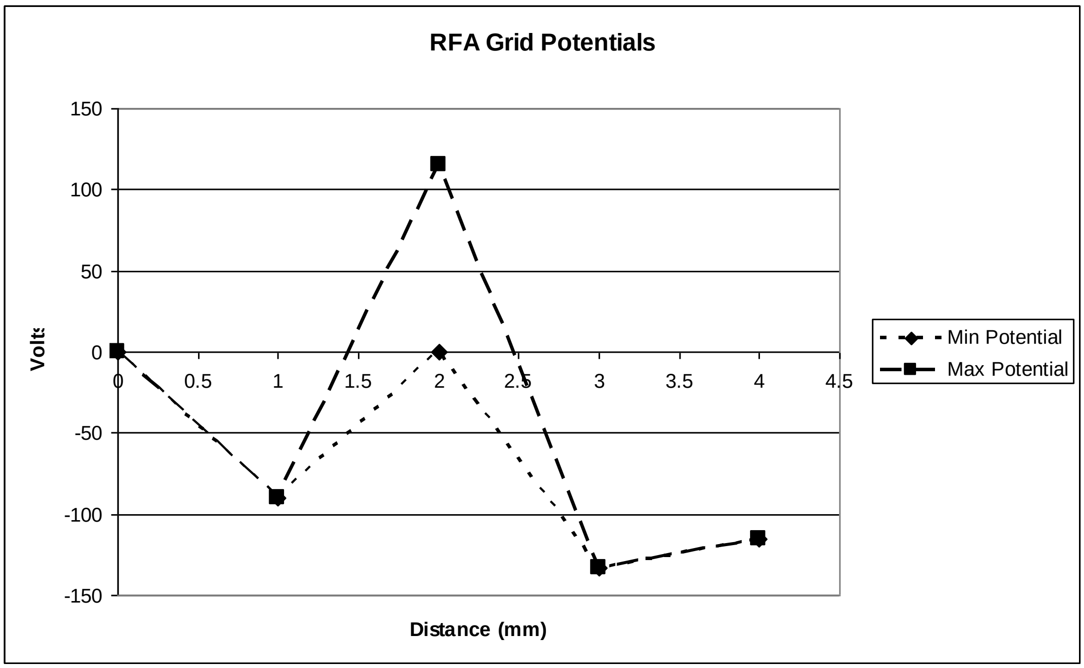

Figure 3.3: Graph of electric potential inside RFA chassis

The measured current is run through a Stangenes transformer that electrically isolates the RFA from the rest of the circuit and steps up the voltage signal. The output voltage is also filtered with a 1.5 μs low-pass RC filter. The RFA boxes used in this experiment were inserted radially from the side of the chamber onto the plasma axis downstream of the thruster. They were fixed in position downstream, but could be rotated so that the input orifice faced the plasma source or was perpendicular to the plasma source.

Section 3.5B: Interpretation of the Ion Energy RFA Results:

A succession of shots is taken with the RFA, increasing the bias voltage on the discriminator grid until the ion current to the collector plate is negligible compared to the initial signal. Plotting current as a function of discriminator voltage indicates what fraction of the ion population is above a particular energy, directed along the axis of the RFA. Taking the derivative of this curve with respect to voltage gives the distribution of ion directed energies in terms of electron volts. Assuming all the ions are of the same species, singly charged argon, the energy distribution can be plotted as a directed velocity distribution.

A few difficulties in interpreting the RFA results need to be addressed. The first is that the RFA probe chassis and first grid are tied to the chamber ground when they are placed in the plasma flow downstream of the source region. Similar to the Langmuir probe, this would normally mean that a sheath will develop between the RFA and the plasma that would accelerate ions into the RFA depending on the electron temperature. This would appear in the data as an increase in the energy of all the ions entering the RFA, an effective shift upwards in directed energy. As stated earlier in the section discussing Langmuir probe assumptions, this is normally the case for a stationary plasma, and the sheath does not form in quite the same way for a flowing plasma such as in this experiment. The clearest way to demonstrate this with the RFA is to rotate the probe so that the orifice is perpendicular to the axis, and thus perpendicular to the expected direction of the plasma flow. If there is a sheath formed between the probe and the surrounding plasma, this sheath should still accelerate ions into the RFA probe when oriented perpendicular to the flow, since it is clear from radial density profiles that downstream of the source the plasma flow is significantly wider than the RFA and the probe should be surrounded by plasma. The results show that the measured ion current drops to zero when the probe is oriented perpendicular to the thruster axis, which contradicts the idea of a large acceleration due to a sheath. This also supports the previous results in Prager et al [10] that suggested the ion beam was cold, and that there is little motion of the ions perpendicular to the flow of the plasma.

Additionally, if the ions were being accelerated by a sheath potential drop of anywhere between 10 and 50 volts based on the electron temperature, this would be measurable in our results as it is identifiable in the results of another experiment that uses similar RFA probes. As a consequence the velocity profile determined by RFA would be significantly higher than in reality, with a bulk velocity increase for the plasma population. However, comparisons between the bulk velocity determined by the RFA and by time of flight estimates from multiple Langmuir probes do not show a dramatic difference in the velocity estimate.

A second difficulty in interpreting the RFA data is determining how much of the plasma ion population makes it through to the end of the RFA and is collected at the suppressor grid or the collector plate. Each of the grids is only 55% transparent and the channel leading from the orifice to the collector plate is narrow, only 5 mm in diameter. The two collecting electrodes are biased at a large negative potential to gather as many ions as possible. It is not known how many of the ions are lost to the grids or the walls of the RFA, or if there is a segment of the population at such low directed energy that they cannot reach the collector. Since the RFA probes were all custom made in house, they have not been calibrated with a known plasma source. Instead, most of the time RFA data is presented in “Arbitrary Units” rather than in terms of particle flux to reflect this. The common technique for this experiment is to measure the plasma density at the same position with a Langmuir probe, and make the assumption that there is no significant segment of the population that can’t be detected in the RFA, so that the density measurement of the Langmuir probe can be used to normalize the signal of the RFA to an ion density.

Chapter 4: Diamagnetic Perturbations Downstream of the Source

Section 4.1: Plasma Detachment from the Magnetic Field Downstream of the High Power Helicon

The plasma output of the HPH flows from the source region with a background magnetic of 300-400 gauss into the expanding dipole region downstream with a significantly weaker magnetic field, transitioning from a region of low plasma beta to a high beta. Additionally, the plasma is accelerated out of the source region at >12 km/s, so that it transitions to a super-alfvenic plasma as the magnetic field strength drops. Determining what effect the dipole magnetic field of HPH will have on the downstream plasma behavior is critical to understanding the expected behavior in a space-like environment. The expectation is that downstream the plasma particle energy, both thermal (represented in the plasma beta of equation 1.14) and kinetic (represented in the square of the Alfven mach number of equation 1.15), will dominate over the magnetic field energy density and the plasma will detach from the magnetic field as it flows away from the thruster. The difficulty is in determining how the electrons will become de-magnetized and how the plasma particles will warp the magnetic field as they leave the thruster.

One mechanism through which plasma particles become detached from the magnetic field is through collisions. If the particles are interrupted in the course of their gyro-orbit around the magnetic field, they will not return to their initial position even if the magnetic field is uniform over their gyro-orbit. This will allow plasma particles to move perpendicular to the magnetic field even when the field is strong enough to keep the gyro-orbit small compared to the scale length of the magnetic field. In the high power helicon experiment the source region is where the magnetic field is the strongest (300-400 gauss), but it is also the region where the plasma particles experience the most collisions with neutrals and each other. In the case of the plasma ions (typically singly ionized argon), collisions with neutrals and other ions keep the ions from being magnetized. If the ions are assumed to be the same temperature as the electrons and well thermalized (the ion-electron collision frequency is ~90 MHz), then for Ti = 10 eV the ion-neutral collision frequency and ion-ion collision frequency are both ~500 kHz, which is larger than the ion gyrofrequency of ~15 kHz [17]. This means that the ions could not complete their gyro-orbits without multiple collisions, so they can't be magnetized to the source field. Additionally, the gyro-orbit of the ions at 10 eV is larger than the antenna diameter, so that the ions would hit the walls of the source antenna before completing the orbit. If the ions are assumed to be much colder than the electrons, such as 1 eV, than the gyro-orbit of the ions is small enough to fit within the confines of the antenna. However, as the ion temperature drops the coulomb collision frequency between the ions in the source region dramatically increases to ~18 MHz, making it less likely that the ions could complete a gyro-orbit before colliding with each other. If the ions have an anisotropic temperature, such as with a higher temperature parallel to the magnetic field than perpendicular to allow a higher ion temperature while keeping the ion gyro-radius small, then we still expect the scattering of the ions from the ion-neutral collisions to keep the ions from completing their gyro-orbits and being well magnetized. In summary, it is expected in the source region that collisions prevent the ions from being magnetized by the base magnetic field.

In the case of the electrons in the source region, the lighter free electrons are expected to be magnetized. With the intense magnetic field the electron gyro-radius is ~0.2 mm and the gyrofrequency is ~1.1 GHz, which is roughly a factor of ten larger than the frequency of collisions for electrons in the source region. Initially as the neutral population in the source region is high while the plasma is being ionized, the electron-neutral collision frequency is ~0.11 GHz, while later in time when the plasma is mostly ionized the electron-electron collision frequency of ~0.16 Ghz and the electron-ion collision rate of ~0.09 GHz dominate. These collision rates are high enough to expect some transport of electrons perpendicular to the field and into the walls of the antenna, but the higher gyrofrequency suggests that the electrons go through many gyro-orbits between collisions and the bulk of the electrons will be magnetized by the base magnetic field in the source region [17].

In the region immediately downstream of the source, when the magnetic field is decreasing like a dipole and the collision rate is dropping, different mechanisms come into play for detaching plasma particles from the magnetic field. In the case of the ions, the collision frequencies are still larger than the gyro-frequency of the ions, so they will still not be magnetized to the field lines of the source magnets. Also, the ion gyro-radius has become large compared to the scale-size of the magnetic dipoles maintaining field, so the ions are not expected to see a uniform magnetic field over their gyro-orbit. This is in contrast to the case of the plasma electrons, where the collision rate between the electrons and the other particles has decreased faster than the magnetic field has dropped off. This is due to the significantly decreased neutral population in the vacuum chamber downstream of the source, as well as the decrease in the plasma density as the plasma is expanding. The neutral population was measured with a capacitive monometer over the course of a typical shot. After the field has decreased to ~100 gauss the electron gyro-frequency is ~280 MHz, while the highest collision frequency is the electron-electron collision rate of ~1.6 MHz. Collisions are no longer a practical mechanism for detaching electrons from the magnetic field, and two other mechanisms begin to play the dominant role.

As the ions move away from the source region they are not well magnetized to the base magnetic field, while the electron still are. As the two populations begin to separate, ambipolar electric fields are generated to accelerate the electrons towards the ions and vice versa. The electrons have difficulty moving across the magnetic field to reach the ions which are more massive and respond slower to the ambipolar electric fields than the electrons. The two mechanisms to bridge this gap and maintain quasi-neutrality are: the electrons finding an alternate path to the ions, and the modification of the magnetic field to allow electrons to move more freely. In the first case the electrons are able to take advantage of the conducting chamber wall of the experimental apparatus to find an alternate path to the ions. The plasma begins to reach the chamber wall and build up a sheath between the conducting wall and the plasma within 100 μs of the experiment being turned on. The large thermal speed of the electrons, ~1,800 km/s, allows the free electrons to be able to move along the magnetic field from the source region to the chamber wall, move along the conducting surface of the steel wall, and then back along the magnetic field in a short period of time compared to the ion movement across the magnetic field, which is in the range of 5-20 km/s. Another path the electrons can take is back into the source region: by following the field back into the source region, collisions can allow the electron to move perpendicular to the field given sufficient time, and then travel out of the source region closer to the dipole axis of the magnetic field and winding up further downstream with the ions. It is expected that once there is sufficient contact between the plasma and the chamber wall, more electrons will take the first path because it doesn't rely on a longer collision time to move across the magnetic field. In this case the electrons are not yet fully detached from the magnetic field, but are in effect able to move across the magnetic field by using the conducting chamber wall.

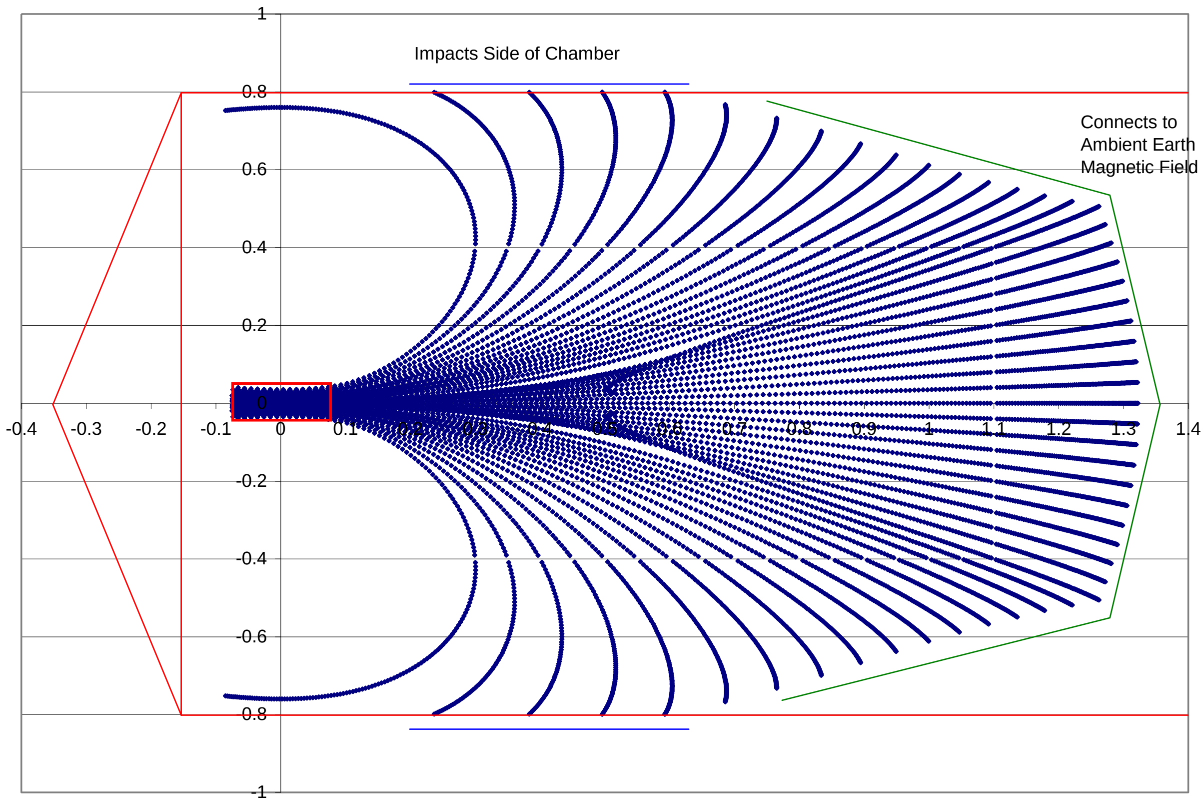

Figure 4.1: Top down view of dipole magnetic field lines emerging from the source region and connecting to either the conducting chamber walls or the ambient magnetic field of the Earth, directed down. Ion motion across the magnetic field lines forces the electrons to take a longer path through the conducting chamber wall when they cannot modify the magnetic field.

The second mechanism by which the electrons can become detached from the magnetic field of the source is plasma particles modifying the magnetic field. As the ions are demagnetized and the electrons aren't, the gyromotion of the electrons around the field relative to the ions (which aren't gyrating) generates an electric current that is diamagnetic to the base magnetic field. This will weaken the magnetic field, increasing the electron gyro-orbit and making it easier for the electrons to move across the field. If there is sufficient thermal energy density in the electrons compared to the magnetic energy density of the base magnetic field, that is if plasma beta is > 1, then this will create a diamagnetic cavity where the magnetic field is low enough for electrons and ions to both pass through without deflection by the field. Across this cavity, and particularly at the edge, there will be a large variation in the local magnetic field and the electron gyro-radius. The electron gyro-radius will be large inside the cavity and small at the edge, leading to a diamagnetic current at the edge of the cavity to sustain it. Similar to how the local magnetic field is reduced inside the diamagnetic cavity, the field is increased at the edge of the cavity where the field of the diamagnetic current and the field from the source magnets reinforce each other. The electrons inside the cavity will be demagnetized because their gyro-radius will be large compared to the length-scale of the source magnetic coils and the diamagnetic cavity diameter. The electrons at the flanks of the cavity (where the field is reinforced) will remain magnetized until the field gets so weak that their gyro-radius is also large compared to the length scale of the background magnetic field. This detachment of the electrons from the base magnetic field of the source by modification of the magnetic field is expected to be the dominant mechanism if the experiment were fired in space without the conducting chamber boundary.

The last point to consider in terms of the interaction between the plasma particles and the magnetic field is when the plasma has moved far enough away from the source that the base magnetic field is no longer dominant over the Earth's magnetic field. Instead of flowing along a diverging magnetic dipole field, the plasma will now be moving perpendicular to a relatively uniform weak magnetic field with a scale length that is large compared to the chamber. Previous experimental observations of the HPH plasma in this region showed the plasma moving across the magnetic field seemingly unhindered, at roughly the same velocities as closer to the source region. This is similar to other laboratory experiments such as those by Wessel et al [18] where a plasmoid was launched perpendicular to a uniform magnetic field and passed through it without modifying the magnetic field or slowing down. In that case as the plasmoid moved across the magnetic field, the differential motion of the ions and electrons due to the Lorenz force developed a polarization electric field across the plasmoid that was perpendicular to both the magnetic field and the direction of motion. The ExB drift of this electric field combined with the perpendicular magnetic field accelerates the ions and electrons in the plasma in the original direction of flow, so that the plasma flows across the magnetic field at approximately the same speed as if the magnetic field wasn't there at all [18].

For the case of the high power helicon firing perpendicular to the ambient Earth magnetic field (~0.5 gauss) the ion gyro-radius is significantly larger than the chamber while the electron gyro-radius is ~20 cm. The electron gyro-orbit is small enough for the electrons to complete their orbits without hitting the chamber wall or colliding with other particles, so we'd expect the electrons to be significantly deflected by the Lorentz force as they moved across the magnetic field. If the electrons are moving perpendicular to the flow independent of the ions, a polarization electric field could be expected to develop across the plume to allow the plasma to flow across the magnetic field with little change in velocity. The electric field would be weak enough that we wouldn't expect any significant deflection of the ions, but the ExB drift of this field on the electrons should act to move them across the magnetic field in the flow direction to keep up with the ions. Whether this effect would dominate over the previously mentioned mechanism where the electrons flow along the chamber wall to keep up with the ions is unclear, but in both cases there would be little to no modification of the background magnetic field as the plasma flows past and little to no change in velocity of the ions.

The experiment by Wessel et al [18] also showed that there was significant deflection of their plasma beam when it was fired into a perpendicular magnetic field that also contained an ambient plasma density that was comparable to the density of the moving plasmoid. In that example, the polarization electric field was reduced to almost nothing, resulting in a large divergence of the plasmoid beam [18]. The same would likely be true when firing the HPH across a magnetic field in space with an ambient plasma density that was comparable to that of the plume. We would expect a significant change in the behavior of the plume as it interacted collisionlessly with the ambient plasma, either exerting a pressure to push it aside and modifying the magnetic field at that location, or diverging rapidly as it moved across the field with little to no polarization electric field.

To summarize the detachment of the plasma from the background field of the HPH source, the ions are not particularly well magnetized anywhere. The electrons are magnetized in the source, with some losses across the magnetic field due to collisions. Downstream of the source the electron collision rate has dropped so that collisions aren't the dominant mechanism for moving electrons across the magnetic field. The bulk of the plasma is near the thruster axis and is mostly traveling along the magnetic field, but near the flanks where the ions are moving across the magnetic field the electrons most likely keep up by moving along the chamber wall instead of modifying the magnetic field. Near the axis there is a significant diamagnetic modification to the magnetic field and it's expected that the electrons are demagnetized in this diamagnetic cavity and follow with the ions. Details of the diamagnetic perturbation are presented later in this chapter. Farther downstream of the source where the magnetic field is weaker the ion gyro-radius becomes larger than the chamber while the electron gyro-radius reaches ~20 cm, so that electrons still have difficulty moving across the magnetic field when they are far enough from the walls to make complete orbits. As the plasma flows across the ambient magnetic field of the Earth, most likely a polarization electric field forms and allows the plasma particles to flow across the magnetic field without slowing down.

Section 4.2: High Beta Effects and Diamagnetic Perturbations in Laboratory Plasmas

One of the mechanisms mentioned in the previous section for detaching plasma particles from the base magnetic field was a large diamagnetic decrease of the magnetic field near the axis. A diamagnetic current develops when the gradient in the plasma pressure is perpendicular to the magnetic field, with the plasma pressure trying to push the plasma across the field and the Lorentz force keeping the plasma particles from moving outwards. As the diamagnetic current develops it acts to weaken the strength of the magnetic field to allow greater expansion of the plasma at the expense of thermal energy from the plasma particles. For this reason the local magnetic field strength will be expected to decrease in the case of large plasma beta, where the plasma pressure gradients are higher and there is more thermal energy available compared to the background magnetic field [3].

In the general case of a high beta plasma that is stationary relative to a background magnetic field, the plasma thermal pressure of the electrons acts to push the magnetic field out of the plasma leading to a diamagnetic decrease of the magnetic field inside the plasma. For plasma beta > 1 this could lead to a complete expulsion of the magnetic field from the plasma, with a large diamagnetic current flowing through the plasma to sustain this change in the magnetic field, with the field decreasing on a time scale related to the conductivity of the plasma [19]. When the plasma is instead moving from a region of low magnetic field into a region of higher magnetic field, the plasma pressure should push aside the magnetic field and have it pile up until the magnetic pressure can balance the plasma pressure, both thermal and dynamic. The opposite case of plasma flowing from a strong magnetic field into a weaker one should result in the plasma warping the magnetic field to push the higher background field into the region of weaker field by driving internal currents to oppose the change in the magnetic field. These effects are seen most commonly in high conductivity space plasmas like the solar wind, which is a high beta plasma that extends the magnetic field of the Sun into the solar system as the interplanetary magnetic field, and exerts a pressure on the magnetospheres of planets like Earth [20].

Laboratory plasmas with electron temperatures in the range of 5-10 eV can still be built up to high plasma beta by increasing the density of the plasma or lowering the background magnetic field. The low electron temperature and higher plasma density results in more frequent coulomb collisions, which increases the resistivity of the plasma and the rate at which magnetic field will diffuse through the plasma. There are also significant loss mechanisms for the laboratory plasma such as recombination and interaction with the chamber wall that aren't present in the space plasma environment. The combination of these loss mechanisms has the effect that in the laboratory environment high beta plasmas produced with dense electron populations of 5-10 eV do not produce the same magnetic perturbations that are common in space plasmas where these loss mechanisms don't play a role.

The effects of high beta plasmas on their surrounding magnetic fields in the laboratory environment have been demonstrated with limited success. An experiment by Stenzel et al [21]. conducted in a uniform background axial field (B_0 = 5 G, $n_e \leq 8 \times 10^{11}$ cm^{-3}, $kT_e \leq 5$ eV) was able to cancel the base field for a plasma thermal beta ratio of 5 but not for $\beta_{thermal} = 1$ as would be expected. Even though $\beta_{thermal}$ exceeded unity for more than 150 μs in the afterglow of the discharge, the magnetic field returned to ~5 G much faster than expected based on diffusion of the field into the plasma. The return to 5 gauss of the magnetic field was correlated in time with the loss of the high energy tail of electrons (kT_e ~ 50 eV) that were responsible for light production in the discharge and not with the bulk thermal electron population providing the plasma pressure used to estimate $\beta_{thermal}$ [21] as shown in the following paragraphs. It is a similar situation to what is seen downstream of the HPH, where the electrons are mostly magnetized to the field with a limited collision rate while the ions experience too many collisions along their orbit to be well magnetized to the field.

One key difference is that the plasma downstream of the HPH source is flowing outward, while the experiment by Stenzel et al [21] features mostly stationary plasma that is sustained near the axis of the chamber against plasma loss rate towards the walls, with the magnetic field limiting the flow of plasma perpendicular. This gives a pressure gradient towards the axis where the plasma density is highest, and this pressure gradient drives a diamagnetic current that acts to weaken the magnetic field on axis where the plasma density is highest, effectively forcing the magnetic flux off the axis and piling it up at the flanks of the plasma column. However, since the ions are unmagnetized they can flow across the field away from the axis driven by the pressure gradient while the electrons cannot move across the field. This builds up an electric field and the ExB drift of the electrons due to this field is opposed to the diamagnetic drift of the electrons. Stenzel et al [21] concluded that these opposing electron motions caused the diamagnetic signal to significantly decrease, forcing the plasma beta to be greater than 1 to expel the magnetic field from the axis. An experiment conducted by Banerjee et al. [22] under similar conditions reported that even with $\beta_{thermal} \sim 10$ their base magnetic field was not entirely cancelled on axis.

A more recent experiment was performed by Corr et al. [19] with a helicon source firing into a dipole field along the axis. Their results indicated a 2% decrease along the axis of the 34 G base field for $\beta_{thermal} = 2$, or a total field change of < 1 gauss. Their magnetic field strength was high enough to magnetize the ions in the plasma plume, unlike the case of Stenzel et al. [21], but they also concluded that the lack of a strong diamagnetic signal was the result of the field rapidly diffusing into the plasma [19].

Unlike other laboratory experiments, the high beta plasma flowing from HPH is shown in the following to significantly distort the magnetic field downstream, exhibiting a diamagnetic perturbation that is 2-5 times higher than what was previously observed. In this chapter I describe these diamagnetic perturbations and their evolution with time in the downstream plasma plume. This includes a diamagnetic decrease along the axis that indicates a complete expulsion of the background magnetic field, which will have significant impact on how the plasma near the axis detaches from the magnetic field and flows away.

Section 4.3: Diamagnetic Perturbations in Previous HPH Results

In the early work on the high power helicon (HPH) experiment, Ziemba [9] also measured a perturbation of the base magnetic field downstream of the source. It developed as the plasma flowed downstream and lasted for a few hundred microseconds. It was a few gauss in strength on the axis and was diamagnetic, similar to what was measured by Stenzel [21] and Corr. [19]. The measurement was made with a radial cut across the source region, showing a diamagnetic perturbation that peaked on the axis and fell off away from the source near the chamber walls.

Early estimates of the plasma velocity downstream of the high power helicon (HPH) by Ziemba et al [8] using the time of flight between Langmuir probes revealed that the plasma was accelerating downstream of the source, with the bulk of the plasma traveling at 4 km/s within the first 15 cm, but traveling at 7 km/s by the time it was 70 cm downstream. It was uncertain at the time whether this acceleration was due to the formation of a double layer similar to that seen by Charles et al [23], or if it could be the result of the helicon wave continuing to couple energy into the plasma downstream of the source region. Measurements of the directed ion energies (>20 eV) by Prager [10] with a retarding field energy analyzer (RFEA) similar to that of Conway et al [24] indicated that the Alfvén mach number was greater than unity within 10-20 cm of the source region along the thruster axis.

In order to characterize the helicon wave downstream of the plasma source and determine if it could be responsible for the downstream plasma acceleration, Prager [2] measured the magnetic component of the helicon wave downstream of the source with an integrated B-dot coil near the frequency of the antenna (~560 kHz). Estimates of the wavelength (~30 cm) closely matched what was expected given the length of the half-wave antenna (15 cm). The wave magnitude was strongest near the source and decreased along the axis, propagating through the plasma as far as 60 cm downstream [2]. At the same time, an axial measurement of the diamagnetic perturbation was made, showing a similar perturbation as was previously measured (at most a few gauss), that also extended down the axis as far as 60 cm downstream. This perturbation was correlated in position and time with the wave magnetic field, with the perturbation disappearing within tens of microseconds of the antenna being turned off and the wave was no longer being driven [2].

To further study whether the measured helicon wave was responsible for the diamagnetic perturbation and the downstream acceleration of the plasma, I modified the antenna and power supply of HPH to have a left-handed pitch similar to the type 'R' antenna discussed by Light et Al [25]. To test the coupling between the new antenna and power supply, data was taken with the wave propagation and plasma flow anti-parallel to the magnetic field as it was for the work by Prager [2], as well as with the flow parallel to the field. The case with anti-parallel propagation resulted in a diamagnetic perturbation of at most a few gauss similar to the previous results, but with the field directed parallel to the field there was a dramatic increase in the magnitude of the diamagnetic perturbation measured downstream. The two cases are plotted together compared to the base magnetic field in Figure 4.2.

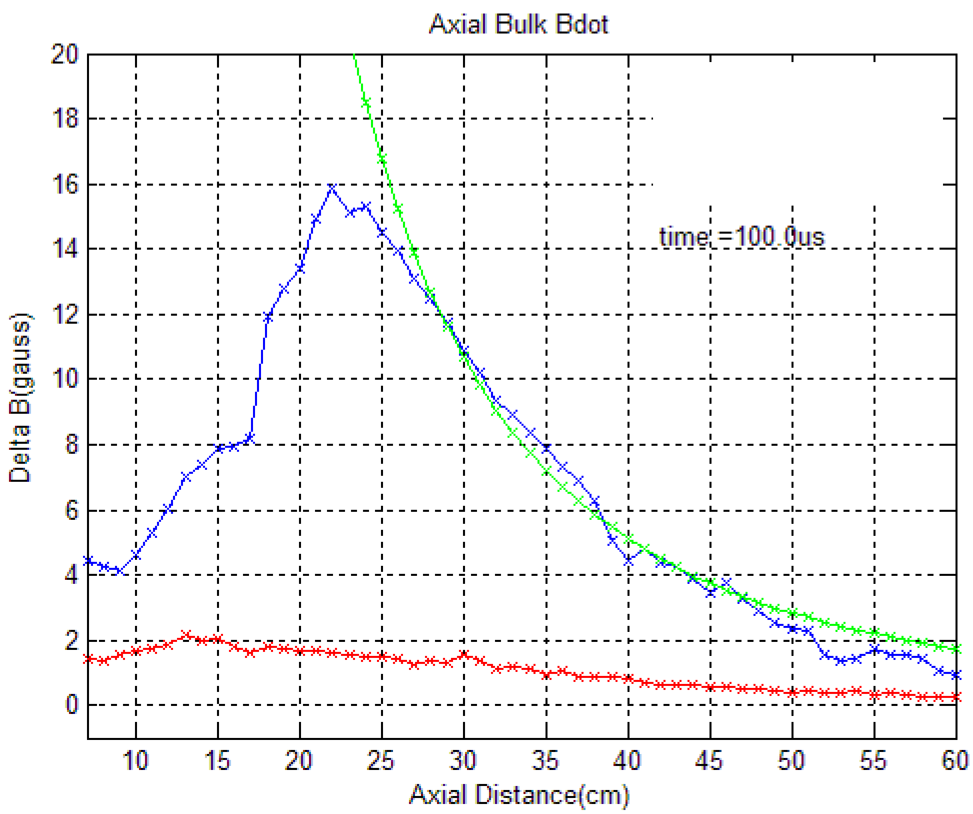

Figure 4.2: Axial diamagnetic perturbation relative to the base magnetic field. The red trace is for propagation anti-parallel to the magnetic field, while the blue trace is for parallel propagation. The green trace is the magnitude of the base magnetic field

The two cases displayed in Figure 4.2 are for the same magnetic field magnitude, helicon antenna, and input power from the antenna. The only difference is the direction of the magnetic field compared to the direction of plasma and wave propagation. The anti-parallel propagation case has a peak in the perturbation of ~2 gauss as previously observed, peaking near the antenna and decreasing in magnitude down to a fraction of a gauss 60 cm from the plasma source. In contrast, the diamagnetic perturbation in the parallel propagation case is ~4 gauss near the source antenna and then increases to a peak of ~16 gauss roughly 20-30 cm downstream. At this point the diamagnetic perturbation is about the same magnitude as the base magnetic field but in the opposite direction, suggesting the total magnetic field on the axis is ~0 gauss. Further downstream the diamagnetic perturbation decreases from this peak at the same rate the base magnetic field decreases, maintaining the condition of the magnetic field being near 0 along the axis. To study this dramatic increase in the diamagnetic signal, magnetic probes were used to study the perturbation near the axis along with axial measurements of the wave magnetic field similar to those conducted by Prager [2]. These results are presented in the following sections.

Section 4.4: Diamagnetic Perturbations along the Axis

The base magnetic field of HPH falls off like a dipole field and drops in magnitude from hundreds of gauss near the exit of the source down to the terrestrial field strength within 1.5 m of the source. This was done to simulate space-like conditions where it is not feasible to maintain a uniform field far downstream of the spacecraft.

The planar probe indicated a flowing plasma population similar to that seen in Prager [2], with the peak density decreasing as the probe is moved further from the source. The antenna was shut off at 200 μs and the decrease in the downstream density is delayed by the time it takes the plasma to flow downstream at the bulk plasma speed. This plasma density is shown as function of time in Figure 4.3 for axial locations at 15 cm, 30 cm, and 45 cm (with time relative to the antenna activation). These density data are compared with the measurement of the perturbation to the bulk magnetic field along the axis at the same location. Prior to the arrival of plasma at the locations 15 cm and 30 cm downstream there is no change in the bulk magnetic field. Within

~10 μs of the plasma density increase the B-dot detects a diamagnetic change in the bulk axial magnetic field at that same position.

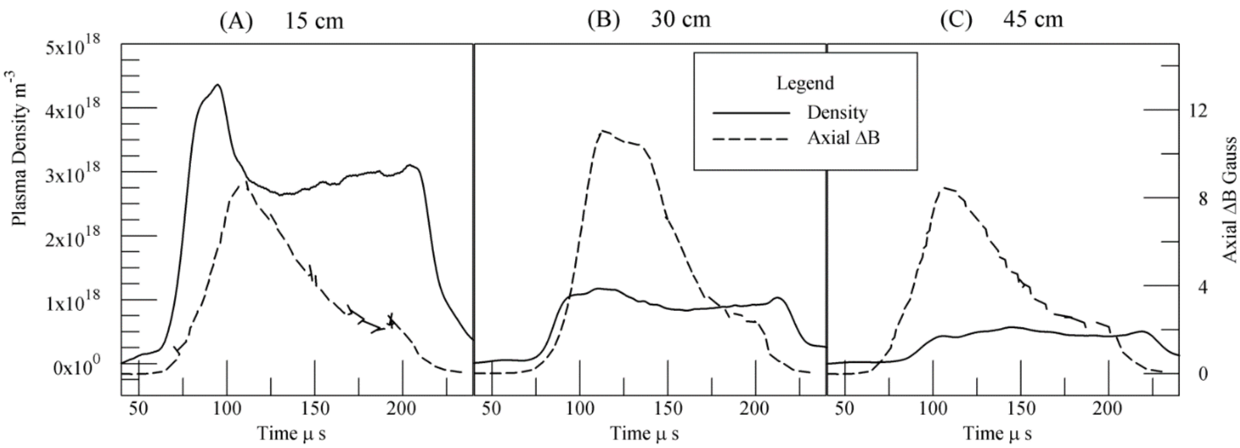

Figure 4.3: The axial component of the measured magnetic perturbation (Gauss) is shown in the dashed line along with the electron density profile shown in the solid line at the same location. The direction of the ΔB was diamagnetic, decreasing the total magnetic field.

The diamagnetic perturbation increases over a period of ~30 μs at each of the downstream locations in Figure 4.3 and builds to a peak value of 8-12 G. At each position the ΔB begins to fall with time after 110 μs and decreases to ~2 G which is more typical of earlier measurements. This suggests the perturbation is decreasing with time either because the population of particles carrying the diamagnetic current are propagating away or being damped out (independently of the bulk population measured by the planar probe), or because the effect is being damped out by plasma increasingly interacting with the chamber wall.

At 200 μs the antenna is shut off and at each point downstream in Figure 4.3 the magnetic perturbation decays away in less than 10 μs, even though the density measurements indicate that source plasma is still flowing downstream from the helicon for more than 10 μs after shutoff. This is similar to the results of Stenzel et al [21] in which their diamagnetic perturbation disappeared within 100 μs of their source being shut down, even though the measured plasma pressure still indicated a $\beta_{thermal} > 1$. This indicates that part of the diamagnetic perturbation late in time is being driven by the source antenna, and is strongly damped out as soon as the source is shutoff.

Previous experiments with a low background field of ~5 G indicated that a high plasma pressure ($\beta_{thermal}$ >1) was capable of canceling out most of the axial magnetic field, while the work of Corr et al [19] used a significantly higher background field of ~34 G that could not be cancelled out with their helicon source. In these results from HPH it was observed that once the axial field strength had decreased to <15 G the peak of the diamagnetic perturbation was approximately the same magnitude as the base magnetic field. Figure 4.4 shows the axial magnetic perturbation plotted as a function of axial distance for six characteristic times throughout the plasma shot. For comparison the axial component of the base magnetic field is plotted on the same scale, but the ΔB is diamagnetic so that the two fields have opposite signs.

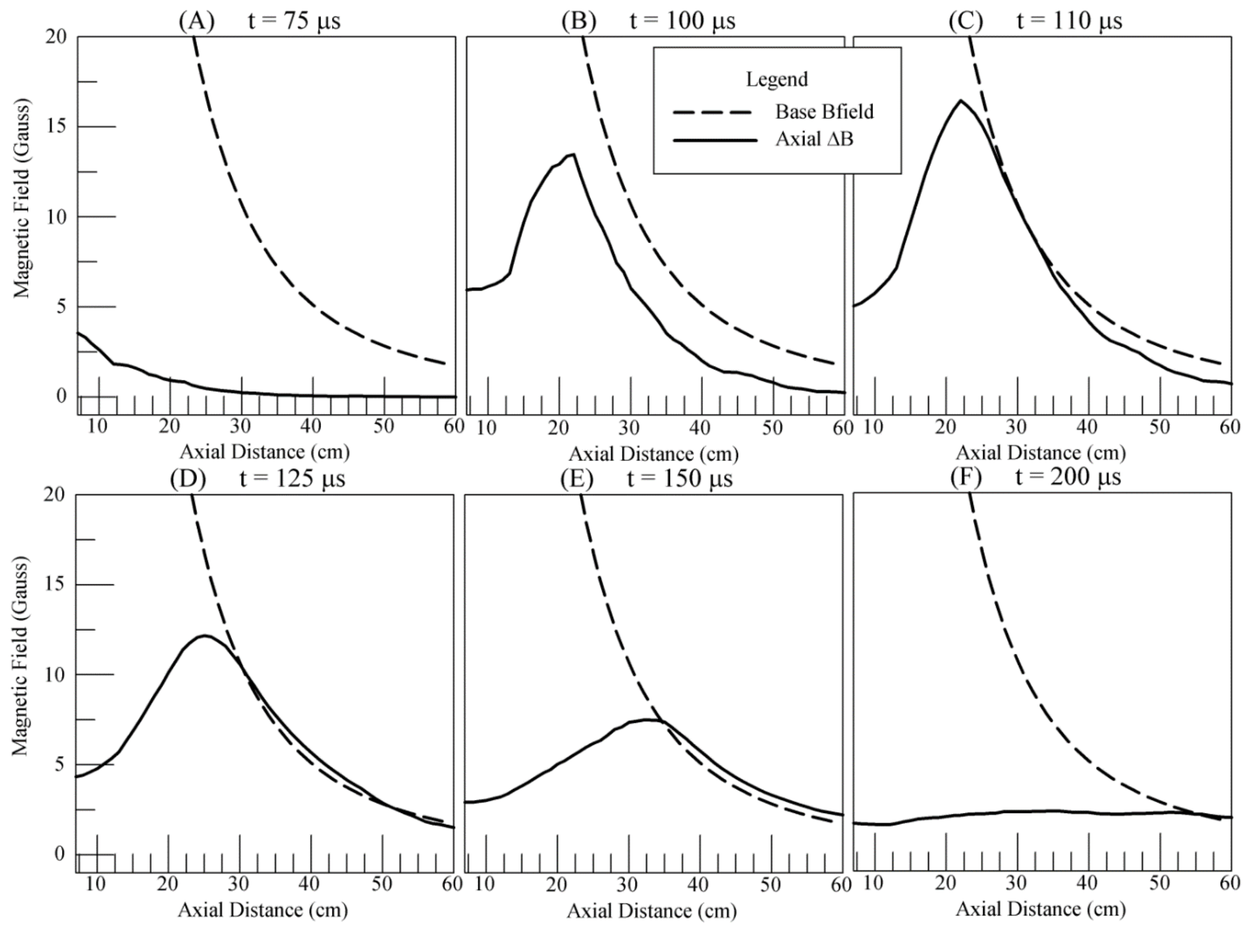

Figure 4.4: The axial magnetic perturbation ΔB downstream of the source is shown as the solid line for six separate times. The axial component of base field is plotted as a dashed line to show the comparative strengths, but the two fields are opposite in direction (diamagnetic).

Early in time at t = 75 μs (Figure 4.4a) the perturbation is only ~4 G and is restricted to near the source antenna. The diamagnetic perturbation builds in strength and reaches a peak value of >15 G on axis at 110 μs (Figure 4.4c), between 20 and 30 cm downstream of the plasma source. The perturbation falls off in intensity farther downstream in Figure 4.4c, but beginning at ~25 cm downstream the perturbation is comparable to the base magnetic field. The magnitude of the perturbation roughly follows the fall in strength of the axial base magnetic field downstream of the peak. In time the peak of the perturbation shifts further downstream, decreasing in magnitude with the base magnetic field as shown in Figure 4.4d and Figure 4.4e and canceling the axial field downstream of the peak. By the time of antenna turnoff at 200 μs, the magnetic perturbation has become a more uniform ~2 G field along the axis, which is still large enough to cancel the base magnetic field at 50 cm downstream. This large diamagnetic perturbation of the field (>15 G) is significantly higher than what was measured with previous versions of HPH or reported in other helicon sources. This indicates that from 110 μs and later in time there is an extended region along the axis downstream where the magnetic field has been fully expelled from the axis and the axial component of the total magnetic field (the dominant local field) is ~0.

Section 4.5: Comparison of Diamagnetic Perturbation with Helicon Wave Magnetic Field

A smaller 3-axis magnetic field probe was used to observe waves propagating downstream of the source similar to those of Prager et al [11] and was described in Chapter 3. The temporal and spatial evolution of the wave magnetic field is directly tied to the evolution of the total axial magnetic field, as shown for six times in Figure 4.5. The external base magnetic field provided by the dipole magnets and the diamagnetic perturbation to the axial field are combined to form a total axial field represented by a dashed curve.

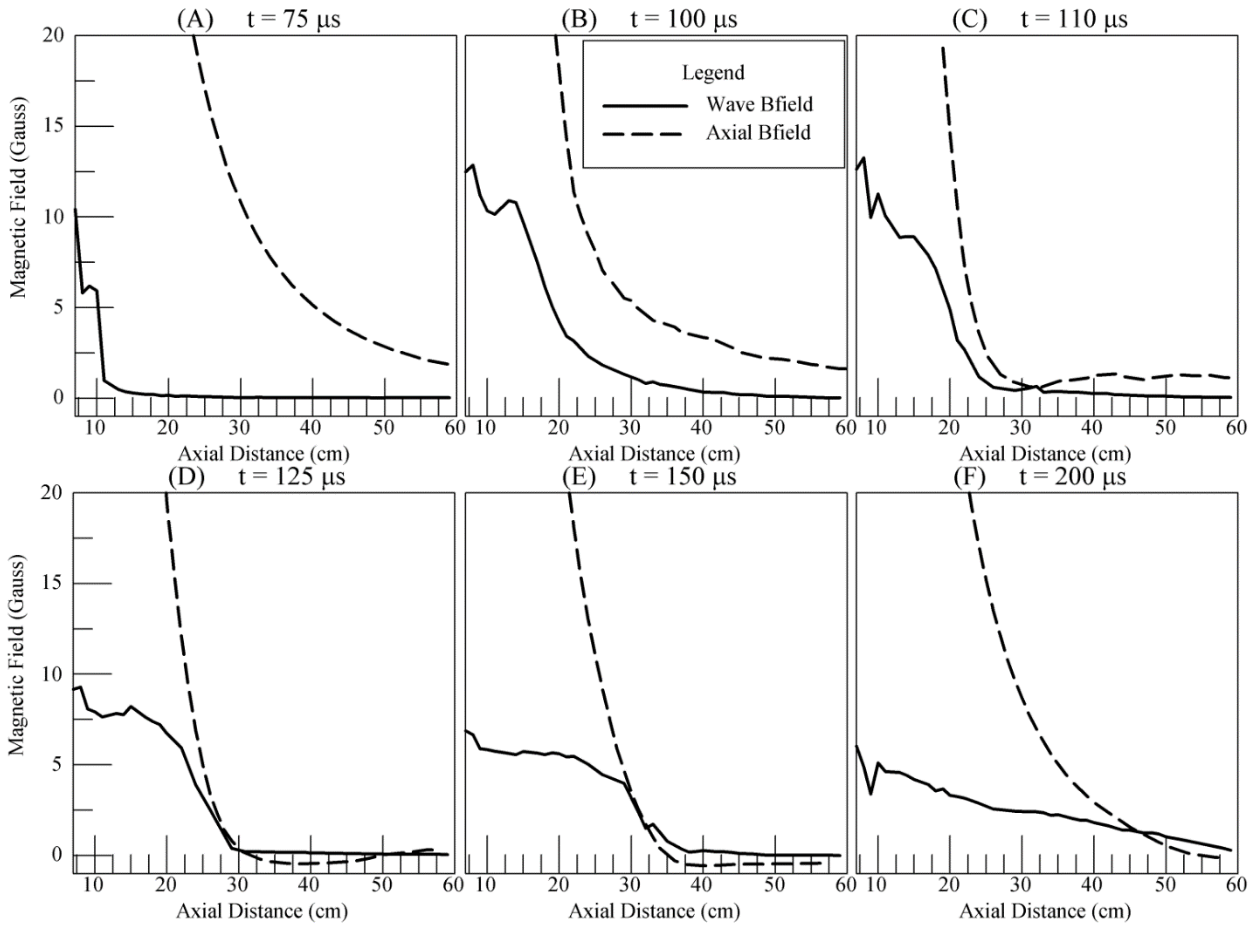

<u>Figure 4.5: Comparison of the wave magnetic field magnitude (solid line) to the total axial magnetic field magnitude (dashed line) downstream of the source at six times. Downstream of the source the wave magnetic field driven by the antenna is comparable to the axial magnetic field.</u>

As the oscillating wave magnetic field propagates downstream with the plasma it is initially bound by the edge of the plasma, but as the total field begins to drop when the external magnetic field is expelled from the axis the wave magnetic field is clearly being bound on the right-hand side by the drop in axial magnetic field as seen in Figure 4.5c. The wave magnetic field decreases in magnitude following the axial magnetic field, dropping from ~2 G 25 cm downstream in Figure 4.5b to ~0 G at the same position in Figure 4.5c.

Later in time in Figure 4.5d and Figure 4.5e the point at which the axial magnetic field drops to zero has moved farther downstream, and the wave magnetic field has propagated farther downstream as well, still following the decrease in the axial magnetic field. This is good evidence that the external magnetic field is being 100% expelled from this region near the axis because the helicon wave requires a base magnetic field to propagate, the lack of the helicon wave suggests that the local field strength is ~0. Beginning at 150 μs it is possible that the wave field is beginning to penetrate into the region at a lower magnitude, perhaps because the diamagnetic effect has begun to damp away and it no longer is completely expelling the field.

The ratio of the wave magnetic field to the total axial field in Figure 4.5 is significant because most helicon sources are thought to produce a linear plasma wave, with the wave magnetic field being a small perturbation of the total field. In the case of the High Power Helicon (HPH), the plasma wave being produced by the source is a non-linear perturbation of the wave field, being perhaps >10 G in the source region (compared to 400 G peak base field), and 4 G downstream of the source when the total axial field has dropped to ~4 G. This region where the wave magnetic field is the same magnitude as the total field could be part of the explanation why the peak in the diamagnetic perturbation occurs so far downstream of the source, since the diamagnetic effect is at least partially driven by the antenna late in time.

Section 4.6: Correlating Antenna shutoff and Diamagnetic Perturbations in time

In order to further correlate the dramatic drop in the diamagnetic perturbation along the axis with the shutoff of the helicon antenna and the loss of the helicon wave being generated, the shot length of the experiment was varied over several hundred microseconds. Figure 4.6 compares the axial diamagnetic signal compared to the base magnetic field for the case of three different shot lengths for the 20 μs immediately following turnoff.

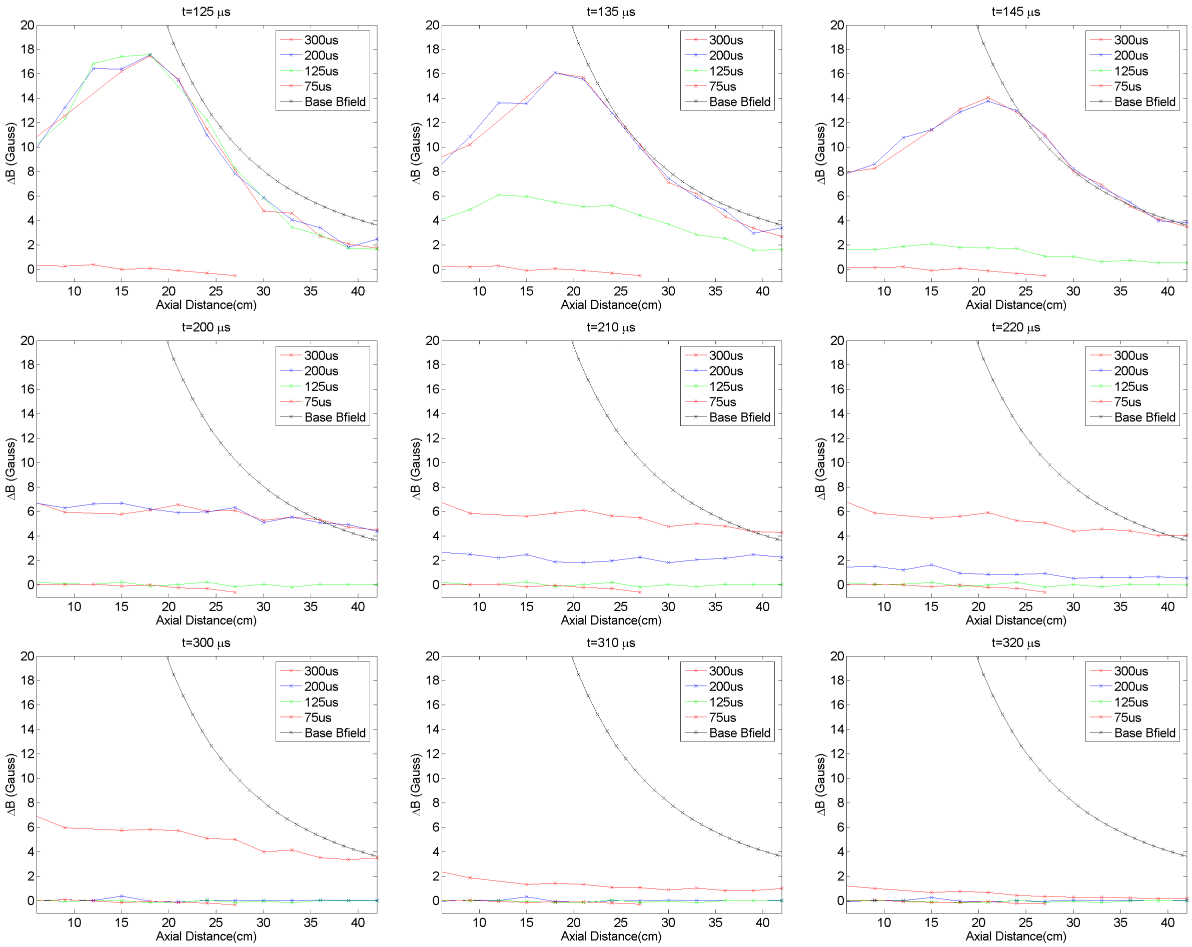

Figure 4.6 Shutoff of the Helicon antenna at 125, 200, and 300 μs. The perturbation mostly disappears over the 20 μs after shutoff, while the plasma characteristics do not dramatically change on that timescale. These images correlate the antenna shutoff with the fall of the diamagnetic perturbation, rather than a change in the plasma pressure.

In the case of the 125 μs shot, the antenna is turned off before the diamagnetic signal reaches its peak, even though the bulk of the high beta plasma is still flowing downstream. For the ~20 μs after the source antenna is turned off the plasma population downstream of the source will continue flowing roughly the same as seen in the density profiles of Figure 4.1. In the top row of Figure 4.6 the shot which was shutoff at 125 μs dramatically decreases over the next 20 μs while the two shots with the antenna being left on continue to show a large diamagnetic signal and a reduction of the field along the axis to zero. This indicates that the peak diamagnetic perturbation is not associated with a plasma pulse created in the source prior to 125 μs that is just propagating downstream, but is instead being driven constantly by the antenna, resulting in the early shutoff case in the top row of Figure 4.6 never reaching the same peak perturbation downstream as in the two shots where the antenna was left on longer.

For the second row of Figure 4.6, the diamagnetic perturbation has settled into a uniform perturbation of 5-6 gauss for a long distance downstream. When the antenna is shutoff at 200 μs, the diamagnetic perturbation again damps out rapidly while the plasma population downstream is again relatively unchanged. The shot which remains on for 300 μs maintains the same uniform perturbation for another 100 μs until it is shutoff in the third row of Figure 4.6. This indicates a relatively stable value for at least a few hundred microseconds for the diamagnetic perturbation to achieve. Again, the diamagnetic perturbation drops immediately when the antenna is shutoff.

The rapid decrease in the diamagnetic signal measured on axis when the antenna is shutoff indicates that the diamagnetic perturbation isn't simply being carried by the plasma downstream, but is being driven by the antenna and is being strongly damped by another mechanism, so that the magnetic field on axis returns to normal within ~20 μs.

Section 4.7: Estimate of the Diffusion Rate for Magnetic Field onto the Axis

In both the Stenzel et al [21] and Corr et al [19] experiment, rapid diffusion of the magnetic field into the plasma is suspected to be the reason why the diamagnetic signal is smaller than expected. Following the example of Corr et al [19], they estimated that for magnetic field diffusing into a collisional stationary plasma, the characteristic time would be given by:

$$\tau = \frac{\mu_0 L^2}{\eta} \tag{4.1}$$

where L is the characteristic length scale of the magnetic field (in this case the radius of the magnetic dipole) and η is the resistivity of the plasma assuming that the dominant term is the coulomb collision of electrons and ions, which is true downstream of HPH. For a laboratory plasma with an electron temperature of ~10 eV like in the case of the collisional region immediately downstream of HPH, $\eta \sim 1.65\text{x}10^{-5}$ ohm-m. Plugging in the dipole magnet radius of ~7 cm, this yields a value of $\tau \sim 375$ μs. This time scale is longer than the value from Corr et al [19] of ~50 μs, where colder electron temperatures of 5 eV and below were used. In this case we'd expect the time needed to diffuse the magnetic field from the edge onto the centerline to be on the order of hundreds of μs for a 5-10 eV plasma. This is long compared to the rapid falloff in diamagnetic signal measured on axis of the HPH, which is usually on the order of tens of μs. This suggests that the plasma is either far more collisional than estimated so far, or there is a separate mechanism responsible for the rapid drop in diamagnetic field when the antenna is switched off.

Section 4.8: 2-D Spatial Variations of Diamagnetic Perturbations Near the Axis

To study how the perturbation of the base field changes near the axis in finer detail, an array of seven, 3-axis bdots was used. This probe array was described in Chapter 3 and produced a 2D data set that is ~50 cm long and ~12 cm wide in a vertical plane along the axis of the thruster. The z component of the B-dot array was used to measure the axial component of the diamagnetic field perturbation and ΔBz is shown as a function of position for four separate times in Figure 4.7. The scales on the plots are distorted due to the probe being able to move a much farther distance axially downstream than the radial width of the probe array.

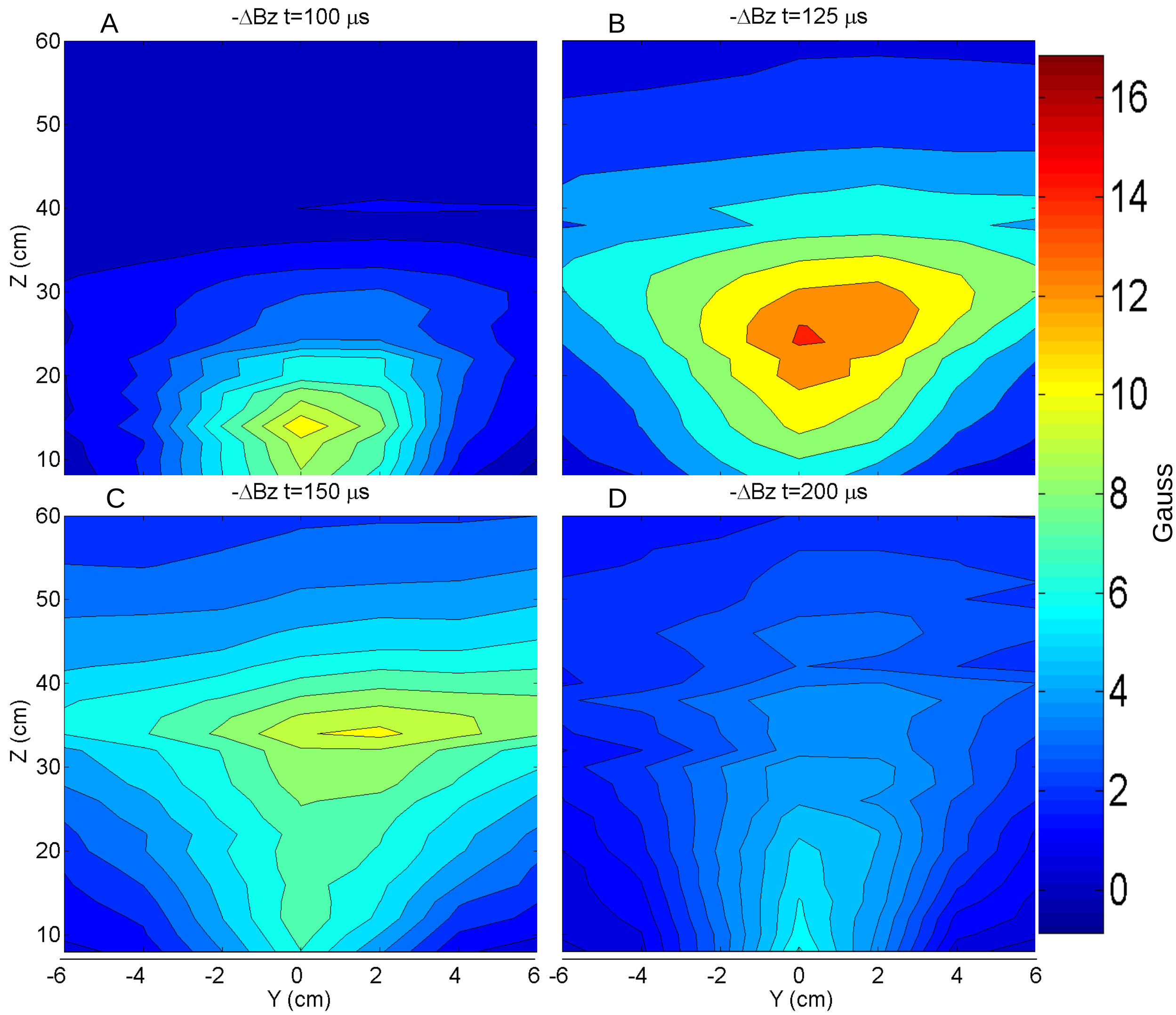

Figure 4.7: The -ΔBz component of the magnetic perturbation downstream of the source at four times, with the z-axis is aligned with the thruster axis. This effectively axial perturbation to the field is anti-parallel to the axial component of the base field in each frame. The -ΔBz is the largest component, and the color scale for this figure covers a larger range than the others.

Early in time at t = 100 μs in Figure 4.7a the diamagnetic perturbation is restricted to near the antenna source, peaking at 15 cm downstream and not extending more than a few cm off the thruster axis. In Figure 4.7b at t = 125 μs, the perturbation has propagated farther downstream and peaks at ~25 cm, and extends further from the axis as the base magnetic dipole field diverges from the axis. The magnetic perturbation has already expanded beyond the edge of the probe array, with the ΔBz > 5 G at 6 cm away from the axis. The diamagnetic perturbation appears roughly symmetric and is centered on the source axis, with the magnitude falling off radially as the axial component of the external dipole field decreases.

This evolution in time is similar to the results of the axial probe: a diamagnetic perturbation is built up downstream and propagates away from the source, with the peak of the ΔBz roughly equal to the base magnetic field strength, leading to a cancellation of the field as the peak moves past it and expelling the external field. Figure 4.7 indicates that the magnetic perturbation is not just limited to near the source axis but is part of a large diamagnetic effect over an extended region downstream of the source. If the decrease in axial magnetic field near the axis was due to flux being pushed outward by the diamagnetic effect as was thought in Ziemba [9], it would appear in the data set as an increase of the base magnetic field on the radial edge of the ΔBz or further downstream of the source. There is no indication of an enhanced axial field in the bulk B-dot array results near the axis in Figure 4.7, though it is expected it be there in order for the divergence of the magnetic field to be zero. It is possible that the increase in flux would only be measurable tens of centimeters off the axis as was seen previously, which would put it too far off axis to measure with this probe array centered on the axis.

The y-axis of the bdot array is oriented vertical to the ground and perpendicular to the thruster axis, so that the y-axis gives effectively the radial component of the magnetic perturbation, taking into account the change in sign across the axis. The ΔBy component of the magnetic perturbation is shown as a function of position for four separate times in Figure 4.8. Early in time in Figure 4.8a, ΔBy is limited to within 15 cm of the source antenna and peaks a few cm off the axis. The sign of the ΔBy is opposed to the y component of the base magnetic field, pointing radially inwards towards the axis while the diverging dipole base field is pointed away from the axis, indicating that this is a diamagnetic perturbation as well. This suggests that early in time and near the source, the region in which the external field is entirely expelled is extending radially off axis for at least a small distance.

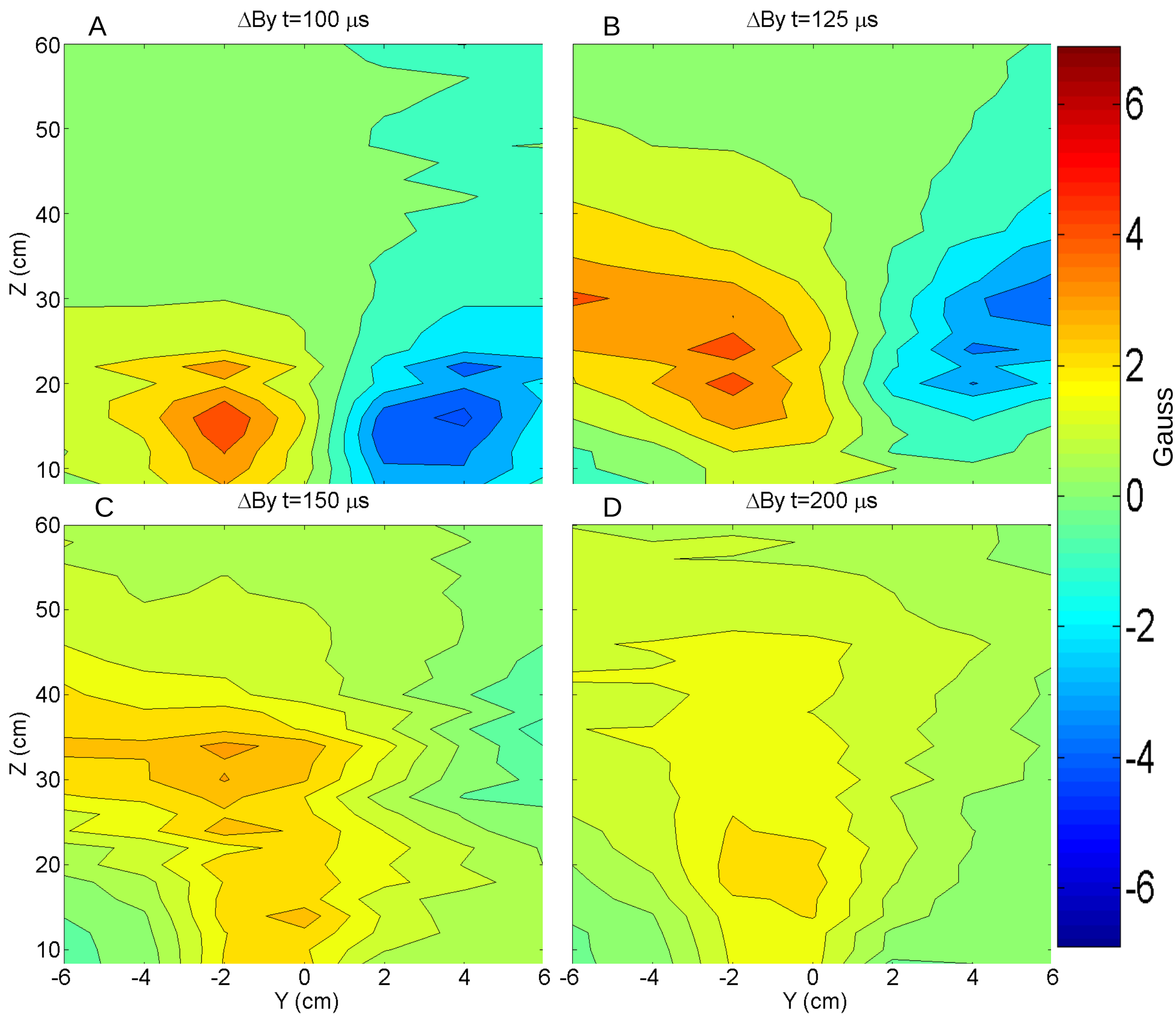

<u>Figure 4.8: The ΔBy component of the magnetic perturbation downstream of the source at four times, with the y-axis being vertical. This (effectively) radial component of the magnetic perturbation is initially diamagnetic and points towards the thruster axis, but late in time becomes uniformly upward. Note that the color scale for ΔBy has a smaller range than the dominant ΔBz.</u>

Even though the base magnetic field coils provide a symmetric field with a radial component point away from the axis, there is an additional field component due to the Earth's magnetic field. At the latitude where these data were taken the Earth's magnetic field is ~0.5 G vertically downward, and part of the asymmetry is likely due to the magnetic perturbation opposing the total magnetic field: the dipole magnets and Earth's field together. The addition of the Earth's field by itself is not enough to explain the asymmetry, but since the magnetic perturbation has expanded beyond the limits of the probe this suggests that the probe array is only sampling part of a larger region of ΔBy.

The x-axis of the B-dot array is pointed horizontally to the left looking along the z-axis and gives effectively the azimuthal component of the magnetic perturbation around the axis, after accounting for the change in sign. The ΔBx component of the magnetic perturbation is shown as a function of position for four separate times in Figure 4.9. For each of the four times, the ΔBx is mostly positive (to the left) above the source axis and negative (to the right) below the axis, making this (effectively) azimuthal perturbation of the magnetic field left-handed around the source axis. For the vertical cut measured along the axis by the B-dot array, both the base magnetic field dipole and the Earth's magnetic field only have significant components in the axial and radial direction (the y-axis and z-axis). There should not be any external base magnetic field component along the x-axis, in the azimuthal direction, so the magnetic perturbation ΔBx is not diamagnetic and is instead an increase in the magnetic field in that direction. Early in time in Figure 4.9a the ΔBx is restricted to near the source antenna, but there is an asymmetry in the magnitude, with the perturbation above the axis peaking at ~5 G and the perturbation below the axis peaking at half of that. Each region has expanded to be roughly the same size, but is more diffuse below the axis and peaked above it. In Figure 4.9b at t = 125 μs, the ΔBx has expanded beyond the edge of the probe array on both sides, with the peak of the perturbation above the axis being on or near the edge of the probe array.

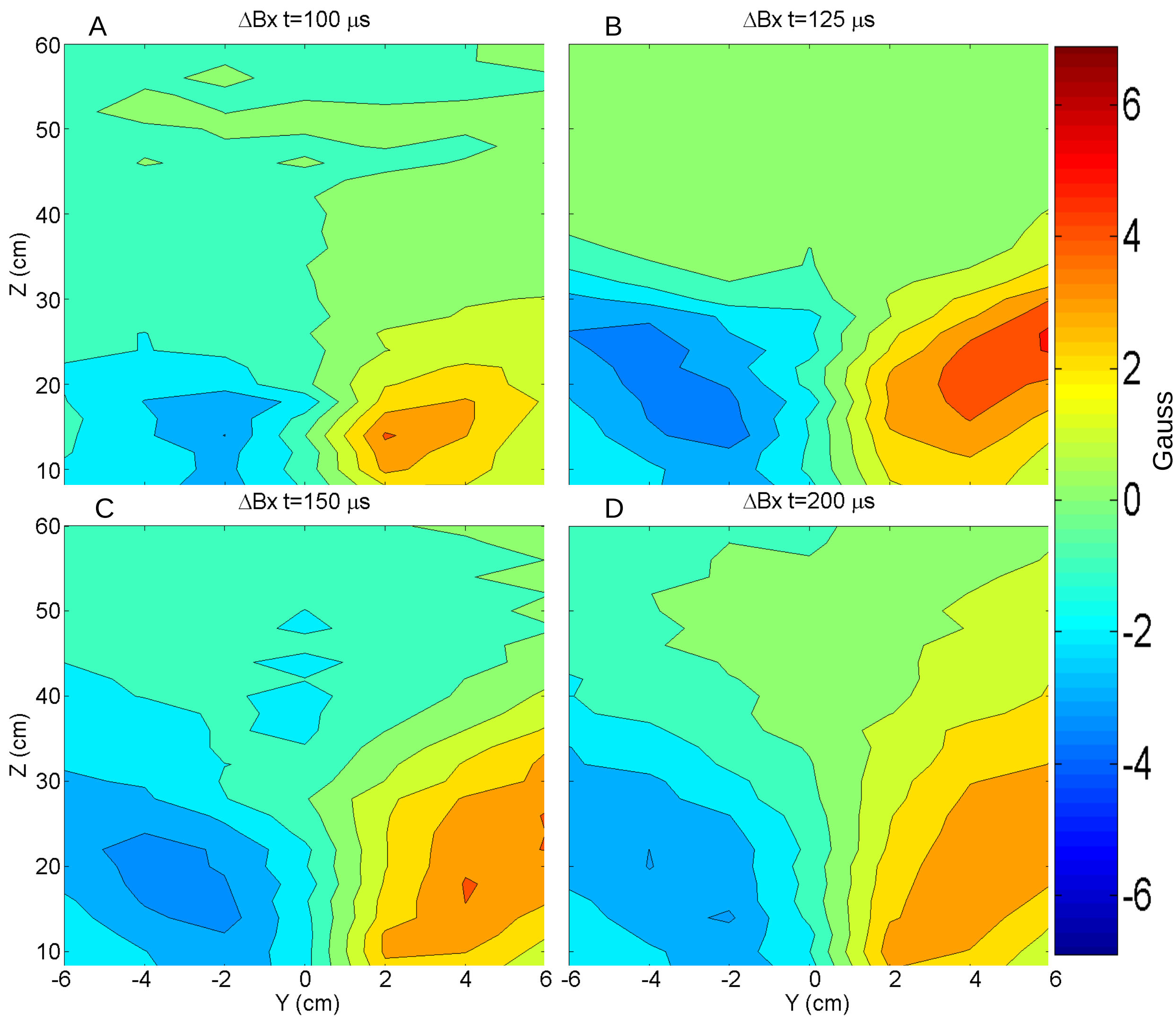

Figure 4.9: The ΔBx component of the magnetic perturbation downstream of the source at four times, with the x-axis being horizontal. This (effectively) azimuthal component of the magnetic perturbation is a left-handed perturbation around the thruster axis. Note that the color scale for ΔBx has a smaller range than the dominant ΔBz.

The three axes of the B-dot array taken together suggest that the magnetic perturbation is a macroscopic effect that begins near the source region and expands downstream and radially away from the source building up to a peak value. Then the perturbation propagates downstream off the edge of the probe array as well as expanding radially away from the axis beyond where the probe can measure. Near the time when the antenna has turned off there is an extended region downstream with a magnetic perturbation ≥1 G and near the source the perturbation is still >5 G until the antenna is turned off, at which point the magnetic perturbation disappears within tens of microseconds. The ΔBz diamagnetic perturbation is the dominant term, building to a peak >15 G more than one antenna length away from the source. The ΔBy term was in some cases diamagnetic but was also asymmetric later in time above the axis. The ΔBx term was not diamagnetic because there was no base magnetic field in the x direction along the axis of the probe array.

Section 4.9: Summary of Diamagnetic Perturbation Data:

Early tests of the previous version of the HPH system using anti-parallel wave propagation exhibited diamagnetic perturbations at most a few gauss, similar to what has been published associated with other helicon plasma thrusters. This was originally a radial profile which peaked on axis and was not large enough to cancel out the base magnetic field, even with the plasma beta >1 and the plume being both supersonic and super-alfvenic [9]. Subsequent tests using a modified version of HPH measured an axial diamagnetic perturbation of the magnetic field of at most a few gauss along the thruster axis downstream as far as 60 cm. The helicon wave was also measured along the axis downstream to determine how far the wave was propagating and how quickly the wave was damping out away from the source antenna [2]. Initial tests of the version of HPH that I used for my research were done with the magnetic field reversed so that the wave and plasma were propagating anti-parallel to the field. This configuration produced a diamagnetic perturbation of a few gauss, similar to what was seen with the previous HPH system. It was not until the magnetic field was aligned downstream that the large diamagnetic perturbations were observed.

The peak in the diamagnetic perturbation downstream increased by almost a factor of 10 after the magnetic field was aligned downstream, with the wave and the plasma both propagating parallel to the field. The peak in the diamagnetic perturbation is measured 20-30 cm downstream of the source where the magnitude of the base magnetic field has decreased enough for the perturbation to roughly cancel out the field from the magnets, for a net field of ~0 on axis.

Beyond this point the diamagnetic perturbation decreases in magnitude roughly as the base magnetic field falls, so that the perturbation cancels out the field but does not seem to reverse it.

The perturbation decreases with time down to a value of ~2 gauss which is similar to previous results and other experiments, but the decrease is not associated with a change in the bulk plasma density. Plasma density downstream of the source is relatively uniform as the perturbation decreases in magnitude over the shot length. After the antenna is shut off, the perturbation decays away within tens of microseconds even far downstream of the antenna, while the plasma population decreases as a slower rate because plasma is still flowing downstream from the source.

When comparing the magnitude of the wave magnetic field along the axis with the diamagnetic perturbation, two interesting properties are observed. The first is that the wave magnetic field strength drops to zero in the region along the axis where the diamagnetic perturbation has cancelled out the base field. This is further confirmation that the field along the axis is ~0, since the helicon wave needs a magnetic field to propagate along. The second interesting property is that the wave magnetic field is roughly equal to the total magnetic field strength in the region just upstream of the large diamagnetic perturbation. This is further evidence of the non-linear nature of the HPH plasma wave. Initially the magnitude of the wave magnetic field is >10 gauss but decreases over time as the wave reaches farther downstream. This most likely indicates that the wave energy is piled up near the source region early in time before the plasma has had time to move farther downstream and the diamagnetic decrease in the field also acts to keep it restricted close to the source. Over time the plasma expands farther and the diamagnetic perturbation is weaker but over a larger region, at the same time the wave magnetic field is measured further along the axis.

When the antenna is shut off the diamagnetic perturbation decreases in strength rapidly, even far downstream of the source. This is independent of the plasma population which decreases on a slower time-scale once the antenna is shut off, and at the time of antenna shut off is still high beta enough to suggest a large diamagnetic effect. When estimating the time needed to have the background magnetic field diffuse back through the conducting plasma along the axis, the time predicted based on the conductivity is larger than what is observed. This suggests that there is a strong damping mechanism at work that is overpowered by the antenna while it's on, but quickly damps out the diamagnetic perturbation once it is shut off.

The diamagnetic perturbation is three dimensional, with the strongest component being the axial diamagnetic perturbation. There is an additional radial perturbation that is opposed to the diverging base magnetic field, pointing inwards towards the axis when strongest. There is also an azimuthal magnetic perturbation that is not diamagnetic because the expanding dipole field from the source doesn't have an azimuthal component. This component is left-handed around the axis and is a few gauss in strength, suggesting perhaps that either some magnetic field is being twisted into a left-handed shape, possibly associated with an axial current with electrons flowing out along the axis and returning along the flanks. The diamagnetic perturbation extends not only far downstream, but also a significant distance away from the thruster axis. The 2D data of the magnetic perturbations near the axis, combined with some assumptions about symmetry, can be used to estimate the strength of the currents in the plasma that are generating the perturbations. The discussion of these currents and the broader question of the source of the diamagnetic perturbations will be discussed in Chapter 5.

Chapter 5: Estimated Diamagnetic Currents based on Diamagnetic Perturbations and Discussion of Ion Energy Enhancement

Section 5.1: Estimating Current Density from Magnetic Perturbations:

The volume of plasma downstream of the source has only been partially measured with the diagnostics available, but with some assumptions of symmetry an estimate of the currents produced can be developed. The first assumption that must be made is that the plasma plume and the magnetic perturbation are azimuthally symmetric. This allows the 2D cut from the bulk B-dot array presented in chapter 4 to provide sufficient information to determine the downstream current density. Previous measurements of the plasma density with Langmuir probes support this assumption, indicating a mostly symmetric plasma plume downstream.

From the differential form of the Maxwell-Ampère equation:

$$\nabla \times \mathbf{B} = \mu_0 \left(-\frac{\partial \mathbf{D}}{\partial t} + \mathbf{J} \right) \tag{5.1}$$

The magnetic perturbation we measure is present for longer than 100 μs, and the dominant axial component of the ΔB suggests that the curl of the magnetic field perturbation is predominantly in the azimuthal direction around the plasma axis. This makes it unlikely that there are azimuthal displacement fields building up for the bulk of the plasma shot time. So if we assume that displacement fields are small, then:

$$\nabla \times \mathbf{B} = \mu_0 \mathbf{J} \tag{5.2}$$

The spatial resolution in the magnetic field perturbation measurements is limited to 2 cm over an area that is 12 cm wide by 52 cm long, and since the curl of the magnetic perturbation depends on the partial derivatives, the estimates of the current density are further limited. In the Cartesian coordinates used in the lab measurements (where 'z' is parallel with the thruster axis and 'y' is vertically upward) [3]:

$$\nabla \times \mathbf{B} = \left(\frac{\partial B_z}{\partial y} - \frac{\partial B_y}{\partial z} \right)\hat{\mathbf{x}} + \left(\frac{\partial B_x}{\partial z} - \frac{\partial B_z}{\partial x} \right)\hat{\mathbf{y}} + \left(\frac{\partial B_y}{\partial x} - \frac{\partial B_x}{\partial y} \right)\hat{\mathbf{z}} \tag{5.3}$$

The partial derivatives with respect to y and z can be read from the B-dot array results, only the derivatives with respect to x are absent. The $\partial B_z / \partial x$ in the second term of eq. 5.3 can be assumed to be small because of the observed symmetry of the ΔB_z. Only the $\partial B_y / \partial x$ in the third term of eq. 5.3 can still complicate the assumption of azimuthal symmetry. Therefore if we are assuming azimuthal symmetry and that the vertical yz plane that the probe measured is typical of any cut across the plasma, we expect it to be accurate with the possible exception of a correction to the current density in the z direction along the axis.

Section 5.2: Estimated Azimuthal Diamagnetic Current:

The x component of the curl represents an azimuthal current around the source axis and is shown as a function of position for four separate times in Figure 5.1. The (effectively) azimuthal current is left-handed about the thruster axis, in the same direction as the azimuthal magnetic perturbation. The current peaks 2-3 cm off the source axis and is ~20 kAm^{-2} in density. The high current density is the result of the sharp radial decrease of the ΔB_z away from the source axis, suggesting a current source that is restricted to a few square centimeters near the axis.

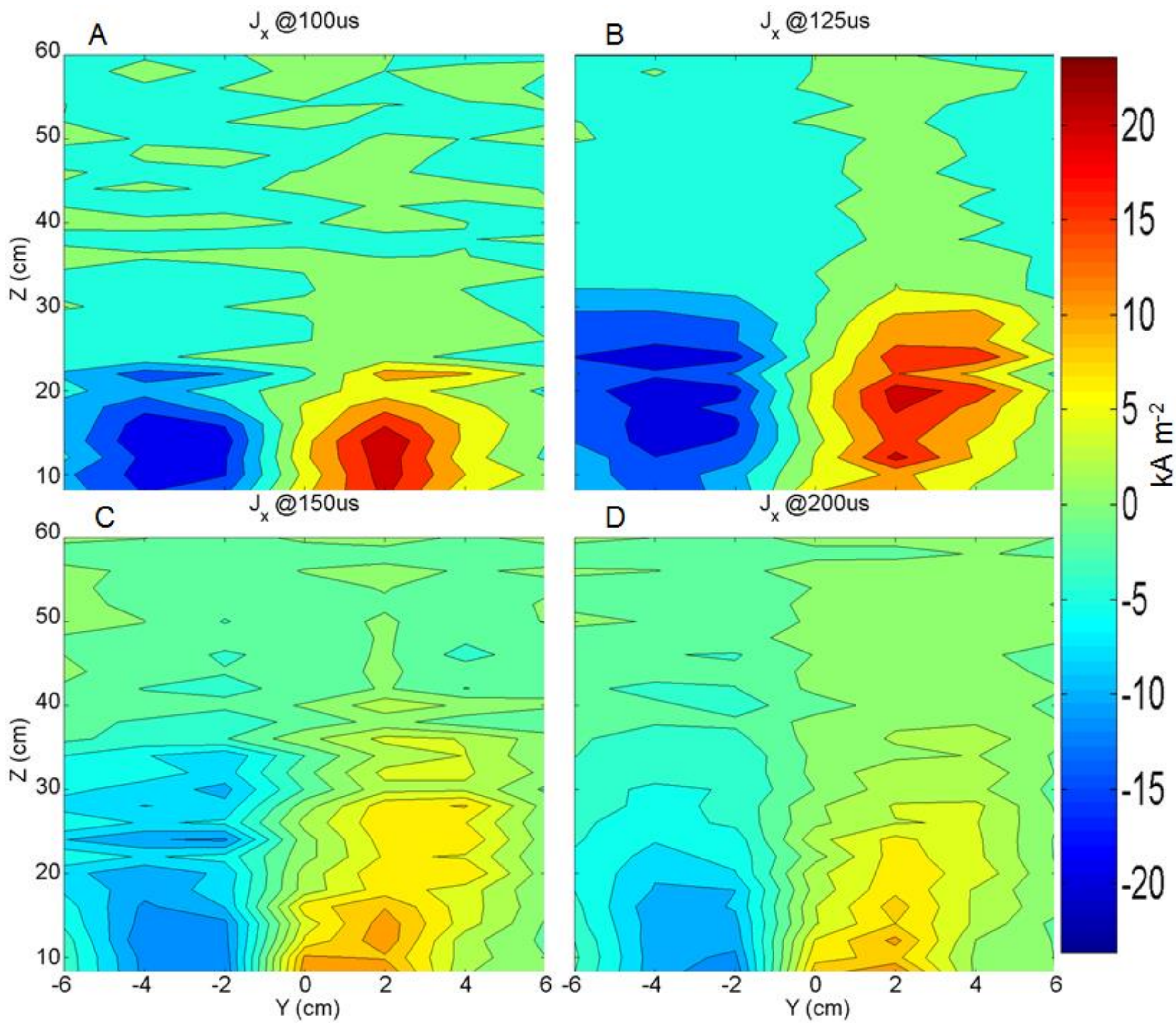

Figure 5.1: Estimated J_x current density downstream of the source at four times. The (effectively) azimuthal current is oriented left-handed about the axis, such that the field that would be induced by this current has its normal anti-parallel to the base magnetic field, resulting in the axial diamagnetic field.

Early in time in Figure 5.1a, the region with azimuthal current has extended roughly one antenna length (15 cm) downstream. The current density peak reaches ~20 kA m^{-2} at 2-3 cm from the axis and has decreased to 5 kA m^{-2} at the edge of the probe array, suggesting that the effect does not extend much farther beyond the edge of the array. At t = 125 μs in Figure 5.1b, the J_x region has expanded to 30 cm downstream and radially off the edges of the probe array, but the peak of the J_x remains within 4 cm of the axis and >15 kA m^{-2}. In Figure 5.1c the peak of the current density has decreased to ~10 kA m^{-2} and is peaked near the helicon source rather than 1-2 antenna lengths downstream. The current drive region extends downstream but has grown more diffuse. By the time of antenna turnoff in Figure 5.1d, the peak in the J_x current density is beyond the inner edge of the probe array towards the source, while the downstream region has a J_x that is 1-10 kA m^{-2} over the extent of the B-dot probe array.

The azimuthal current is consistent with the kind of diamagnetic current we would expect to find in a high beta plasma plume with a radial gradient in plasma pressure. However, late in time the azimuthal current is peaked near the source region and damps out immediately after the antenna is shutoff. This suggests that at least part of the diamagnetic current we measure is being driven by the antenna, though it could only be important for the lower current density observed after 150 μs, while the peaked azimuthal current observed before 150 μs could be predominantly a pressure driven diamagnetic current.

Section 5.3: Estimated Axial and Radial Current Density:

In addition to the J_x, which is effectively an azimuthal current around the axis, there are also J_y and J_z which are effectively radial and axial currents. While the J_x current density is azimuthal and closes with itself to form a current ring, the J_y and J_z current components connect with each other to close a larger system of currents. For this reason the sum of the two currents $J_{yz} = (J_y^2 + J_z^2)^{1/2}$ is shown for four separate times in Figure 5.2, along with arrows indicating the direction of the current (J_y, J_z) in the y-z plane. The current is found to flow inward radially from the sides downstream of the magnetic perturbation and converges on the thruster axis, where it flows upstream towards the source region and diverges again at the inner limit of where the probe array can reach. Within the first 20 cm downstream of the source, an axial current flowing away from the source is found along the flanks of the bulk B-dot array.

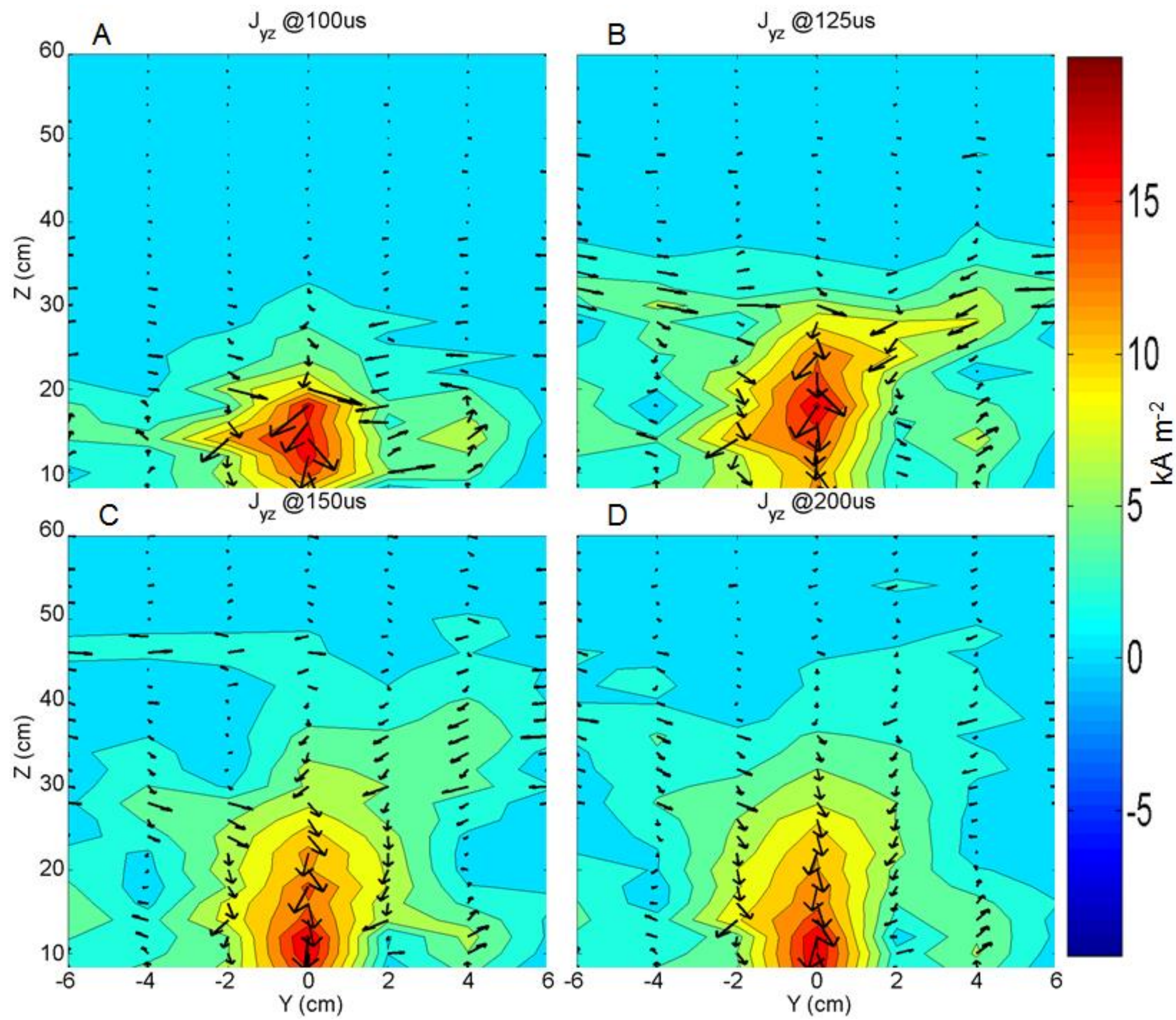

Figure 5.2: Estimated J_{yz} Current Density and direction for four separate times. Colored contours indicate sum of the two current componets, while arrows indicate the direction and relative magnitude of the current. Note the color bar scale has changed from the previous figure.

Even early in time in Figure 5.2a at t = 100 μs the J_{yz} is only partially measured by the probe array. Current flows out along the flanks, then converges on the axis downstream, and finally comes back upstream along the axis to close the path: above the axis a small loop of current can be discerned going out from the source along the edge and then converging on the axis to return. At 20-25 cm downstream current is flowing in radially from the edge, suggesting that the structure of currents has already expanded past the limit of the probe array. Later in time at 125 μs in Figure 5.2b, the J_{yz} has propagated downstream and expanded well beyond the edges of the probe. Rather than seeing the whole loop of the current like in the previous frame, in

Figure 5.2b only the strong axial current flowing upstream to the source (>15 kA m^{-2}) and the radial current flowing inwards from the edge of the probe array (1-5 kA m^{-2}) can be discerned. Additionally, only some of the current flowing downstream and radially outward at the flanks is observed. In Figure 5.2b the radial current is dominated by a thin band 30-40 cm downstream flowing inward from beyond the reach of the probe to converge onto the axis.

In Figure 5.2c at t = 150 μs the thin band of J_y has broadened to be from 30-50 cm downstream of the source. Additionally the current along the axis has grown more uniform, with smaller J_y components and a more uniform J_z. This trend continues through the time of antenna turnoff at t=200 μs in Figure 5.2d, with current entering the probe area from the sides over a large area downstream, converging onto the axis, and flowing upstream into the source region. In the lower left and right hand corners of Figure 5.2d the edge of the current region flowing outward and downstream can be seen. After the antenna is shutoff, the magnetic perturbations fade away within tens of μs and these currents vanish with them.

<u>Section 5.4: Discussion of correlation between currents and the wave field:</u>

The estimated current densities given above in Figures 5.1 and 5.2 are assumed to be the source of the magnetic perturbations discussed in Chapter 4. Determining the origin of these currents is important to the understanding of the plasma behavior downstream. The dominant current density is the azimuthal current density J_x plotted in Figure 5.1. One explanation for the origin of this current, which is responsible for the strong axial diamagnetic perturbation, is that it is a pressure drive diamagnetic current being carried by the plasma electrons. Downstream of the HPH the plasma density is peaked along the thruster axis, decreasing away from the axis towards the flanks. This gradient in density creates a gradient in the plasma pressure radially towards the axis, resulting in a diamagnetic current that is azimuthal and acts to weaken the magnetic field along the axis. Additionally, as the plasma moves downstream near the axis the magnetic field begins to diverge. Since the ions are not well magnetized but the electrons are, there needs to be a mechanism to keep the electrons from diverging with the magnetic field. One such mechanism mentioned earlier in Chapter 4 is that as the dynamic pressure of the plasma (carried by the ions) acts to force the electrons across the magnetic field, there is a Lorentz force that drives the electrons in an azimuthal current to weaken the magnetic field to allow the electrons to move through. With sufficient plasma pressure (either thermal pressure or dynamic pressure), these diamagnetic currents create a diamagnetic cavity where the ions and electrons can flow downstream unhindered.

An alternative explanation for the origin of the azimuthal current is that it's being directly driven by the helicon wave propagating through the plasma. Comparing the magnitude of the wave magnetic field along the axis in Figure 4.5 with the axial position of the azimuthal current density in Figure 5.1, there is correlation between where the wave magnetic field falls off in strength and the edge of the current drive region. Early in time at t=100 μs the wave magnetic field does not extend past 20 cm, and neither does the azimuthal current ring. Later in time at t=125 μs both have extended to ~30 cm downstream of the source. Later in time both have extended further down the axis, falling off in magnitude the further from the source.

This wave magnetic field is perpendicular to the base magnetic field and rotates in a right-handed fashion in time around the base magnetic field. This wave magnetic field is >10 gauss in magnitude near the source early in time and is >5 gauss as far as 20 cm downstream at the time of peak current density in Figure 5.1. This wave magnetic field is strong enough to magnetize the electrons (electron gyro-radius is <2 cm), so that as the magnetic field rotates in time around the base magnetic field the electrons will be dragged along with the magnetic field. Moving the electrons in a right-handed fashion around the magnetic field without affecting the ions results in an azimuthal current in the direction measured in Figure 5.1. However, even if the wave magnetic field could be driving the electrons around at the wave frequency, collisions between the electrons and other plasma particles can interrupt this azimuthal motion. The electron-ion collision frequency is ~900 kHz and the electron-electron collision frequency is ~1.5 MHz, which are 1.5-3 times higher than the wave frequency of ~600 kHz. This would mean that a current being driven by the wave carrying electrons would be strongly damped by collisions.

To make a simple estimate, consider the case at t=125 μs plotted in Figure 5.1b: the current density is peaked 2-4 cm off the axis ~20 cm downstream, and the wave magnetic field shown in Figure 4.5 at the same time indicates that the wave field is strong enough to magnetize the electrons at this position, but not the ions. Considering a current flowing 3 cm off axis, carried by the plasma electrons rotating at 600 kHz. The electron density is ~$3x10^{18}$ m^{-3} at this position, so if all the electrons were rotating with the wave at the angular speed, this would give a current density of 54 kA/m^2. Since the collision rate is roughly 3 times higher than the angular rotation rate, we can estimate that perhaps only 1/3rd of the electrons can make it around on average without colliding with something. Reducing the electron density carrying the current to $1x10^{18}$ m^{-3} yields an estimated current density of 18 kA/m^2, which is roughly equal to the peak current density at that position plotted in Figure 5.1b.

If the plasma wave is directly driving electrons in an azimuthal current at the angular velocity of the wave rotating, then increasing or decreasing the frequency at which the wave rotates should have a measurable effect on the plasma currents. Unfortunately, adjusting the frequency at which the helicon wave is driven has other consequences on the ionization and acceleration of the plasma, since it is also responsible for the generation of the plasma in the source. The issues and results involving the changing of the antenna frequency to alter the angular velocity of the wave will be discussed later in Chapter 7.

Section 5.5: Discussion of the meaning of axial and radial current:

In addition to the diamagnetic perturbations to the field (B_z, B_y) discussed in Chapter 4, there was an additional perturbation to the field in the azimuthal direction B_x plotted in Figure 4.9. This perturbation was not diamagnetic because there was no azimuthal component to the base magnetic field. This perturbation was directed in a left-handed fashion around the axis in the same direction as the azimuthal current plotted in Figure 5.1. To sustain this azimuthal magnetic field requires a current to flow both axially and radially around this region, with the current responsible for this perturbation plotted in Figure 5.2.

If the current density in Figure 5.2 is carried by the plasma electrons, this suggests a population of electrons moving out away from the source along the axis towards the downstream edge of the plasma. These electrons then move out across the plasma towards the flanks at the limit where the probe can detect them. The electrons then travel back along the flanks of the dipole magnetic field back towards the source region to complete the loop. It was already shown in section 5.3 that the current appears to be conserved. The peak current density along the axis in Figure 5.2 is ~15 kA/m^2, and staying within 10-20 cm downstream of the source. If this current is being carried by the plasma electrons along the axis with an electron density n_e~$3x10^{18}$ m^{-3}, then this suggests the electrons moving downstream along the axis at ~31 km/s. This velocity is much less than the thermal speed of the electrons at T_e ~ 10 eV, which is ~1,800 km/s. This means that only a small drift of the electrons compared to their thermal motion is needed to generate this current.

The following sections discuss the velocity of the plasma ions downstream and if the increased diamagnetic currents result in increased acceleration of the ions.

Section 5.6: Ion velocities measured on Axis:

In Chapters 1 and 2 it was described how the wave driven by the high power helicon is at a frequency well above the ion cyclotron frequency and well below that of the electron cyclotron frequency. This allows the helicon antenna to directly affect the electrons while the ions are relatively motionless. To maintain quasi-neutrality, as the electrons are accelerated downstream of the HPH an ambipolar electric field develops that accelerates the ions to move downstream at the expense of the electron energy. These ions are not well magnetized, and once accelerated downstream they move across the magnetic field with little to no deflection while the electrons need several mechanisms to move across the magnetic field to keep up with them (as described in Chapter 4). Measuring the velocity of these heavy, directed ions is a useful diagnostic to study the plasma characteristics downstream of the HPH source.

Two experimental methods were used to measure the downstream velocity of the plasma. The first was using pairs of langmuir probes to make time-of-flight estimates of the velocity of the plasma. By comparing the difference in time between the peak plasma densities measured at two different probes downstream, an estimate of the bulk velocity of the plasma could be obtained. Previous work on HPH by Prager [2] used this method to estimate the bulk flow velocity at 8-9 km/s. More recent time of flight estimates taken as part of this research also indicated a bulk speed of 8-11 km/s at similar input power levels. This was based on measurements of the plasma density at 3 downstream locations with floating double-langmuir probes as described in chapter 3. This langmuir data is shown below in Figure 5.3.

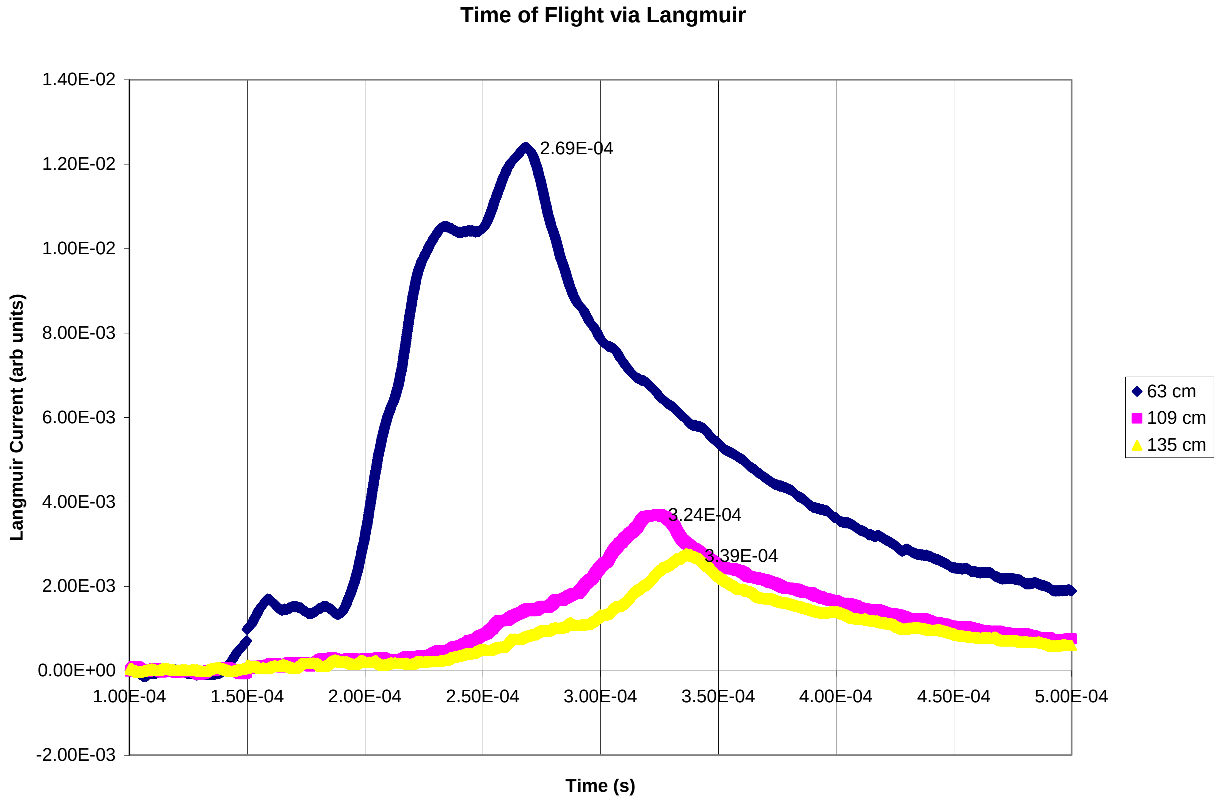

Figure 5.3: Plasma density as a function of time on axis for three locations downstream of HPH. The difference in time between the peaks is used to estimate the bulk speed of the plasma.

The time of flight method for estimating the ion velocity is most applicable when the ion population is moving together at close the same speed and does not speed up or slow down between the langmuir probes. This makes it less useful for measuring the ion speeds downstream of HPH because it has been shown in previous work by Ziemba [9] and Prager [2] that the ion population is increasing in speed downstream of the source and so it is likely that the velocity would not have been constant between the two probes. Since the langmuir probe data is taken with the probe in saturation, it is measuring ions with a range of energies and displaying the total current received, even though the ions that contributed to the peak signal in the first curve of Figure 5.3 are not necessarily the same ions which generated the peak signal in the third curve of Figure 5.3.

The second experimental method of measuring the downstream plasma velocity addresses this problem by measuring the kinetic energy of the plasma particles using a retarding field energy analyzer (RFA) as described in Chapter 3. The RFA measures the ion energies along the axis of the detector, which is typically aligned with the thruster axis to measure the directed energy of the ions downstream of the source along the axis. As the potential on the retarding grid is raised, fewer ions in the plasma have enough energy to get through the device to the collected plate at the rear of the detector. By taking the derivative of the ion current to the collector as a function of retarding potential voltage, we can measure the ion energy distribution function parallel to the axis (and the magnetic field). If we also assume that the ions striking the plate are all singly ionized argon, the directed energy along the axis of the ions can be converted to a measure of ion velocity into the detector using equation 5.4:

$$v_{ion} = \sqrt{\frac{2E_{RFA}}{m_i}} \qquad (5.4)$$

where v_{ion} is the estimated ion directed velocity, E_{RFA} is the energy of the ion as measured by the RFA in electron-volts, and m_i is the mass of the argon ions.

One possible complication with making this measurement is if the ions are accelerated relative to the detector so that the measured velocity given by the RFA is not the same as the flow velocity of the ions. This could be caused by the plasma forming a sheath around the probe (as described in chapter 3) that acts to accelerate ions towards the grounded chassis of the RFA. This would increase the measured energies of the ions by an amount roughly equal to plasma potential between the flowing plasma and ground. It would also have the effect of accelerating ions into the detector along the sides of the RFA, and if the potential difference is larger than the directed energy of some of the ions, even backwards into the rear of the RFA. This population of ions has been observed in measurements by Charles et al [23] in their system and was used as an estimate of the plasma potential. This effect is not observed in the plume downstream of HPH, as observed by Prager et al [10]. This was determined by rotating the RFA input orifice relative to the thruster axis and measuring the decrease of ions entering the source as the angle between them increased. Once the RFA detector orifice was perpendicular to the output of the HPH thruster, the measured ion current dropped to zero, which should not have occurred if there was a population of ions being accelerated into the RFA by a plasma sheath. Measurements of the ion speed by the time of flight method mentioned earlier also roughly matched the velocities measured by the ion energy distribution, making it unlikely that the measured ion energies were significantly altered from what they were in the plasma plume.

For the two magnetic field configurations discussed in chapter 4, one with the wave propagating parallel and the other anti-parallel, there is a significant difference in the ion velocity distribution function (IVDF) when the wave propagation is parallel and the large diamagnetic perturbation is observed. In Figure 5.4, the two cases are compared for six different times and the IVDF is presented as measured 60 cm downstream of the source along the thruster axis:

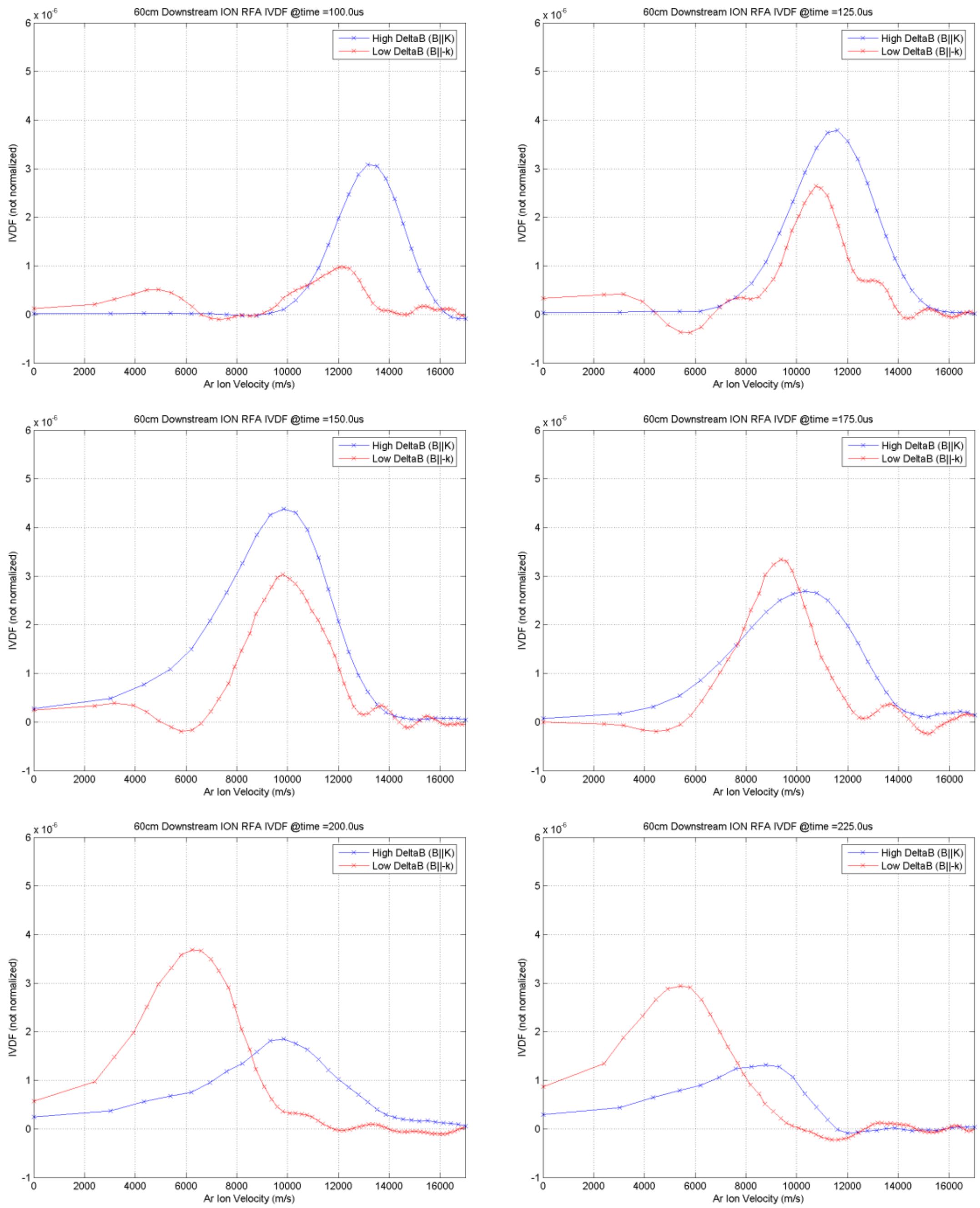

Figure 5.4: Ion velocities on axis 60 cm downstream of the HPH with two different magnetic field configurations previously mentioned in chapter 4. The configuration with magnetic field parallel to the wave vector k is associated with large diamagnetic perturbations and is correlated with a significant increase in the population of fast ions. The red trace was measuring a smaller population of ions and there is a larger margin of error in the shape of this distribution.

In the first panel of Figure 5.4, which represents the early in time population from the source to arrive 60 cm downstream, there are significantly more of the fast ions present in the parallel propagation case than the anti-parallel case. Additionally, the ions of the parallel propagation case are ~2 km/s faster than the anti-parallel case. Over the next 50 μs in the subsequent two panels of Figure 5.4 the IVDF of both cases shifts to lower velocities while the magnitude increases, possibly a result of slower ions arriving later or changes in how the ions are being accelerated both in the source region and downstream. In both panels the IVDF of the parallel case has an increased number of ions over the energy range compared to the anti-parallel case, as well a slightly faster population of ions present in the parallel case but not the other. In the final three panels of Figure 5.4 the number of ions measured in the parallel case decreases but maintains a relatively high velocity, while the anti-parallel case has a slower decrease in ion number but a decrease in velocity of ~2-3 km/s. This set of data suggests that there is a mechanism that is accelerating ions in the parallel case that is weakened or absent in the anti-parallel case.

Section 5.7: Discussion of when the ions begin moving super-sonic and super-Alfvenic:

The measurements of ion velocity through time of flight estimates and the RFA in the previous section were both made further than 60 cm downstream of the source region. Previous measurements by Prager et Al [10] with the RFA indicated that at 20 cm downstream of the source the peak of the ion population had a velocity of ~6.5 km/s early in time which increased to ~8.5 km/s by the time the source antenna was shut off. When the same detector was moved to 50 cm downstream, it measured the velocity of the peak of the ion population to be ~10.9 km/s early in time and ~10.2 km/s when the antenna was shut off. This suggests that more than 50% of the acceleration of the ions is occurring within the first 20 cm of the source region, but that there is still a mechanism accelerating the ions between 20 cm and 50 cm downstream by as much as 1-4 km/s at different times [10].

As the ion velocity increases beyond the sound speed of the plasma or the alfven speed, the behavior of the downstream plasma can change. The sound speed of the plasma is given by [3]:

$$v_s = \sqrt{\frac{kT_e + \gamma_i kT_i}{m_i}} \tag{5.5}$$

where T_e and T_i are the electron and ion temperatures respectively, γ_i for the ions is ~5/3, and m_i is the mass of the ions. This is the speed at which ion acoustic waves can travel through the plasma. For electron temperatures of ~10 eV and assuming T_i~0 (cold ions), this gives a sound speed of ~4.9 km/s for the downstream plasma. For an ion temperature of 1-2 eV, the sounds speed increases to 5-6 km/s, and for 10 eV ions the sound speed is ~8 km/s. In the case of HPH, the ion temperature was measured to be at most 1-2 eV in the previous work by Prager [2], so the ions are expected to be colder than the electrons and the sound speed to be 5-6 km/s. Based on the velocity measurements from the time of flight probes, the plasma bulk speed is comparable or higher than the sound speed of the plasma. The RFA measurements also indicate that the plasma is flowing faster than the sound speed with 20 cm of the source exit [10]. Comparing the directed ion speed to the sound speed of the plasma gives the Mach number of the plasma, but it is more convenient in equation 5.6 to consider the square of the Mach number:

$$M_s^{\;2} = \frac{v_i^{\;2}}{v_s^{\;2}} = \frac{m_i v_i^{\;2}}{kT_e + \gamma_i kT_i} = \frac{2E_i}{kT_e + \gamma_i kT_i} \tag{5.6}$$

where M_s is the Mach number and E_i is the directed energy of the ions as measured by the RFA. It's convenient to use the square of the Mach number because as the directed energy of the ions becomes greater than half the thermal energy of the plasma particles, it is clear that the Mach number will be greater than 1 and the flow will transition to super-sonic. The directed energy of the ions is the plasma property measured by the RFA.

The Alfven speed of the plasma is given by [3]:

$$v_A = \frac{B}{\sqrt{\mu_0 n_i m_i}} \tag{5.7}$$

where B is the magnetic field strength, and n_i and m_i are the density and mass of the ion population. Typically the B used in this calculation for laboratory plasmas is the strength of the background magnetic field without adding the modifications to the magnetic field by the plasma particles. In the case of HPH where there is a significant diamagnetic decrease in the field, this would result in a local decrease in the Alfven speed, so the Alfven speed being considered here (using the unmodified B_0) will be an upper limit to the speed. The Alfven speed will also be changing as a function of time as the plasma flows downstream and the ion density varies. Comparing the directed ion speed to the Alfven speed yields the Alfven Mach number of the plasma, but again it is more convenient in equation 5.8 to consider the square of the Alfven Mach number:

$$M_a^{\ 2} = \left(\frac{v_i}{v_a} \right)^2 = \frac{n_i m_i v_{\mathrm{i}}^{\ 2}}{\left(B^2 / \mu_0 \right)} = \frac{\tfrac{1}{2} n_i m_i v_{\mathrm{i}}^{\ 2}}{\left(B^2 / 2\mu_0 \right)} \tag{5.8}$$

where M_a is the Alfven Mach number. It is convenient to use the square of the Alfven Mach number because then equation 5.8 indicates that as the directed energy density of the ions begins to exceed the magnetic energy density of the background field, the plasma is expected to transition to a super-Alfvenic regime. This ratio of particle energy density to magnetic energy density is similar to the measure of plasma Beta which considers the ratio between thermal energy density of the plasma electrons and magnetic energy density, or alternatively the electron pressure compared to the magnetic pressure. Equation 5.8 considers a dynamic pressure of the ions flowing downstream compared to the magnetic pressure, and can also be referred to as the dynamic plasma beta [7].

The background plasma population varies with time and position downstream of HPH, and the following three figures illustrate the change in Alfven speed and the balance between electron energy and magnetic energy (plasma beta) along the source axis. These plots correspond to the case from Figure 5.4 when the wave vector was parallel with the magnetic field and there was a strong diamagnetic signal with a faster ion population. Figure 5.5 plots the energy density of the electrons, energy density of the magnetic field, and the calculated Alfven speed of the plasma along the axis for time early into the shot before the bulk of the plasma has moved far downstream. At this time the energy in the electrons downstream has risen to the point where they have comparable energy to the background field from about 20 cm downstream of the source and beyond. The Alfven speed is 10-12 km/s immediately downstream of the source, but as the field decreases in strength it becomes ~5 km/s. This early in time when there no significant plasma far downstream of the source the Alfven speed does not continue to decrease with distance from the source as the plasma density is low, but this is not the case for the rest of the shot.

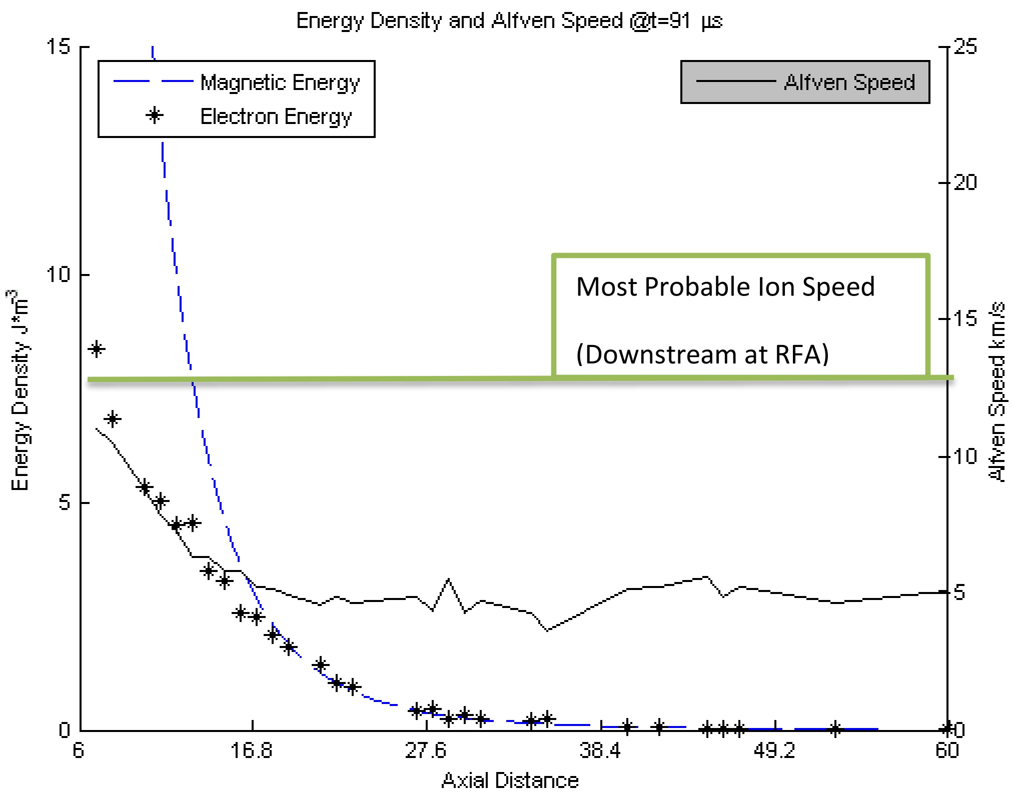

Figure 5.5: Comparison of the energy density of the electrons and the magnetic field downstream of the source along the axis at 91 μs, along with the estimated Alfven Speed. The energy densities are plotted along the left axis in units of Joules per cubic meter, while the Alfven speed is plotted along the right axis in km/s.

The ion velocity measured at 60 cm downstream of the source in Figure 5.4 indicated the ion peak flowing with a velocity of 12-14 km/s at approximately this time, so that far downstream the plasma flow is super-Alfvenic and super-sonic. If the bulk of the ion acceleration or all of it is occurring in or close to the source region early in time, then the fast ions measured downstream could be super-Alfvenic within 10 cm of the source region.

Looking later in time in Figure 5.6, the ion density downstream of HPH has risen enough to decrease the Alfven speed far downstream, while a decrease in plasma near the source exit has caused the Alfven speed to rise within the first 10 cm of the source region:

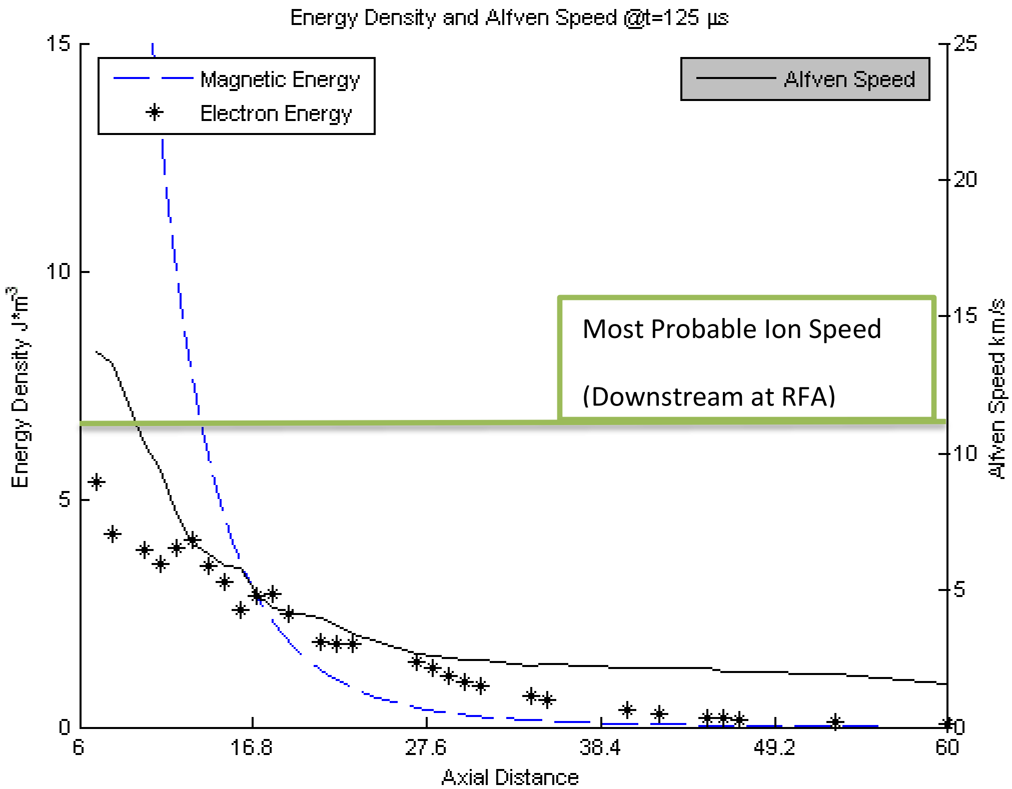

Figure 5.6: Comparison of the energy density of the electrons and the magnetic field downstream of the source along the axis at 125 µs, along with the estimated Alfven Speed. The energy densities are plotted along the left axis in units of Joules per cubic meter, while the Alfven speed is plotted along the right axis in km/s.

By this point in time the energy density of the electrons has begun to exceed that of the magnetic field beginning at ~17 cm downstream and becoming most dramatic at ~25 cm downstream of the source region. Plasma beta in this region is >1, and downstream it can be several times higher than 1.

Figure 5.7 plots the energy densities and Alfven speed near the time of antenna shut off at 200 µs. By this time the plasma density has decreased further near the source so that the electron energy does not match the magnetic field energy density until ~ 25 cm downstream, where Beta ~1. The velocities of the ions in Figure 5.4 have also decreased somewhat at this time, with the ion peak moving at ~10 km/s. This drop in velocity along with the increase in Alfven speed near the source suggests the plasma may not be super-Alfvenic until ~25 cm downstream, rather than closer to the source as was the case earlier in time.

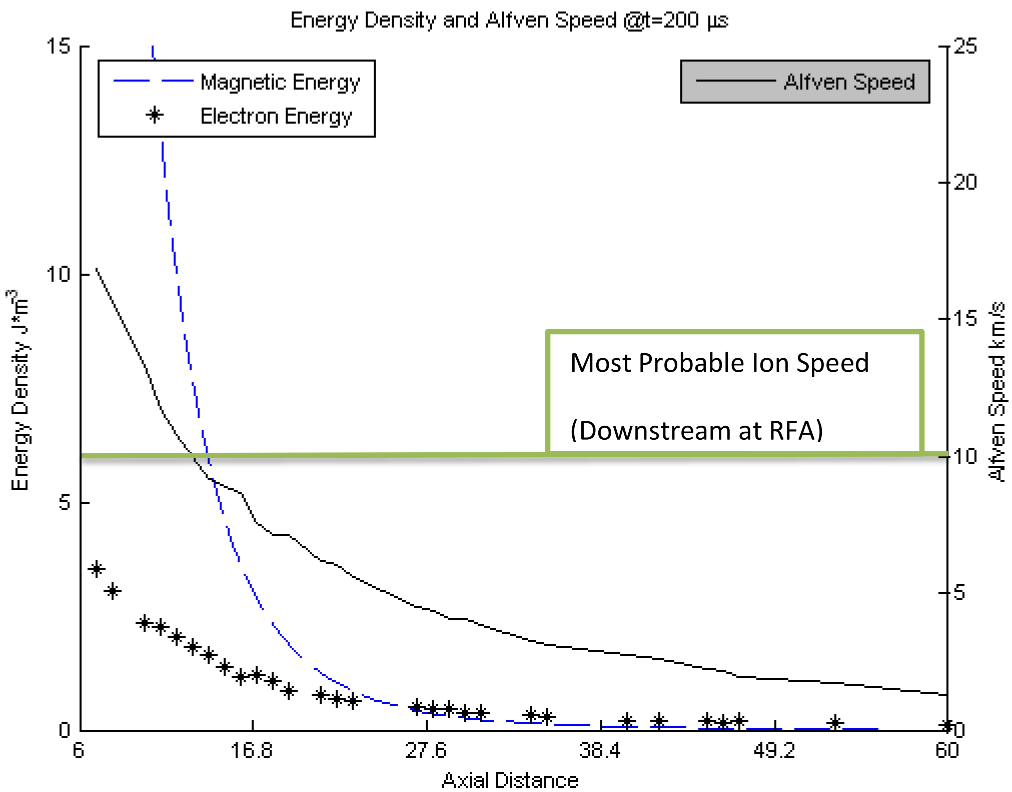

Figure 5.7: Comparison of the energy density of the electrons and the magnetic field downstream of the source along the axis at 200 µs, along with the estimated Alfven Speed. The energy densities are plotted along the left axis in units of Joules per cubic meter, while the Alfven speed is plotted along the right axis in km/s.

Based on these three figures and the velocity estimates from Figures 5.3 and 5.4, we can conclude that the plasma transitions from sub-Alfvenic to super-Alfvenic flow roughly 15-30 cm downstream of the source region. Early in time the transition happens closer to the source at ≤15 cm, but by the time the antenna is turned off it may not be occurring until >25 cm downstream. The two early values roughly match with the induced azimuthal current region shown in Figure 5.1. In Figure 5.1a the current density peaks close to the source, roughly 8-12 cm downstream. But 25 µs later the current has decreased in the region within 10 cm of the source, and the peak has moved downstream to ~20 cm. This could be correlated in time and position with the rise of the Alfven speed near the source region. The region where the transition to super-Alfvenic flow is estimated to occur also correlates in position and time with the region along the axis where plasma beta ≥ 1 near the source region.

This discussion of the Alfven speed has been limited to the data set in Figure 5.4 where the wave number 'k' is parallel with B_0. In the other case, where 'k' is anti-parallel to B_0, the ions are significantly slower later in time. In the anti-parallel case the diamagnetic perturbation to the field is significantly smaller, and measured induced currents are also smaller. This correlation between the increase in ion velocity and the presence of large diamagnetic currents, together in the region where the plasma is thought to be transitioning into super-sonic and super-Alfvenic flow, suggests that it could be responsible for the acceleration of the plasma downstream of the source.

Section 5.8: Estimated Acceleration by JxB Forces:

When there are currents flowing in a plasma perpendicular to the magnetic field, there is a Lorentz force on the plasma particles carrying the current given by:

$$F = JxB \tag{5.9}$$

where F is the force density in N/m^3, J is the current density in A/m^2, and B is the magnetic field in tesla. This force acts both on the ions and electrons in the plasma even if the bulk of the current is being carried by the electron motion, so the energization of the plasma is usually determined by the force on the much heavier ions.

A different plasma thruster concept known as "Faraday Acceleration with Radio-Frequency Assisted Discharge" or FARAD proposed by Choueiri et Al [26] uses a helicon plasma source to generate plasma downstream that is then accelerated by a large azimuthal current induced by a separate coil for a pulse roughly 1-2 μs long. The azimuthal current is across a radial magnetic field of several hundred gauss and results in an axial acceleration of the plasma (in the form of a moving plasma sheet). In their initial results, the inductive coil downstream was pulsed with 20 kA of current, which induced a current density in the plasma roughly 1 MA/m^2 and was combined with an induced radial magnetic field of ~600 gauss (.06 T). This force acted on argon plasma that had a density of $\sim 10^{20}$ m^{-3} for roughly 1μs, leading to an estimated acceleration of ~1 km/s. Choueiri et Al [26] suggest that perhaps not all of the plasma is picked up and accelerated by the current sheet, leading to a less dense volume of plasma accelerated to a higher velocity.

Downstream of the HPH there is also an azimuthal current being driven, which was plotted as a function of position near the source axis in Figure 5.1. The current downstream of HPH peaks at 20 kA/m^2, which is two orders of magnitude lower than that driven by the FARAD inductive coil, but the current is driven for a significantly longer time of more than 100 μs. Another key difference is that the inductive coil of FARAD induces a strong radial magnetic field of ~600 gauss, with the axial magnetic field approximately zero. The magnetic field immediately downstream of HPH near the axis is mostly an axial magnetic field on the order of 100 gauss, with a much smaller radial component. This means the JxB acceleration downstream of HPH not only has an axial component, but also a radial component as well. The radial component of the JxB force is the y component, and is plotted for four times downstream of the source in Figure 5.8.

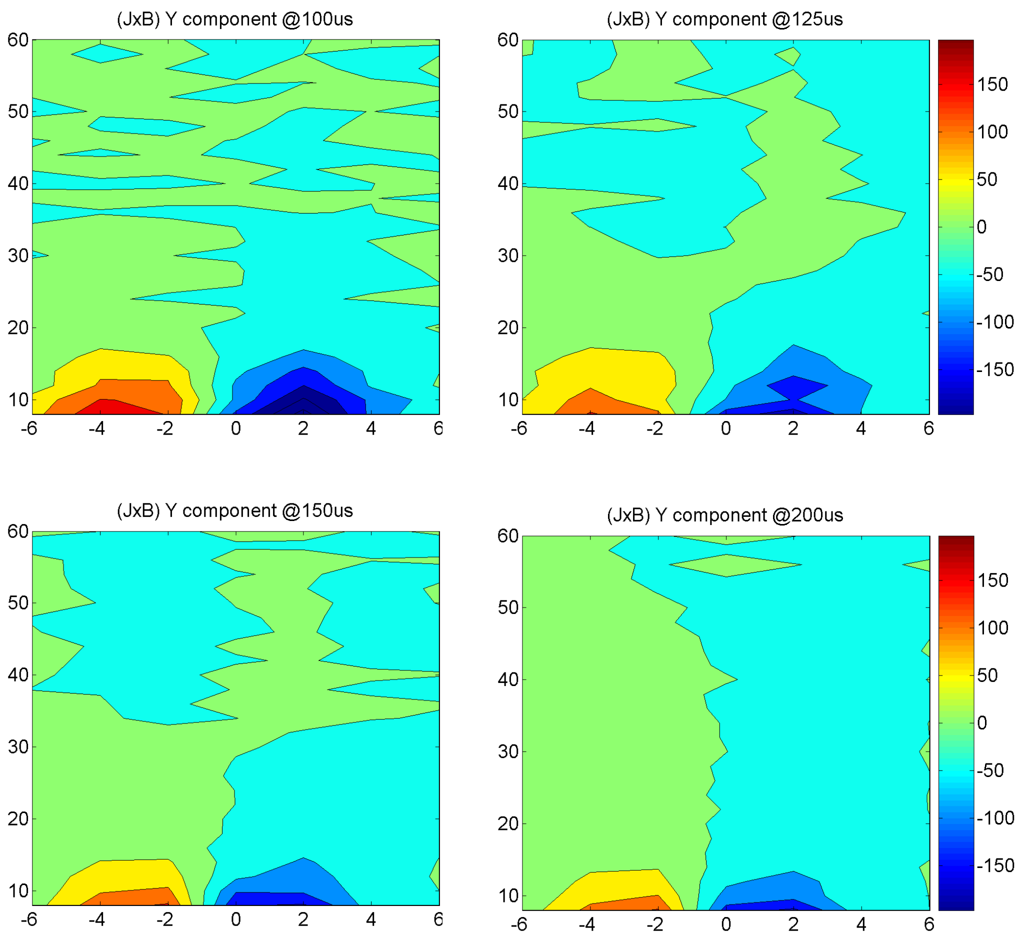

Figure 5.8: Y component of the JxB force in units of N/m^3 at four times downstream of HPH. The direction of the force changed sign across the axis, indicating that this force is directed towards the axis both above and below the thruster.

This component of the JxB force is the result of the azimuthal current J_x and the axial magnetic field B_z, and it switches sign moving across the axis, indicating that both above and below the thruster axis the force is directed towards the axis. The force reaches a maximum of ~200 N/m^3 at the radial location where the current density is highest, but peaks axially where the B_z component of the magnetic field is strongest and rapidly decreases as the field weakens downstream of the thruster. The peak of the force is more determined by the strength of the magnetic field in this case than the current density, meaning that the point where the current density peaks has the magnetic field too weak to significantly contribute. If the plasma is traveling near the source region downstream at 5-10 km/s, then plasma particles will only be in the region of the strong JxB force in Figure 5.8 for a few microseconds. If the plasma density is roughly 3x10^{18} m^{-3}, then the mass density near the source of the plasma is ~2x10^{-7} kg/m^3. So if the plasma is acted on by a 200 N/m^3 force for ~4 μs at a mass density of 2x10^{-7} kg/m^3, then the estimated acceleration towards the axis is roughly 4 km/s. This acceleration towards the axis near the source region should have a significant effect on the plasma ions, forcing them onto the thruster axis.

The axial component of the JxB force is the result of the strong azimuthal current J_x interacting with the relatively weak radial magnetic field B_y near the thruster axis. This Z component of the JxB force is plotted for four times in Figure 5.9.

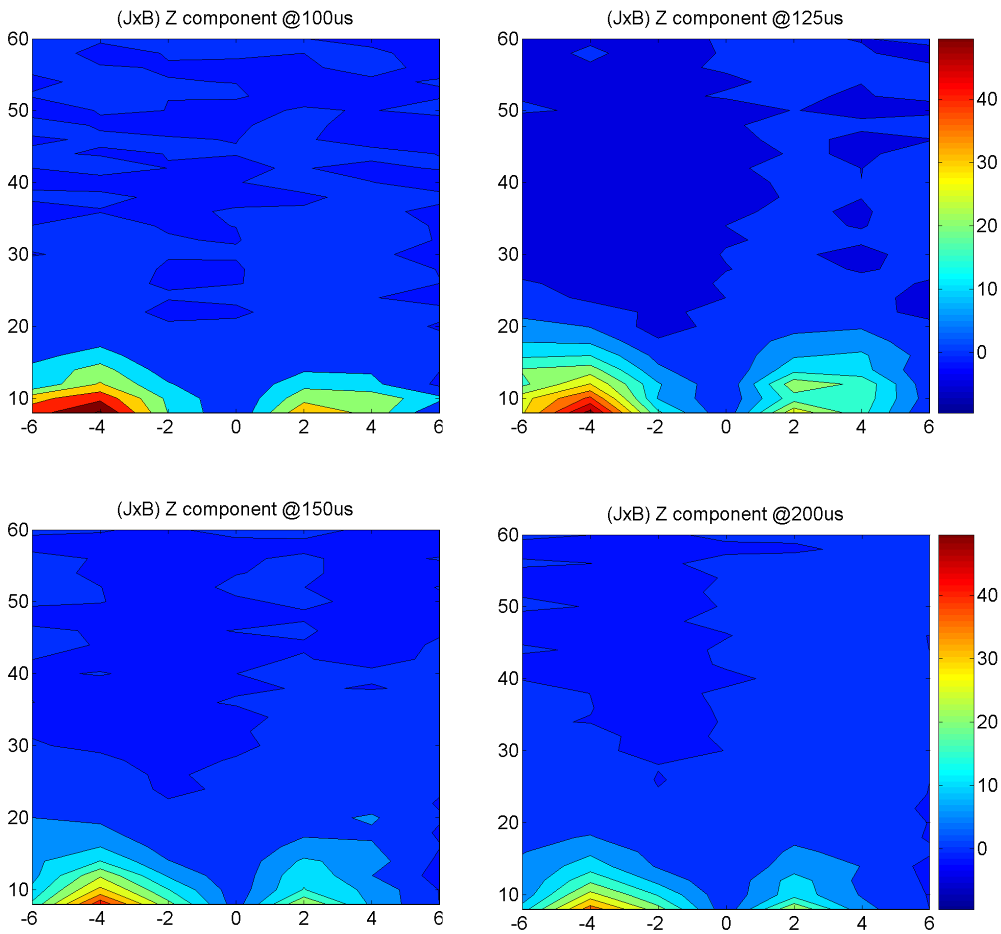

Figure 5.9: Z component of the JxB force in units of N/m^3 at four times downstream of HPH. The force is directed downstream away from HPH. Note the change in color bar scale from previous figure.

The JxB force directed axially downstream of HPH plotted in Figure 5.9 is significantly weaker than the force directed towards the axis in the previous figure. The peak force is roughly 50 N/m^3, down by about a factor of 4 from the peak radial force. By making a similar estimate to before using this weaker force, the axial acceleration downstream of the plasma can be estimated to be ~1 km/s. This is low compared to the previously changes in velocity of ions near the source versus far downstream. Additionally, this JxB force is only significant within the first 20 cm of the axis, rather than for tens of centimeters downstream of the source. Note again how the peak JxB force is closer to where the magnetic field peaks (away from the axis for B_y) rather than where the current density peaks. To compare where the azimuthal current peaks relative to the radial component of the magnetic field, the two components are plotted side by side for two separate times in Figure 5.10.

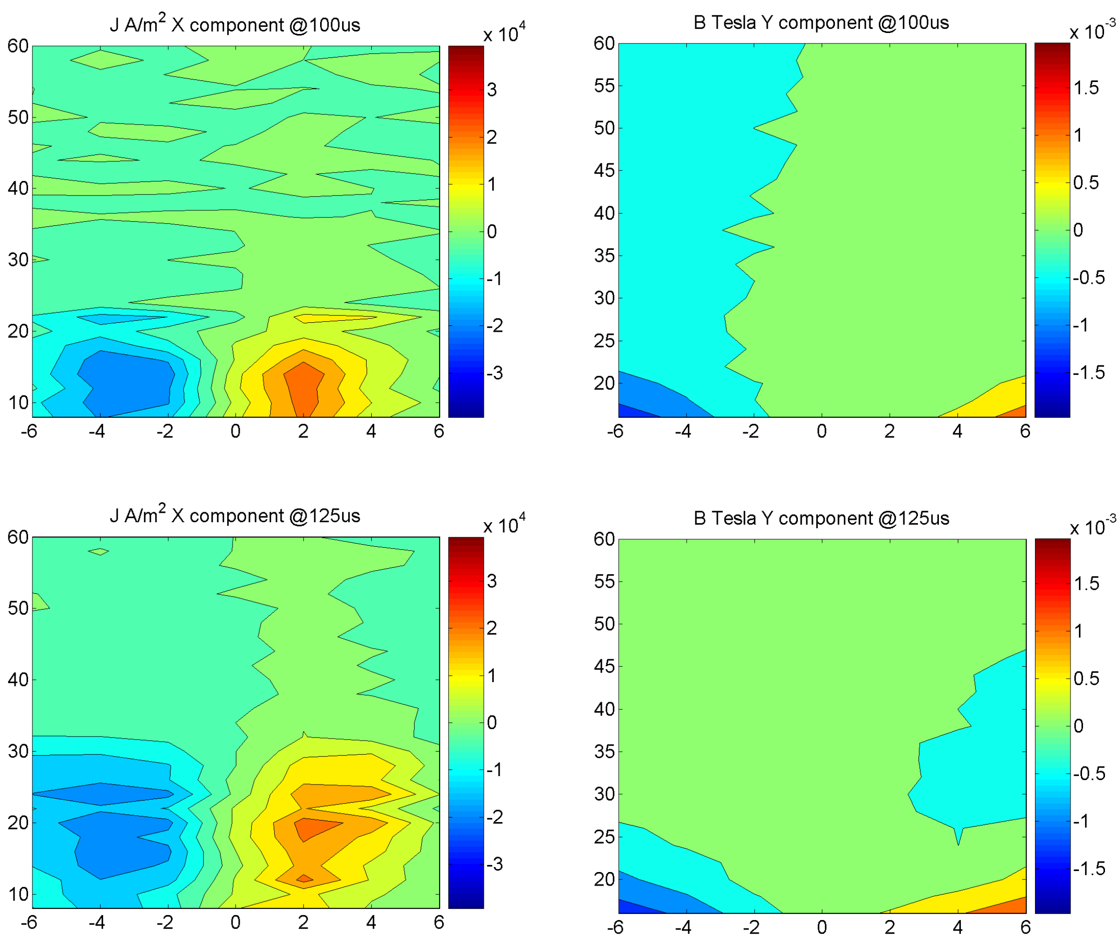

Figure 5.10: Comparison of the dominant component of the current density J_x in units of A/m^2 and the B_y component of the downstream magnetic field in units of tesla as a function of position at two times. These two components together gave the axial (z) component of the JxB force.

The current density plotted in the left two frames of Figure 5.10 peaks within a few centimeters of the axis and extends 20-30 cm downstream of the source region early in time, while the radial component of the magnetic field is low near the axis and only begins to become significant more than 5 cm from the axis even close to the source region. The JxB force plotted above in Figure 5.9 is the result of the weaker regions of the current density interacting with the weaker regions of radial magnetic field since there's no real overlap between the two peaks. Part of the reason for this is that the diamagnetic perturbation described in chapter 4 weakens the radial component of the magnetic field near the axis.

If the JxB force is the acceleration mechanism responsible for the downstream acceleration of the plasma, it's possible that the weaker force is not accelerating the bulk of the plasma and instead only a fraction of it as proposed for the FARAD experiment [26]. It's also possible that some of the radial acceleration near the source forces enough plasma onto the axis that the increase in plasma pressure ends up accelerating the plasma along the axis further downstream since there's nothing to contain the plasma on the other end. The JxB results presented here suggest that it was a lack of magnetic field density overlapping the region where the current density was highest that was preventing the JxB force from becoming more significant. Chapter 6 presents results from modifying the downstream magnetic field with magnetic nozzles and the effect this has on the downstream ion velocities.

Chapter 6: Effect of Magnetic Nozzles Downstream of HPH

Section 6.1: Increasing the Magnetic Field Downstream of the Source

The base magnetic field generated by the coils around the source region decreases like a dipole downstream of the source, falling to a few gauss within 50 cm and becoming dominated by the Earth's magnetic field within 150 cm. Increasing the magnetic field downstream of the source region by placing additional magnet coils downstream of the source region along the thruster axis is expected to have several effects on the plasma flow. The primary effect is to act on the plasma like a magnetic nozzle, focusing the plasma outflow and increasing the electron density near the axis. This will slow the thermal expansion of the plasma due to the electron temperature and extend the region where the plasma is near the axis and continues to be accelerated by the interaction with the source region. Additional effects will include changing the Alfven speed and the position downstream where the plasma detaches from the magnetic field.

Lastly, the increased magnetic field will increase the electron gyro-frequency relative to the electron collision rate, resulting in more strongly magnetized electrons. The ambipolar electric fields that develop between the electrons and the colder ions may change how the ions are accelerated downstream of the source region and affect the measured ion velocities. It is also expected that the increased magnetic field downstream of the source may affect the generation of JxB forces that were discussed in Chapter 5. While the electrons are expected to be magnetized downstream of the source with the increased magnetic field, the same is not necessarily true of the ions.

In Chapter 4 it was described how downstream of the source (without additional magnet coils) the ions were not expected to be well magnetized. In order for the ions to be well magnetized downstream of the source, several conditions needed to be satisfied: the ions would need to be able to gyrate several times within the plasma without hitting the walls or leaving the plasm, the ion gyro-radius needed to be less than or equal to the scale length of the magnetic field in order for the field to be relatively uniform over the course of a gyro-orbit, and the collision frequency for the ions needed to be lower than the ion gyro-frequency. The difficulty that arises is that in the regions where the magnetic field is strong enough to satisfy the first condition, the plasma density is typically high enough for the second condition to be violated. To compare the magnitudes involved, the first condition depends on the ion gyro-radius given by [17]:

$$r_{ci} = 1.02 \times 10^2 \sqrt{\frac{m_i}{m_p}} \frac{1}{Z} \frac{\sqrt{T_i}}{B} \sim 645 \frac{\sqrt{T_i}}{B} \qquad 6.1$$

where r_{ci} is given in centimeters, T_i is the ion temperature in eV and B is the magnetic field magnitude in gauss. If the magnetic field downstream is only a few gauss, then for even reasonably cold ions of ~1 eV the gyro-radius of the ions will be on the scale of meters, which is on the same order as the chamber diameter. This would suggest that even for cold ions, weak magnetic fields would not result in magnetized ions because they would collide with the chamber wall before completing a gyro-orbit. If the magnetic field is raised downstream to be on the order of ~100 gauss, then for reasonably cold ions of ~1 eV the gyro-radius would be < 10 cm. This suggests that for ions not much warmer than 1 eV, a magnetic field on the order of 100 gauss would keep the gyro-orbit small enough compared to the radius of the magnets generating the field that the first condition could be satisfied.

To consider the magnitudes involved for the second condition, the ion gyro-frequency downstream of the source is given by [17]:

$$f_{ci} = 1.52 \times 10^3 \frac{Z\, m_p}{m_i} B \sim 38\, B \qquad 6.2$$

where B is the magnetic field strength in gauss. So for a downstream magnetic field on the order of 100 gauss that could satisfy the first condition, the ion gyro-frequency will be on the order of ~3.8 kHz. The second condition will be satisfied if this gyro-frequency is larger than the ion collision frequency given by [17]:

$$\upsilon_i = 4.8 \times 10^{-8} Z^4 \sqrt{\frac{m_p}{m_i}} \ln \lambda \, \frac{n_i}{T_i^{\frac{3}{2}}} \sim 7.6 \times 10^{-8} \, \frac{n_i}{T_i^{\frac{3}{2}}} \qquad 6.3$$

where ln(λ) for normal cold plasma laboratory conditions can be approximated as 10 and n_i is the ion density per cubic centimeter. For the case given above where the gyro-frequency is ~3.8 kHz and the ion temperature is ~1 eV, in order to satisfy the second condition the ion density must be less than 5×10^{10} cm^{-3}. This is unrealistic because even without any downstream modification to the base field the plasma density downstream of the source was on the order of 10^{11}-10^{12} cm^{-3}, and data taken with a field increase to ~100 gauss as described had a density on the order of 10^{13} cm^{-3} in that region (this data is presented below in section 6.x). Increasing the ion temperature can lower the coulomb collision frequency between the ions, but in order to make up for the 3 orders of magnitude difference the increase in temperature has to be dramatic, far more than is realistic given the estimates of ion temperature parallel to the magnetic field made by Prager [2].

The modification of the magnetic field downstream by adding a subsequent coil was made to observe some of the effects listed above and their subsequent effect on the exhaust velocity of the plasma outflow. The intention of the magnetic coils is for it to affect the plasma as a magnetic nozzle, shaping the plasma outflow to result in a faster and more directed plasma plume. In this chapter these additional magnetic coils will be referred to as nozzles for this reason.

Section 6.2: Plasma flow in a converging magnetic nozzle.

For a conventional fluid nozzle of the Laval type, the nozzle is shaped to have three distinct regions: a converging section where the decreasing cross section causes the fluid to increase in flow speed to conserve flux, a throat section where the choked flow of the fluid transitions from sub-sonic to trans-sonic flow, and a diverging section where the super-sonic fluid accelerates away from the nozzle [1]. In each section the fluid flow velocity is increasing at the expense of the thermal energy of the fluid. When considering plasma flow in a magnetic nozzle instead of neutral flow into a physically constricting nozzle, it is not necessarily true that the velocity of the plasma will increase going into the converging section of the magnetic nozzle. This will depend on the degree of magnetization of the plasma particles. In the case of HPH and many other helicon experiments the electrons are well magnetized and slow down to conserve magnetic moment (as described below). If the ions are also magnetized, they will slow down as well. If the ions are not well magnetized such as in the case of HPH, instead of slowing to conserve magnetic moment the ion velocity is determined by the electric potential established by the electrons.

In the case of a converging magnetic field, as the plasma particles move into the increasing magnetic field the gyro-motion of the particles will increase at the expense of the parallel motion of the particles as they act to conserve their magnetic moment, given by [20]:

$$\mu \equiv \frac{1}{2}\frac{v_{\perp}{}^{2}}{B} \qquad 6.4$$

where $v_{\perp}$ is the velocity of the particle perpendicular to the magnetic field. As the magnetic field increases, the gyro-motion of the particle will increase to keep the magnetic flux contained within the particle's path conserved. This increase in perpendicular velocity comes at the expense of parallel velocity for the energy of the particle to be conserved, so as it gyrates around the field faster it slows in its parallel motion along the magnetic field [20].

This would suggest that for a converging magnetic nozzle with magnetized electrons and ions both, the plasma flow would slow down as it enters the converging magnetic field and the individual particles act to conserve magnetic moment. There is some experimental confirmation of this in the work by Inutake et Al [27] in adding a magnetic nozzle shaped to be similar to a Laval nozzle downstream of a magneto-plasma dynamic thruster. In their results the axial flow in the converging region was decreased compared to the case without the magnetic nozzle, while the axial flow downstream of the nozzle was increased relative to the non-nozzle case [27].

A separate case is treated by Arefiev et Al [28] which considered cold, un-magnetized ions and magnetized electrons in a converging magnetic nozzle field. In their model the ions were cold and began at rest, while the electron temperature was comparable to that of laboratory plasmas and high enough so that the converging field is not a magnetic bottle. The electrons entering the converging magnetic field were slowed by conservation of magnetic moment as well as being slowed as they moved away from the ions. This established an electric potential that accelerated the ions into the converging magnetic nozzle field, increasing in ion velocity until the sound speed was reached at roughly the throat of the nozzle. While some of the electrons did not have enough parallel energy to pass through the magnetic nozzle, most did and continue to establish the ambipolar electric field on the diverging side of the magnetic nozzle. In this region, the electrons are accelerated away from the magnetic nozzle in the diverging field to conserve magnetic moment, increasing the ambipolar electric potential and accelerating the ions above the sound speed of the plasma. In this case, the ions passing through the nozzle are not slowed by the nozzle, but instead are increasing in velocity all the way through the nozzle [28].

The model developed by Arefiev et Al [28] assumed that the electron and ion temperatures were isotropic in the converging magnetic field region and the ions were accelerated only up to the ion sound speed which was determined by the electron temperature as described before in Chapter 5. In a separate treatment by Saka [29] that does not require the plasma to be isotropic, the critical flow speed to which the ions can be accelerated by the ambipolar electric field of the electrons in the converging magnetic field is dependent on the ratio between the pressure of the plasma parallel and perpendicular to the magnetic field. For conditions where the parallel pressure of the plasma flow dominates over the perpendicular pressure (discussed in Chapter 5 as being super-Alfvenic), the critical flow speed exceeds the ion sound speed by as much as 2-3 times and the ions can continue to be accelerated to super-sonic speeds even in the converging region of the magnetic field [29].

These two models together suggest that in the case of HPH with its cold, unmagnetized ions and strongly directed plasma flow, the ambipolar acceleration of the ions by the electrons can still transition to a super-sonic flow speed even if the magnetic field is modified with a magnetic nozzle to have a converging magnetic field geometry. As long as the electrons have enough parallel energy to move through the magnetic nozzles without being turned back, they can continue to cool and slow down while accelerating the plasma ions even well downstream of the source. If there was no additional energy being added to the electrons by the antenna being on, the electrons would lose the bulk of their thermal velocity accelerating the ions and have a cold temperature similar to the ions. If the antenna can continue to heat the electrons downstream of the source, this can keep the electron temperature warmer for longer and continue to accelerate the ions to a higher directed energy.

Section 6.3 Acceleration of the plasma in a diverging magnetic field:

On the other side of the magnetic nozzle where the field begins to diverge again, it is expected that the plasma flow will increase in speed. This is the result of conservation of magnetic moment for the electrons increasing their parallel velocity, which through the ambipolar electric field accelerates the ions. To the extent that the ions are magnetized, they will also be sped up by conservation of magnetic moment in the diverging region of the magnetic field [28]. The acceleration and detachment of the plasma from a diverging magnetic field has been studied in several different models such as by Arefiev et Al [28] and Little et Al [30], and while the specific mechanism is not determined by these models it is expected to behave in the case of HPH as a combination of the detachment mechanisms described earlier in Chapter 4.

An additional consideration is the effect of the converging and diverging magnetic field on azimuthal diamagnetic currents such as those measured in the previous chapters. In the case of the converging magnetic field, the diamagnetic current with the radially inward magnetic field generates a JxB force that is anti-parallel with the axis and is expected to slow the flow of plasma. In the diverging field the JxB force with the radially diverging magnetic field is directed parallel with the axis and is expected to accelerate the plasma flow downstream [27]. This means that depending on where the currents are being driven, the introduction of a magnetic nozzle downstream could result in speeding up or slowing down the plasma outflow as a result of this JxB force.

Section 6.4: Introduction of a single magnetic nozzle downstream

The diamagnetic signal described in Chapter 4 peaked ~25 cm downstream. This position was also roughly one wavelength downstream of the source region. To determine whether this peak in the diamagnetic signal was correlated with the magnitude of the background magnetic field at that position, a magnetic nozzle was added to increase the field 25 cm downstream to ~100 gauss in magnitude. This nozzle was 11 cm wide and 26 cm in diameter, positioned with its center at 25 cm downstream of the quartz face where the previously measured diamagnetic signal peaked. This is also the position where it was expected that the plasma was transitioning from sub-Alfvenic to super-Alfvenic flow as described in Chaper 5. The axial component of the magnetic field in this new configuration is compared to the previous magnetic field configuration in Figure 6.1.

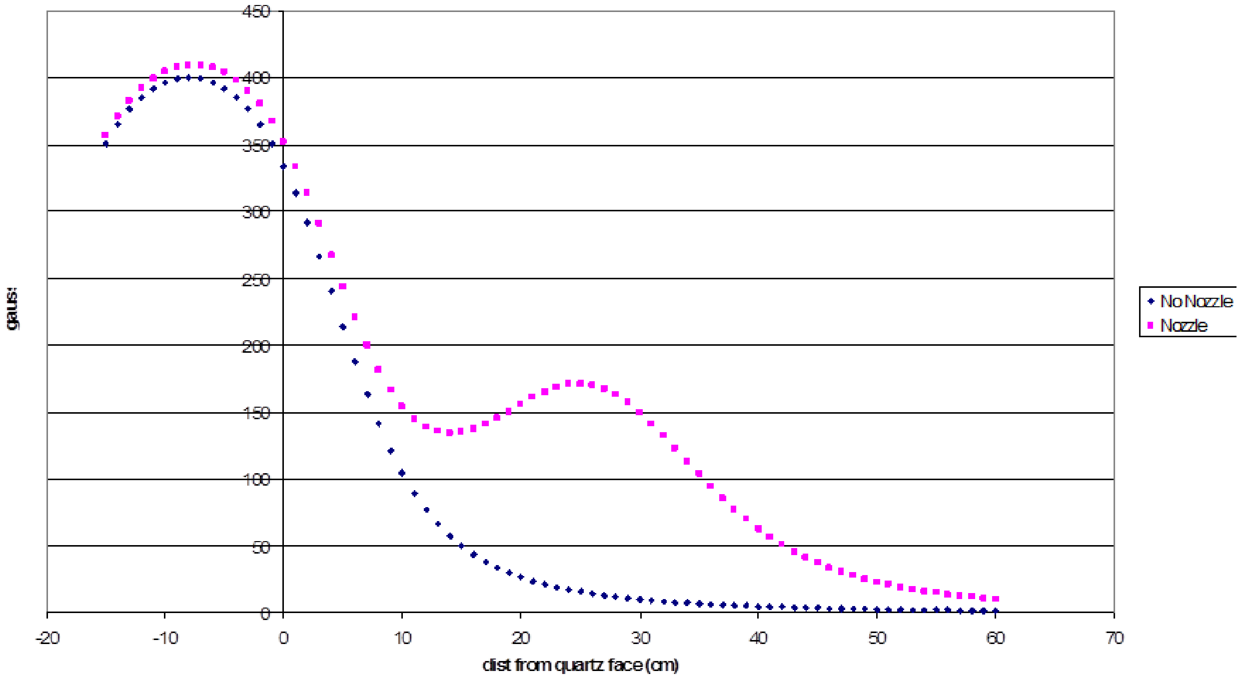

Figure 6.1: Modification to the axial magnetic field with a nozzle positioned downstream, centered 25 cm from the end of the source region.

The magnetic field in the source region is not significantly affected, so that the plasma production in the source region was similar in both configurations. The magnetic field strength falls off slower downstream of the magnetic nozzle as a result of the larger magnet radius for the nozzle as compared to the base magnet coils. A side view of the magnetic field geometry is plotted in Figure 6.2

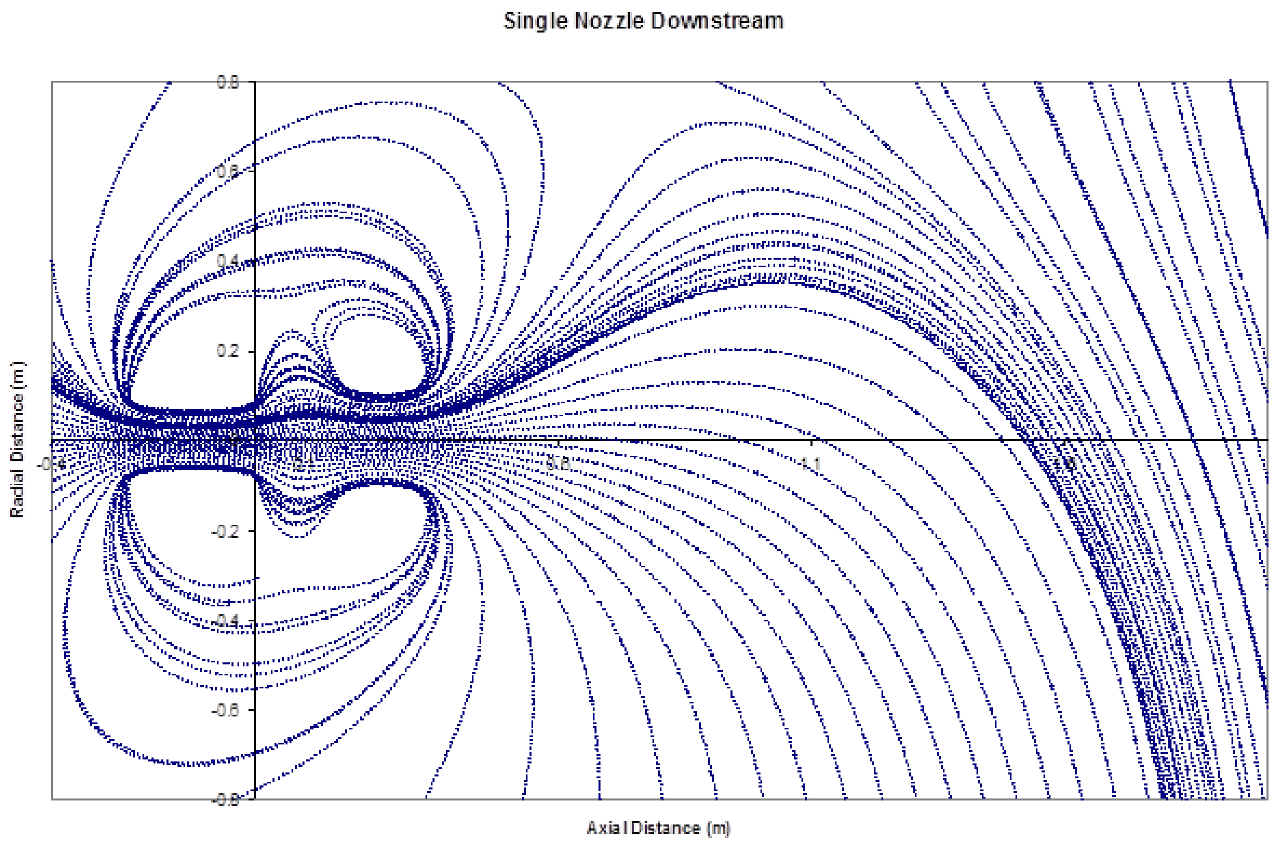

Figure 6.2: Magnetic Field configuration with a single nozzle downstream together with Earth's magnetic field. The magnetic field from the source region diverges for a short distance before entering the nozzle, and then diverges downstream before joining with the Earth's field.

The side-view of Figure 6.2 shows the magnetic field diverging briefly as it leaves the source region before converging again into the magnetic nozzle. Downstream of the magnetic nozzle the field widens up and connects with the Earth's magnetic field roughly 1.5 m downstream of the source region. The introduction of the magnetic nozzle had a significant effect on the collimation of the plasma, the exhaust speed of the ions, and the diamagnetic perturbation of the magnetic field. These effects are described in the following sections.

Section 6.5: Collimation of the plasma beam with a single magnetic nozzle:

With the increased magnetic field along the axis downstream, the magnetic pressure of the background field was increased and this resulted in more plasma close to the axis. The electron density along the axis after the plasma has reached far downstream (~100 μs) is plotted in Figure 6.3, along with the electron density from the non-nozzle case for comparison. Near the source region where the field modification is minimal the densities are comparable, it is mainly in the region downstream of the source surrounding the nozzle position at 25 cm and further that are strongly affected.

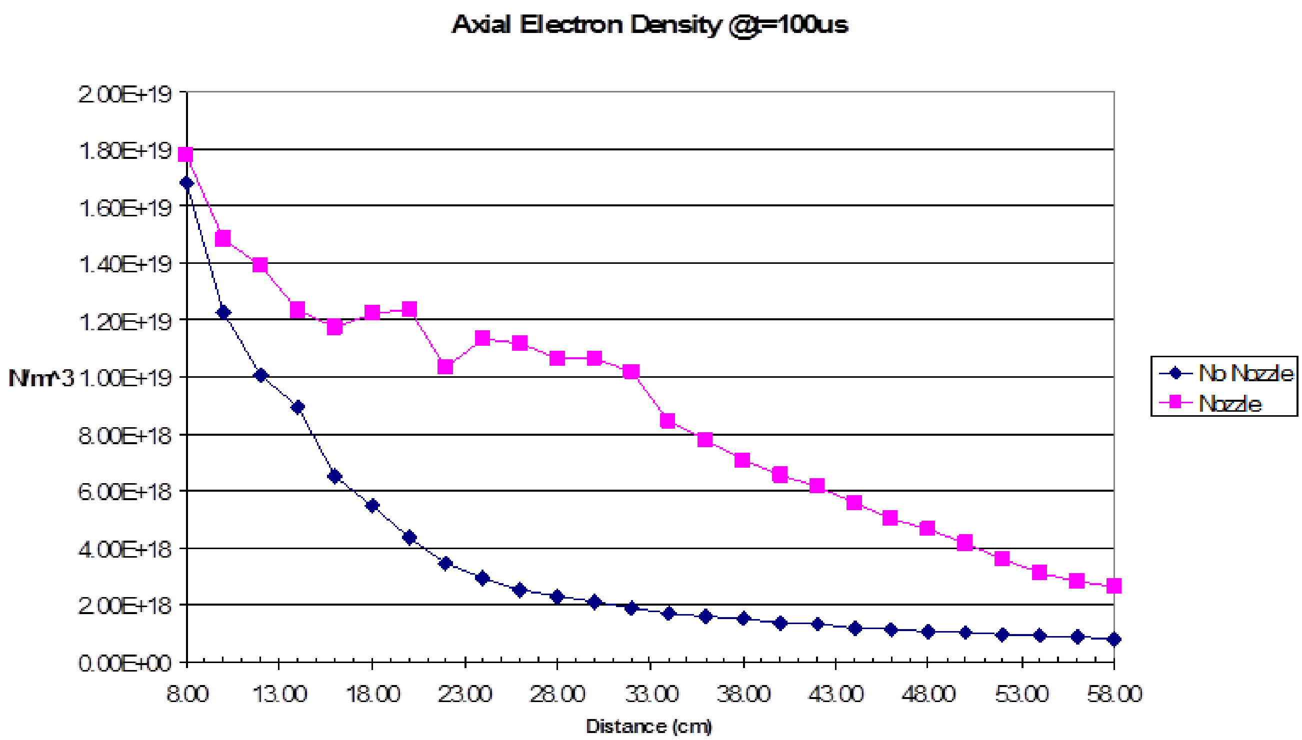

Figure 6.3: Comparison of the electron density as a function of distance from the source with and without the nozzle, showing increased plasma density on the axis.

In the non-nozzle case, the plasma density 25 cm downstream where the diamagnetic effect was strongest was ~$3x10^{18}$ m^{-3}, while in the nozzle case the plasma density is ~$1x10^{19}$ m^{-3} that distance downstream, and doesn't decrease into the low 10^{18} range until far downstream. Since the input power in the source region, magnetic field, and neutral gas profiles are unchanged the total plasma output of the source is unchanged, and this increase in density is coming from an improved collimation of the beam. This collimation of the beam is measured with a radial density profile, a Langmuir probe positioned 10 cm downstream and between the source and nozzle, and displayed for four separate times in Figure 6.4. The first panel of Figure 6.4 shows a broader distribution early in time while the plasma density is still increasing at 10 cm downstream. The second panel is taken at 100 μs when the plasma density has built up downstream, and instead of a broad distribution the profile is quite narrow. The third panel shows the distribution at 200 μs when the antenna is turned off, and the distribution is still narrow. The final panel is 50 μs later when the density has decreased the distribution has broadened again.

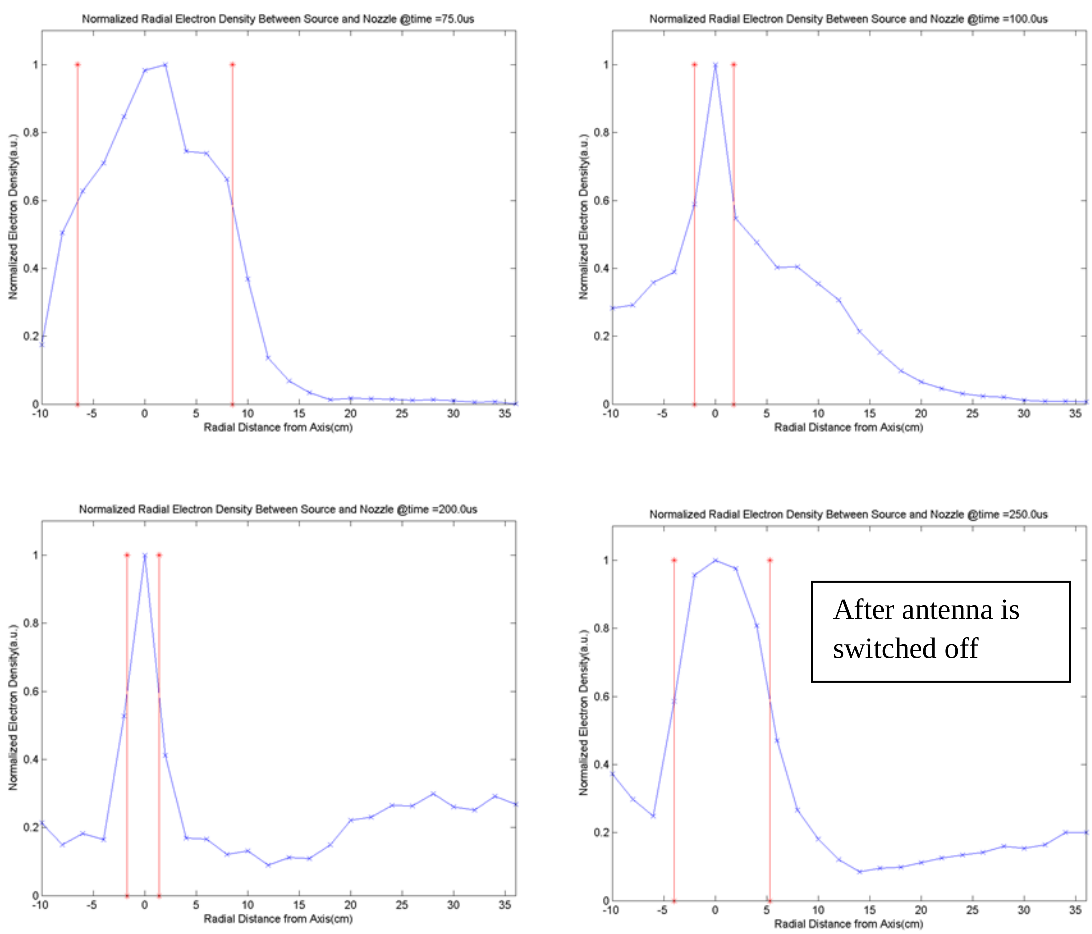

Figure 6.4: Radial profile of normalized electron density between the source region and the nozzle at 4 separate times. A fit for the full width at half max is plotted in red.

Each profile in Figure 6.4 shows the normalized electron density of the radial cut in blue at 10 cm downstream of the source. The red lines are a fit for the full width at half max of the density profile, which is used as an approximation of the beam width. These density profiles are then used to calculate the FWHM for the density profile over the whole shot. This is presented below in Figure 6.5.

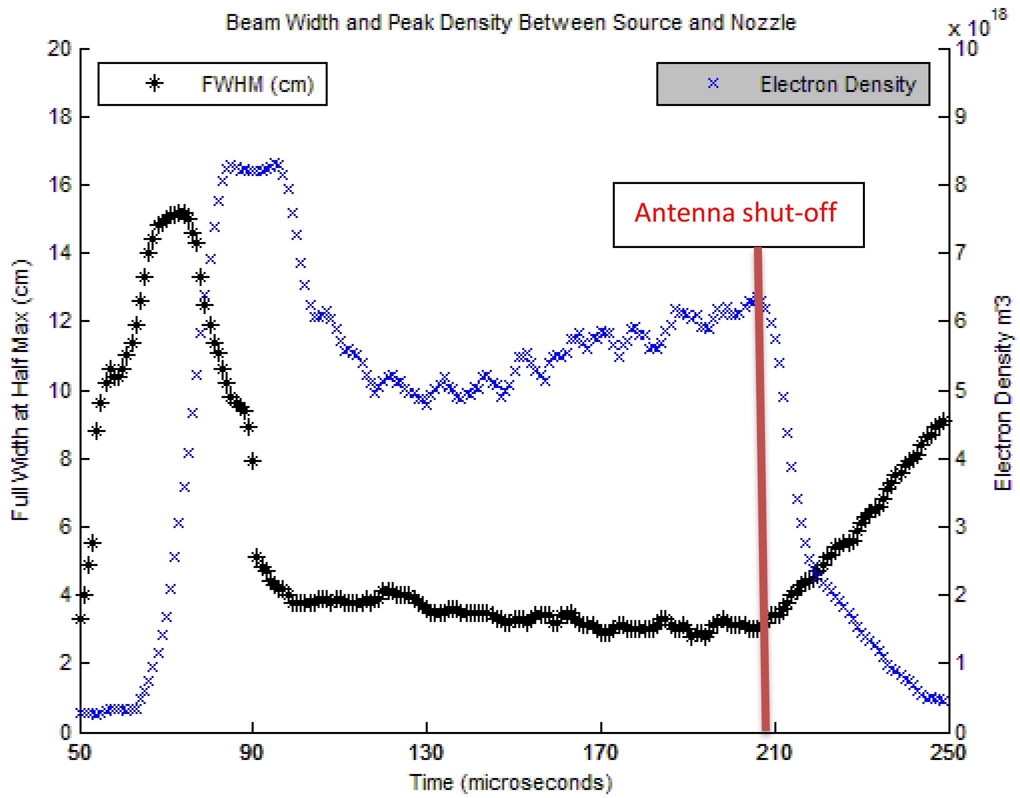

Figure 6.5: The fitted full width at half max of the radial profile between the source and the nozzle is plotted in black as a function of time along the left axis, and the peak electron density at the same time is plotted along the right axis in blue.

The time in Figure 6.5 is relative to the antenna being turned on. Initially the beam width is broad as the plasma density is low for the period after the antenna has begun to load and the density in the source region is increasing. At ~ 80 μs the plasma density along the axis at 10 cm reaches a peak value and the beam width is ~12 cm across. At this point the width of the beam is already decreasing. As the measured plasma density is roughly constant for the next 20 μs, the width of the beam drops from ~12 cm across to ~4 cm across. Over the next 30 μs the peak density measured along the axis drops to about half of what it was while the beam width continues to slowly narrow. From 130 μs until the antenna is shutoff at 200 μs the plasma density increases ~20% while the beam width narrows by ~25%. After the antenna is shutoff and production of plasma in the source region drops off, the density along the axis drops rapidly while at the same time the width of the beam widens out again.

This narrowing of the beam between the source and the nozzle while the antenna is on suggests that there is a force acting to push plasma onto the axis while the antenna is on and plasma is downstream. This is similar to the estimated JxB force towards the axis measured in Chapter 5. With the increased axial magnetic field between the source and the nozzle, it's possible that the region where the azimuthal diamagnetic current crossed with the axial magnetic field results in a force towards the axis has been extended over a longer region, so that rather than restricted to a few centimeters near the source exit it is acting over a longer region and results in a larger acceleration. Normally the electron thermal pressure would be acting to expand the plasma beam across the magnetic field and would be balanced out by an azimuthal diamagnetic current causing a JxB force towards the axis and a radial electric force caused by the motion of the electrons relative to the colder ions, as described by Stenzel et Al [21]. This narrowing of the beam suggests that the forces acting to confine the beam are dominant over the electron thermal pressure of the beam between the source and the nozzle.

A second radial profile of the plasma beam was taken downstream of the nozzle at 66 cm which is more than two magnet radii downstream of the magnetic nozzle. In Figure 6.6 the normalized radial electron density is plotted for four separate times, again with the full width at half max plotted in red.

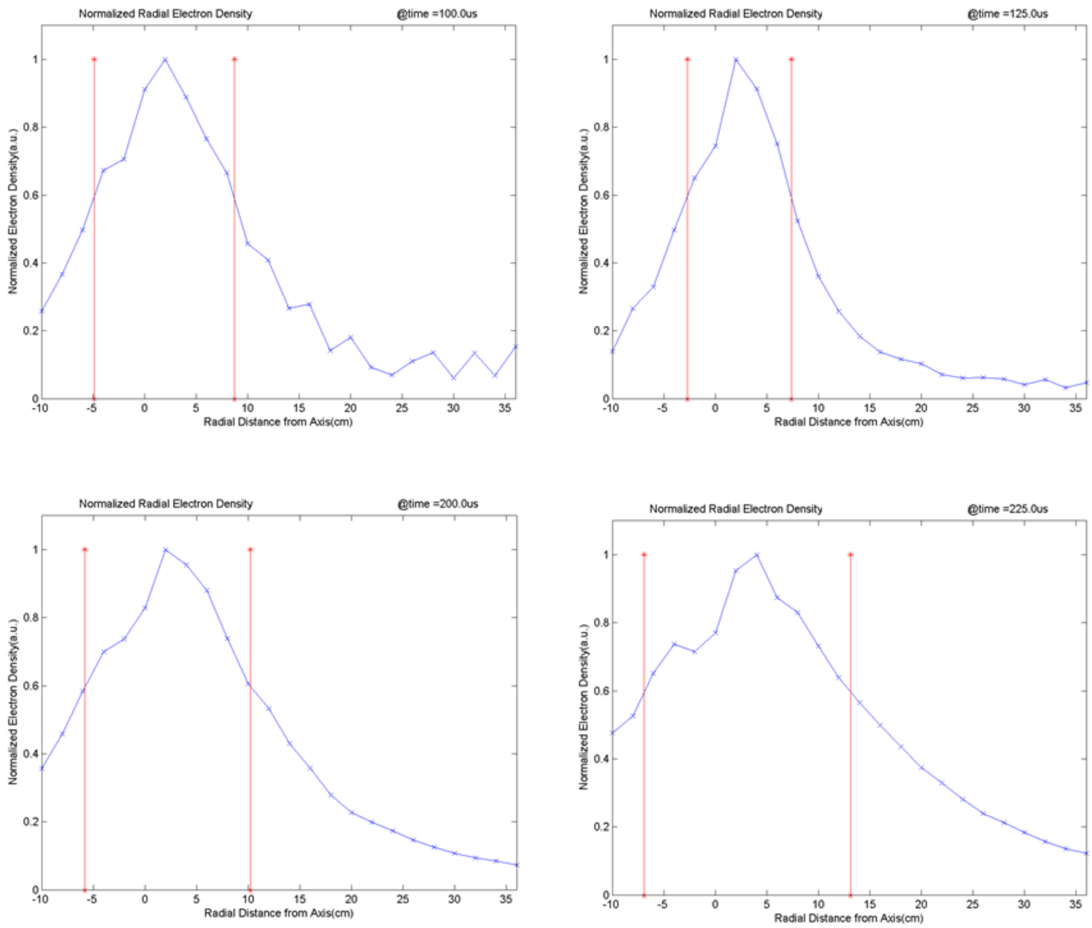

Figure 6.6: Radial electron density 66 cm downstream of the source and more than two magnet radii downstream of the nozzle. Normalized density is in blue while the full width at half max is displayed in red

As in the converging field case, early in time the distribution is broad when the density is low and narrows down as the plasma density increases, this time reaching a minimum of ~ 10 cm for the width of the beam. However, unlike the previous case the beam width widens out over the course of the shot to ~15 cm when the antenna is shutoff and continuing to broaden afterward. The beam width and peak plasma density at this position downstream of the nozzle are plotted as a function of time in Figure 6.7.

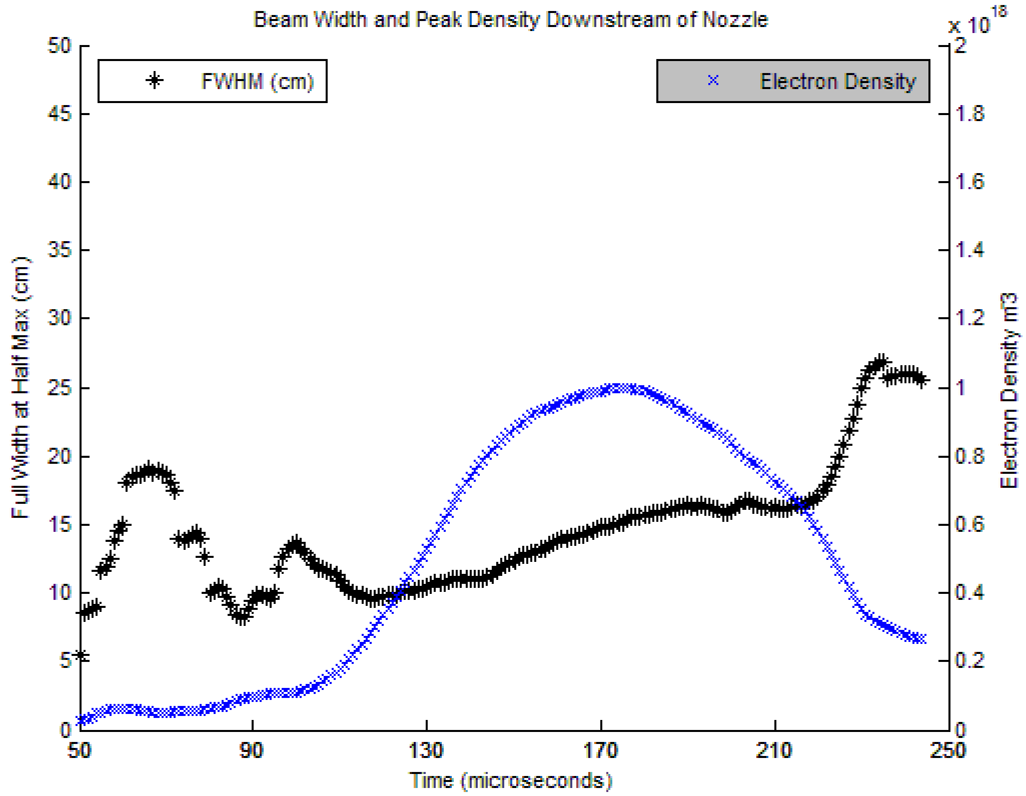

Figure 6.7: The fitted full width at half max of the radial profile downstream of the nozzle is plotted in black as a function of time along the left axis, and the peak electron density at the same time is plotted along the right axis in blue. This was measured at 66 cm downstream.

At this position far downstream the density profile builds slowly and peaks relatively late in time. This is because it's far enough from the source region that faster plasma particles arrive much earlier than the slower particles and the density profile is broadened out in time as a result. As opposed to the profile measured upstream of the nozzle where the density was increasing in time while the beam width was narrowing, at this point well downstream of the nozzle the beam is widening over time from ~10 cm to ~15 cm across over the course of the shot, while over the same time period the density both increases and decreases. This suggests that the confining force which was keeping the beam width narrow upstream of the nozzle in the converging field case is not as dominant over the plasma density in the downstream case. However, the beam diameter widening by a factor of 2-3 is comparatively low considering the background magnetic field strength has decreased from 150 gauss to < 10 gauss and this measurement was made more than two dipole radii downstream of the nozzle.

After the antenna is shutoff there is a rapid broadening of the beam width as there was in the upstream case, but the plasma density at this position does not fall as quickly. This is because at this position downstream the plasma being measured was produced earlier in time and had to propagate to 66 cm downstream, while in the 10 cm case the plasma did not have to travel far from the source region to reach the probe. The same dramatic increase in width with a slower decrease in density suggests that the beam width is correlated with the antenna shutoff as well as with the plasma pressure at that position.

Section 6.6: Ion velocity downstream of a single magnetic nozzle:

Measurements of the ion velocity at 66 cm downstream of the source region similar to those presented in Chapter 5 were made downstream of the magnetic nozzle to compare to the non-nozzle case. The beam width and plasma density measurements presented in Figure 6.7 were taken at the same position downstream as these ion velocity measurements. The ion velocity distribution of the nozzle and no-nozzle cases are presented for separate times in Figure 6.8, with the non-nozzle velocities plotted in red while the nozzle case is plotted in blue.

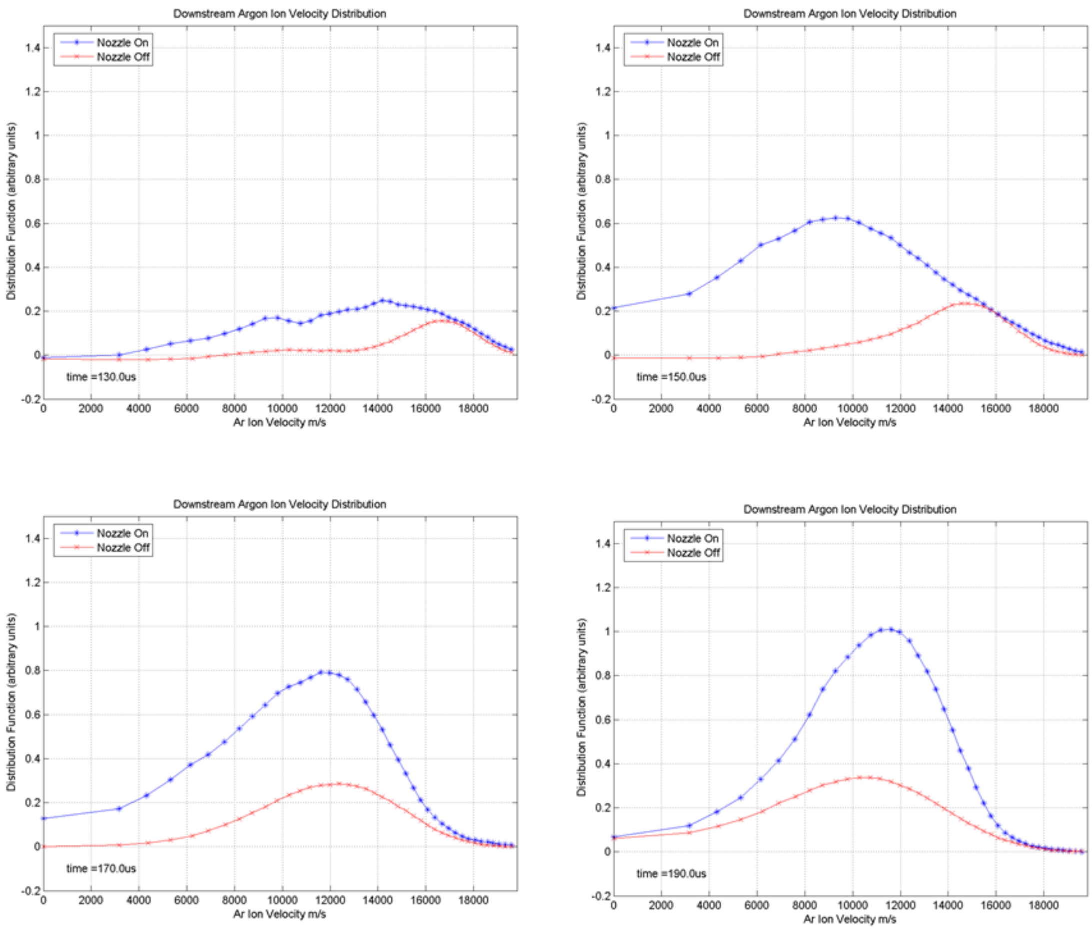

Figure 6.8: Ion velocity distribution downstream of the magnetic nozzle, 66 cm from the source region, for four separate times. The peak of the distribution increases over time for the nozzle case between 150 and 200 μs, but not the case without the nozzle.

In the first panel of Figure 6.8 at 130 μs the beam width is at its narrowest and the plasma density has begun to build at the position where the velocity is measured. The non-nozzle case and the nozzle case have the same population of fast ions above 16 km/s, but there are dramatically more ions at the speed of 14 km/s and slower reaching the detector for the nozzle case. In the second panel 20 μs later the high velocity population again overlap, but the increase in slower ions 6-12 km/s in speed is even more dramatic.

In the third panel at 170 μs the two distributions begin to differ in the case of fast ions as well. At this point in time the beam width of the nozzle case has widened to ~14 cm and so is broader than earlier in time but the plasma density on axis has reached a peak. In the non-nozzle case the peak of the distribution has moved to lower velocity and there are fewer fast ions than before. In contrast, the nozzle case at 170 μs has had the peak of its distribution shift to the right and higher velocity, not only having more of the slower ions but significantly more ions in the 12-16 km/s range as well. While the peak of the distribution is shifting to the right at 170 us, there are fewer slower ions in the nozzle case than there were at 150 μs. This suggests that either the source region is no longer producing the slower ions, or that the slower ions have been accelerated up to higher velocity.

In the final panel of Figure 6.8 at 190 μs near the antenna turn-off, the non-nozzle case has continued to shift its distribution slowly to the left and lower velocity, with fewer fast ions than the previous panel. In contrast, the nozzle case has continued to shift its distribution to the right, with fewer slow ions reaching the detector and more fast ions being measured. The peak in the distribution (the most probable speed) is now 11-12 km/s and there is a significant population between 12-16 km/s late in time, compared to the case at 150 μs. In place of a comparatively broad spread in velocities for the ions, the distribution moves to a narrower profile with a faster peak velocity at 190 μs than at 150 μs, but whether this is the result of accelerating slower ions to higher velocity or simply a result of collimation of the ion beam is not fully determined. Comparison to the red trace without the nozzle shows a substantial increase in number of ions reaching the detector, both of the slow and the fast ions.

Section 6.7: Diamagnetic perturbation of the axial field along the axis with a single nozzle:

With the implementation of the single nozzle downstream, there was an increase in both plasma density and directed ion velocity on the axis downstream of the nozzle. In the previous chapters the increase in density and velocity compared with the earlier work of Prager et al [10] was correlated with an increase in the diamagnetic perturbation of the axial field along the axis. The magnetic nozzle was positioned at ~25 cm so that the largest increase in the downstream magnetic field was at the same position where the diamagnetic perturbation peaked before, and the beginning of the region where the diamagnetic perturbation was as large as the background magnetic field. The axial diamagnetic perturbation is plotted as a function of axial distance for both the nozzle case and the non-nozzle case for four separate times below in Figure 6.9.

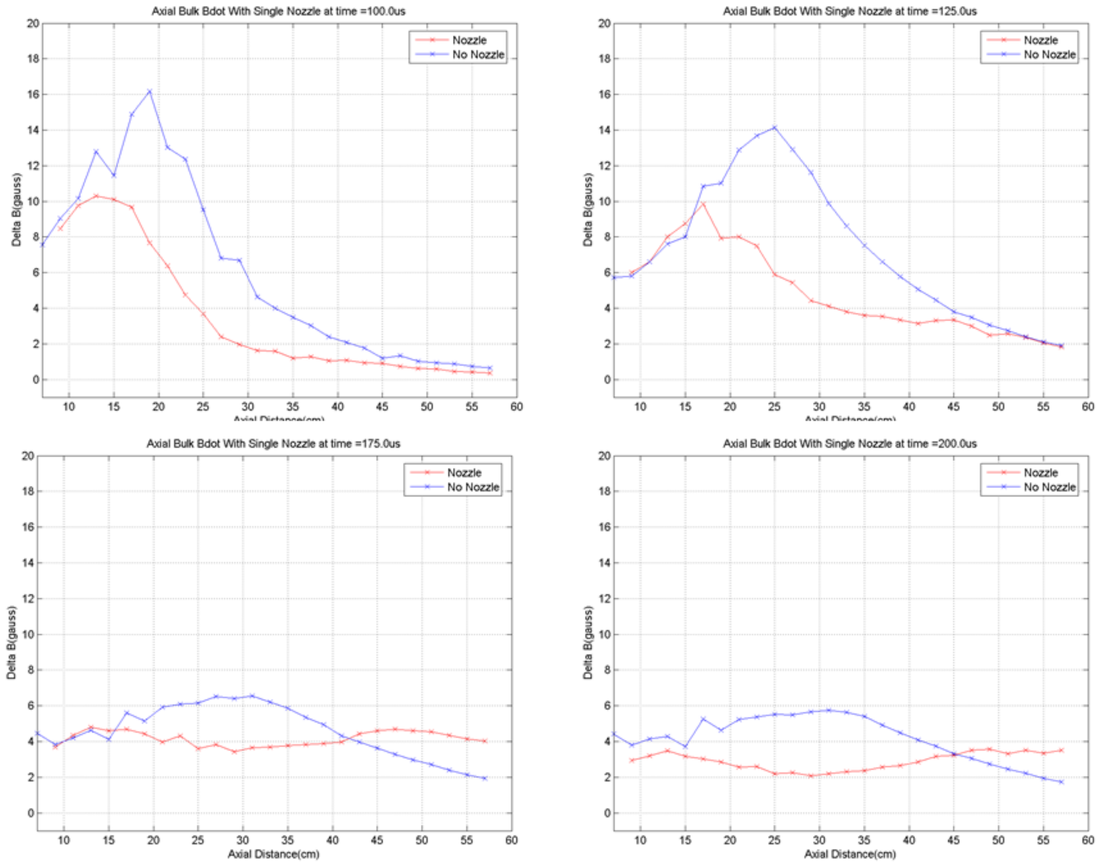

Figure 6.9: Axial diamagnetic perturbation of the magnetic field along the axis for four separate times, with the non-nozzle case plotted in blue and the nozzle case plotted in red. The nozzle is centered at 25 cm downstream.

In the first two panels of Figure 6.9 it is apparent that the magnetic perturbations are the same near the source region where the field is relatively unmodified by the nozzle, and only begins to significantly diverge more than ~12-15 cm downstream of the source region. It is also apparent that the large peak in the diamagnetic perturbation 25 cm downstream of the source is missing in the nozzle case. Instead the peak in the diamagnetic perturbation for the nozzle case is ~10 gauss, roughly half of the non-nozzle case, and it peaks in the region where the field lines have diverged between the source and the magnetic nozzle. After this peak it falls off rapidly through the nozzle region and is only a few gauss downstream of the nozzle.

In the last two panels of Figure 6.9 the behavior of the two profiles late in time near when the antenna is shutoff are compared. The non-nozzle case peaks downstream at 5-6 gauss and then falls off downstream as the background field decreases. The nozzle case suggests an extended region of ~4 gauss in magnitude near the source region and downstream of the nozzle, while dropping to ~3 gauss in the region under the nozzle where the magnetic field is high. The dip in the diamagnetic perturbation is most pronounced in the final panel which shows the diamagnetic perturbation dropping to ~2 gauss under the nozzle at the time of antenna turn-off.

The position of the nozzle prevented the array of bdot probes used in Chapter 4 from making a 2D cut of the magnetic field perturbations between the source and the nozzle region, but based on the axial magnetic perturbation data and the collimation of the beam a rough estimate of the current density can be made. From the results of the previous chapters, for a peak diamagnetic perturbation of 10-15 gauss close to the axis this resulted in a diamagnetic current of ~10-20 kAm^{-2} positioned 2-3 cm from the axis. From the radial Langmuir data it is apparent that the beam width is ~4 cm for most of the shot, suggesting a similar radial profile is possible. Since the dominant component of the current was proportional to the radial derivative of the axial magnetic field perturbation (as described in Chapter 4), the scaled down current estimate should be proportional to the drop in the diamagnetic perturbation measured. While in the non-nozzle case the diamagnetic perturbation had a large effect on the total magnetic field, in the case of the single nozzle the diamagnetic perturbation of the axial field is small compared to the background magnetic field as plotted in Figure 6.1 as far out as 50 cm downstream.

This means that near the source region early in time, the diamagnetic perturbation being roughly half what is measured for the non-nozzle case suggests a current density of 5-10 kAm^{-2} in the region 15-25 cm downstream of the source. In the same position the magnetic field of the nozzle case is ~100-150 gauss, instead of diamagnetically reduced to near 0. This suggests an estimated force density of ~150 Nm^{-3}, which is comparable to that measured near the source region for the non-nozzle case. What becomes more significant is the region over which the force is acting, which was a few centimeters long in the non-nozzle case but is tens of centimeters in the nozzle case. Late in time the diamagnetic perturbation of 3-4 gauss yields a current estimate of 4-5 kAm^{-2} over the extended region through the nozzle, while the magnetic field over that region is still 100-150 gauss even far downstream. This gives an estimate of 50-75 Nm^{-3} out as far as 35 centimeters downstream of the source region. So even though this is only a third of the force acting near the source region in the non-nozzle case, it's operating over a length scale more than 15 times longer, yielding a more significant acceleration of ions towards the axis. This extended current drive region and the acceleration towards the axis is most likely what is responsible for the improved collimation observed in Section 6.5.

Downstream of the nozzle a 2D cut was made using the array of bdot probes used in Chapter 4 to measure the axial component of the diamagnetic perturbation near the axis as close as possible to the nozzle exit. This perturbation is plotted for a representative time in Figure 6.10, though note that the color axis has a different magnitude than those in Chapter 4.

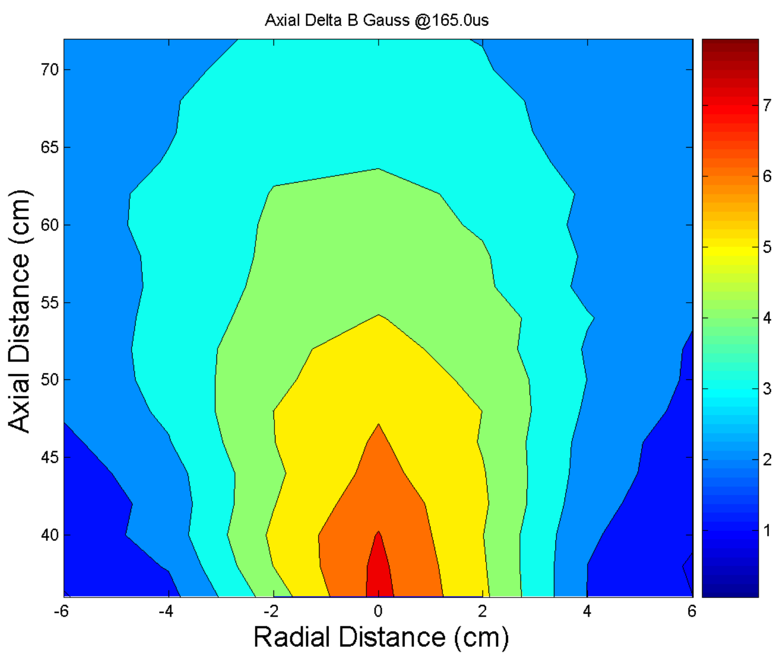

Figure 6.10: Axial component of the diamagnetic perturbation downstream of a single magnetic nozzle. The peak of the color scale is at 7 gauss, rather than the larger scale used for the strong perturbations near the source region in Chapter 4.

This measurement of the diamagnetic perturbation near the axis has a narrow region that peaks at 7 gauss, compared to the 4 gauss measured with the axial probe. This suggests there could be a narrow region of diamagnetism that is small compared to the diameter of the axial bdot (~2.2 cm) and so was not measured in the axial sweep but was apparent in the array data. This suggests that the measured axial perturbations between the source region and the nozzle could be off by a factor of 2 if the probe partially missed this narrow region. Another important thing to note from Figure 6.10 is that far downstream of the nozzle where the background field has dropped to a few gauss, the diamagnetic signal is ~ 3 gauss and so we expect the same sort of detachment behavior from the diverging nozzle magnetic field as we did from the diverging source magnetic field. Far enough downstream of the nozzle the diamagnetic effect reduces the total magnetic field to ~0 and the ions and electrons both can detach from the nozzle magnetic field.

Since the diamagnetic perturbation of the base field is negligible for the first 50 cm, the Alfven speed is going to be determined mostly by the strength of the base magnetic field and the plasma density. The Alfven speed on axis is plotted below in Figure 6.11, with the Alfven speed in km/s in blue, the fast ion population measured 66 cm downstream in red, and the most probable speed late in time measured 66cm downstream in green.

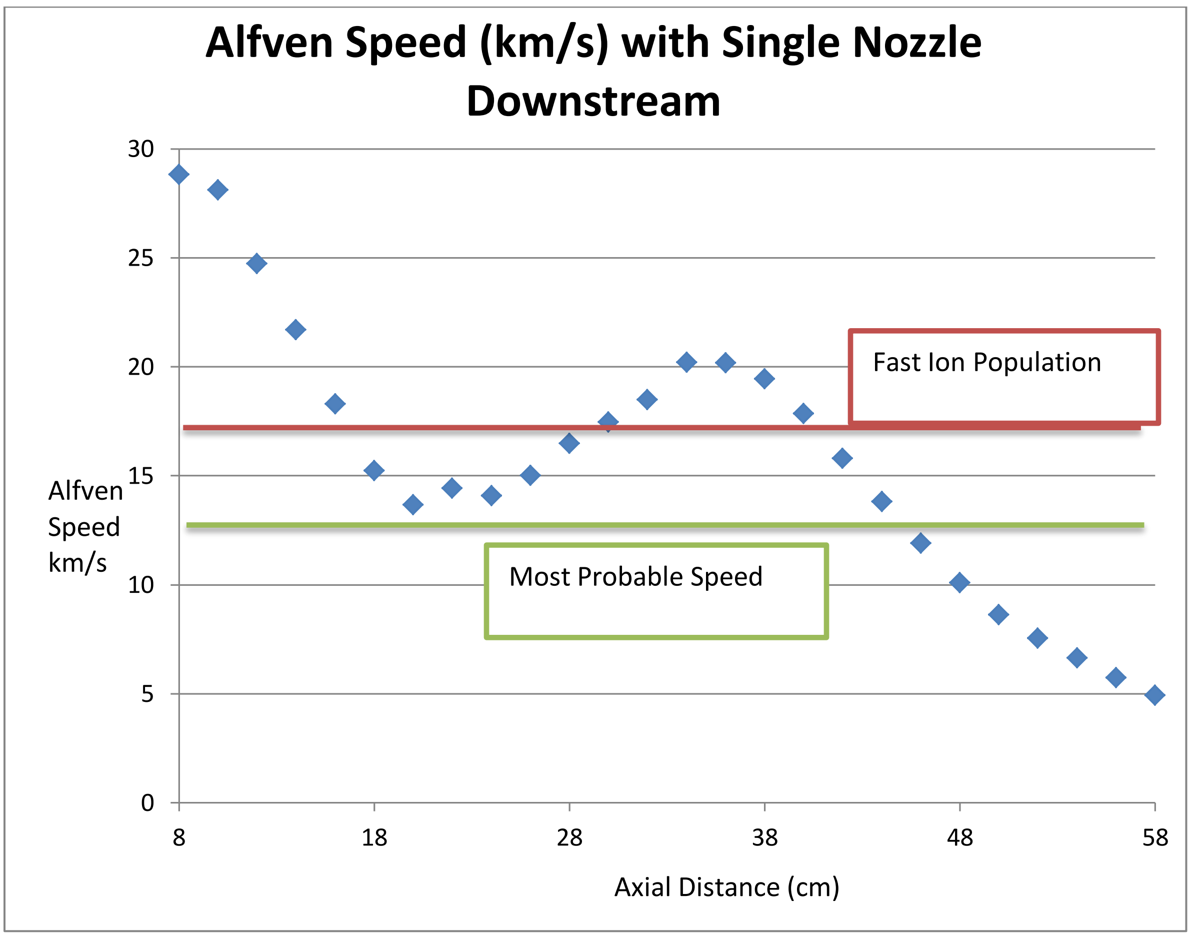

Figure 6.11: Alfven speed downstream along the axis with a single magnetic nozzle. The blue points represent the Alfven speed at that position, while the red line is the measurement of the fast ion population at 66 cm downstream and the green line is the most probable speed of the ions measured at 66 cm downstream.

The increase in the magnetic field downstream has increased the Alfven speed downstream dramatically. The increase is high enough that it is likely only that the fastest component of the ion velocity distribution becomes super-alfvenic upstream of the magnetic nozzle. It is likely that most of the ions don't become super-alfvenic until the diverging section downstream of the nozzle. Since the large diamagnetic perturbation observed in Chapter 4 weakened the magnetic field near the axis the ions were predicted in Chapter 5 to have become super-alfvenic roughly 20-25 cm downstream of the source, while now that is expected to happen roughly 1-2 magnet radii downstream of the magnetic nozzle.

Section 6.8: Ion energies upstream and downstream of a second magnetic nozzle:

A second magnetic nozzle was added downstream of the first nozzle to further increase the magnetic field downstream. This second nozzle had the advantage of being twice the diameter of the first nozzle, ~50 cm, and was capable of generating magnetic fields of hundreds of gauss. This allowed the second nozzle to make the magnetic field along the axis downstream of the source on the same magnitude as the source region, but with a larger radii so that the field fell off at a slower rate. The axial component of the magnetic field for this new configuration of two nozzles is presented in Figure 6.12.

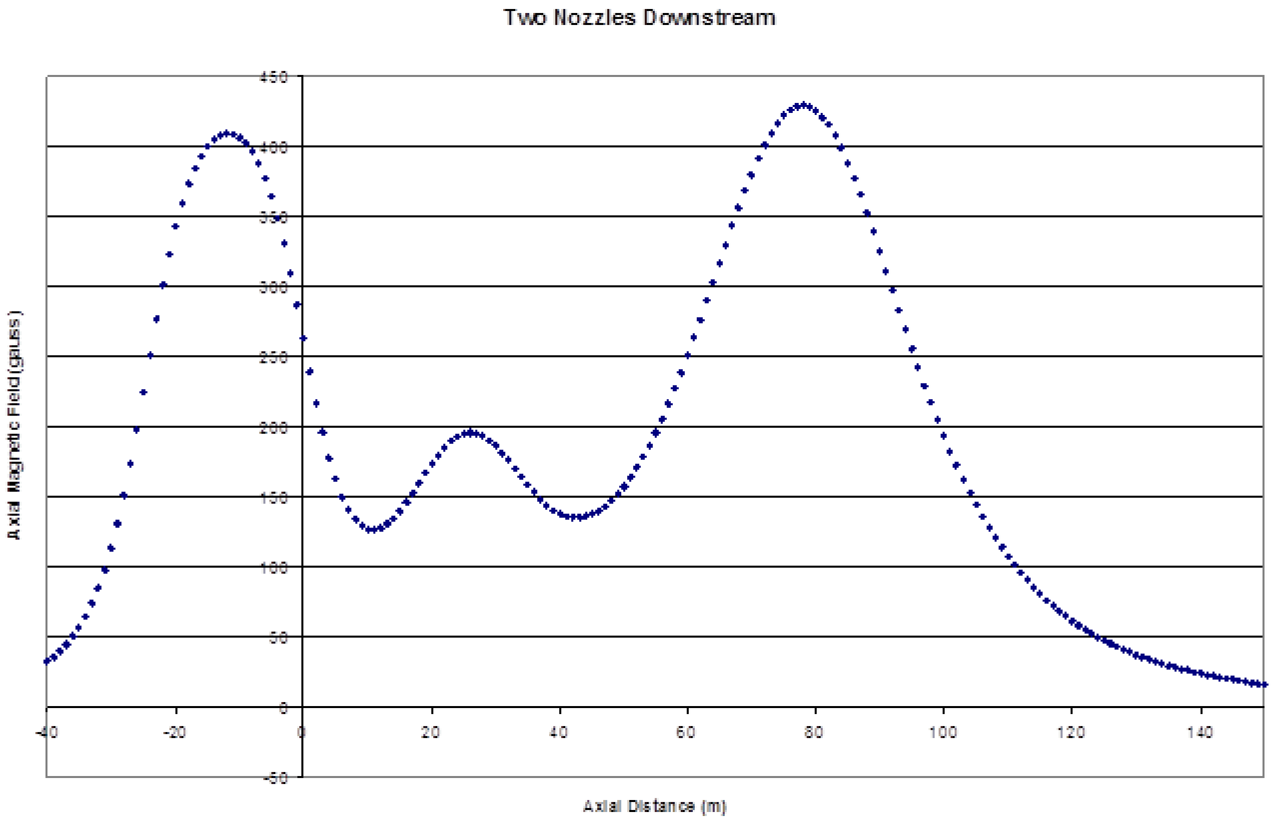

Figure 6.12: A second nozzle is added downstream of the first centered ~78 cm downstream of the source region. The second nozzle has a diameter twice that of the first nozzle, which itself is twice that of the base magnetic field coils.

The second nozzle was positioned far enough downstream of the first nozzle so that the RFA positioned at 66 cm which took the ion velocity measurements presented above was now measuring the ion energies in the converging region of the nozzle, while a second RFA positioned 144 cm downstream could be used to measure the ion energies more than 2 magnet radii downstream of the second nozzle exit. A side-view of the magnetic field geometry of these two nozzle coils together with the Earth's magnetic field are presented in Figure 6.13.

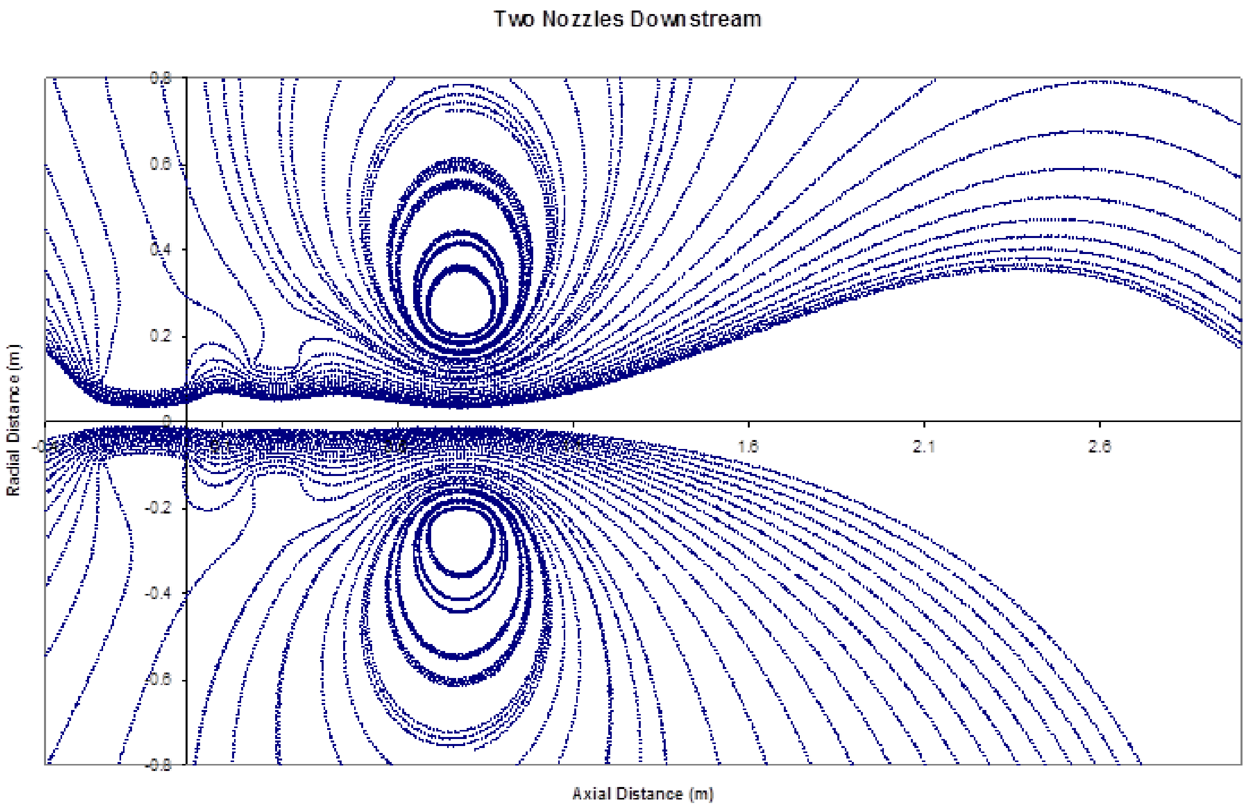

Figure 6.13: Magnetic field of the two nozzle configuration with the Earth's magnetic field. Magnetic field does not drop below 100 gauss until more than 1 m downstream of the source region.

This new configuration has a larger magnetic pressure than the previous nozzle configuration downstream, and so it's expected that the bulk of the plasma stays near the axis from the source region through the second nozzle. Also similarly to the previous case with one nozzle, radial profiles of the plasma density upstream of these nozzles show a well collimated plasma beam near the axis, that has the beam width decrease over the course of the shot.

One concern with a large converging magnetic field was whether part of the plasma population would be slowed down or turned back by the nozzle. In the converging nozzle data of Inutake et al, there was a decrease in the directed ion energy as a result of the converging magnetic field. To determine if this was occurring with the nozzles of HPH, ion energies were measured both upstream and downstream of the second magnetic nozzle. The integrated current to the RFA upstream of the nozzle as a function of ion energy is presented in Figure 6.14.

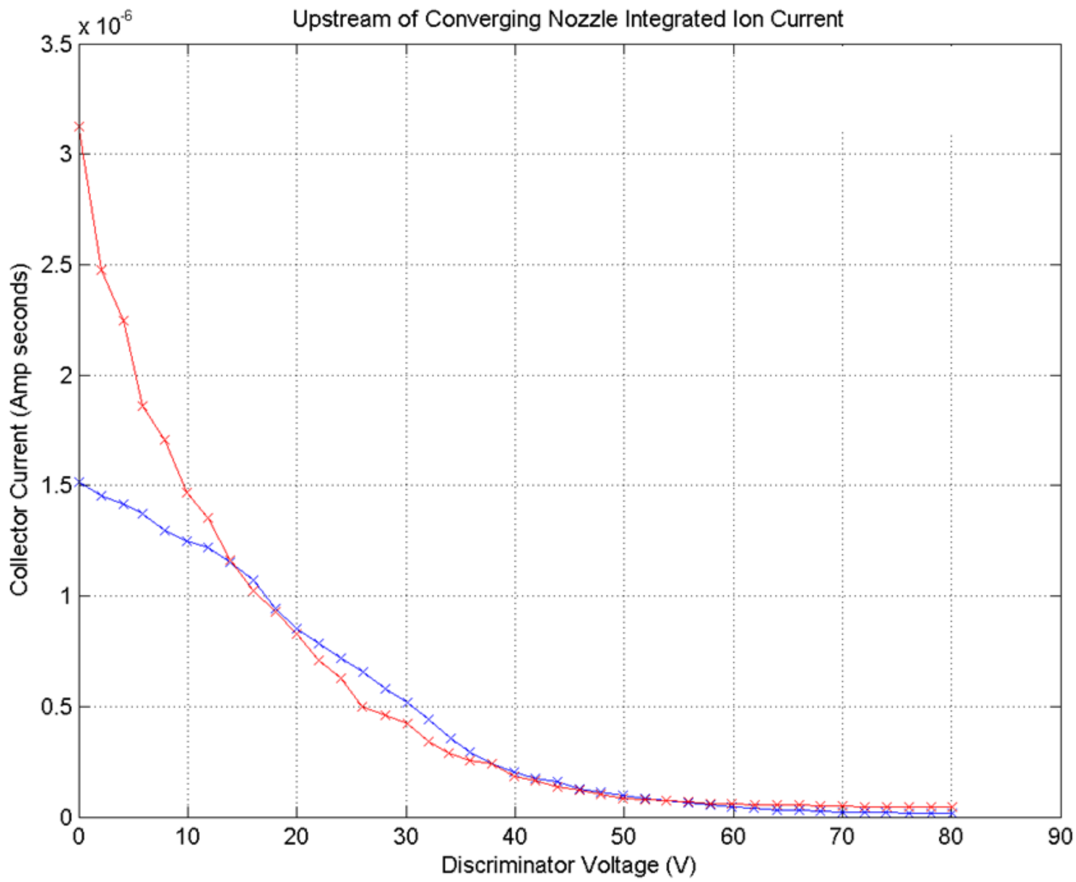

Figure 6.14: RFA Collector Current as a function of retarding voltage integrated over the entire plasma shot, upstream of the second magnetic nozzle. The blue curve represents the ion population with the second nozzle turned off, while the red curve is with the second nozzle on.

The RFA collects ions that have a directed ion energy greater than or equal to the retarding potential on the discriminator grid. By integrating the current received at the RFA over the course of the whole plasma shot and plotting it as a function of discriminator voltage, it can be determined if there is a significant portion of the ion energy population that is being slowed or turned back upstream of the second magnetic nozzle. For the higher energy ion components above 40 eV, the non-nozzle case and the nozzle case match up well and it does not appear as if the higher energy ions are slowing down. It's possible that the population of ions with energies 20-40 eV are being partly slowed down by the converging magnetic field, as there are fewer of them on the axis than in the non-nozzle case. There is also roughly twice as many low energy ions on axis in the nozzle case as there are in the non-nozzle case. The same measurement was also made 145 cm downstream of the source region on the other side of the second magnetic nozzle and more than 2 magnet radii downstream of it. These results are presented in Figure 6.15.

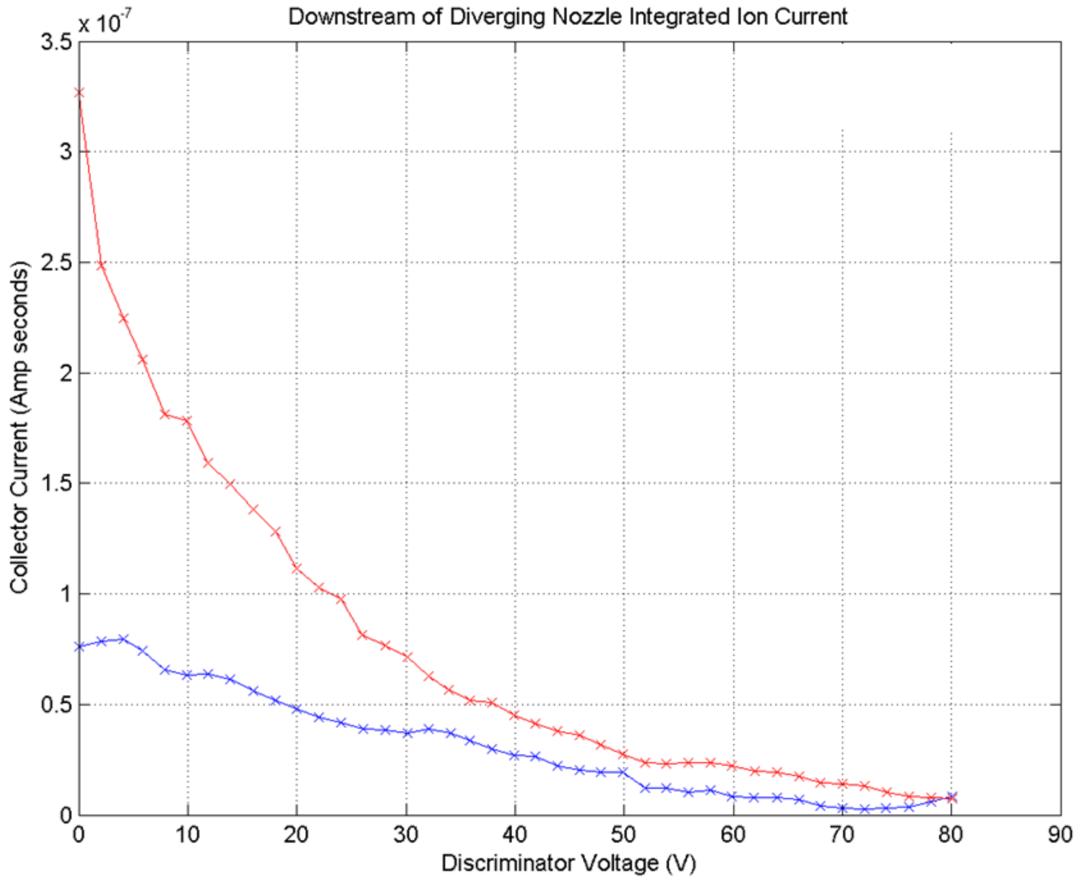

Figure 6.15: RFA Collector Current as a function of retarding voltage, integrated over the entire plasma shot, downstream of the second magnetic nozzle. The blue curve represents the ion population with the second nozzle turned off, while the red curve is with the second nozzle on.

Comparing the two populations in Figure 6.15 downstream of the second nozzle, it does not appear as though there is a significant population of ions that is prevented from passing through the second nozzle downstream. At each energy level there are as many or more ions downstream of the nozzle with it than with it off, with the difference being roughly a factor of 2 for the higher energy ions and a factor of 5 for the lower energy population. So even though the magnetic field inside the second nozzle is on the same order as the base magnetic field in the source region, it is unlikely that there is a significant population of ions that are trapped by the second nozzle and not able to get through. It is more likely that the case of HPH is closer to the model described by Arefiev et Al [28] of cold ions that are unmagnetized being accelerated through the nozzle instead of slowing to conserve magnetic moment.

Modifying the magnetic field downstream of the source region with magnetic nozzles had a substantial impact on the collimation of the plasma beam and the flow velocity of the plasma downstream. In the next chapter results from modifying the downstream magnetic field with both nozzles and a second helicon wave source to improve the collimation and ion velocity further are presented.

Chapter 7: Increased Helicon Wave Power with the Addition of a Second Antenna Downstream

Section 7.1: Wave Frequency, Input Power, and Effect on Performance

In the previous chapter, modifications made to the magnetic field downstream of the helicon source by magnetic nozzles resulted in an increase in downstream directed ion velocities and axial collimation of the plasma plume. This magnetic field configuration caused the diamagnetic perturbation along the axis to be reduced in magnitude compared to the measurements presented in Chapter 4 but was observed over a longer axial distance. One possible explanation for this was that the increase in the background magnetic field prevented the diamagnetic perturbation from effectively reducing the magnetic field to ~0 (as was measured in Chapter 4) and this allowed the wave driven by the antenna to propagate further along the axis. By propagating further downstream this extended the region over which a diamagnetic current was driven in the plasma by interaction with the helicon wave and increased the region of JxB acceleration of the plasma particles, resulting in a faster ion population downstream on axis with the nozzle on. As discussed previously in chapters 4 and 5 there is a correlation between the diamagnetic perturbation observed in the plasma and the magnitude of the helicon wave magnetic field (measured in gauss) measured downstream, with the wave magnetic field being roughly equal to the total background field in the data presented in chapter 4. The diamagnetic perturbation had already been correlated in time and space with the antenna being on, and the next step in my research was to correlate the diamagnetic perturbation with the frequency and power of the wave magnetic field so that we have a mechanism in hand in order to further enhance the effect.

In Chapter 5 I suggested the possibility that the diamagnetic current that was measured downstream was being directly driven by the wave magnetic field as it rotated some fraction of the electron population around the axis at the antenna frequency before they were stopped by collisions with other plasma particles. The collision rate for electrons downstream was roughly 3 times that of the antenna frequency, so that if only about a third of the particles were contributing to the current that would roughly match the measured current density. If this was the case, then increasing or decreasing the frequency of the helicon wave being driven downstream would increase or decrease the current density in the plasma directly. The difficulty mentioned in chapter 5 with testing this was that changing the frequency of the wave being driven downstream required changing the frequency of the source antenna, and that would have other consequences on the plasma output of the source region.

In the standard model of helicon wave propagation developed by F.F. Chen and others [12], the dispersion relationship of the helicon wave propagating along a uniform axial magnetic field with a uniform plasma density and with an insulating boundary is given by:

$$\frac{B_0}{n_0} = \frac{\omega}{k_z}\frac{eu_0 a}{3.83}, \qquad 7.1$$

where B_0 is the background magnetic field strength, n_0 is the background plasma density, ω is the angular frequency of the wave, e and u_0 are constants, and 'a' is the radius of the boundary layer and antenna wrapped around it. While these conditions don't hold downstream of the source region of the HPH, they are similar to the conditions inside the source region of HPH where the neutrals are ionized into plasma and the background magnetic field is more uniform. Previous work with the HPH by Prager et Al [11] established that axial wavelength of the plasma wave was determined by the physical length of the antenna and the angular frequency was determined by the frequency at which the oscillating current in the source antenna was driven by the power supply, similar to other helicon experiments. Re-writing equation 7.1 to reflect this, we have the relationship:

$$n_e = \frac{B_0}{af\lambda}\frac{3.83}{eu_0}, \qquad 7.2$$

where n_e is the electron density, f is the frequency of the source antenna, and λ is the wavelength of the source antenna (the physical antenna is half-wavelength as described in chapter 2). Equation 7.2 suggests that the stronger the background magnetic field in the source region the higher the resultant electron density will be, and this was confirmed by observations made by Ziemba [9] and Prager [2] up until the limits of the antenna power supply were reached. This is because unless there is enough power coupling from the source antenna to the plasma to sustain the discharge against losses due to recombination and flow of the plasma out of the source region [2] the electron density cannot be increased further. This established the upper limit of the performance of the HPH plasma source to be mostly determined by the limitation of the rate at which power can be deposited by the source antenna into the plasma [9].

The frequency of the helicon wave in eq. 7.2 is inversely related to the background electron density, suggesting that if we increase the antenna frequency we would need to increase the background magnetic field B_0 proportionally to keep the same background density. However, increasing the background magnetic field will affect other areas of the plasma production, such as determining the plasma beta and the Alfven speed. Increasing the background magnetic field will also alter the relationship between the magnitude of the wave magnetic field and background magnetic field discussed in chapters 4 and 5, possibly altering the behavior of the wave downstream. If the background magnetic field is instead kept the same, then the expectation would be for the density in the source region to decrease. This will decrease the plasma beta as well, and there will be fewer electrons in the source region and downstream to flow in diamagnetic currents.

Because of these consequences to the plasma source production with the change in the source antenna frequency (as well as wave amplitude as seen in the following section), it is difficult to determine the relationship between the measured diamagnetic currents downstream of the source and the wave frequency by just modifying the frequency of the source antenna. Instead, for the bulk of this chapter a second helicon antenna is introduced downstream of the source antenna that can be modified independently of the source antenna. This allows for the modification of the antenna frequency of the second antenna without significantly affecting the plasma production in the source region. The introduction of the second antenna is shown to produce an increase in the performance of HPH and will be detailed in the following sections.

Section 7.2: Results from Increasing Frequency, Decreasing Antenna Current of the Source Antenna

Prior to the introduction of the second downstream antenna, the frequency of the source antenna was changed to measure some of the effects on the measured diamagnetic perturbation downstream. As described in Chapter 2, the frequency of the power supply for the source antenna is determined by the natural frequency of the LRC network formed by the source antenna and the power supply leads (the inductor) and a bank of high voltage capacitors. By decreasing the size of the capacitor bank the oscillating frequency of the tuned LRC network increases, but this has an effect on the performance of the power supply as well. As the frequency of the oscillations increases, the impedance of the inductor (the relationship between the voltage across the inductor and the current flowing through it, similar to resistance) also increases. This means that as the frequency of the oscillations in the source antenna increase, the effective resistance of the antenna also increases, making it more difficult to drive current through the antenna. This has the result that with the limitation of the power supply in terms of output power and voltage, when operating at a frequency that was twice that of the measurements taken in the previous chapters (switching to 1.2 MHz from ~600 kHz), the current oscillating in the antenna decreased by a factor of 3 and is shown in Figure 7.1.

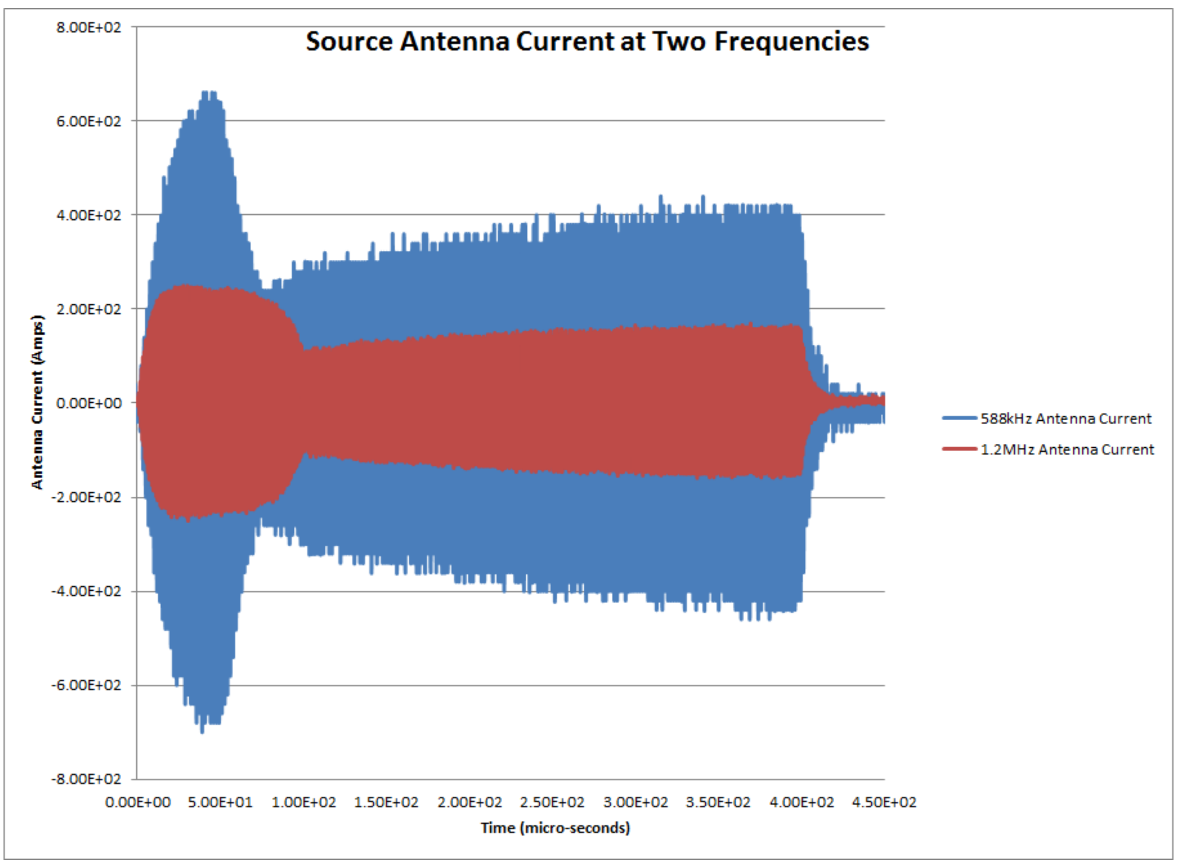

Figure 7.1: Oscillating current in the source antenna at both the frequency used for the previous results (blue) and at the higher frequency (red) measured for comparison.

With the current reduced by a factor of 3, the magnetic field driven by the antenna that couples into the plasma (as described in Chapter 2) is also reduced by a factor of 3 compared to our previous results in the earlier Chapters. This decrease in the wave magnitude resulted in a significant decrease in the ability of the source antenna to ionize plasma and eject it downstream. In addition to the change in wave frequency, this would also result in a large decrease in the amplitude of the wave fields downstream of the source compared to what was measured in Chapter 4. In order to roughly match the original loading profile of the antenna at the decreased current, the background magnetic field and the neutral density both had to be decreased by roughly a factor of 3 as well. This had significant effects on the downstream plasma profile, dropping the plasma density by roughly a factor of 3 and the diamagnetic perturbation by a factor of 3 as well.

Overall this change resulted in a dramatic decrease in performance of the HPH. The decrease in the diamagnetic perturbation as the plasma density and input wave field dropped suggests that the magnitude of the plasma wave could be more significant than the frequency of the oscillation of the wave due to the large number of coulomb collisions near the source region, and this will be discussed further when the frequency of the downstream antenna is modified below.

Section 7.3: Addition of a Second Antenna Downstream

In order to introduce an increase in the power of the helicon wave downstream without significantly affecting the plasma production in the source region as well as providing an opportunity to modify the frequency of the wave downstream independent of the source antenna, a second helicon antenna was made to be positioned downstream of the source region. A side-view of this second antenna is shown in Figure 7.2.

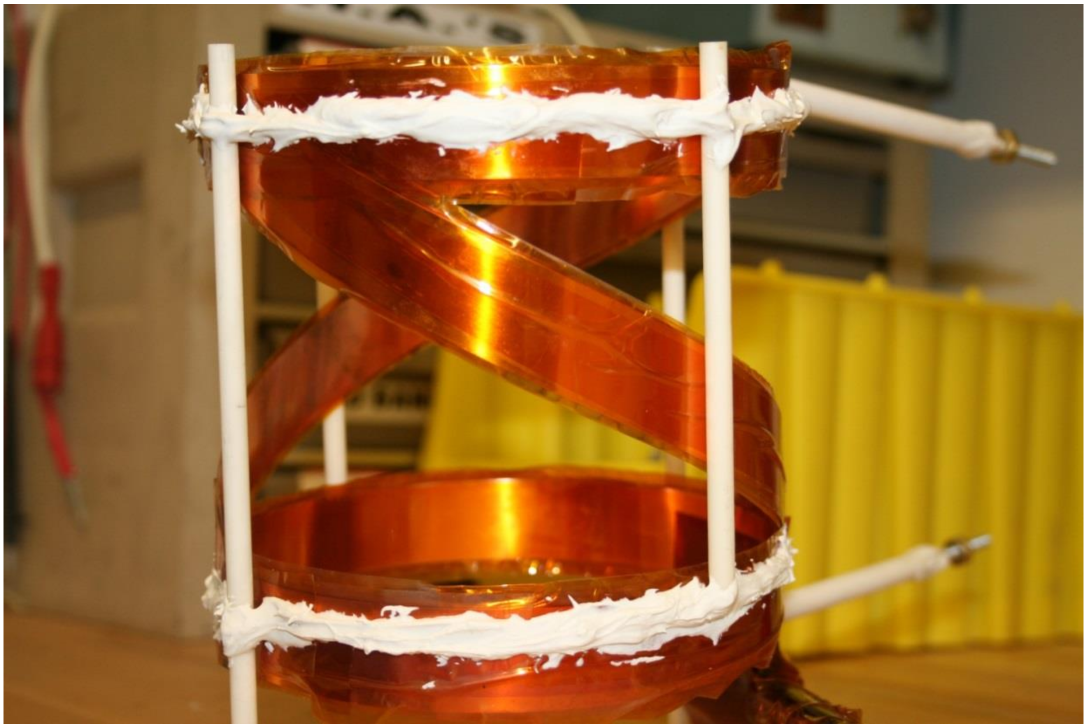

Figure 7.2: Side-view of the additional downstream antenna. It is designed to be a larger version of the source antenna (diameter is doubled) that is directly exposed to the plasma rather than wrapped around a quartz tube.

The source antenna (as described before in chapter 2) is 15 cm long and 7 cm in diameter, made of ¼" wide copper braid, and wrapped around a quartz tube to isolate it from the plasma. In contrast this downstream antenna is 15 cm long and 15 cm in diameter, made of 1" wide copper stripline, and not wrapped around an insulator. The length of the second antenna was chosen so that the wavelength of the driven plasma wave from each antenna would be the same (both antennas are half-wavelength antennas). Previous work by Prager et Al [11] has shown that the plasma wave downstream of the source helicon had a wavelength close to twice the length of the antenna, and the expectation was that the same would hold true for the downstream antenna. In the two antenna experiment performed by Gilland [31] the second antenna was shortened to drive a lower wavelength plasma wave to better couple with a higher density plasma going by the relationship in eq. 7.2. In this experiment I chose to have the antennas the same length in the hope that the two antennas could be driven together and constructively add their effects on the downstream plasma.

In order to help prevent the two antennas from destructively interfering with each other, the second antenna was placed downstream with a half-wavelength spacing between the two antennas. This required a modification to the background magnetic field from the previous nozzle work presented in Chapter 6. This new magnetic field geometry is shown Figure 7.3:

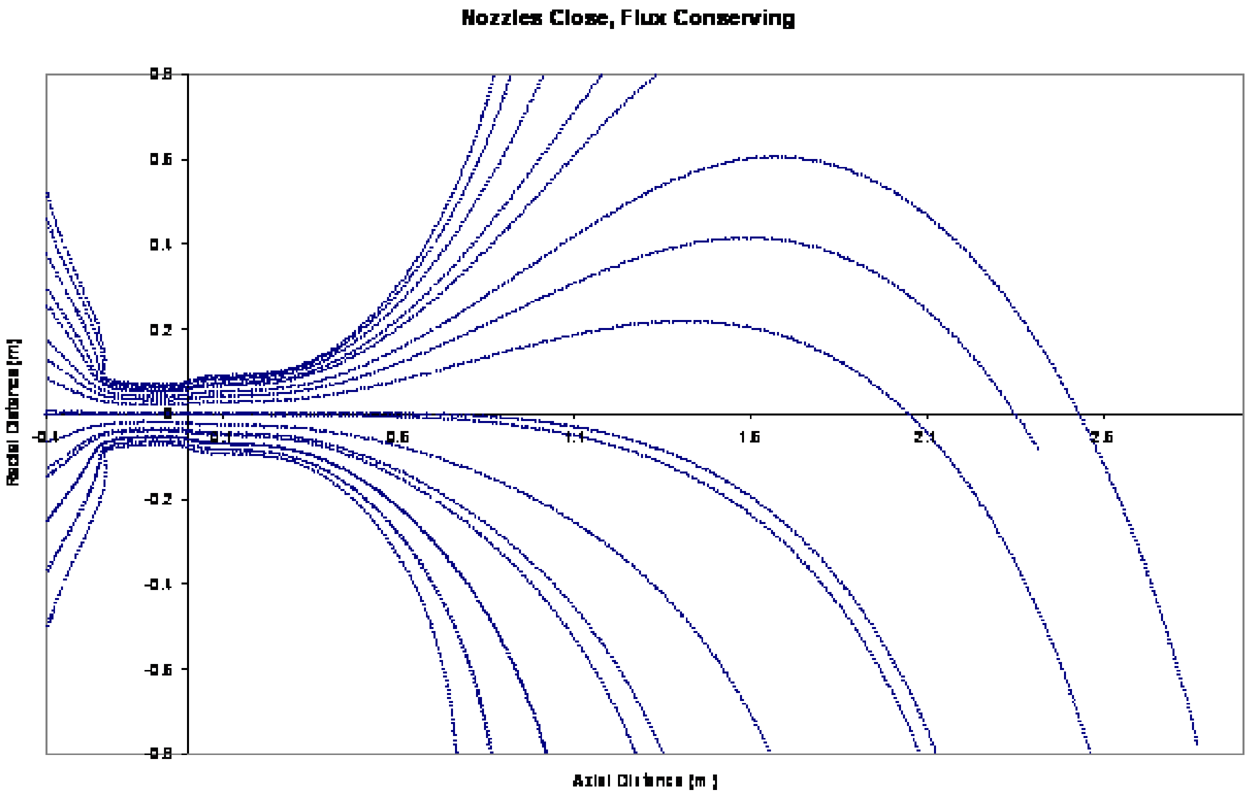

Figure 7.3: Side-view of the magnetic field geometry with the addition of the downstream antenna. The magnetic field diverges upon leaving the source region but still passes through the larger diameter downstream antenna before significantly diverging or connecting with the Earth's magnetic field more than 60 cm downstream.

In this diagram the source antenna is positioned from -15 cm to 0 cm along the axis, while the downstream antenna is positioned from 15 cm to 30 cm downstream along the axis. The magnetic field lines that pass through the source antenna (within ~3.5 cm of the axis) expand out slightly when passing through the region where the downstream antenna is positioned, but do not approach the physical boundaries of the second antenna, which are ~7.5 cm from the axis. Radial electron density profiles taken 15 cm downstream of the source region where the electrons are still well-magnetized (as discussed in Chapter 4) indicate that the bulk of the plasma is near the axis and has not expanded radially across the magnetic field a significant distance. This means that the majority of the plasma particles that exit the source region will still be near the axis when they enter the second antenna and will not have expanded far enough radially to pass outside the second antenna.

As the magnetic field from the source region and the downstream nozzles expand, the axial component of the magnetic field decreases. For the region where the second downstream antenna is operated, the magnetic field along the axis has decreased by roughly a factor of 2 from what it was in the source region, going from varying between 400-480 gauss in the source region to 200-280 gauss in the downstream antenna. In both cases the magnetic field decreases along the length of the antenna instead of being a uniform solenoid field. It was anticipated that the diverging and decreasing magnetic field would improve the acceleration of the plasma out of the source region and out of the downstream antenna region. The axial profile of this magnetic field is shown in figure 7.4:

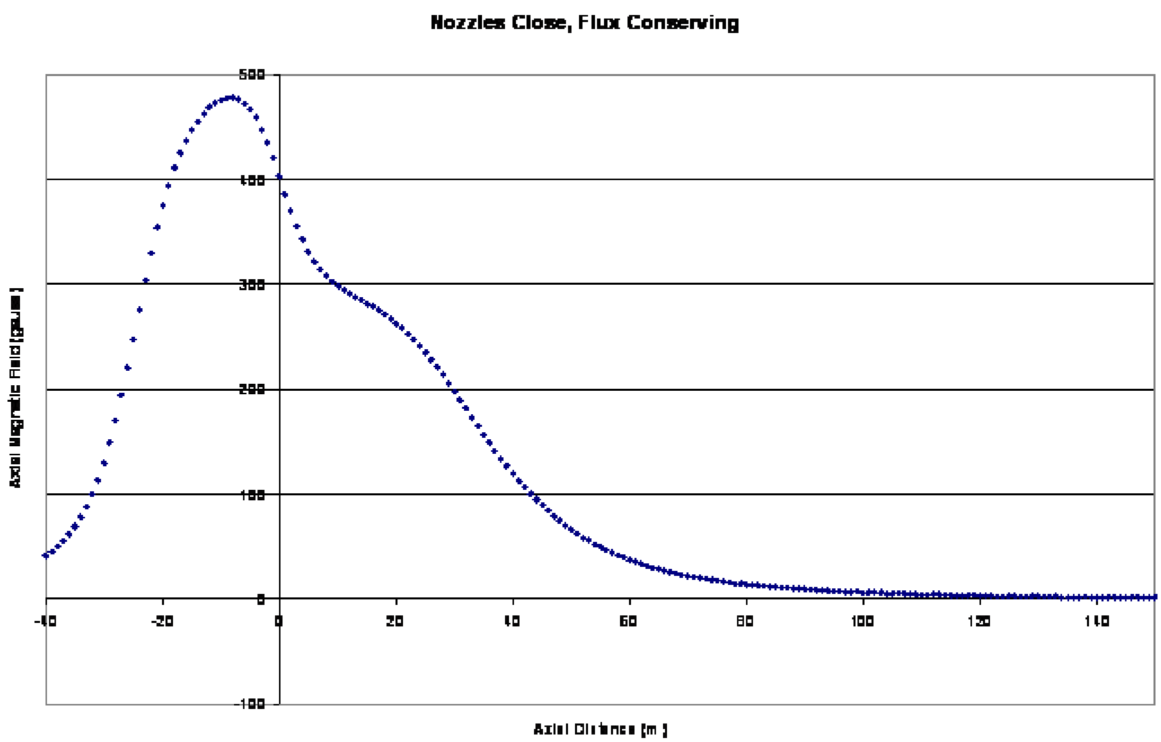

Figure 7.4: Profile of the axial component of the base magnetic field along the axis in the new configuration to support the downstream antenna. The magnetic field peaks near the rear of the source antenna and is between 400-480 gauss in the source region. The magnetic field decreases in the downstream antenna region to 200-280 gauss before falling off like a dipole field beyond the last set of magnetic coils.

The decrease in base magnetic field is necessary because the downstream antenna with its larger diameter is expected to drive a weaker magnetic field along the axis than the source antenna. Even if the same power could be coupled through both antennas, the increased volume of the second antenna suggests that the energy density of the driven magnetic field should be lower in the downstream antenna than the source antenna. In Chapter 4 it was found that downstream of the source with no nozzles present the diamagnetic perturbation was strongest when the wave magnetic field of the source along the axis was comparable in magnitude to the base magnetic field. So by having the magnetic field decrease by roughly a factor of 2 at the same time the distance from the antenna coils to the axis increased by a factor of 2, there is a better chance at keeping the ratio of wave magnetic field to base magnetic field in the non-linear regime.

Section 7.4: Initial Effect of the Downstream Antenna on Ion Energies

Initial tests of the downstream antenna were performed with the second antenna operating at the same frequency for the full 400 microseconds that the source antenna was on, being turned on at the same time as the source antenna. To compare the effect of the second antenna being active on the plasma, the argon ion energies were measured well downstream of the exit of the second antenna. It became apparent quickly that while the HPH source produced a nearly identical plasma population each shot, with the downstream antenna on the plasma population was not being reproduced in a repeatable matter. In Figure 7.5, the ion current measured by the downstream RFA is presented at four discriminator voltages, firing the system for 10 shots in succession with the second antenna on (red) compared to firing for 5 shots in a row with the antenna off (blue).

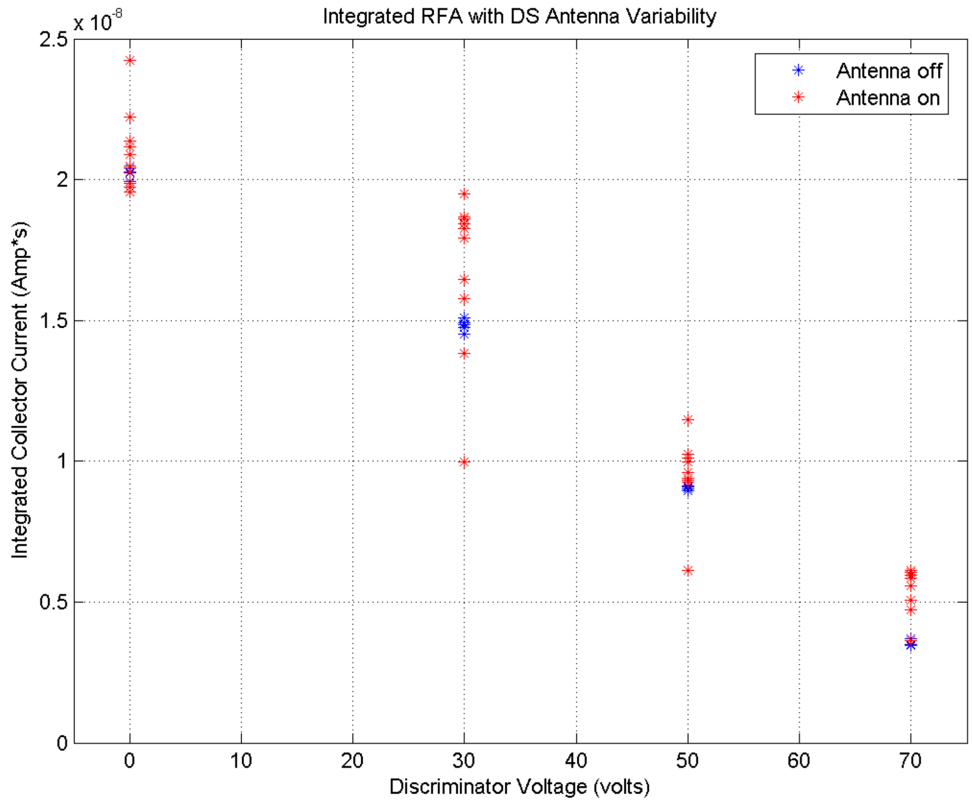

Figure 7.5: Shot to shot variability of ion current to the collector at four discriminator voltages prior to adjusting the downstream antenna. The downstream antenna is shown to be capable of both increasing and decreasing the population of energetic ions downstream, though it more frequently increases them by some amount.

For the first set of data points with 0V on the discriminator grid (where all the ions reach the collector), the total amount of argon ions reaching the downstream RFA on axis is roughly the same for many of the shots. It is expected that the total ion population is not significantly increased because the second antenna is not expected to ionize a significant amount of neutral argon. The neutral argon atoms are not expected to move beyond the source region while the downstream antenna is on because the sound speed of the neutral argon is slow compared to the short operation time of the experiment and the distance to the second antenna from the gas puff. Instead, this increase of ions reaching the detector comes from a decrease in ions drifting away from the axis missing the RFA on axis.

The next significant set of data for the ions with energies greater than 30 eV show that with the second antenna on there a significant increase in the number of ions with energies above 30 eV for the bulk of the shots taken. But at the same time, there were also examples of roughly the same amount of ions at the energy, and one significant case where there are dramatically fewer ions with energies >30 eV, which shifts both up and down of roughly 33%. This characteristic is seen again for the shots taken measuring the ion population with energies >50 eV. Depending on the shot taken, the second antenna is either enhancing the number fast ions, diminishing the number of fast ions, or doing nothing. For the case of argon ions with energies >70 eV, there was no example of the second antenna decreasing the population, but several examples of it nearly doubling the amount of energetic ions measured at the downstream RFA.

To help determine what the mechanism was behind whether the second antenna was accelerating ions, decelerating ions, or doing nothing, the loading profile of the downstream antenna was examined for 3 of the shots taken with the ion currents at different extremes. Figure 7.6 represents the loading profile where there was maximum acceleration of the ions, Figure 7.7 represents the case where there was maximum deceleration of the ions, and Figure 7.8 is the case where there was no significant difference between when the antenna was on or off.

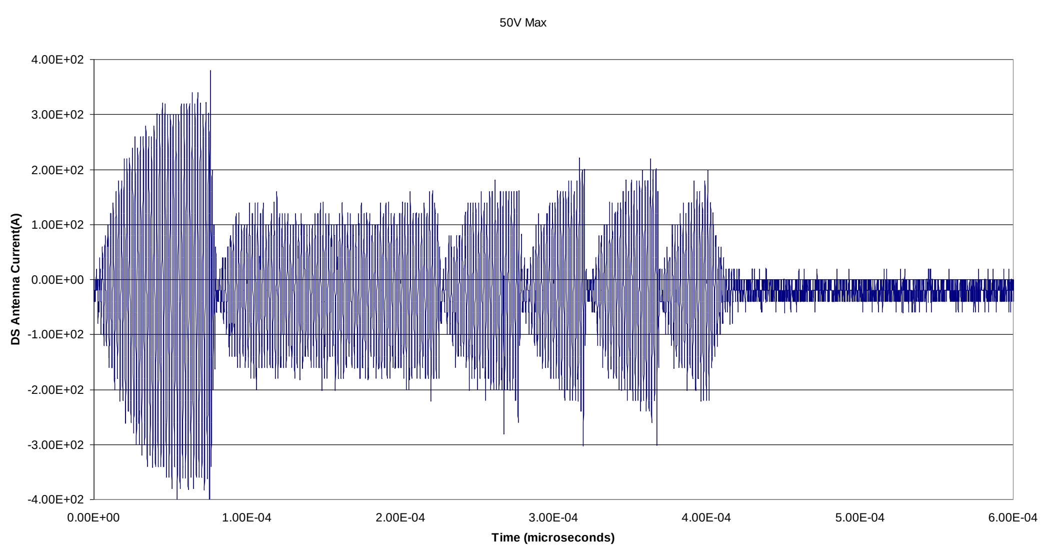

Figure 7.6: Current profile of the downstream antenna that resulted in the maximum current of energetic ions to the downstream RFA. This represents the case where the second antenna is providing a maximum acceleration to the ions.

Significant properties of this loading profile include: there is a dramatic change in the current in the antenna at roughly 80 microseconds in when the bulk of the plasma from the source antenna reaches the second antenna. For roughly 150 microseconds the loading profile is flat, but this is followed by several events when the antenna seems to change its loading profile repeatedly for the rest of the 400 microseconds.

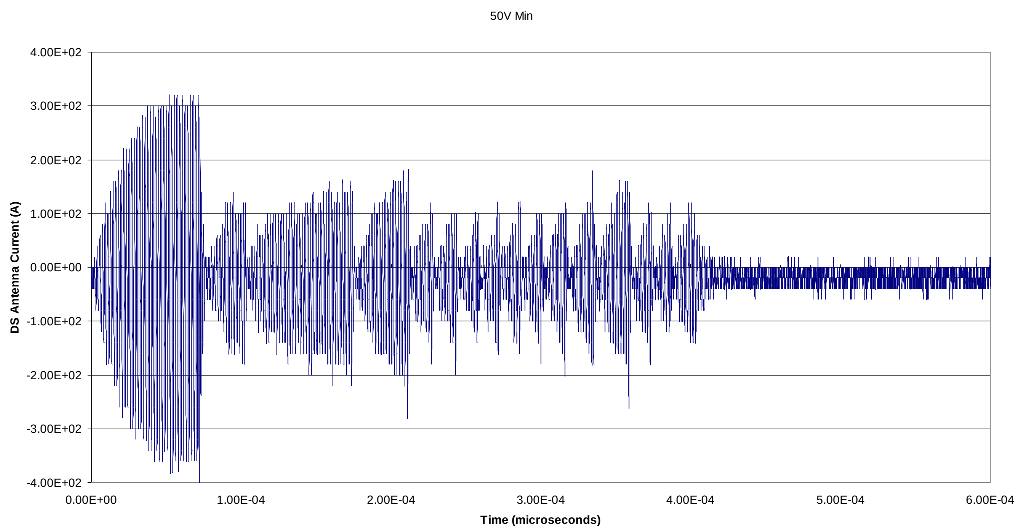

Figure 7.7: Current profile of the downstream antenna that resulted in minimum current of energetic ions to the downstream RFA. This represents the case where the second antenna is providing a significant deceleration to the ions and the plasma outflow is slower than with the second antenna turned off.

In this profile the plasma appears to arrive at the same time, but instead of a relatively stable period there is even more erratic behavior in the loading profile. It isn't immediately clear what aspect of the profile results in a deceleration of the ions rather than acceleration.

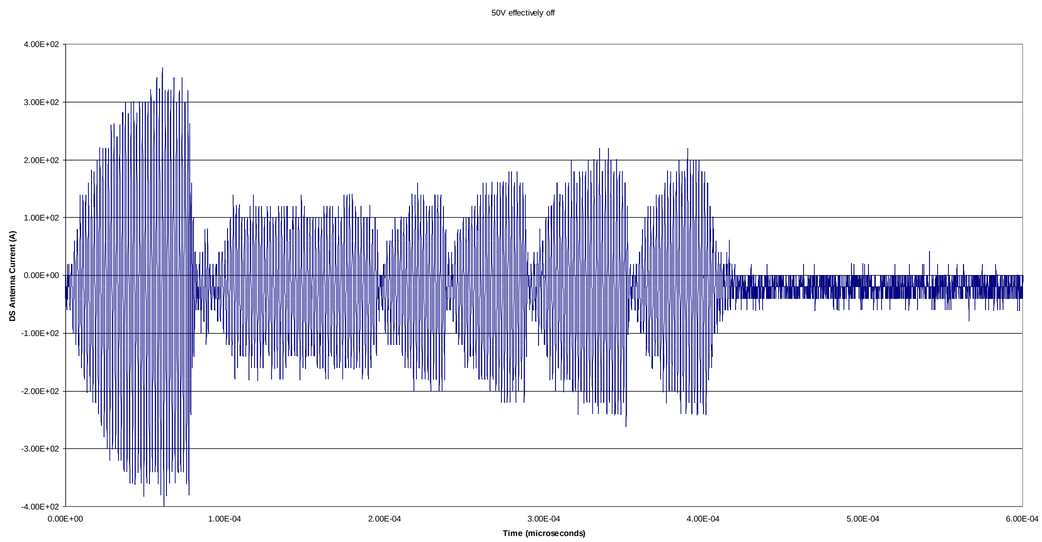

Figure 7.8: Current profile of the downstream antenna that resulted in roughly the same number of energetic ions reaching the RFA as when the second antenna is turned off. This represents the case when the second antenna is oscillating but has a net effect of zero.

In this last profile, the loading profile appears to be very similar to the profile in 7.6 which results in the maximum acceleration, with a period of loading after the plasma arrives followed by several events where the antenna appears to unload and load again repeatedly. The main difference between the two is that the profile in 7.8 does not have as long as a stable period of loading as occurred in 7.6.

By comparing these loading profiles, it wouldn't be feasible to identify the real performance of the downstream antenna unless the antenna was configured to repeatedly generate the same accelerated population shot to shot without this large variation in effect. This involved both identifying why the loading profile of the second antenna varied so much and to come up with a method to limit it.

Section 7.5: Synchronizing the Downstream Antenna

In each of the loading profiles shown above (7.6-7.8) there is a dramatic change in the antenna current profile roughly 80 microseconds after the source antenna is turned on and the bulk of the plasma from the source antenna arrives inside the downstream antenna. In these first 80 microseconds when there is plasma present under one antenna but not the second, my expectation is that the two antennas (even though they are being driven at the same time at the same frequency) are not in phase, and there is an abrupt shift when the plasma arrives under the second antenna along with the plasma wave from the source antenna. Later in the shot after the bulk of the plasma pulse has passed through both antennas and moved downstream, there is a non-repeatable series of loading/unloading events like seen in the previous loading profiles.

Because of these two properties, the second antenna is not turned on until both plasma and the driven plasma wave from the source antenna are present under the antenna, roughly 85.76 microseconds after the source antenna is turned on. Similarly, rather than leave the second antenna on and have the non-repeatable loading pattern the antenna is turned off ~160 microseconds after the second antenna was turned on when the plasma population under the second antenna has fallen off in density. Both of these values were arrived at through repeated firing of the experiment and adjusting the settings of the two antennas to arrive at a repeatable configuration of the second antenna that also resulted in an accelerated ion population similar to the maximum seen in Figure 7.5. The loading profile of this configuration is shown below in Figure 7.9.

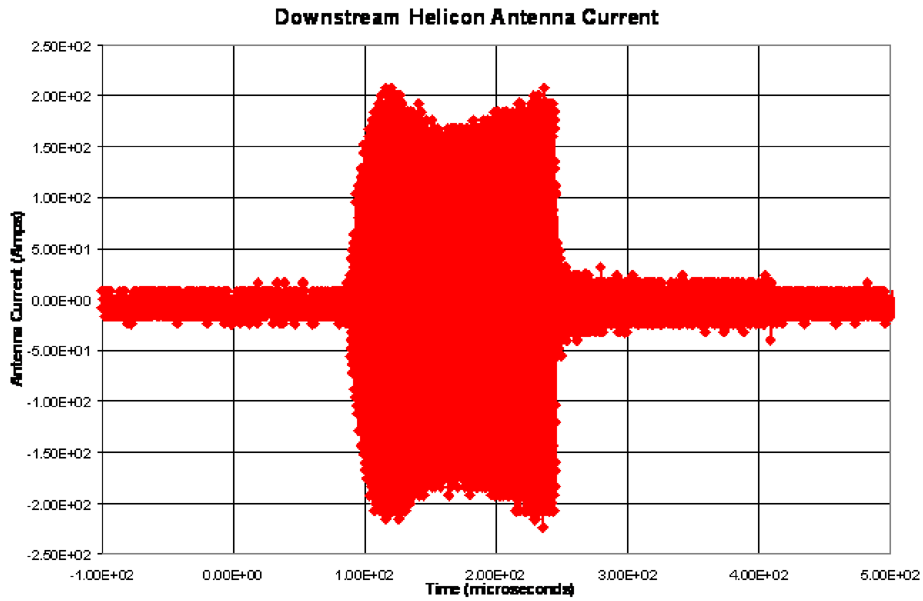

Figure 7.9: Loading profile of the downstream antenna that is repeatable shot to shot and results in a significant increase in the downstream ion energies. Note that the second antenna current is lower than the source antenna, and is only active for a fraction of the time.

The current in the downstream antenna does not ring up to as high of a current as seen when there is no plasma present under the second antenna, but the maximum current measured (300-400 Amps peak to peak) is higher than what was observed during the relatively stable loading region in Figure 7.6 by 50-100%. There is some variation in the loading profile as the bulk of the plasma arrives and leaves similar to that seen in the source antenna when the neutrals are ionized and then ejected from the source region. For comparison, the loading profile of the source antenna for the same configuration is show below in Figure 7.10:

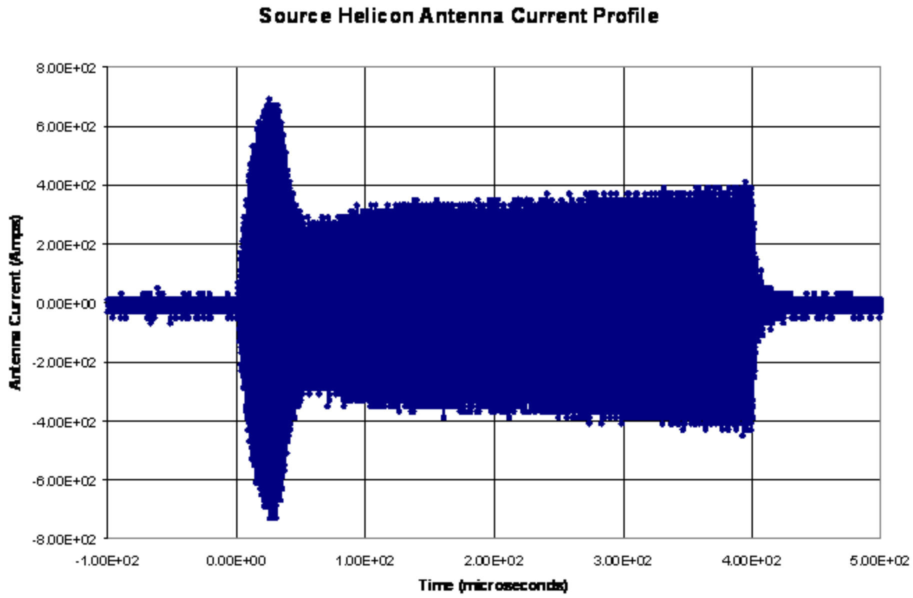

Figure 7.10: Loading profile of the source antenna. This matches closely with the loading profile measured with the data taken in the previous chapters and can be directly compared.

This loading profile matches closely with what was previously measured for the source region in the previous chapters when the source antenna was on for 400 microseconds. There is significantly more current oscillating in the source antenna compared to the downstream antenna, and the source is continuing to ionize neutrals into plasma for 150 microseconds after downstream antenna is turned off. Unfortunately the downstream antenna was not able to reliably load in that period to keep accelerating the ion population made late in time. This configuration of the two antennas was repeatable shot to shot comparable to the previous data presented in the earlier chapters with just the source antenna.

Section 7.6: Increased Ion Velocities with the Downstream Antenna

With this new repeatable configuration a series of shots was taken and the ion energy distribution function of the ions downstream of both antennas was measured similar to the data presented in chapters 5 and 6. The current profile at the RFA on axis at a time of peak signal is shown below in Figure 7.11:

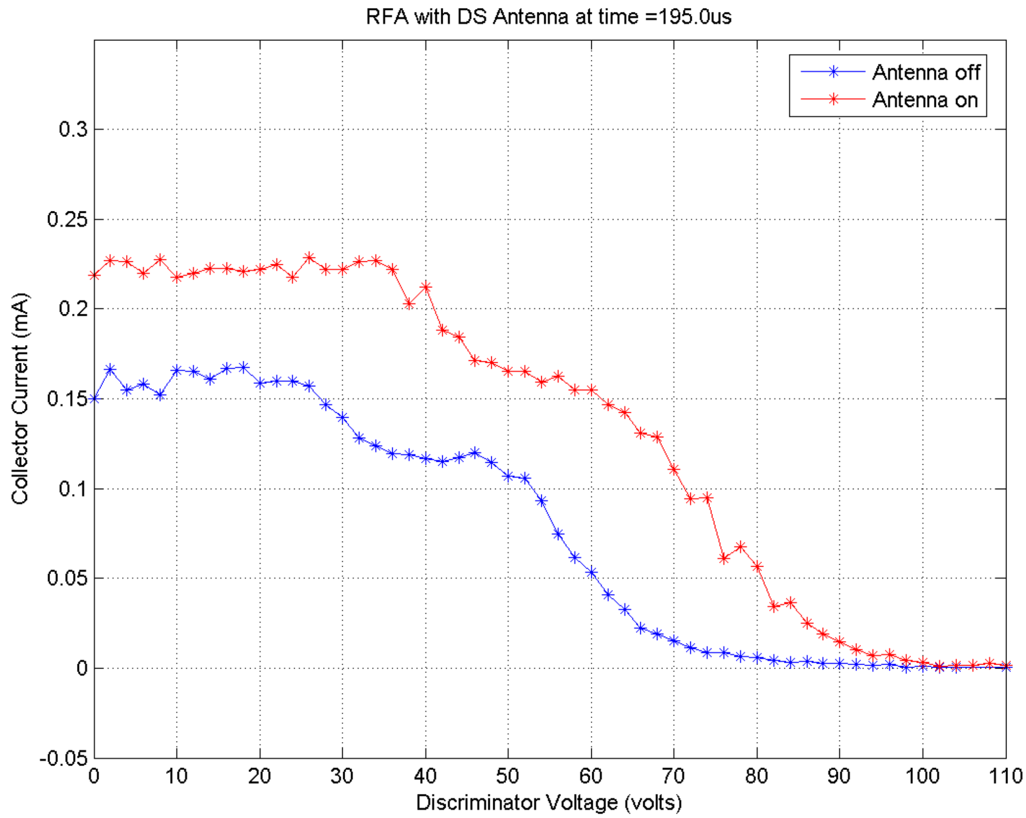

Figure 7.11: Current to the downstream RFA as a function of retarding voltage at a characteristic time for the case of the second antenna being turned on (red) and off (blue). There is a significant increase (~30%) in the downstream ion population reaching the detector on the axis, as well as an increase in the ion directed energies.

The current profile indicates that there were more ions arriving at the detector on axis at the peak, and that the majority of these ions were at a higher energy than those seen with just the source antenna operating. By taking the derivative of the current profile at the detector we can obtain an ion energy distribution at this characteristic time, which is shown below in Figure 7.12:

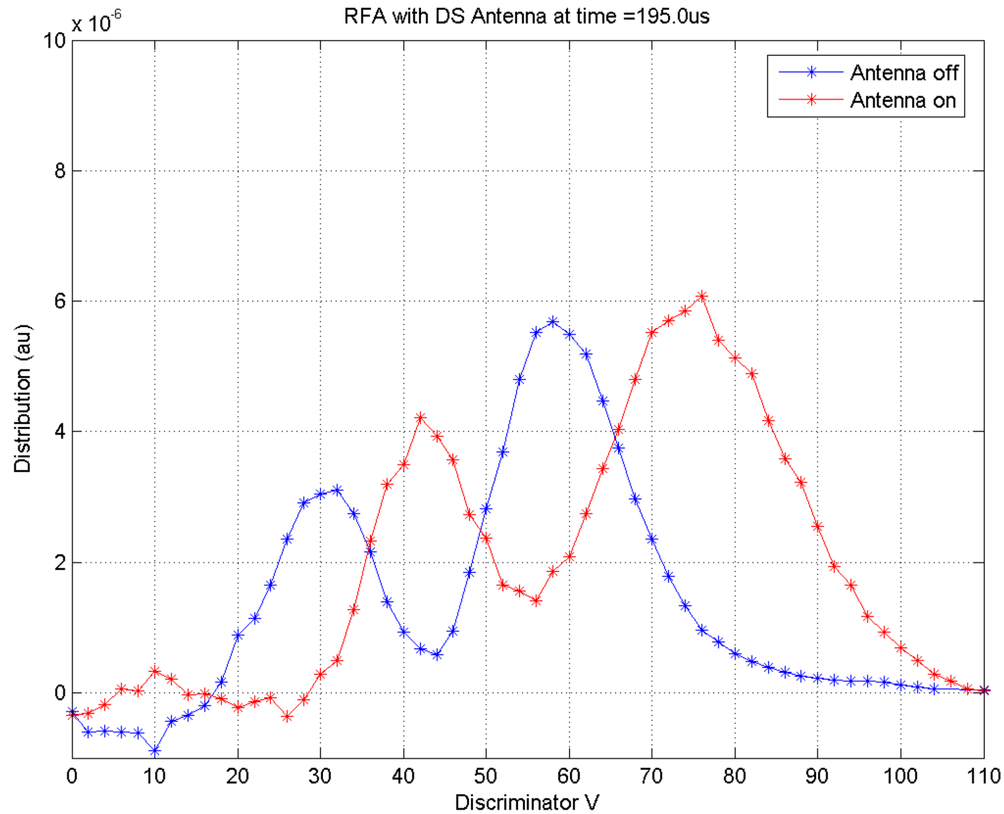

Figure 7.12: Ion energy distribution function in arbitrary units with the downstream antenna powered on (red) and off (blue). There is a shift to higher energies for both the slower population of ions and the faster population.

The ion population is clearly divided into two-peaked distributions for both cases of the antenna being on or off, and is likely a result of the changes made to the magnetic nozzle configuration to get the second antenna implemented. Since the more energetic peak is at twice the energy of the lower energy peak in each case, the most likely explanation is that the lower peak is the result of doubly-ionized argon entering the detector at the same velocity as the singly ionized argon. The RFA uses a retarding potential to measure directed ion energy, so the doubly ionized particles would be stopped at half the potential as the singly ionized argon if both are travelling at the same speed (and the current signal appears higher than it should because each doubly ionized argon contributes a much larger signal than the singly ionized argon ions. Introducing the more confined nozzle configuration likely resulted in increased ion collisions near the axis that doubly ionized a small fraction of the total ion population after the ions had already been accelerated, resulting in a two peaked distribution whether the second antenna is on or off.

The case of the second antenna being on (red) has the singly ionized population shifted up by ~ 20-25 eV. Additionally, the width of the population is broader in the case of the second antenna being on with an extended tail with some ions having >100 eV. Making the same assumptions made earlier with respect to the RFA (no significant plasma potential acceleration, singly ionized argon, etc), the ion energy distribution function can be converted into an ion velocity distribution function for the same time in Figure 7.13:

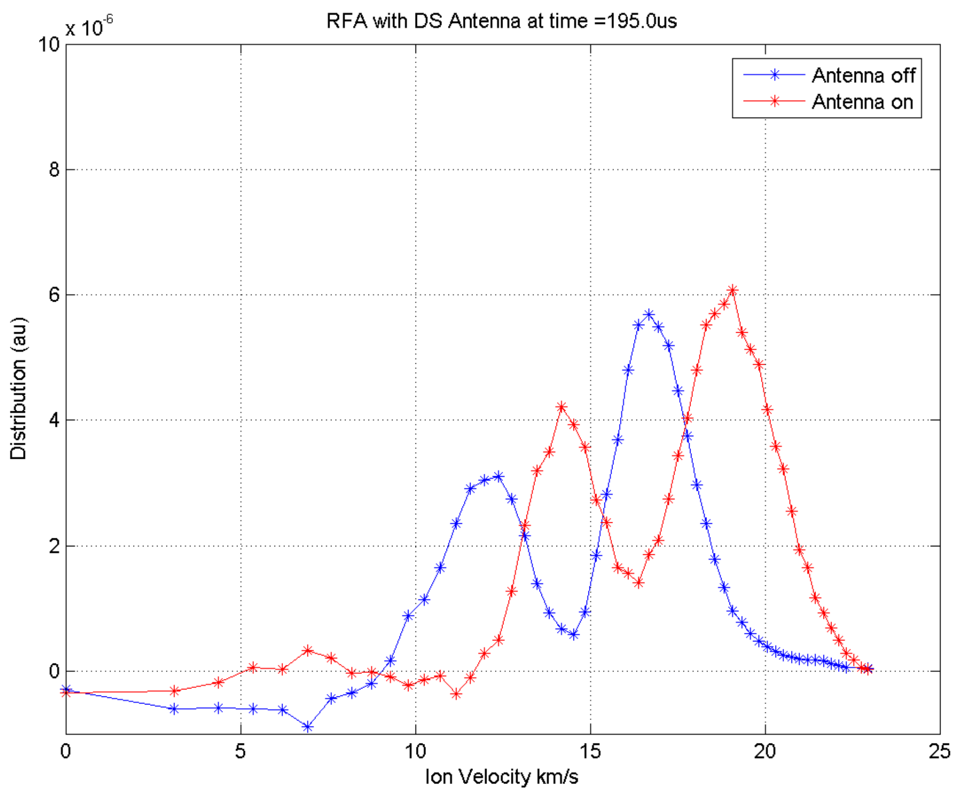

7.13: Ion velocity distribution function for the case of the downstream antenna powered on (red) and off (blue). The ion population is 2-5 km/s faster with the second antenna on.

It's clear in this result that the ion population has been accelerated by the downstream antenna by several km/s in the downstream direction. The bulk of the plasma population is travelling 18-22 km/s which is a significant increase over the velocities previously measured with HPH using only one antenna. A more detailed description of the ion energies as a function of time will be presented later in this chapter in section 7.11.

Section 7.7: Improved Collimation of the Beam with the Downstream Antenna

In addition to the increased ion velocities measured downstream of the second antenna, there was an improvement in the collimation of the plasma plume downstream of the second antenna when it was on compared to just the single antenna. The blue light emission from the ionized argon in the downstream antenna is shown below in Figure 7.14:

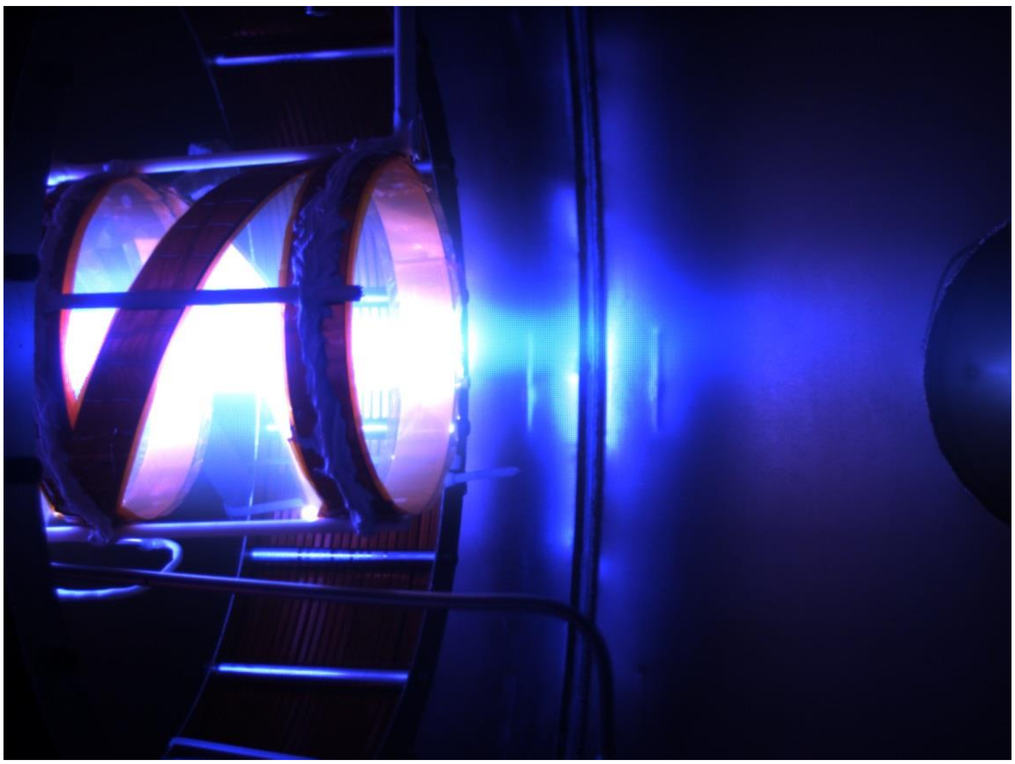

Figure 7.14: Side view of the second antenna downstream while firing. This is a 400 microsecond exposure that captures the entire experimental run, and it can be clearly seen that there is a blue column of ionized argon along the axis of the second antenna. The occasional bright spot on the antenna suggests there could be some direct interaction between the plasma and the copper of the antenna.

As described earlier in section 7.3, the bulk of the plasma is expected to be near the axis while inside the second antenna due to the magnetic field of the nozzles and this is visually apparent from the intense light emission in Figure 7.14, with only a diffuse glow off the axis and near the copper surface of the antenna. Beyond the exit of the second antenna and the magnetic nozzles, a radial profile of the electron density was made 109 cm downstream of the source where the ion energies were measured with the RFA to show the collimation of the beam more than one nozzle diameter downstream of the nozzle exit. This radial profile is shown below in Figure 7.15 at the characteristic time shown above in the ion RFA results:

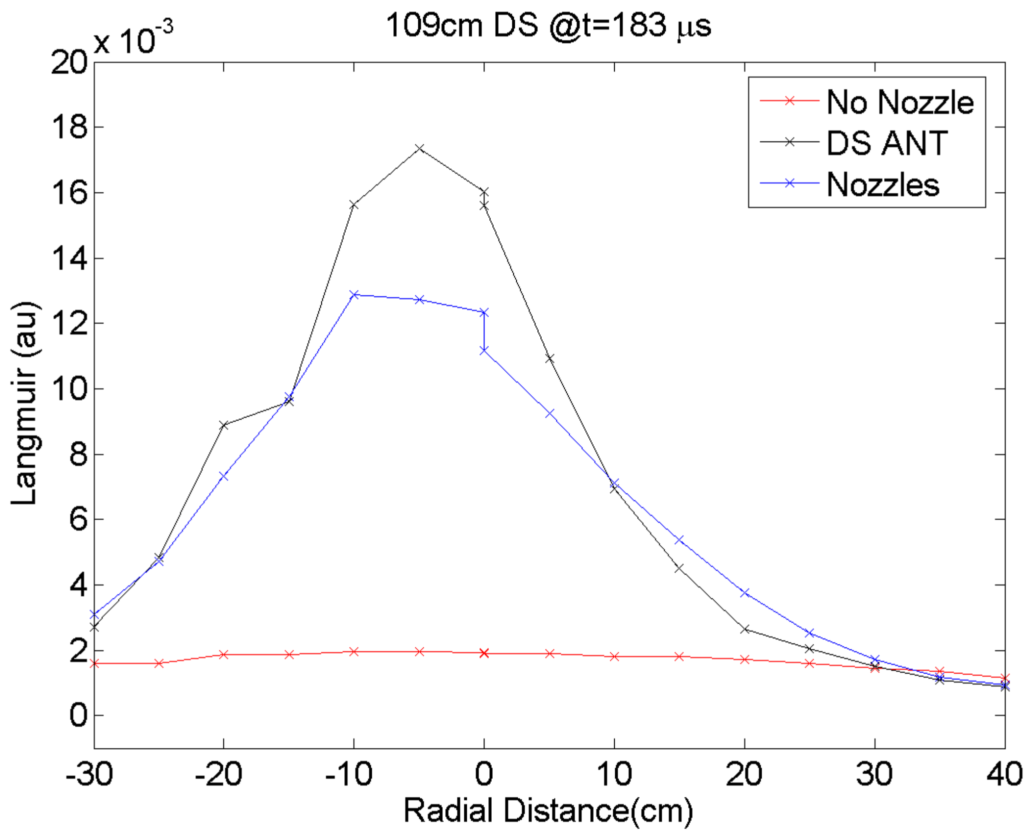

Figure 7.15: Radial profile of the electron density taken with a symmetric double Langmuir probe for the case of the downstream antenna being on (black), the downstream antenna being off but with the nozzles power on (blue), and without either the downstream antenna or the nozzles (red). There is an increase in density along the axis of ~30%; similar to what was measured with the downstream RFA at approximately the same axial location.

The trace in red shows the radial profile of the plasma with only the source antenna active and none of the magnetic nozzles similar to the plasma produced in the data presented in chapter 4. The blue trace is the plasma profile with only the source antenna on, but with the magnetic nozzles on in the configuration to support the second antenna. Lastly, the black trace is the case with both antennas and the nozzles on, showing that there is an increase in the plasma density along the axis (and decrease off axis) with the second antenna being on as high as 30%. This corroborates the increase in current measured by the collector of the RFA. Enhancing the directed ion energies and collimation of the ion population is a primary goal of this work, and the next step is to see if the magnetic diagnostics similar to those used in previous chapters can help explain the improvement seen with the second antenna downstream.

Section 7.8: Diamagnetic Perturbation with the Downstream Antenna

Using an axial magnetic field b-dot probe like the one used in chapter 4 to measure the diamagnetic perturbation to the base magnetic field, the axial diamagnetic perturbation was measured both between the two antennas and downstream of the second antenna. The mounting for the probe was too large to fit inside the second antenna, so there is a gap in the data for nearly 20 cm when the probe had to be moved around the downstream antenna. In this region the magnetic field supplied by the nozzle is large compared to these perturbations (as shown in Figure 7.4), and even though the axes in the graphs are positive, this is a diamagnetic perturbation of the background magnetic field. The diamagnetic perturbation of the axial component of the background field is shown for both the case of the source antenna only (blue) and both antennas firing (red) is plotted for characteristic times during the build-up of the shot below in Figure 7.16:

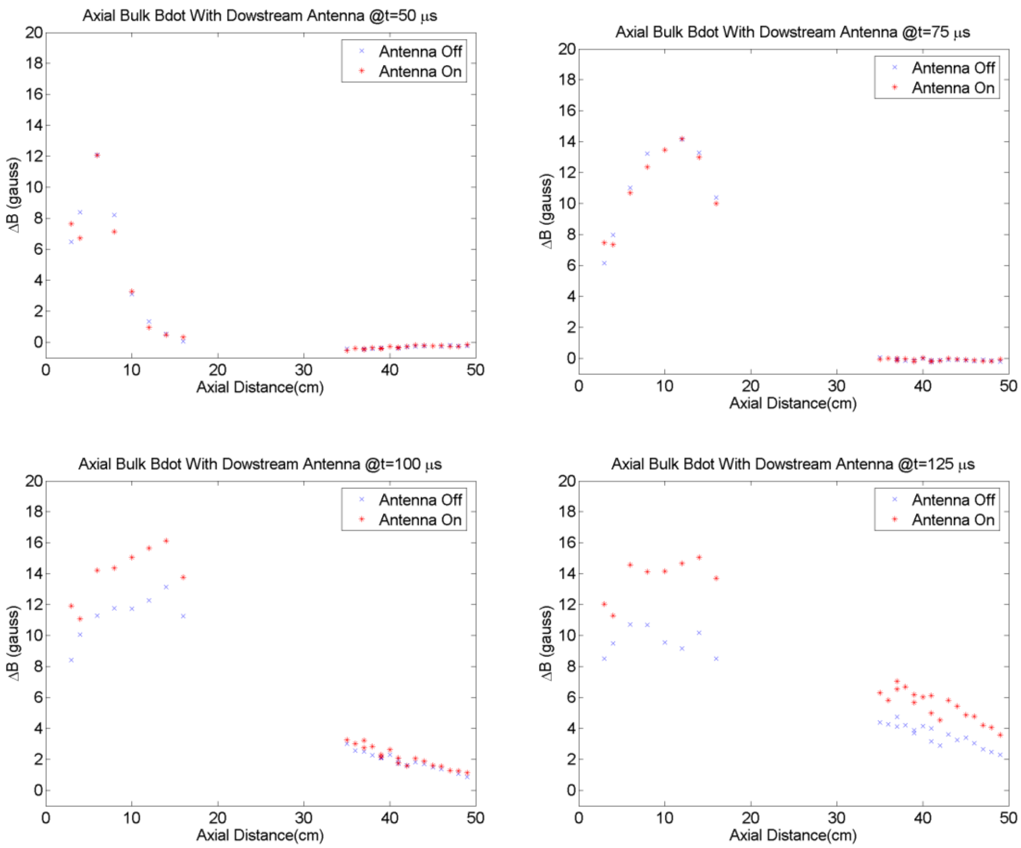

Figure 7.16: Axial component of the diamagnetic perturbation to the magnetic field taken with the axial bulk Bdot probe both upstream of the downstream antenna and downstream as well (there is a gap in data under the second antenna) for four characteristic times with the second antenna powered on (red) compared to powered off (blue). The upper two panels are taken before the downstream antenna is turned on. The lower two panels show the diamagnetic perturbation changing upstream of the second antenna shortly after turn on as well as later on when the plasma has propagated downstream of the second antenna.

In the first two panels of Figure 7.16 it is early enough in time that the plasma has not propagated all the way through the second antenna and so it hasn't been turned on yet, leading to the two traces to overlap. There is the build-up of a large diamagnetic perturbation near the exit of the source region where the magnetic field is diverging as was seen in earlier in chapter 4, but falls off axially downstream as the bulk of the plasma hasn't expanded there yet. The second antenna is turned on at ~85 microseconds in the red trace and remains off in the blue.

The second two panels of Figure 7.16 show the diamagnetic perturbation measured after the downstream antenna is turned on. In the third panel, measured ~100 microseconds after the source antenna was turned on and roughly ~15 microseconds after the second antenna was turned on, the diamagnetic perturbation between the two antennas is increased by 2 gauss with the second antenna on, a change of ~15-20%. At the same time, downstream of the second antenna the bulk of the plasma hasn't expanded far enough and the two traces are still low and roughly equal. In the fourth panel of Figure 7.16 measured at 125 microseconds the diamagnetic perturbation between the two antennas remains high for the case of the second antenna on, but has decreased for the case of the downstream antenna off, making the enhancement an improvement of ~40% in the region between the two antennas. There is also a difference in the behavior of the diamagnetic perturbation far downstream of the second antenna, with an increase of ~2 gauss again, this is an increase of ~50% over the case of just the source antenna acting by itself in the region well downstream of the antennas.

To look at the behavior of the perturbation later in time and near the turn-off of the antennas, the diamagnetic perturbation for the two cases is plotted for four additional times below in Figure 7.17:

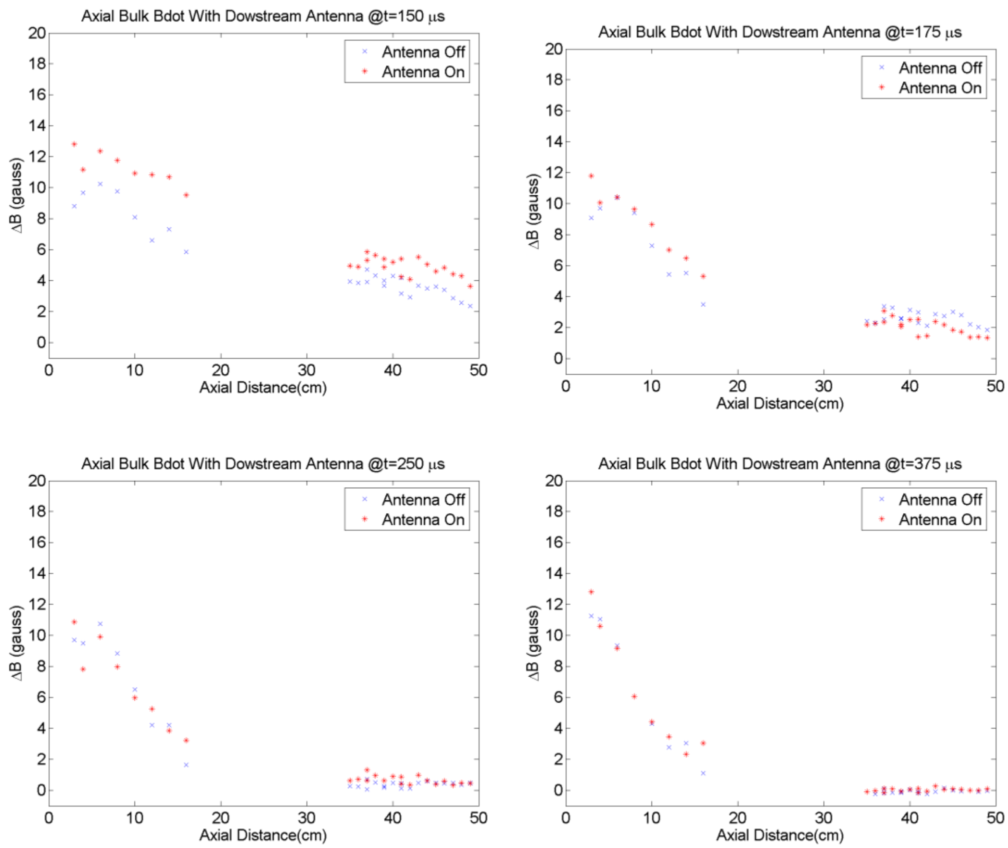

Figure 7.17: Axial component of the diamagnetic perturbation to the magnetic field taken with the axial bulk Bdot probe both upstream of the downstream antenna and downstream as well (there is a gap in data under the second antenna) for four characteristic times showing the evolution of the profile with time and after the second antenna is shut off. The upper two panels are taken before the downstream antenna is turned off and show the maximum downstream diamagnetic perturbation as well as the decrease later in time after the bulk of the plasma has moved through the second antenna. The lower two panels show the diamagnetic perturbation after the downstream antenna is shut off but while the source antenna is still active.

In the first panel of Figure 7.17, 150 microseconds into the shot the diamagnetic perturbation has begun to decrease in both traces, as the bulk of the plasma moves out from the region of the two antennas and downstream of the thruster. In the gap between the antennas there is still a ~2-4 gauss increase while downstream of the second antenna it has fallen to a difference of ~1-2 gauss, or an increase of ~25-40% over the case with only the source antenna on. In the second panel of Figure 7.17 at 175 microseconds since the source antenna turned on (and ~100 microseconds since the downstream antenna turned on), the diamagnetic perturbation has decreased to a steep fall-off between the two antennas, going from 10-12 gauss near the exit of the source antenna down to 4-6 gauss near the second antenna. Downstream of the second antenna the diamagnetic perturbation is 1-3 gauss, without a significant difference between the cases of the second antenna being on or off. This is most likely because the bulk of the plasma has moved downstream of the second antenna and the coupling between the antennas and the plasma has significantly diminished.

The last two panels of Figure 7.17 show the diamagnetic perturbation after the second antenna is turned off but the source antenna is still on. There is a steep falloff in the perturbation from ~10 gauss near the source region to 0.5-1 gauss downstream of the second antenna (which is no longer powered). This final state persists until the source antenna is shut off.

In addition to the axial profile of the diamagnetic perturbation presented above in Figures 7.16 and 7.17, there was also a radial profile made of the perturbation at 66 cm downstream of the source region, so partway between the exit of the downstream antenna and where the ion energies were measured at 109 cm. This profile was taken with a b-dot coil similar to that used in the above measurements but with a larger diameter (~5 cm) which was capable of being moved radially across the plume. The probe was pushed 20 centimeters beyond the thruster axis and then pulled across the plume in a succession of shots to make a radial cut of the axial component of the diamagnetic perturbation to the base magnetic field similar to what was done in Chapter 4 but over a larger distance from the axis. This radial profile is presented below for four characteristic times in Figure 7.18:

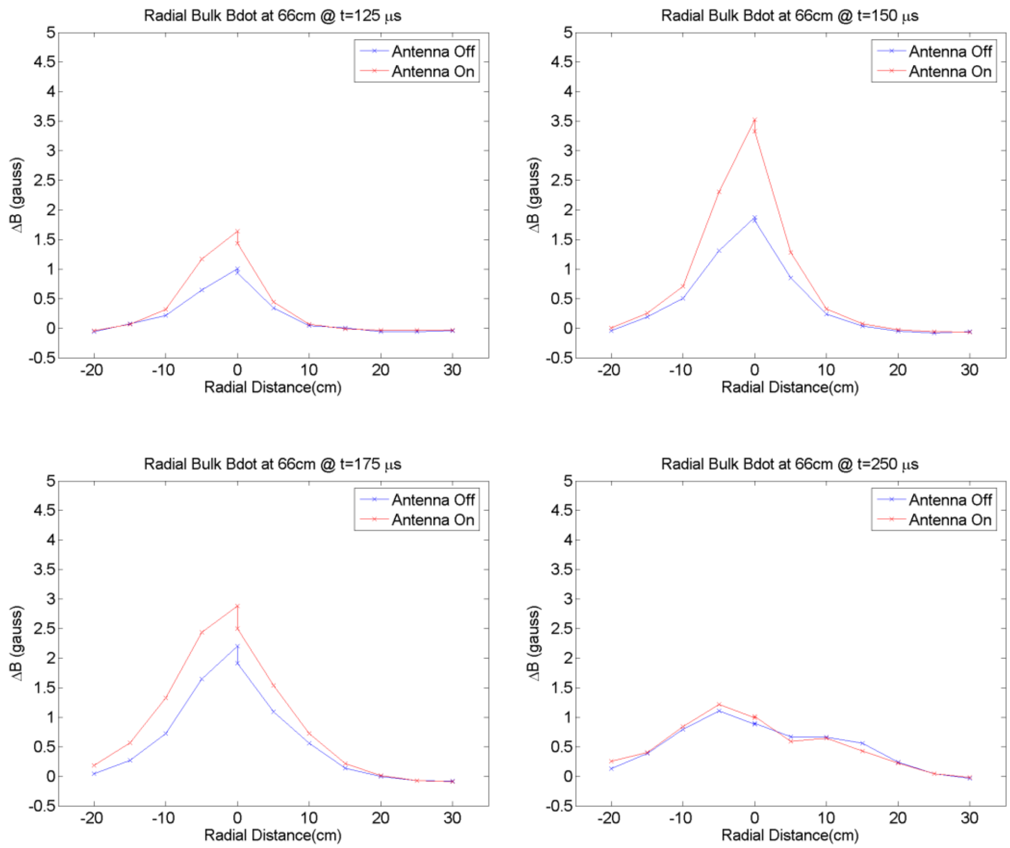

Figure 7.18: Radial profile of the axial component of the diamagnetic perturbation to the base magnetic field for four characteristic times with the downstream antenna powered on (red) and off (blue). There is a significant increase in the perturbation of the field along the axis while the second antenna is on.

The first two panels of Figure 7.18 reveal that early in time after the downstream antenna is switched on there is a diamagnetic perturbation near the axis that is increased by as much as a factor of 2 far downstream of the second antenna, but that this perturbation doesn't extend further from the axis than ~10 cm. The final two panels of Figure 7.18 show that over time the diamagnetic perturbation widens out and can be seen more than 10 cm from the axis, but by this point the magnitude of the diamagnetic perturbation has weakened. In each case, the magnitude of the diamagnetic perturbation is increased or the same with the second antenna on compared with just operating the source antenna.

Section 7.9: Wave Energy Downstream with the Downstream Antenna

In the previous results with only one antenna (Chapter 4) there was a correlation between the axial diamagnetic perturbation and the magnetic field component of the measured plasma wave at the frequency of the antenna. The diamagnetic perturbation was intense in the region where the wave magnetic field was strong, and as the total magnetic field approached zero along the axis the wave magnetic field also approached zero. With the increased magnetic field due to the magnetic nozzles, the magnetic field near the downstream antenna is too high for the diamagnetic perturbation to fully cancel out. Hence when plotting the axial diamagnetic perturbation the total field, still being high, is usually not shown. By measuring the 3 components of the wave magnetic field using the same wave bdot probe used in Chapter 4 (described in Chapter 3), an estimate can be made of the average magnitude of the wave magnetic field. This was done by integrating the magnitude of all 3 components over a period of 5 microseconds to get an estimate of the average magnitude. This wave magnitude was again correlated in time and position with the axial diamagnetic perturbation. To compare with the diamagnetic perturbation at the same time (shown in the fourth panel in Figure 7.16), the average wave magnetic field magnitude for the same time is shown below in Figure 7.19:

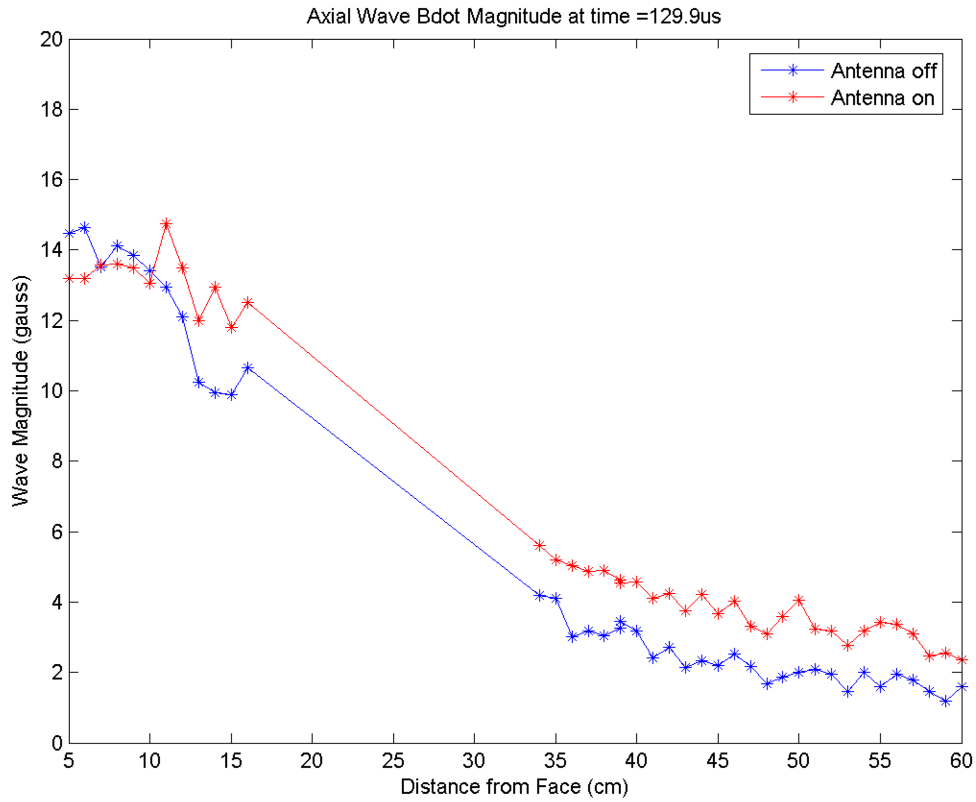

Figure 7.19: Magnitude of the rotating wave magnetic field measured with the wave Bdot probe both with the second antenna on (red) and off (blue) showing the maximum increase of the wave magnetic field downstream of the second antenna. The magnitude of the wave field downstream increases by roughly 50-100% with the second antenna on.

Even after some averaging over 5 microseconds (more than two antenna periods), this variation of wave magnetic field with position is not smooth and shows considerable variation between adjacent positions, especially between the two antennas. In the region between the two antennas there is a deviation in magnitude of the signal close to the downstream antenna, with the second antenna raising the magnitude by perhaps 20-30%. Though not exactly the same as the difference seen in the diamagnetic perturbation (~40%), this is at least comparable. Downstream of the second antenna the wave magnetic field with the second antenna on is 50-100% higher than with just the source antenna alone, which is also consistent with the difference in the diamagnetic perturbation shown in Figure 7.16.

The increase of 50-100% to the wave magnitude downstream of the second antenna within one wavelength of the second antenna suggests that the additional antenna was able to drive a plasma wave further downstream than with just the source antenna by itself, suggesting that additional wave power added downstream of the plasma source can make a significant contribution to the wave and particle population downstream of the source.

The above results were obtained after working to get the two antennas oscillating in phase at the same frequency. But despite these efforts, the second antenna would only load repeatedly for a short period of time, and in this period the two antennas were not exactly in phase with each other. The following section describes an attempt to drive the second antenna at a lower frequency than the source but near half the source frequency, so that one antenna would be operating near a harmonic of the other.

Section 7.10: Operation of the Downstream Antenna at Lower Frequency

While the source antenna and downstream antenna were both operated near 630 kHz for the previous results in this chapter, here the downstream antenna was re-tuned to oscillate at ~300 kHz. This was done by altering the tuning capacitors in the antenna power supply, but due to a limitation on the supply size and the number of capacitors available, the frequency is not precisely half that of the source antenna power supply. Despite this, operating the second antenna at the lower frequency allowed for a repeatable loading profile for much longer than was possible for the higher frequency case. This loading profile is shown below in Figure 7.20:

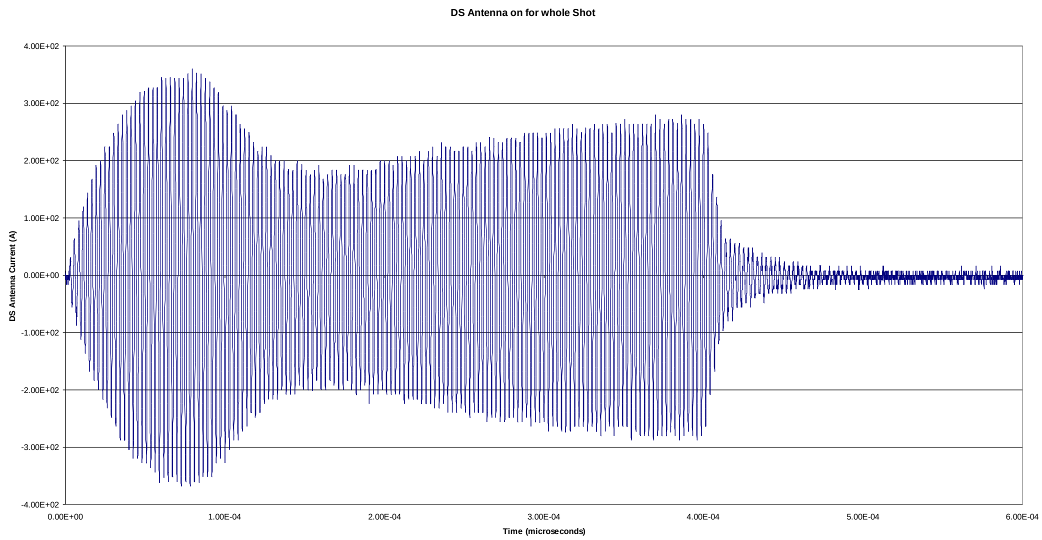

Figure 7.20: Loading profile of the downstream antenna when operated at the lower frequency (~300 kHz) compared to the source antenna for the whole 400 microseconds that the source antenna is active.

In order to compare with the data from the previous section which was operated for only a short period (~160 microseconds), measurements were also taken with the second antenna oscillating at the lower frequency but only at the same times that the higher frequency antenna was operated, this loading profile is shown below in Figure 7.21:

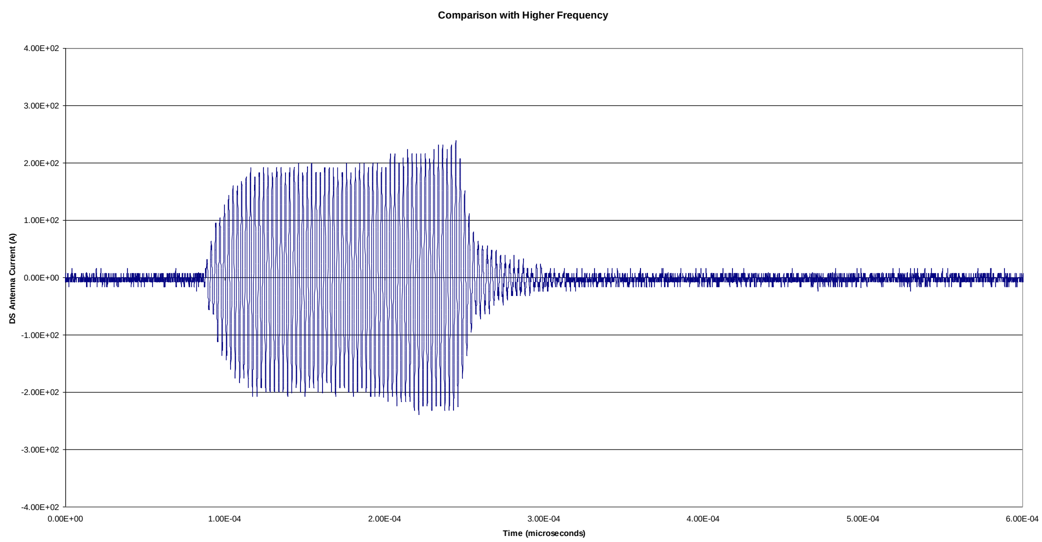

Figure 7.21: Loading profile of the downstream antenna when operated at the lower frequency (~300 kHz) compared to the source antenna for the short pulse period to compare with the results in sections 7.5-7.9, when the second antenna is only on for a short time.

In both of these loading profiles, the current oscillating in the downstream antenna is comparable with the higher frequency case during the 160 microseconds it was on, but the downstream antenna in the lower frequency case oscillated at a higher current before and after this time.

When the antenna is operated at the 365 kHz frequency roughly the same number of total ions are arriving at the downstream RFA, but there is a significant drop in the number of higher energy ions arriving compared to the high frequency case. At this point in the shot there is not a significant difference between the two low frequency profiles, suggesting that turning on the second antenna earlier did not have a large contribution to the peak plasma population. Taking the derivative of the curves and making the same assumptions as before, the ion velocity distribution is plotted below in Figure 7.22:

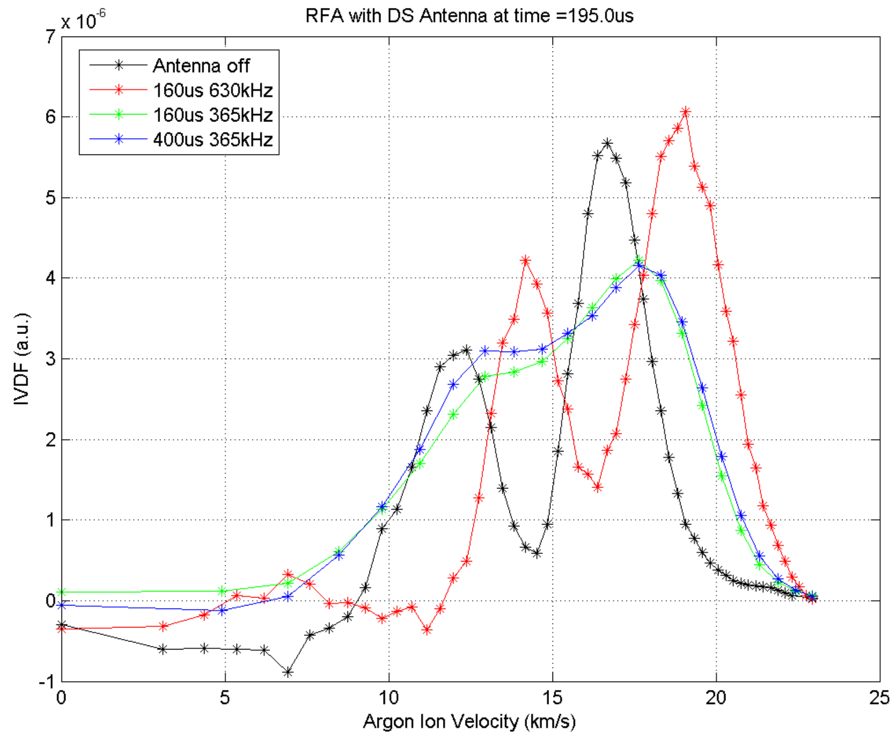

Figure 7.22: Ion velocity distribution functions measured by the RFA for the cases of the second antenna turned off (black), operated at the same frequency as the source antenna for the short pulse (red), operated at roughly half the frequency of the source antenna for a short pulse (green), and operated at half the frequency of the source antenna for the full 400 microseconds that the source antenna is on (blue).

While the velocity distribution for the lower frequency case also appears to be a two peak distribution, there is not as much separation between the peaks as there is in the case of the second antenna being turned off, or operated at the higher frequency. There are an increased number of lower energy ions seen in the lower frequency case than with the antenna off, as well as more high energy ions. This is discussed further in the following section.

Section 7.11: Ion Energy Populations and Comparison of Antenna Power:

In the previous section when the ion energy distributions were presented, it was at a characteristic time near the peak signal of the downstream RFA (~109 cm downstream of the source). In order to look at the total population of ions moving downstream, the following series of plots are the energy flux of ions within a particular velocity range:

Figure 7.23: 15-20 km/s, the bulk of the accelerated plasma

Figure 7.24: >20 km/s, the low density, higher energy portion

Figure 7.25: 5-10 km/s, the slower population seen with low frequency antenna

arriving at the detector as a function of time, giving information on whether each antenna configuration is slowing down or speeding up particles. The magnitude of the signal is the sum of the directed kinetic energy arriving at the collector.

Looking at the higher velocity components of the population, which represent the bulk of the energy arriving at the detector, the higher frequency second antenna is dominant during the time the antenna is on.

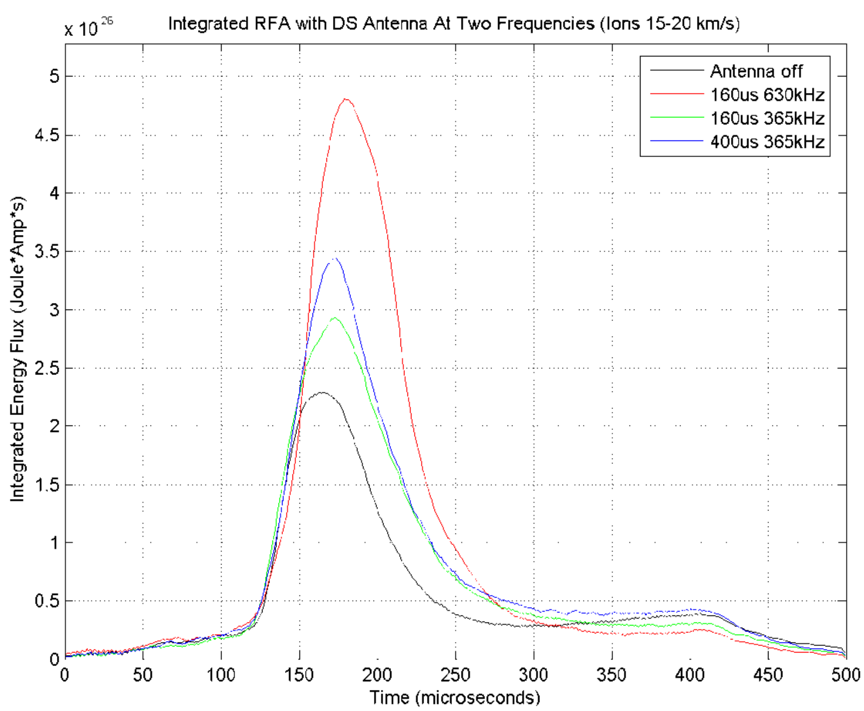

Figure 7.23: Ions with velocity 15-20 km/s received at the downstream RFA as a function of time for the four downstream antenna configurations considered.

For the ions travelling 15-20 km/s there is an exaggerated case of the high frequency second antenna increasing the energy of the particles downstream by more than a factor of two, while there is less of an increase for the case of the lower frequency antenna. The ions with velocities 10-20 km/s represent the bulk of the kinetic energy arriving at the detector downstream ~80%, and there is a definite advantage of the high frequency antenna over the lower frequency antenna (in terms of operating the downstream antenna. When looking at the highest velocity ions:

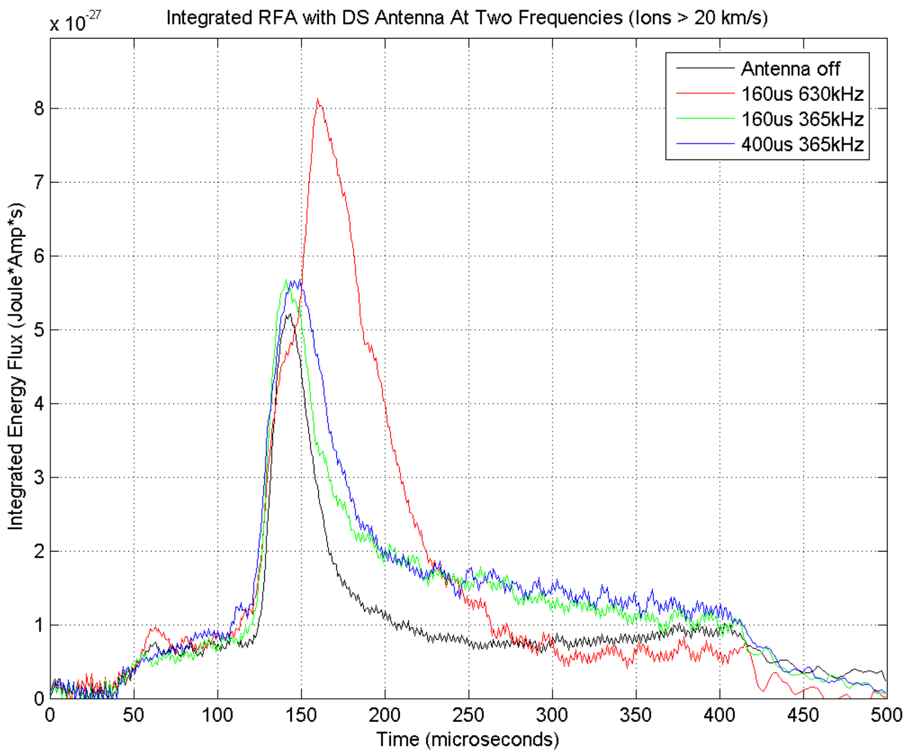

Figure 7.24: Ions with velocity >20 km/s received at the downstream RFA as a function of time for the four downstream antenna configurations considered.

there is a comparable burst of high velocity ions (>20 km/s) early in time for the lower frequency antenna and the source antenna by itself, it’s only the case of the higher frequency downstream antenna that a significant number of high velocity ions are contributing to the energy flux later in time during the bulk of the plasma flow. This suggests that the lower frequency antenna configuration is less suited to producing higher velocity ions to carry the energy flux downstream compared to more low energy ions.

To further illustrate this, we consider the lower velocity populations such as below in Figure 7.25:

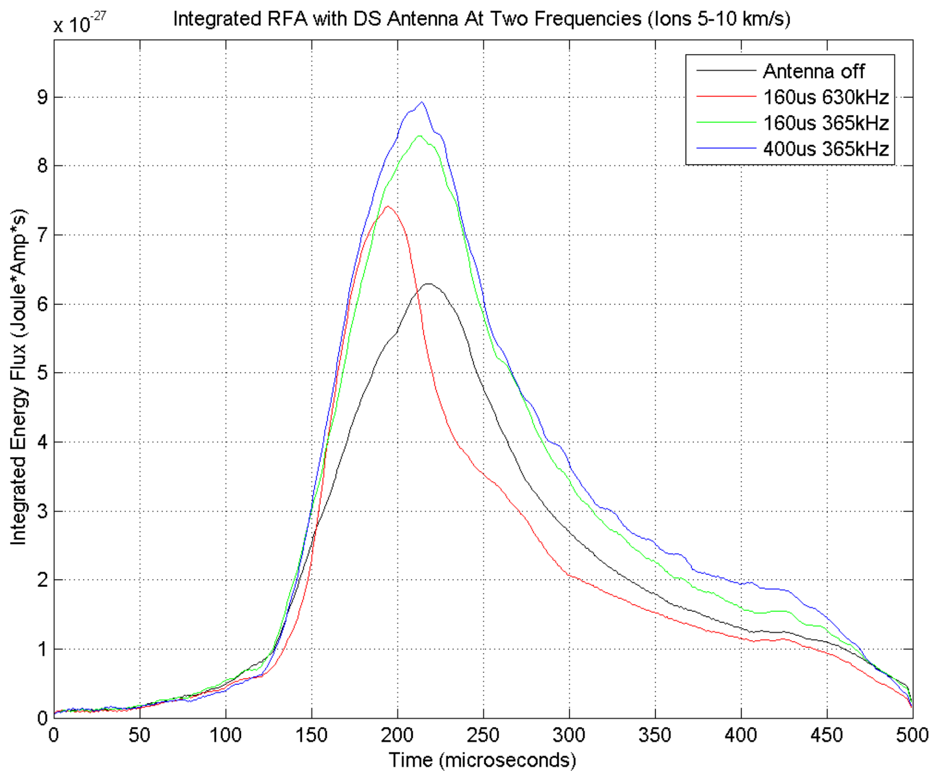

Figure 7.25: Ions with velocity 5-10 km/s received at the downstream RFA as a function of time for the four downstream antenna configurations considered.

where it is seen that the lower frequency antenna is putting more energy into lower velocity particles than the higher frequency configuration. The amount of energy coming from these lower velocity particles is only ~10% of the total energy flux.

While the second antenna is on, there is a dramatic increase in the amount of energy arriving at the collector in the form of the directed energy of ions, as seen in the large increase from 150 microseconds to 225 microseconds. The higher frequency downstream antenna has the largest contribution during this period. Later in time this is no longer the case, with the higher frequency second antenna dropping to the lowest of the four. This is the result of differing contributions between low velocity and high velocity ions to the total energy arriving at the detector. Before moving into the narrower velocity ranges, it is interesting to compare the total energy received at the collector over the entire shot for the different configurations compared to having the second antenna off (source antenna by itself).

160 microsecond pulse, 630 kHz (same as source antenna): ~32.9% increase

160 microsecond pulse, 365 kHz (roughly half the source): ~23.3% increase

400 microsecond pulse, 365 kHz (roughly half the source): ~33.6% increase

It is interesting to note that the lower frequency antenna needed to be operated for a much longer time to result in a comparable increase in the downstream kinetic energy of the particles.

To summarize, the high frequency configuration (in which the downstream antenna matches the source antenna frequency) puts more of its energy into the higher velocity ions which arrive earlier with the bulk of the plasma pulse, and seems to be the only configuration that can produce a significant amount of ions with velocity above 20 km/s later in time. In contrast, the lower frequency configuration puts more of its energy into the lower velocity particles of which some arrive much later in time and with the extended shot length can continue to put energy into ions with velocities below 20 km/s later in time after the bulk of the plasma has moved downstream. This requires the lower frequency configuration to be on for a longer period of time to achieve the same increase in the energy flux of the ions, while the higher frequency configuration puts most of its energy into high velocity ions during the short period when the bulk of the plasma is near or inside the downstream antenna. This partly explains why the ion velocity distribution for the lower frequency configuration has more fast ions than the source antenna alone, but also more slow ions than the source antenna by itself. At the same time, the higher frequency configuration is nearly just a shift upwards in ion velocity compared to the source antenna alone.

To get a rough idea of how much additional energy needed to be supplied to the experiment to account for this ~33% increase in energy flux with the second antenna downstream, we can compare the current oscillating in the source antenna relative to the downstream antenna when they were being driven at the same frequency. The measured inductances of the two antenna coils were measured to be comparable, with the source antenna at ~0.848 microhenries and the larger downstream antenna at ~0.936 microhenries (the difference is a combination of the size of the antenna compared with shape of the coil legs). When comparing the energy flowing into each inductor to sustain that current, we can come up with a rough estimate of how much additional power needed to be supplied to run two antennas in place of one.

Comparing the two loading profiles (Figures 7.9 and 7.10) during the 160 microseconds that the second antenna is on suggests an estimated 29.2% increase in power while the downstream antenna is in operation. The second antenna is not expected to contribute to the ionization of particles, so the power oscillating in the downstream antenna is expected to directly contribute the driving of the plasma wave and the acceleration of particles. This 29.2% increase in power into the system is roughly approximate to the 32.9% in ion energy flux observed downstream. One possible explanation for this is that the source antenna spends the bulk of its power in the first 80-90 microseconds just ionizing the plasma particles and accelerating them out of the source region and up to ~6.5 km/s (as discussed in Chapter 5). Then over the next ~200 microseconds the power of the source antenna went mostly into accelerating the bulk of the plasma ions up to a higher velocity and increasing the energy flux of the ions. Turning on the second antenna during this time period directly contributed to this effect, getting an increase in downstream ion flux roughly equivalent to the power going into the second antenna. The increase in the diamagnetic perturbation along the axis and the wave magnetic field suggests, just as in Chapters 4 and 5, that these are connected to the acceleration of the plasma downstream of the source antenna.

Unlike the results in the earlier chapters, we now have a comparison with a lower frequency antenna configuration of roughly the same power. Comparing the antenna current in the loading profile of Figure 7.21 to the source antenna in the same fashion of above, we can estimate that operating the second downstream antenna in the lower frequency configuration is an increase in power of ~30.5% for the 160 microseconds that it is on, but for only a ~23.3% increase in downstream ion energy flux. This is the result of the lower frequency configuration putting more of its energy into larger numbers of lower velocity ions than in the smaller numbers of high velocity particles. The result is that the lower frequency mode is less effective than the higher frequency mode in this case at building up the kinetic energy of the ions downstream even for the same amount of input power. Note that it does not decrease by a factor of 2 even though the frequency has decreased by almost half, so there is still not a simple dependence on frequency. The end result of a broader velocity distribution with the antenna in the lower frequency mode could mean that the damping mechanism is more pronounced in the lower frequency case, leading to a higher temperature in the directed energy of the ions.

So while the variation of power and frequency of the source antenna in section 7.2 suggested that input power was the dominant factor in producing the energetic plasma beam with the frequency dependence not being obvious, these results suggest that power and frequency of the antenna have a direct effect on the ion energy flux downstream and the ion velocity distribution, with the higher frequency being more effective.

Section 7.12: Limitations of the Downstream Antenna and Proposed Improvements

The most severe limitation in introducing more power into the system with a second antenna was getting the downstream antenna and the source antenna to work in concert to result in a consistently accelerated plasma population. The solution for this problem was to either only fire the downstream antenna for a short period while there was a dense plasma population connecting the two antennas, or to lower the frequency of the downstream antenna to roughly half that of the source antenna. Both of these solutions resulted in an improvement in the energy flux downstream and an increase in higher velocity ions, but the lower frequency antenna configuration resulted in less of a performance increase by making an increased number of slower ions as well as faster ions.

The limitation of only firing the second antenna when there is a dense plasma connecting the source antenna with the downstream antenna requires a dramatic improvement in the feeding of the source antenna in order to sustain that rate of flow for a longer period of time. The method described in Chapter 2 of letting neutral gas flow into the source through a tube at the thermal speed of the gas is inadequate for this task, which limited the effective shot length to ~240 microseconds. To improve on this requires a method of increasing the neutral flux into the source region to sustain this effect over a longer time period, or a way to make repeatable pulses of neutrals into the source with the antenna system only being active during those periods, to maximize the effectiveness of the pulses.

Similarly, increasing both the power and frequency of the antennas are expected to result in an improvement based on the modifications that were made to the system. The most effective way to increase the performance would be to increase the power coupled from the antenna to the plasma, while keeping the frequency the same or higher than in these results.

Together with the intense diamagnetic perturbations discussed earlier, these results indicate that increasing the amount of power into the downstream plasma results in a more extended diamagnetic perturbation and overall significant improvement in terms of exhaust velocity for the plasma and collimation of the beam. The presence of a large diamagnetic perturbation (and in some cases a diamagnetic cavity near the axis), suggests that this experiment can demonstrate some high beta plasma effects that are likely to be observed in space operation of a thruster, but are typically not seen in laboratory experiments of this type.

Cited References:

[1] Sutton, Rocket Propulsion Elements, Wiley-Interscience, 2000

[2] Prager, Experimental investigation of plasma downstream of a high power helicon, Thesis (Ph. D.)--University of Washington, 2008

[3] Chen, Physics of Plasmas Vol 1, Springer, 2006

[4] Hutchinson, Principles of Plasma Diagnostics, Cambride University Press, 2002

[5] Sovey, NASA SOLAR ELECTRIC PROPULSION TECHNOLOGY APPLICATION READINESS (NSTAR) http://www.grc.nasa.gov/WWW/ion/past/90s/nstar.htm

[6] Snecma, PPS®1350-G SPACE PROPULSION STATIONARY PLASMA THRUSTER, http://www.snecma.com/IMG/files/fiche_pps1350g_ang_2011_modulvoir_file_fr.pdf

[7] Winglee, Simulation and laboratory validation of magnetic nozzle effects for the high power helicon thruster, PHYSICS OF PLASMAS 14, 063501, 2007

[8] Ziemba, Plasma characteristics of a high power helicon discharge, Plasma Sources Sci. Technol. 15 (2006) 517–525

[9] Ziemba, Experimental investigation of the mini-magnetospheric plasma propulsion prototype, Thesis (Ph. D.)--University of Washington, 2003

[10] Prager, Ion energy characteristics downstream of a high power helicon, Plasma Sources Sci. Technol. 17 (2008) 025003 (12pp)

[11] Prager, Wave propagation downstream of a high power helicon in a dipolelike magnetic field, PHYSICS OF PLASMAS 17, 013504, 2010

[12] Chen, Generalized theory of helicon waves. I. Normal modes, Phys. Plasmas 4 (9), September 1997

[13] Boswell, Very efficient plasma generation by whistler waves near the lower hybrid frequency, 1984 Plasma Phys. Control. Fusion 26 1147

[14] Cassady, VASIMR Performance Results, 46th AIAA/ASME/SAE/ASEE Joint Propulsion Conference & Exhibit 25 - 28 July 2010

[15] Miljak, Density limit in helicon discharges, Plasma Sources Sci. Technol. 7 (1998) 537–549

[16] NIST Atomic Spectra Database, http://www.nist.gov/pml/data/asd.cfm

[17] Huba, NRL PLASMA FORMULARY, Naval Research Laboratory, 2011

[18] Wessel, Plasmoid propagation in a transverse magnetic field and in a magnetized plasma, Phys. Of Fluids, Vol. 31, No. 12, December 1988

[19] Corr, High-beta plasma effects in a low-pressure helicon plasma, PHYSICS OF PLASMAS 14, 122503, 2007

[20] Parks, Physics of Space Plasmas, Westview Press, 2004

[21] Stenzel, Electron magnetohydrodynamic turbulence in a high-beta plasma. I. Plasma parameters and instability conditions, Phys. Plasmas, Vol. 7, No. 11, November 2000

[22] Banerjee, A laboratory produced extremely large beta plasma, Phys. Plasmas 13, 092503, 2006

[23] Charles, Laboratory evidence of a supersonic ion beam generated by a current-free ‘‘helicon’’ double-layer, Phys. Plasmas, Vol. 11, No. 4, April 2004

[24] Conway, Evolution of ion and electron energy distributions in pulsed helicon plasma discharges, Plasma Sources Sci. Technol. 7 (1998) 337–347

[25] Light, Helicon wave excitation with helical antennas, Phys. Plasmas 2 (4). April 1995

[26] Choueiri, Faraday Acceleration with Radio-Frequency Assisted Discharge, JOURNAL OF PROPULSION AND POWER Vol. 22, No. 3, May–June 2006

[27] Inutake, Generation of supersonic plasma flows using an applied-field MPD arcjet and ICRF heating, Plasma Phys. Control. Fusion 49 (2007) A121–A134

[28] Arefiev, Ambipolar acceleration of ions in magnetic nozzle, PHYSICS OF PLASMAS 15, 042109, 2008

[29] Saka, Plasma flow characteristics in converging field line geometry in anisotropic plasmas, Adv. Polar Upper Atmos. Res., 19, 80-83, 2005

[30] Little, The Influence of Induced Currents on Magnetic Nozzle Acceleration and Plasma Detachment, 46th AIAA/ASME/SAE/ASEE Joint Propulsion Conference & Exhibit 25 - 28 July 2010

[31] Gilland, The effects of neutral depletion on helicon wave plasma generation, Thesis (Ph. D.)--University of Wisconsin-Madison, 2004